Analysis of energetic materials using enhanced Raman spectroscopy approaches

Ka Chuen To

University College London

Department of Chemistry

This thesis is submitted in partial fulfilment of the requirements

for the Degree of Doctor of Engineering, 2022

DECLARATION

I, Ka Chuen To, confirm that the work presented in this thesis is my own. Where information has been derived from other sources, I confirm that this has been indicated in the thesis.

Ka Chuen To

ACKNOWLEDGEMENTS

Firstly, I would like to thank my primary supervisor Professor Ivan Parkin for giving me the opportunity to pursue this EngD. I am thankful for your guidance, encouragement and letting me drive my own project. Your reassurance throughout my time at UCL has made this journey an enjoyable and rewarding one. I would also like to thank my second supervisor, Professor Chris Blackman for a warm welcome into UCL, always providing insightful discussions and useful advice. I am very grateful to all former and current members of the Parkin and Carmalt Group research group for their practical contributions and generous discussions. I must also thank the Explosives Detection Group within the Defence Science and Technology Laboratory for their sponsorship and training.

I would like to extend my gratitude to many colleagues in the UCL Chemistry Department who have provided valuable advice and help, to Dr. Steve Firth for training on the SEM, PL and Raman systems and for countless hours of discussions, to Dr. Sanjay Sathasivam for help with XPS, to Dr. Martin Vickers for help with XRD, to Dr. Kris Page for helping me with optical tensionmetry measurements and lab issues and to Dr Raul Quesada for technical discussions and scientific insights. I must also thank the staff in the Turner and Graham labs for lending me countless equipment and sharing resources during my EngD – your friendliness and willingness to help has really enhanced my research experience at UCL. I would also like to thank Dr. Sultan Ben-Jaber

for introducing me to the world of SERS and inducting me into many of the techniques covered in this thesis.

I have made some great friends on this journey, sharing the ups and downs with you guys has been an honour, may our friendship last for years to come. To John, Tarn and Mandy, thank you for taking time out to help me with characterisation and discussions. And to my friends outside of UCL, particularly Dan and Freya - thank you for keeping me sane and being there in times of need. Finally, I would like to dedicate this thesis to my family: my parents, sister and brother have been nothing but supportive. Mum – you have been an inspiration for everything I do and I thank you for standing by my decisions.

ABSTRACT

Explosives remain a threat to homeland security, and recent events emphasize the importance of explosive trace detection (ETD) technologies and the need to identify novel approaches. Surface-enhanced Raman spectroscopy (SERS) is a promising technique with many favourable qualities such as: high sensitivity, selectivity, portability and fast analysis times. This thesis focusses on SERS and PIERS, and is divided into three workstreams, described below.

The first experimental chapter explores the relatively new technique, photo-induced enhanced Raman spectroscopy (PIERS), which has received much attention for providing enhancement levels greater than conventional SERS. The chapter details a study into the PIERS effect using a commercially available material. This chapter also identifies two well-known limitations associated with metal oxide semiconductors used for PIERS and the successful solutions described in this chapter have been tentatively proposed as two new variants of PIERS. Furthermore, the potential applications of these modifications have explored for homeland security and environmental monitoring.

Chapter 4 describes the synthesis and characterisation of ZnO nanorods as novel substrates for PIERS. Doped ZnO samples were prepared through chemical bath deposition to produce uniform nanorod structures with high crystallinity. The samples were characterised on a structural and elemental level. Comparison of the PIERS properties showed the doped ZnO samples provided a higher level of enhancement compared with undoped ZnO.

Chapter 5 describes a dual method for detecting explosives using colorimetry and SERS. The assay exploits the formation of a complex between the nitro moiety of nitroaromatic explosives with a ligand, producing a coloured complex. To demonstrate the potential for the assay in real-world applications, a machine-learning algorithm was used to confirm the collected SERS data to be suitable to achieve a high level of detection. Furthermore, a simple image-analysis software was used to show the colorimetric analysis can be easily achieved using a smart-phone camera without modifications.

IMPACT STATEMENT

The detection of trace quantities of explosives is important in many fields, including forensics, environmental monitoring, as well as during the manufacture and storage of explosives. As such, there is a continuing need to improve existing ETD technologies as well as maintain efforts to identify new approaches.

The research described in this thesis has provided new fundamental understanding into a relatively new technique called PIERS. This research has reported the first study into the effect of chemical environment and substrate design on PIERS activity, which opens up a new area of research to optimise PIERS substrates. Furthermore, this formative study can aid colleagues in the research community when considering use of similar materials as sensors and even direct focus on the emergence of a PIERS detection system alongside development of standalone novel substrates. In the latter part of the thesis, doped materials are reported as potential PIERS substrates and these materials add to the relatively limited examples in literature. The work has explored the potential applications in homeland security and environmental monitoring.

There is a continuing need to develop efficient colorimetric kits for the detection of explosives and there is a growing interest in overcoming limitations in selectivity by combing colorimetric sensors with more analytical techniques. The dual colorimetric and SERS assay presented in Chapter 5 shows an alternative approach to detect nitroaromatic explosives, for which there is only one other example in literature. There is a growing trend in the

use of machine learning (ML) tools in many fields including interpretation of sensor data. As such, the availability of open source and accessible ML libraries has become more widely available, making it easier for ML tools to be used with limited prior knowledge. There has also been a growing interest in exploiting the capabilities in conventional smartphones for use as sensors. These trends have been embodied through the work described in Chapter 5, where a SERS assay for the detection of explosives has been developed and subsequently made more practical by utilising ML tools and a smartphone camera to demonstrate the feasibility of automated detection.

Overall, the work in this thesis can benefit not only the academic community but also science and technology colleagues in defence and security. The extensive technology review, part of which is included in this thesis, compares novel approaches for contraband detection against operational requirements and the capabilities of in-use systems. Directions can be drawn on new avenues of research. The research relating to PIERS has also introduced a number of promising avenues to explore and whilst much of the work is in early stages of development, the approach to experimental design, which focused on important factors in the operational environment, may guide future approaches in explosive detection sensors.

CONTENTS

LIST OF FIGURES

LIST OF TABLES

ABBREVIATIONS

Abbreviation	Explanation
AN	Ammonium nitrate
AuNP	Gold nanoparticle
CAS	Chemical abstracts service (number)
DDTC	Diethyl-dithiocarbamate
DNT	2-4dinitrotoluene
EGDN	Ethylene glycol dinitrate
ETD	Explosive trace detection
HEPI	Helium plasma ionisation
HME's	Home made explosives
HMTD	Hexamethlyene triperoxide diamine
HMX	Octahydro-1,3,5,7-tetranitro-1,3,5,7-tetrazocine
HPLC	High-performance liquid chromatography
IEDs	Improvised explosive devices
IMS	Ion mobility spectrometry
LOD	Limit of detection
MOD	Ministry of Defence
MOFs	Metal organic framework
NG	Nitroglycerine
NMR	Nuclear magnetic resonance (spectroscopy)
PETN	Pentaerythritol tetranitrate

PIERS	Photo-induced enhanced Raman spectroscopy
PTFE	Polytetrafluoroethylene
XRD	X-ray diffraction
RDX	1,3,5-trinitro-1,3,5-triazine
SERS	Surface enhanced Raman spectroscopy
SORS	Spatially offset Raman spectroscopy
SPR	Surface plasmon resonance
TATP	Triacetone triperoxide
TNT	Trinitrotoluene
UN	Urea nitrate
UV/VIS	Ultraviolet/visible (spectroscopy)

1

INTRODUCTION

1.1 THE NEED FOR EXPLOSIVE TRACE DETECTION

Explosive trace detection (ETD) technologies play a vital role in maintaining national security. The range of explosive threats are constantly evolving and so technologies must remain relevant. Recent terrorist attacks have highlighted the dangers of improvised explosive devices (IEDs) many of which contain home made explosive (HME) materials. Acid salts such as ammonium nitrate (AN) and urea nitrate (UN), in the presence of a primary explosive or fuel oil have historically been used. Peroxide explosives such as triacetone triperoxide (TATP) and hexamethlyene triperoxide diamine (HMTD) have become popular with terrorists due to the ease of preparation from readily obtainable ingredients. Liquid explosives are also attractive to terrorists due to the difficulties with screening through containers. Ethylene glycol dinitrate (EGDN) can easily be synthesised and hydrogen peroxide, at a critical concentration, can also be used as an explosive.

ETD technologies are used at military sites, to monitor ageing and stability of munitions and to ensure safety and environmental aspects are followed. ETD technologies are also required in environmental monitoring, through waste products of munitions manufacture, as unexploded ordnance or from conflict areas. For example, explosives such as TNT can bind to soils and pose a danger to plant and wildlife and RDX readily dissolves in water which can

leach into the environment and contaminate drinking water. As such, ETD technologies can be installed at sites to monitor and quantify the levels of explosives and related components. A wide range of techniques are used, each with its own limitations and so there is a requirement to improve existing detection methods as well as maintain efforts to identify new approaches.

1.2 AIMS

The overall aim of this research was to develop new methods for the analysis of energetic materials using enhanced Raman spectroscopy approaches. SERS, and the relatively new technique, PIERS, were chosen as the main focus of research due to their potential for rapid detection and non-destructive analysis at trace detection levels. The objectives of the research were:

- To characterise the PIERS effect using a commercially available substrate.
- To overcome limitations in conventional PIERS, relating to; the time-dependent enhancement and distribution of nanoparticles on a superhydrophilic surface.
- To fabricate a novel semiconductor metal oxide substrate for PIERS.
- To explore the development of a dual mode SERS assay for the detection of explosives.

1.3 SCOPE

The thesis begins with an overview of the principles of Raman spectroscopy and SERS. To gain insight into the feasibility of the work in this thesis towards a usable sensor, there was a need to understand the detection capabilities, limitations and strengths of existing techniques. Chapter 2 provided a literature review, covering a broad range of technologies in addition to Raman spectroscopy, including animal olfaction, sensors, ion mobility spectrometry and colorimetry. Examples of systems in operational use are also presented, along with insights into their analytical capabilities.

Chapters 3-5 described the experimental work in this thesis, which is split into three workstreams. In Chapter 3, the PIERS effect was characterised using a commercially available TiO_2 substrate, Pilkington Activ™. The PIERS lifetime was determined and improved upon by conducting experiments under a low oxygen environment using a custom chamber. To overcome the issue of nanoparticle deposition on a photoinduced superhydrophillic surface, PIERS was carried out using a mask (termed m-PIERS), which resulted in higher enhancement factors. These improvements to the conventional PIERS approach were further verified by applying detection to trace explosives and the pesticide thiram.

Chapter 4 described the synthesis and characterisation of ZnO nanorods for use as a PIERS substrate. ZnO nanorods were synthesised using the chemical bath method and compared with Ag and Cu doped variants. The films were characterised using photoluminescence, diffuse reflectance spectroscopy, EDX, XRD and XPS.

And finally, Chapter 5 showed the development of an assay to detect nitroaromatic explosives using colorimetry and SERS. The dual detection assay

was tested using TNT, tetryl and picric acid. To demonstrate the potential for the assay to be used in the field, a simple paper-based sensor was developed with colorimetric analysis achieved using a smartphone camera. The robustness of the assay was further confirmed using machine learning.

1.4 PRINCIPLES OF RAMAN SPECTROSCOPY

Raman spectroscopy is a widely used chemical analysis technique which involves the collection and analysis of scattered light from a material. The main advantages of Raman include: high selectivity, fast analysis times, minimal sample preparation and the ability to analyse solid, liquid and gaseous samples. In addition, analysis is carried out in a non-destructive manner and the technique offers stand-off detection capabilities. Raman analysis can provide information on molecular vibrations, which can be used to infer chemical structure and identification, molecular interactions, crystallinity and provide quantitative analysis.

The Raman effect was discovered by Dr. Chandrasekhara Venkata Raman, who noticed light deflected off a transparent material had a different wavelength to the incident light [1]. The theory of Raman scattering can be explained through classical wave or quantum particle interpretations. The classical wave theory considers light as electromagnetic radiation and composed of electric and magnetic fields oscillating at a given frequency. The oscillating electric field component interacts with the electron clouds within a molecule, resulting in a change in the molecule's polarizability. On the other hand, the quantum particle interpretation considers light as a photon, and interaction with a molecule results in the inelastic scattering of the incident light.

1.4.1 *Classical interpretation*

For a simple diatomic molecule, the molecular motion can be modelled by considering two atoms as masses connected by a spring (Figure 1). The spring constant, 'k', which describes the 'stiffness' of the spring, represents bond strength and molecular vibrations arise from displacement of the atoms by distance 'x', from the resting equilibrium. This can be represented using Hooke's Law (Equation 1).

$$F = -kx \tag{1}$$

The negative sign shows that the force is directed opposite to the elongation. Combining Hooke's Law with Newton's second law of motion, a relation can be established showing the motion of the atom as a harmonic oscillation (Equation 2). As such, the molecule vibrates in a cosine pattern with a frequency proportional to the bond strength and inversely proportional to the reduced mass (consisting of masses m_1 and m_2).

$$\nu_{\mathrm{m}} = \frac{1}{2\pi}\sqrt{k(\frac{1}{m_1}+\frac{1}{m_2})} \tag{2}$$

The vibrational spectra of molecules arises from both the atoms and bonds in a molecule. As molecules undergo vibration, the polarizability of the molecule also changes, which is observed as changes in the emitted frequencies. When incident light interacts with a molecule, it induces a dipole moment, which is equal to that of the product of the polorizability of the molecule and the electric field of the incident light source. When expressed mathematically (not shown here), the induced dipole moment shows there are three components with different frequencies, describing two effects when incident light interacts

with molecules. These are the Rayleigh and Raman scattering effects. In Rayleigh scattering the frequency of the scattered and incident light is the same (elastic scattering). In Raman scattering (also called inelastic scattering), two outcomes are possible whereby the scattered light can be shifted to lower or higher frequency than the incident light. A decrease in frequency is known as Stokes shift, whereas an increase in frequency is known as Anti-Stokes shift. This is represented pictorially in Figure 1.

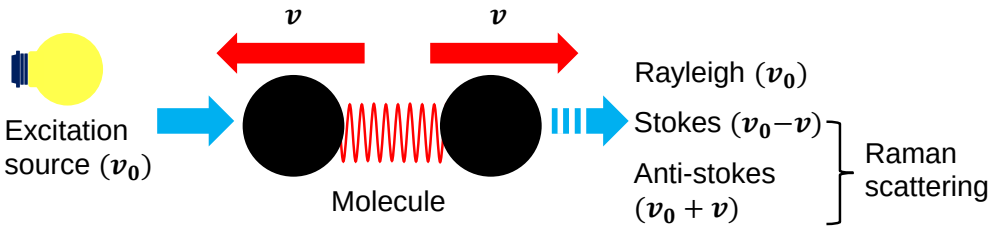

Figure 1: *Raman and Rayleigh scattering*

1.4.2 *Quantum particle interpretation*

The quantum particle interpretation of light scattering can be shown using a Jablonski diagram, by considering the excitation of the molecule through quantum energy transitions (Figure 2). Here, light scattering is considered a two-stage process. Firstly, the incident photon excites the molecule into a virtual energy state. Secondly, a photon is emitted and in the process, the molecule can return to ground state or jump to an excited state. If the energy of the scattered photon is the same as the incident photon, the process is called Rayleigh scattering. If the energy of the scattered photon is lower than the incident photon, the process is called Stokes scattering. Another possibility is the molecule already exists in excited state and is further excited to a higher virtual state, before returning to ground state. If the subsequent emitted

photon is of higher energy than the incident photon, the process is called Anti-Stokes scattering. Under normal conditions, the majority of molecules will be at ground state and so conventional Raman spectroscopy is carried out by monitoring Stokes-shifted light.

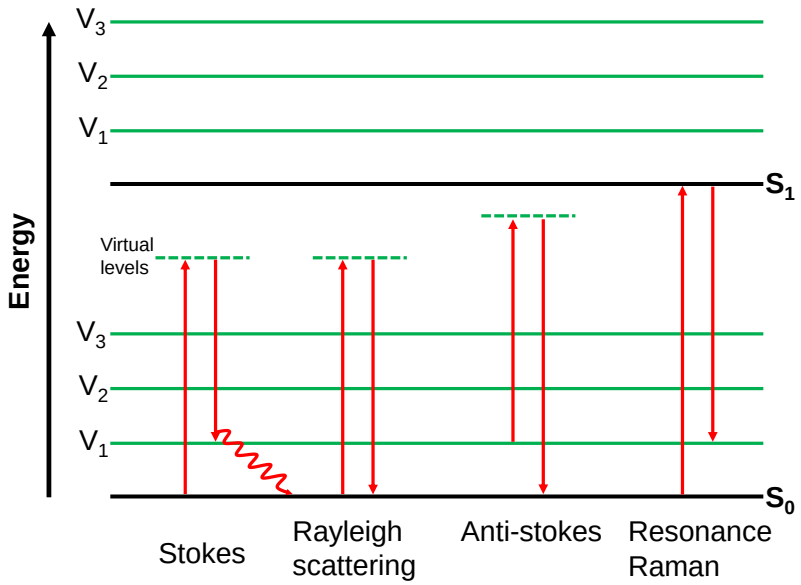

Figure 2: *Raman and Rayleigh scattering shown using a Jablonski diagram.*

Figure 2 also shows Resonance Raman scattering (RRS). RRS is one technique which can be used to overcome the weak signals of conventional Raman spectroscopy. Here, the excitation source is selected with energy equal or close to the electronic transition energy of the analyte molecule, which can induce structural distortion. Raman bands which are close to the electronic transition that is responsible for the absorption will be greatly enhanced [2]. With this approach, signals can be enhanced by three or four orders of magnitude compared to non-resonance Raman scattering [3]. Provided there is ease in switching between laser excitation wavelengths in a Raman system, RRS is a simple approach to enhancing Raman signals without the need for sample treatment or additional substrates (discussed in the SERS section below).

1.4.3 *Set-up of a Raman spectrometer*

Figure 3 shows the general set-up of a Raman spectrometer. Typically, a monochromatic laser is directed onto the sample through a series of mirrors and slits. Light scattered from the sample consists of both elastically (Rayleigh) and inelastically (Raman) scattered photons, which are collected by a CCD detector. The Raman signal shows the intensity of photons collected as a function of Raman shift and is given in wavenumbers (cm^{-1}).

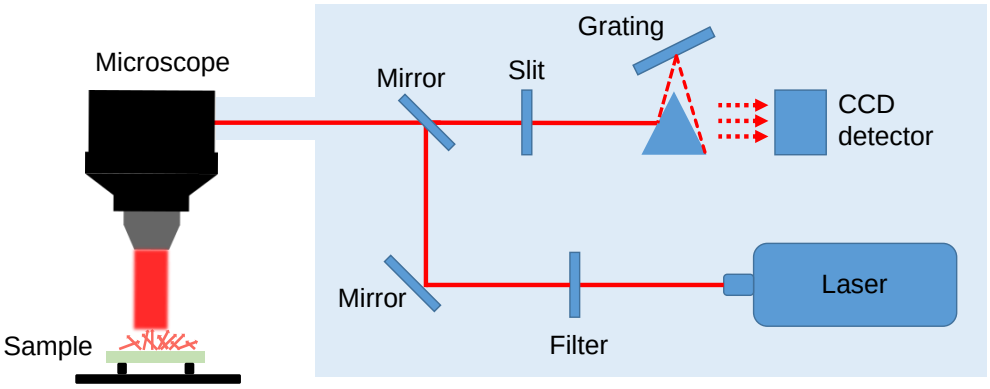

Figure 3: *Set-up of Raman system.*

As described above, molecular polarizability is a measure of how readily a molecule's electrons are displaced by an electric field. For molecules to be Raman active, there must be a change in the polarisability of the electron clouds upon excitation. For this to happen, the incident light source needs to be in resonance with the energy gap between the ground and excited electronic states of the molecule. The power of the scattered light (P_s), is equal to the product of the intensity of the incident photons, I_o, and the Raman cross-section, σ.The Raman cross-section relates the power of the incident light to the power of scattered light by the molecules, or the scattering ability, and is proportional to $1/\lambda^4$, where λ is the incident wavelength. Therefore, the probability of a photon generating Raman scatter is proportional to a molecules

Raman cross-section (Equation 3). Equation 3 shows that using a high power excitation source and a short excitation wavelength can be more beneficial in Raman spectroscopy due to the greater returns in signal strength.

$$P_{\mathrm{s}} \propto \frac{I_{\mathrm{o}}}{\lambda^4} \tag{3}$$

However, a lower laser wavelength (higher energy) can cause fluorescence interference as well as thermal and photodegradation effects on the sample, reducing detection sensitivity. Lasers with higher wavelengths (lower energy) can reduce the effects of fluorescence but may not generate enough detectable Raman scattering. As such, selection of the excitation source is important and requires careful consideration of many factors. Raman scattering is a weak process and the probability of Raman scattering is quite low. For example, typical Raman cross-sections for explosives are in the range 10^{-29} - 10^{-32} cm^2 [4], [5], whereas the absorption cross-sections of chromophores is typically 10^{-15} - 10^{-16} cm^2 [6].

1.4.4 *Vibrational modes*

For a molecule with N atoms, theoretical vibrational modes can be calculated based on the internal degrees of freedom (3N) minus the number of translational and rotational degrees of freedom for linear and non-linear molecules, as shown in the equations below:

$$n = 3N - 5\,(linear) \tag{4}$$

$$n = 3N - 6\,(non\text{-}linear) \tag{5}$$

The majority of these modes will not appear in the Raman spectrum due to symmetry effects (from the Raman selection rules), or may have small magnitudes. The resultant 'Raman active' vibrational modes provide a 'fingerprint' for each molecule, allowing for chemical and structural identification.

1.5 SURFACE ENHANCE RAMAN SPECTROSCOPY (SERS)

One disadvantage of Raman spectroscopy is low sensitivity which limits its use to bulk analysis. As a result, many techniques have been developed to enhance the Raman signal. Examples include: Coherent anti-Stokes Raman spectroscopy (CARS), shell-isolated nanoparticle-enhanced Raman spectroscopy (SHINERS), tip-enhanced Raman spectroscopy (TERS) and surface enhanced Raman spectroscopy (SERS), the latter of which will be the main focus here.

SERS is a relatively new technique with its origins being traced back to 1974. Fleischmann, Hendra and McQuillan were conducting Raman measurements using pyridine on an electrochemically roughened silver surface and found the resulting Raman signals to be unusually high and varied with the potential applied [7]. In 1997, Jeanmaire and Van Duyne *et al.* proposed the mechanism to be due to a combined surface enhancement effect and resonance enhancement from coupling of the scattering process with electronic transitions in the adsorbed molecules [8]. Similar results were also reported by Albrecht and Creighton using colloidal silver suspensions [9]. The technique has since been called Surface Enhanced Raman spectroscopy (SERS).

SERS has become a highly researched area, with diverse applications spanning environmental monitoring, defence and medicine. SERS overcomes the low signals seen in conventional Raman spectroscopy, which arise from

intrinsically low scattering cross-sections, through the use of nanoparticles or nanostructured surfaces. Noble metals such as gold and silver are typically used which can lead to enhancement factors (EF) of 10^4 - 10^6 [10]. The SERS effect arises when an analyte molecule adsorbs onto a rough metallic surface, leading to enhancement of the analyte's Raman signal. Coinage metals such as silver, gold and copper have been extensively used as SERS substrates, due to their stability, biocompatibility [11] and ease of control of optical properties [12]. The SERS enhancement is attributed to both chemical (CE) and electromagnetic (EM) contributions, with the latter giving a much greater enhancement effect [9], [13]–[15].

1.5.1 *Surface plasmon resonance*

Surface plasmon resonance (SPR) occurs when light interacts with a metal, resulting in the collective oscillation of free conduction electrons (Figure 4). In nanoparticles, where sizes are typically similar to the wavelength of the incident radiation, the plasmon resonance is localised to the particle surface and is known as localised surface plasmon resonance (LSPR). For LSPR to occur, the frequency of the incident light needs to be in resonance with the plasmon oscillation frequency. LSPR is responsible for the electromagnetic enhancement and plays a crucial role in amplifying Raman signals of adsorbed molecules.

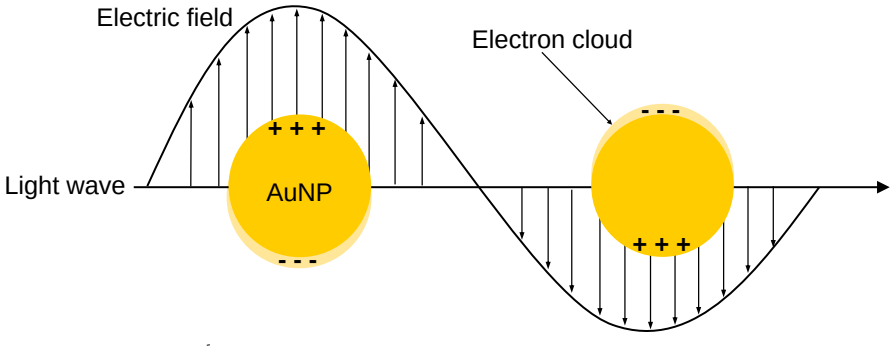

Figure 4: *Diagram of LSPR on gold nanoparticles.*

In 1908, Mie presented a solution to Maxwell's equations, relating the size and absorption properties of spherical particles to the colour observed [16]. Since then, Mie theory has been used to describe the interaction between light and nanoparticles by considering the particle size and dielectric function of both the metal and the surrounding medium. In SERS, Mie theory is used to understand and optimise the plasmonic properties of the metallic nanoparticle substrates, where optical attributes such as absorption and scattering spectra, are calculated as a function of size, shape, and material composition. This information is used to design nanoparticles which can efficiently couple with incident light and produce a strong electromagnetic field at the surface.

For metals such as Au and Ag, the plasma frequency lies in the visible region of the electromagnetic spectrum, with LSPR peak positions typically at ≈530 nm and ≈420 nm, respectively. The intensity and wavelength of the LSPR band in metallic nanoparticles is affected by changes to the density of the electron charge on the particle surface, hence, nanoparticles of different sizes will show SPR shifts and have different colours. In general, silver nanoparticles (AgNPs) produce stronger SERS intensities than gold nanoparticles (AuNPs). One reason is due to AgNPs having a higher SPR frequency which results in a larger electric field enhancement. Dissipation of the LSPR oscillation energy can reduce the performance of plasmonic materials. One factor for

this optical loss is the difference in the frequency of the band edge (at which interband transitions are allowed) and LSPR. In Ag, the band edge frequency is above the LSPR frequency, which means that localised SPRs cannot decay into electron-hole pairs as easily, resulting in stronger EM fields [17], [18]. Despite these factors, AuNPs are more frequently used as SERS substrates due to better chemical stability, biocompatibility, and low cytotoxicity, making them suitable for a range of applications.

1.5.2 *Electromagnetic enhancement*

The EM enhancement arises from the electromagnetic interaction of light with the nanoparticle, leading to LSPR [10]. This phenomenon enhances the local electric fields near the metal nanoparticle surface, in turn leading to enhancements of both the incident and Raman-scattered fields. The EM enhancement ($G_{EM)}$) can be written as shown in Equation 6 and comes from two contributions which are the local field enhancement and radiation enhancement factors, denoted as $M_{Loc}(\omega_L)$ and $M_{Loc}(\omega_R)$, respectively [19], [20].

$$G_{EM} = M_{Loc}(\omega_L) \cdot M_{Loc}(\omega_R) \tag{6}$$

When a laser with excitation wavelength close to the plasmon resonance of a metallic nanoparticle interacts with the metal's surface, the local electric field (near field), E_{Loc}, oscillating at incident frequency ω_L, is enhanced compared with the incident electric field (E_{Inc}) [10], [21]:

$$M_{Loc}(\omega_L) = \left[\frac{E_{Loc}(\omega_L)}{E_{Inc}(\omega_L)}\right]^2 \tag{7}$$

Metallic nanoparticles can act as optical antennaes, transmitting the Raman signal from the near field to far field [18]. The local electric field induces a Raman dipole, the magnitude of which is proportional to the square of enhanced electric field at the scattered frequency, ω_{R} [10], [21]:

$$M_{\mathrm{Loc}}(\omega_{\mathrm{R}}) = \left[\frac{E_{\mathrm{Loc}}(\omega_{\mathrm{R}})}{E_{\mathrm{Inc}}(\omega_{\mathrm{R}})}\right]^2 \tag{8}$$

Overall, the SERS EM enhancement consists of the local field enhancement which is related to excitation of the Raman dipole, and the radiation enhancement, which is related to the re-emission of the Raman process [10]. The enhancement factors of both components is comparable (and $\omega_{\mathrm{R}} \approx \omega_{\mathrm{L}}$ shifts being small), which means the expression can be simplified [10], [21]:

$$\begin{aligned} G_{\mathrm{EM}} = M_{Loc}(\omega_{\mathrm{L}}) \cdot M_{\mathrm{Loc}}(\omega_{\mathrm{R}}) &= \left[\frac{E_{\mathrm{Loc}}(\omega_{\mathrm{L}})}{E_{\mathrm{Inc}}(\omega_{\mathrm{L}})}\right]^2 \left[\frac{E_{\mathrm{Loc}}(\omega_{\mathrm{R}})}{E_{\mathrm{Inc}}(\omega_{\mathrm{R}})}\right]^2 \\ &= \left[\frac{E_{\mathrm{Loc}}(\omega_{\mathrm{L}})}{E_{\mathrm{Inc}}}\right]^4 \end{aligned} \tag{9}$$

Equation 9 is known as the $|E^4|$ approximation and this shows that the SERS EM enhancement is approximately proportional to the fourth power of the local electric field enhancement. Figure 5A shows the SERS EM enhancement components pictorially.

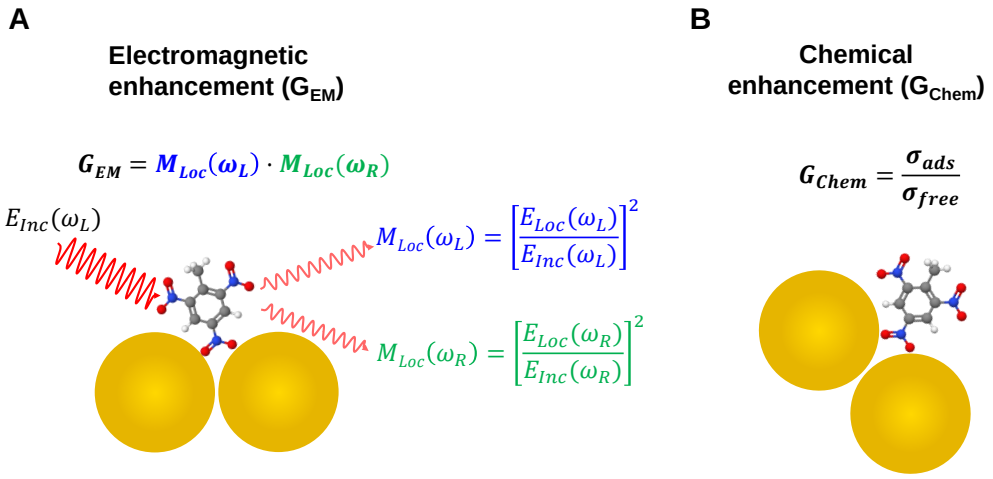

Figure 5: *Diagram showing the overall SERS enhancement is composed of the electromagnetic (G_{EM}) and chemical (G_{Chem}) enhancements: A) SERS G_{EM} arises from the close proximity of a molecule and the plasmonic material (AuNPs in this case). When a laser is irradiated onto a molecule (with electric field E_{Inc}, at incident frequency ω_L), a two-step process occurs. The first step is an enhanced local field around the AuNP at the incident frequency (excitation), and is represented as $M_{Loc}(\omega_L)$. The second step consists of the radiation local field enhancement (re-emission) and represented by $M_{Loc}(\omega_R)$. Since the presence of plasmon-enhanced electric fields near the substrate enhances both the incident and Raman-scattered fields, the intensity of a peak can be interpreted as the magnitude of the electric field squared. E_{Loc} is the amplitude of the local electric field and ω_R is the frequency of the Raman-scattered light, B) SERS G_{Chem}. Interaction between the adsorbed molecule and plasmonic substrate causes structural changes in the molecule and scattering cross-section (σ). As such, the SERS G_{Chem} is defined by a change in the scattering cross-section of molecules asdsorbed onto the plasmonic substrate (σ_{ads}) and free molecules (σ_{free}).*

1.5.3 *Chemical enhancement*

Whilst the EM enhancement is a bigger contributor to the overall SERS enhancement, the chemical enhancement provides in-depth information on the spectral features such as Raman shifts and band intensity ratios. The extent of this interaction will determine the magnitude of the CE component. Molecules can adsorb weakly to the plasmonic substrate via Van der Waals forces or strongly through formation of chemical bonds. Regardless, the interaction between molecule and plasmonic substrate will change the electronic and

geometrical properties of the molecule. This will subsequently alter the Raman cross-section of certain modes compared with the free molecule.

As such, the CE component describes a number of effects which occur between the molecule and metal. These include: ground state interactions, resonance Raman effects in the molecule arising from a suitable excitation wavelength and charge transfer (CT) effects between molecule-metal and metal-molecule [22]–[24]. Of these contributions, CT effects are most relevant and describes the movement of charge between the Fermi energy level of the metal and the HOMO (highest occupied molecular orbital) and LUMO (lowest unoccupied molecular orbital) energy levels of adsorbed molecules. The chemical enhancement is generally considered to be due to charge transfer between analyte and metallic nanoparticles [25]–[27]. The overall CE is defined by Equation 10 and also shown in Figure 5B.

$$G_{\text{Chem}} = \frac{\sigma_{\text{ads}}}{\sigma_{\text{free}}} \tag{10}$$

σ_{ads} is the scattering cross-section of molecules asdsorbed onto the plasmonic substrate and (σ_{free}) scattering cross-section of free molecules.

1.5.4 *Distance dependence between SERS enhancement and metallic nanoparticles*

The EM enhancement is dependent on the strength of the electric field which in turn depends on the distance (d) between analyte and metal surface with

radius a (Figure 6A). The SERS EM enhancement scales with d^{-12} (Equation 11) [28]–[30]:

$$\frac{G_{EM}(d)}{G_{EM}(0)} = \left[\frac{a}{a+d}\right]^{12} \tag{11}$$

By considering shells of molecules around the metal surface, the number for which scales by $(a+d)^2$, the SERS enhancement then scales with d^{-10} (Equation 12) [28], [29], [31].

$$I_{SERS} = \left[\frac{a}{a+d}\right]^{10} \tag{12}$$

I_{SERS} represents the intensity of the Raman mode. Equation 12 represents the distance dependence which should be observed experimentally. However, this will be affected by many factors such as the shape and size of the metallic particles, which can affect the local electric field and hence EM enhancement (Figure 6B). Many nanoparticle synthesis methods, in particular colloidal synthesis, produce particles of different sizes. Interactions between metallic nanoparticles can also result in coupled electric fields, leading to deviations from Equation 12.

As Equation 12 shows, the SERS enhancement drops significantly as the analyte moves a small distance from the nanoparticle surface. Therefore, it is necessary to ensure molecules are close to the metal surface to achieve the highest level of enhancement. Nanoparticles can be modified with surface ligands which can immobilise analytes via either physisorption (i.e H-bonds, π and electrostatic interactions, van der Waals forces) or chemisorption (covalent bond) interactions. These approaches have been successful in providing molecular selectivity to SERS and Figure 8 shows some examples of the different types of surface-affinity ligands which have been used. These approaches

can also be used to improve the CE factor as well as increasing the chance of hotspot formation.

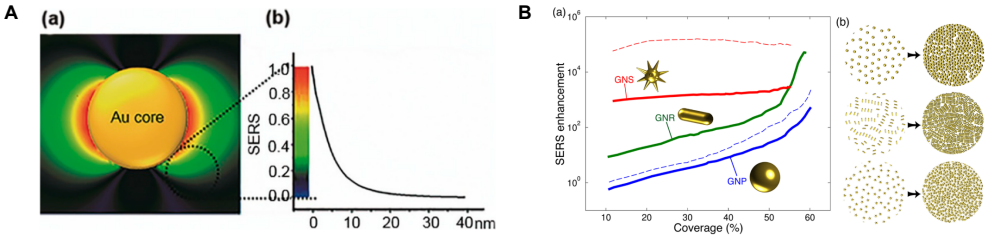

Figure 6: *Properties of nanoparticles which affect the SERS enhancement: A) Simulation of the electric field distribution of an AuNP using finite difference time domain (FDTD). Graph (b) shows the dependence of SERS enhancement on the distance from Au surfaces. Reproduced with permission from [31], B) Density dependence of the SERS performance in nanoparticle monolayers. (a) shows SERS enhancements for planar monolayers of particles with different morphology and (b) shows a sketch of increasing density of nanoparticles in the monolayers. Reproduced with permission from [32].*

1.5.5 *SERS hotspot*

The highest SERS enhancement occurs when analyte molecules are located at nanogap junctions called 'hotspots', which occur when two or more nanoparticles are in close proximity. At the gaps between nanoparticles, or aggregates, electric fields can be greatly enhanced, with SERS enhancements of 10^{10} [33] possible, as well as single-molecule sensitivity [23].

Figure 7 illustrates the SERS hotspot. An external electric field applied to a nanoparticle will cause polarisation and distribution of positive and negative charges at opposite sides of the particle. When nanoparticles are close together, the polarising effect of one will be experienced by the other. In addition, each particle will also experience the effect of the external electric field of the other. Together, these effects increase the electric fields between the particles and hence the SERS signal [28]. The size of the nanogap influences the level of

enhancement and it is generally considered that gaps around 10 nm provide the highest levels of enhancement [34]–[36].

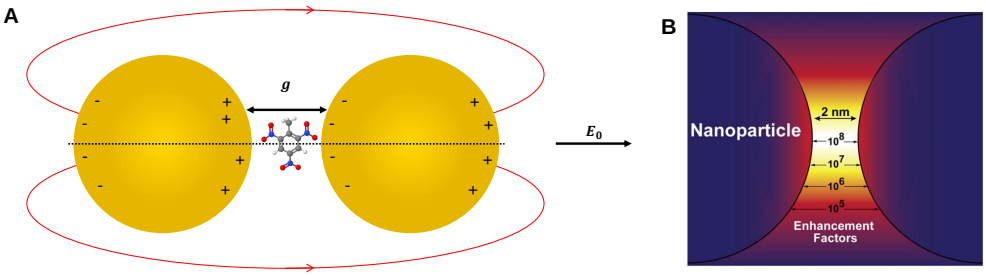

Figure 7: *SERS hotspot: A) Schematic showing a dimer formed by two nanoparticles, separated by a gap (g) and containing a molecule. Polarisation occurs through the action of an external electric field (E_0). Figure drawn with inspiration from [31] and [28], B) Illustration of a SERS hotspot consisting of a nanoparticle dimer, showing the change in SERS enhancement factor with respect to relative position. Reproduced with permission from [35].*

The design and control of hotspots is an important factor when developing SERS substrates. In addition, the distance dependence relationship of SERS means an important criteria for a SERS substrate is ensuring the analyte of interest is within a few nanometers of the nanostructured surface. As such, the ideal SERS substrate is one designed whereby hotspots are selective for the analyte of interest. Whilst, hotspots can be generated through simply evaporating metal nanoparticles from a substrate, difficulties lie in controlling the distribution, geometry and density of the hotspots. Lithography-based techniques enable fabrication of substrates with precise control of nanoparticle shape, size and interparticle distance. Highly uniform and reproducible substrates can be prepared using a range of matrices. Examples include laser etching, Metal Film over Nanosphere (MFON) and E-beam lithography [37].

The functionalisation of nanoparticles can improve the binding of target molecules, enable selectivity in SERS enhancement and generate hotspots. Figure 8 shows examples of approaches used. Assembly-generated hotspots are typically carried out in solution and involve inducing aggregation of nano-

particles in the presence of the target molecule. Nanoparticles can be coated with a small bridging molecule to produce a self-assembled monolayer (SAM) which has a high affinity for the target molecule. Ideal bridging molecules contain thiol, amine carboxyl functional groups which enable strong affinity for the nanoparticle surface and examples include: mercaptobenzoic acid (MBA), p-aminothiophenol (p-ATP) and (3-Aminopropyl)triethoxysilane (APTES). Aptamers, polymers and peptide linkages have specific recognition sites which can be used to achieve high selectivity and sensitivites [38]. Macrocycles such as cucurbit[n]uril, are molecules with a cylindrical-like structure with a hydrophobic cavity, have received a lot of interest in recent years. These structures can induce aggregation of nanoparticles and their hydrophobic centre can 'filter' out solvent molecules whilst bringing target molecules close to plasmonic hotspots [39]. As such these structures can be used to capture a range of guest molecules and they have been used as molecular-recognition assays for the trace detection of biomarkers [40], explosives [41] and metal ions [42].

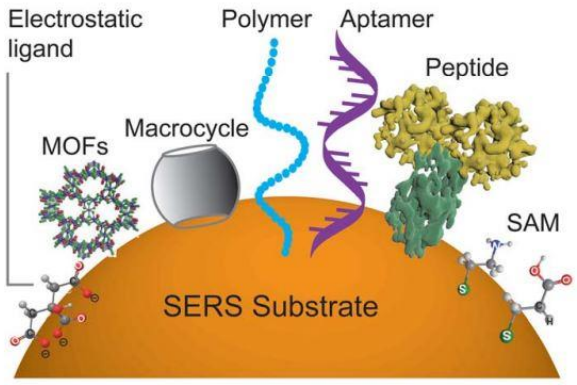

Figure 8: *Schematic showing a range of surface-affinity ligands used to immobilise analytes onto SERS substrates. Reproduced with permission from [43].*

1.6 SERS USING SEMICONDUCTORS

Semiconductors can be used as standalone SERS substrates or combined with plasmonic materials. There are many advantages to using semiconductor nanostructures including: better stability and resistance to degradation, better control over properties such as the band structure, geometry, crystallinity, exciton Bohr radius and dopant [44]. The tunable chemical and optical properties of semiconductors also make them suitable for a wide range of SERS applications which include chemical sensing and recyclable SERS substrates.

However, the enhancement factors from semiconductor substrates are much lower than noble metals, typically in the range 10^3-10^5 [45]. One reason is due to the low electron density in semiconductors. The availability of surface plasmons on metallic nanoparticles allows for LSPR in the visible spectrum, whereas in semiconductors, the highest electron density is found in the valence band with oscillation frequencies in the UV region [45]. Effective chemical enhancement from SERS semiconductors comes from resonance effects at the molecule and semiconductor interface. Charge-transfer (CT) in the semiconductor–molecule system can occur through numerous pathways and is determined by the vibronic coupling, the HOMO/LUMO of the molecular excited state and ground states and the semiconductor valence (VB) and conduction (CB) bands. One approach to improve the SERS enhancement of semiconductors is through tuning the VB and CB to better align with the HOMO/LUMO of analyte molecules to result in more optimal charge transfer routes. This can be achieved through doping [46], oxygen incorporation [47], optimising morphology [48] and introducing surface defects [49].

1.6.1 *SERS using metal-semiconductor systems*

Combining semiconductors with plasmonic materials can improve the interfacial CT processes and lead to greater optimization of SERS substrates. In these heterostructure systems, the enhancement depends on the nature of metal (size, shape etc...), analyte molecule (resonance, HOMO/LUMO gap etc...) and semiconductor (bandgap, morphology etc...), which will affect the CT direction and consequently the additional EM field. A number of CT pathways can exist and some examples are shown in Figure 9.

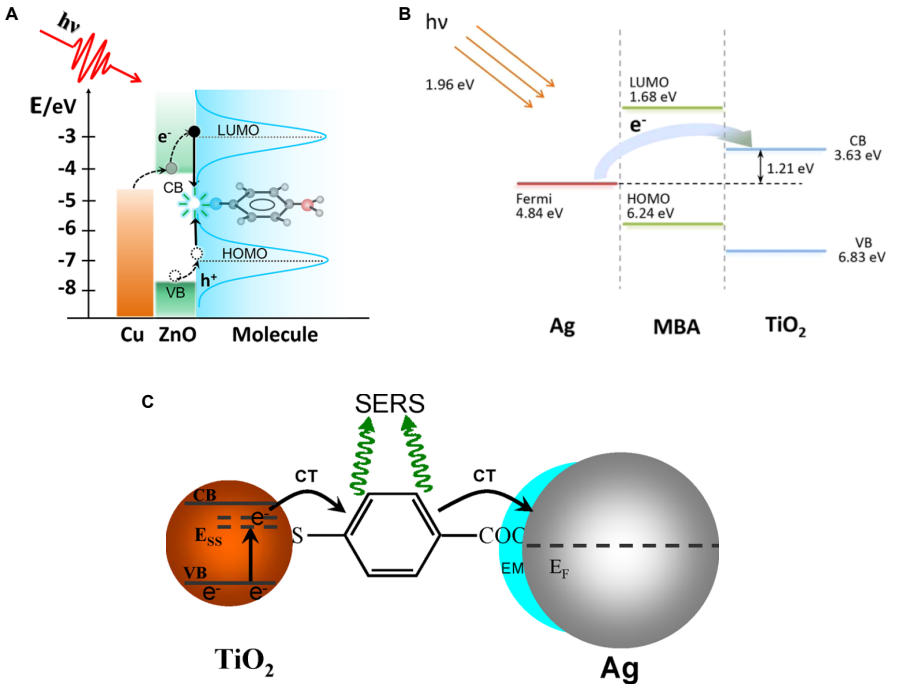

Figure 9: *Examples of CT mechanisms in metal and semiconductor SERS systems: A) Energy-level diagram showing the CT from a metal-semiconductor-molecule system consisting of Cu sheets, ZnO nanorods and p-ATP molecules. Reproduced with permission from [50], B) Energy-level diagram showing the CT from a metal-molecule-semiconductor system. Reproduced with permission from [51], C) CT of a SERS sandwich-structure assembly consisting of Ag(Au)/MBA/TiO_2). Reproduced with permission from [52].*

Mao *et al.* showed the irradiation of Cu–ZnO–p-ATP films using UV, visible and infra-red excitation wavelengths resulted in photoinduced interfacial

CT. Using a UV excitation source resulted in multiphonon resonant Raman scattering processes and additional enhancements of specific Raman transitions [50] (Figure 9A). CT can also occur from metal-to-molecule-to-semiconductor and from semiconductor-to-molecule-to-metal, shown by examples in Figures 9B and 9C, respectively.

REVIEW OF EXPLOSIVE TRACE DETECTION TECHNOLOGIES

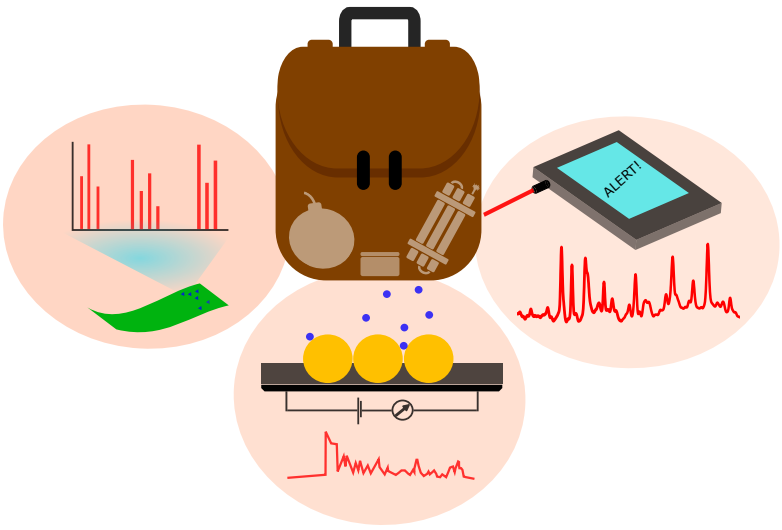

2

LITERATURE REVIEW

2.1 INTRODUCTION

The aim of this review is to report on the latest developments in several key technologies used for ETD. Explosive detection remains a dynamic research area, as evidenced by the number of new publications each year. Animal olfaction has been included as it remains the benchmark which emerging technologies are compared with. Ion mobility spectrometry (IMS), colorimetry and Raman are traditional methods used in many areas of contraband detection. However recent developments in portable sensors, nanomaterials and multi-modal sensors have shown potential for selective, sensitive and faster screening. Each section will cover the characteristics, advantages and limitations of each technology. In-field devices are also described, in order to provide insight into current detection requirements and capabilities.

2.1.1 *Properties of explosives*

An explosive is any material which contains a high amount of energy which, when released can be dissipated in the form of blast waves, radiation (thermal or ionising) or propulsion of debris [53]. The materials generally used to cause destruction are chemical explosives, which can be classified into two types, (1) high, or (2) low explosives. High explosives dissipate energy through detona-

tion, releasing a blast wave which propagates through the material at speeds greater than the speed of sound, typically 1500 - 9000 m/s [53]. Low explosives on the other hand, dissipate energy through deflagration, or rapid burning. Chemical explosives typically contain a fuel and an oxidizer combined in a single molecule or compound. Most explosives undergo enthalpy-driven reactions upon initiation, marked by a high heat of formation and with typical by-products being CO_2, H_2O and N_2. One exception is TATP, where simulations have shown undergoes an entropic explosion, whereby each molecule of TATP produces three molecules of acetone and one of ozone [54].

Explosives can also be categorised into military, commercial, HME's, or by chemical group, as shown in Figure 10. Nitroaromatic explosives such as TNT and TNP are used in munitions and are an environmental concern as they can contaminate soil and groundwater [55]. Dinitrotoluenes have high vapour pressures and are present in compositions of blasting gelatine as well as impurities in TNT manufacture [56]. Many nitrate esters are liquids and military applications include: propellants, detonators and plastic explosives [57]. Brisance is used to describe the shattering ability of an explosive. This is determined by the detonation pressure, in which a high detonation pressure results in greater detonation velocity and more powerful shockwave propagating through the explosive, culminating in greater fragmentation. RDX and HMX are examples of highly brisant explosives used for military applications. Heat, shock and friction sensitive organic peroxides are commonly used in HMEs. Ammonium nitrate/fuel oil (ANFO) is used as a blasting explosive but is also commonly used as a fertiliser. Along with urea nitrate (UN), both have also been used in improvised explosive devices (IEDs). Due to the different chemical and physical properties of explosives, many types of ETD technologies exist with sampling accomplished through particulates, vapours and liquids.

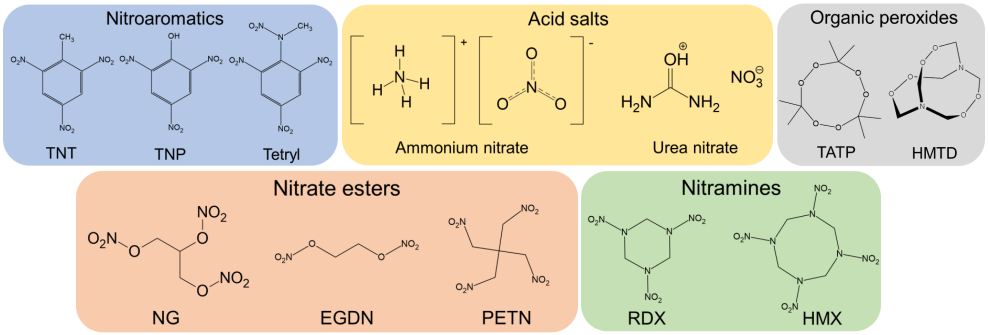

Figure 10: *Classification of explosives by chemical groups. 2,4,6-trinitrotoluene (TNT), 2,4,6-trinitrophenol (TNP), 2,4,6-trinitrophenylmethylnitramine (tetryl), triacetone triperoxide (TATP), hexamethylene triperoxide diamine (HMTD), ethylene glycol dinitrate (EGDN), nitroglycerine (NG), pentaerythritol tetranitrate (PETN), 1,3,5-trinitroperhydro-1,3,5-triazine (RDX) and Octahydro-1,3,5,7-tetranitro-1,3,5,7-tetrazocine (HMX).*

Explosive trace detection is a challenging task. The majority of particulate sampling is achieved through use of sampling wands so direction, pressure and technique are important factors for successful collection of material. Sampling also requires intuition from the security agent to select areas most likely to contain explosive trace. Vapour sampling is even more challenging since many explosives have very low vapour pressures [58]. Sampling liquids raises practical issues and through-barrier screening is limited to a small number of technologies. Many explosives are also considered "sticky" and will adhere to a range of surfaces [59], [60]. For materials with high surface energies, this could result in accumulation of explosive particles, thus limiting the number of analyte molecules per volume of sample.

The operational environment also presents challenges. Passenger screening requires technologies with fast analysis times, low false alarm rates and minimal disruption. Cargo is usually wrapped in protective materials which may restrict efficient sampling. Screening baggage poses logistical issues.

In all cases, there will be interference from benign materials which could cause false positive alarms, so technologies need to be selective. As such, deployment of new detection technologies requires careful consideration of the regulatory (threats, sensitivity, selectivity), operational, civilian and financial requirements.

2.1.2 *Types of detection methods*

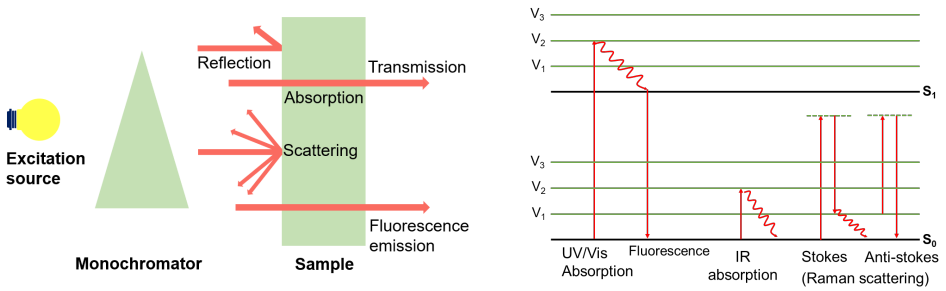

Figure 11: *Examples of spectroscopic phenomena used for explosive trace detection. Diagram representing phenomena shown in addition to Jablonski diagram comparing energy transitions.*

As the name suggests, 'trace' refers to quantities of materials difficult to see with the naked eye. In ETD, this quantity can be considered to be < 1 mg. ETD technologies differ from bulk detection methods, which screen for anomalies in composition. Examples include: X-ray detection, where materials are identified by their density and effective nuclear charge (Z_{eff}) [61] and nuclear-based techniques which compares nitrogen content [62]. Many spectroscopic techniques are used in ETD to identify explosives from their unique molecular signatures (Figure 11). The various properties of explosives has led to different approaches to enhance detection capability. For example, the taggant 2,3-dimethyl-2,3-dinitrobutane (DMNB) is added to plastic explosives [56] due to its high vapour pressure, permeability through clothing and limited commercial

use. The vapour pressures of explosives vary widely across the different classes, from high vapour pressure materials in the parts-per-billion to parts-per-million (ppb-ppm) range such as DNT, EGDN and TATP, to low vapour pressure materials in the parts-per-trillion (ppt) region, such as HMX and nitroguanidine. TNT and TNP, which have been extensively studied as target molecules in gas sensors, have equilibrium vapour concentrations in air at ppb quantities [58]. A comparison of the different vapour pressures for various explosives at room temperature can be found in a papers by Östmark and Ewing [58], [63]. Heating can increase the vapour pressure of non-volatile explosives and improve detection. Pre-concentration by whole-air collection and sorbent enrichment are additional techniques which can be used [64], [65]. To achieve selectivity, many techniques incorporate the use of chemical modification to facilitate binding of specific explosives/explosive groups. For example, to exploit the electron deficient nature of many nitro-explosives, chemically modified silanes containing electron donating groups are frequently used [66], [67]. Charge-transfer complexes are formed and exploited as transducing elements in sensors. Example functional moieties include: amines, thiols and pyrroles [68]–[71]. Computational and experimental studies have found a number of ions to form strong complexes with TATP, including Co^{2+}, Zn^{2+}, In^{3+} [72]–[74] and these properties have been utilised into a range of sensors [75]–[77]. Standoff technologies involve non-contact detection at distance and generally involve optical methods and imaging linked to identification software. These technologies have recently been covered by other authors [78], [79].

2.2 ANIMAL OLFACTORY SYSTEMS

The detection capabilities of animals far exceeds many of the current technologies in use today and as such, there is a continuing need for animals in explosives detection. One of the key advantages of biological systems is concurrent detection of multiple analytes of interest in real-time which is a challenging task and difficult to achieve even with integrated sensing technologies. Examples of animal systems used in explosives detection include: dogs, rats, honeybees and pigs.

Sniffer dogs are the most common animals which are trained for contraband detection and are widely used for their ability to achieve fast, real-time and directional screening. However, a limitation of sniffer dogs is the amount of training required before deployment. Training takes several months, which is time-consuming and costly. The dog-handler interface also affects performance [80], as can screening conditions, with indications that increased panting, as result of overheating, can reduce the ability of dogs to detect explosives [81].

Rats have also been trained to detect explosives and have the benefit of low training and maintenance costs and being lightweight, which makes them ideal for landmine detection [82]. Honey bees have been trained to detect TNT, C4 and TATP explosives at parts-per-trillion levels. The Inscentinel Vasor (Volatile Analysis by Specific Odour Recognition) 136 is portable sensor which uses honey bees. Initially developed in the UK, the systems exploits the Proboscis Extension Reflex (PER) [83], whereby honey bees extend their tongues when their anntenae touch a sugar/honey solution. With pavolovian conditioning, honey bees were trained to respond to TNT, Semtex, PE-4 and C-4 down to detection limits of 78 ppt [84] (Figure 12). The EU-funded 'Biological Method (Bees) for Explosive Detection' project utilises trained

bee colonies to identify landmines [85]. This is realised through active and passive methods, integrating artificial intelligence, drone technology and a semiconducting polymer as a pre-concentrator [86], [87].

Figure 12: *Inscentinel Vasor 136 system. Rothamsted Research Ltd.*

2.3 SENSORS

Efforts to mimic mammalian olfactory systems has led to the development of electronic noses (E-noses). First proposed in 1982, E-noses broadly describe systems consisting of a sensor combined with pattern matching software to achieve vapour detection [88]. Single sensors, for individual analyte detection or sensor arrays, for simultaneous detection of multiple targets can be used. Many sensor technologies have since been used to develop E-noses and examples include: field effect transistors (FET), chemoresistors, quartz crystal microbalance (QCM) and electrochemical sensors [89]. However, even the most advanced systems have yet to reach the capability of their mammalian counterparts. The following subsections will describe some of the sensing technologies used in E-noses.

2.3.1 *Colorimetric sensor arrays*

Colorimetric sensor arrays contain different reagent dyes which can change colour on interaction with solid, liquid and vapour analytes. Chromophores and fluorophores are common reagents and the colour change is measured as a result of the change in absorbance or fluorescence. Advances in image capture technologies have led to the development of sensor arrays which carry out analysis by perturbing the red, green and blue (RGB) intensities of digital images [90]. RGB analysis has already been demonstrated on conventional colorimetric kits using iphone cameras [91]–[93]. The combination of a sensor array with digital image analysis provides a much greater discriminatory power. As such, a range of molecular interactions can be identified through use of combinations of reagents which produce patterns of colour, thus allowing 'optical fingerprinting' to be achieved [94]. Examples of such colorimetric agents exploited for sensing include: pH and redox indicators [95], [96] and derivatives of xanthene dyes, the latter of which is used in the DETECHIP® sensor [97]. The CRIM-TRACK system uses 26 chemoselective dyes spotted onto a chip to form a colorimetric sensor array. Detection of HMTD, TATP and drug molecules are reported, with initial testing in mixed air conditions showing detection limits in the ppt range [98], [99]. In addition, machine learning was successfully used to detect target analytes in contaminated samples. A fluorescence quenching sensor prepared using aerosol-jet printing was reported by Bolse *et. al*. Detection of nitrobenzene, 1,3-dinitrobenzene and DNT was achieved at ppb levels with high classification rates, using an array of six fluorescent spiro and homo-polymers [100], [101].

2.3.2 *Nanomaterials*

Nanotechnology is a rapidly expanding area and the tunable nature of nanomaterials makes them desirable for use as sensor arrays. Nanostructured materials provide high surface areas for detection and selectivity can be achieved by utilising their unique electrical, optical, catalytic, magnetic and mechanical properties. Nanomaterials can be classified in many different ways and Table 1 lists some examples according to chemical composition. The rest of this section will focus on inorganic semiconductor materials used as sensors for ETD.

Table 1: *Different classes of nanomaterial sensors used for the detection of explosives*

Type	Detection method	Materials detected	LOD	Reference
Plasmonic	Au nanoparticles functionalised with 4- Aminothiophenol and N-(1-Naphthyl)-ethylenediamine dichloride (NED)	PETN	0.15 mg L^{-1}	[102]
	Electrochemical sensor consisting of Ag nanoparticles on carbon fibre electrodes	TATP, HMTD	200 ppb (TATP), 250 ppb (HMTD)	[103]
	Cu nanoparticle-incorporated polyfurfural film electrochemical sensor	TNT	41.6 ppb	[104]
Semiconductors	TiO_2 sensor contained within a quartz crystal microbalance	NG	1-10 ppm	[105]
	Optoelectronic sensor using polyoxometalate-doped TiO_2	TATP	50 ppb	[106]
	In_2O_3 amperometric sensor	TATP	2.9 ppb - 2.8 ppm	[107]
	WO_3 and chromium titanium oxide gas sensor	Ammonia, nitromethane, NO_2	Ppm	[108]
Quantum dots	Fluorescent silicon nanodots	TNP	0.92 nM	[109]
	Fluorescent graphene oxide dots	TNP	92 nM	[110]
	L-cysteine-coated CdS quantum dots	TNP	39 ng mL^{-1}	[111]
Carbon-based	Electrochemical sensor using MIP cast on multi-walled carbon nanotube (MWCNT)	RDX	20 pmol L^{-1}	[112]
	SWCNT	TNT	772 ppb	[113]
	Electrochemical sensor using boron-doped diamond/graphene nanowall electrodes	TNT and 2,4,6-trinitroanisol (TNA)	73 ppb (TNT), 270 ppb (TNA)	[114]
Composite	Chemically modified polypyrrole-bromophenol blue QCM sensor	TNT, PETN, RDX and HMX	500 ppt (TNT), 800 ppt (PETN), 1 ppb (RDX) and 2 ppb (HMX)	[71]
	Functionalised SU-8 polymer nanocomposite microcantilevers	TNT, RDX and PETN	1.30 pg (TNT), 0.07 fg (RDX), 0.23 fg (PETN)	[115]
	MoS_2/reduced graphene oxide composite	TATP (precursors)	0.65 ppm	[116]

2.3.3 *Inorganic semiconductors*

Metal oxide (MO_x) semiconductors are promising materials for sensing applications due to their low production costs, ease of use, high thermal, chemical and electrical stability [117]. These properties have led to a range of applications, including: monitoring of volatile organic compounds, environmental and toxic gases [118], [119]. MO_x semiconductors have characteristic wide band gaps (> 2 eV) and electron transition energies in the UV/visible wavelengths of light. Not only is this favourable for optoelectronic and electronic sensors,

but a wide tunable spectral range can also be exploited to improve sensitivity and selectivity. Resistive gas sensors are the most common and the sensing mechanism is based on measuring the change in conductance on adsorption of a target molecule [120]. In ambient conditions, adsorption of O_2 onto the surface of the MO_x leads to the formation of oxygen ions. The conductivity of the MO_x sensor is determined by both 1) the nature of the charge carrier, either electrons or holes in *n* and *p*-type semiconductors, respectively and 2) the oxidative/reductive nature of the target gas (Figure 13).

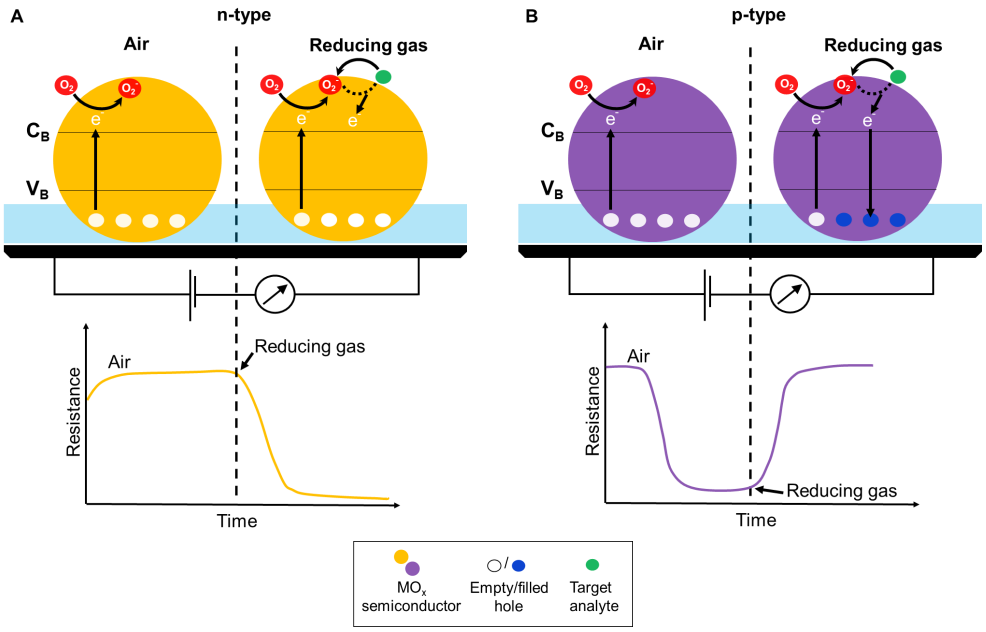

Figure 13: *Mechanisms of metal oxide (MO_x) semiconductor gas sensors for a reducing gas target analyte. When the sensor is exposed to air, adsorption of O_2 onto the surface leads to uptake of electrons from the conduction band (C_B), creating oxygen ions (O_2^-). A) In n-type semiconductors, a redox reaction occurs between the O_2^- and target analyte, leading to injection of electrons into the C_B. As a result, conductance increases and resistance decreases. B) In p-type semiconductors, holes are the dominant charge carriers. However, since the concentration of hole carriers has increased, there is an increase in conductivity. In the presence of a reducing target analyte, reaction between the O_2^- and analyte will lead to injection of electrons into the MO_x and the filling of holes. This results in decrease in the concentration of hole charge carriers, a decrease in conductivity and increase in resistance.*

Many *n*- and *p*-type semiconductor materials have been used for explosives detection and examples include: TiO_2 [73], [121], ZnO [77], [122], Sn_2O [123], [124] and Cu_2O [125]. Efforts to improve the selectivity of MO_x semiconductors towards specific explosives include: changing the operating temperature, using sensor arrays and composite materials. Temperature modulation affects the charge and rate of oxygen adsorbed onto the MO_x surface. As such, sensor response can be used to profile specific gases. Further selectivity can be achieved by combining information from a several sensors with different operating temperatures [117], [126]. Composite MO_x structures can be designed whereby each material is chosen with selectivity to a specific gas analyte [127]. Warmer *et. al* used SnO_2 and WO_3 to detect TATP and DADP. The authors note the oxidising and reducing properties of organic peroxides is temperature dependent and utilise this feature for selectivity towards TATP by temperature cycling of WO_3 films. An LOD in the ppb range is reported [128]. An E-nose using silicon nanowire-field effect transistors (SiNW-FETs) has been developed by Tracense Systems. Chemically modified silicon nanowire arrays provide selective binding of nitro-containing and peroxide-based explosives, with detection achieved through measuring the change in conductance on adsorption of explosives. Parts-per-quadrillion (ppq)-ppt detection was achieved for TNT and peroxides explosives TATP and HMTD, respectively [129], [130].

Quantum dots (QDs) are nanocrystalline semiconductor materials with excellent fluorescent properties due to their quantum confinement effects (Figure 14), which increases their tunability with emission wavelengths achievable from UV to near-IR [131]. QDs also have high quantum yield, broad excitation spectra, narrow emission spectra and high stability, making them favourable for use as colorimetric probes.

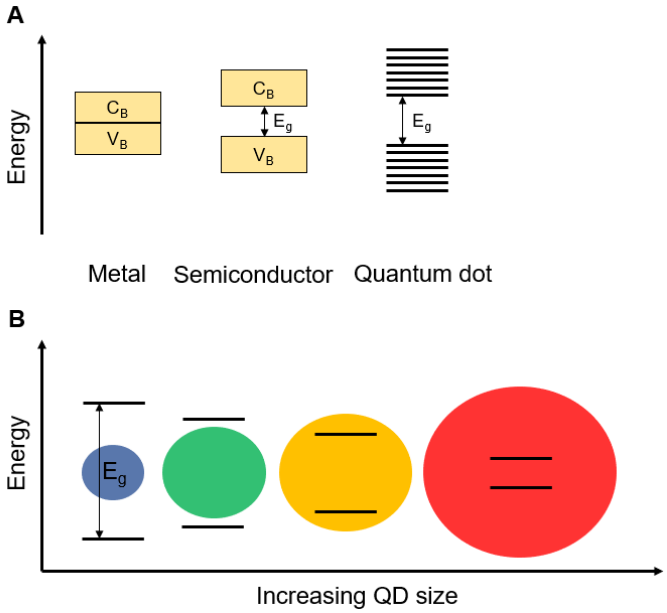

Figure 14: *Properties of semiconductor quantum dots A) Comparison of the band gap energy (E_g) between metals, bulk semiconductors and semiconductor quantum dots, B) Relationship between the size of semiconductor quantum dots and E_g, resulting in different emission energies.*

The electron-rich nature of QDs are suitable for the detection of nitroaromatic explosives as the electron-withdrawing nitro groups can act as fluorescence quenchers. Two mechanisms widely used to achieve such sensing are fluorescence resonance energy transfer (FRET) [132], [133] and photo-induced electron transfer (PET) (Figure 15) [134], [135].

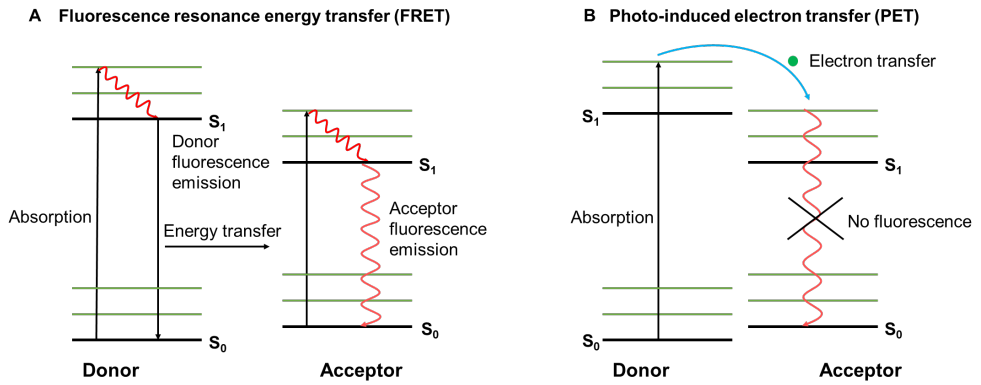

Figure 15: *Energy level diagrams showing generalised FRET and PET processes. A) FRET involves transfer of non-radiative energy from an excited donor moiety to an acceptor. The interaction between donor and acceptor is distance dependent. B) PET involves electron transfer between a donor and acceptor moiety. Fluorescence is quenched in the PET-ON system (i.e. the system is in an 'off' state). Fluorescence emission is observed on disruption of the donor-acceptor system, whereby the system is in an 'on' state (not shown in diagram).*

2.4 ION MOBILITY SPECTROMETRY

IMS remains one of the most popular techniques used in security and is the preferred analytical method for explosives detection worldwide [136]. IMS is also used in the detection of illicit drugs [137], chemical warfare agents [138] and in many areas outside of the security sector. Systems can exist as hand-held or desktop variants and can sample both particulates and vapours. In-field devices are portable, have low detection limits and are easy to use. Another major advantage of IMS when compared with other techniques is the ability to screen samples in seconds. This is particularly beneficial in operational environments such as airports, where fast screening methodologies are needed to process large passenger numbers and minimise delays. Examples of some commercial systems currently in use are shown in Table 2.

IMS functions by analysing ions from vaporised samples and the setup of most commercial systems consists of four main components: a sample

Table 2: *Examples of IMS ETD devices currently in use*

Manufacturer	Model	Sample Type	Swab Type	Ionisation Method	Reference
Bruker Daltonik GmbH	DE-tector	Particulate	Teflon®-coated (PTFE) fiberglass	HEPI	[139]
L3 Technologies	QS-B220	Particulate	Teflon®-coated (PTFE) fiberglass	Photo ionisation	[140]
Smiths Detection	IONSCAN 600	Particulate	Nomex®	Corona discharge	[141]
Thermo Fisher Scientific	EGIS Defender	Particulate, vapour	Teflon®-coated (PTFE) fiberglass	^{63}Ni	[142]

collection and introduction methodology, an ionisation chamber, a drift tube and detector (Figure 16). Particulate or vapour samples are thermally desorbed into the ionisation chamber, where high energy electrons collide with atmospheric or inert gas to generate reactant ions which collide with sample molecules to form product ions. Explosives with nitro or nitrate functional groups are strongly electronegative and favour the formation of negative ions [143], whereas peroxide explosives and drugs are generally electropositive. Product ions are injected into a drift tube via an ion shutter and migrate towards the detector, under the presence of an electric field and an inert carrier gas counterflow to the product ions. A 'reduced mobility' value, K_0, is calculated for each compound, which is compared with reference values and used to set alarm windows [138].

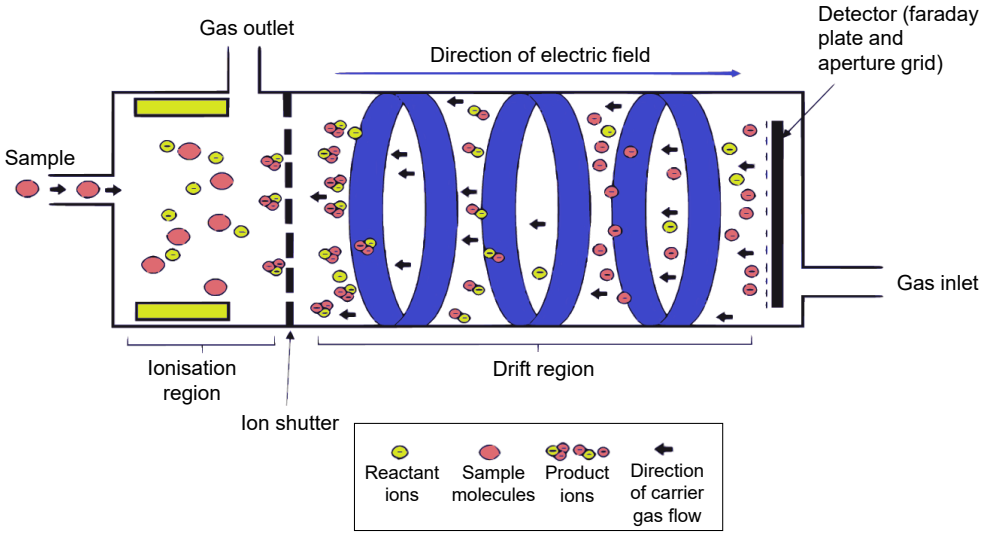

Figure 16: *Typical set-up of an ion mobility spectrometer.*

Many aspects of the IMS system have been extensively studied to improve the speed, sensitivity and selectivity. Recent developments include: chemically modifying swabs [144], [145] and integrating IMS with separation technologies such as mass spectrometry [146], [147] and electrospray ionisation (ESI) [148], [149]. Table 3 shows recent advances in IMS for ETD.

Table 3: *Recent developments involving IMS detection of explosives*

Ionisation source	Carrier gas	Dopant	Materials detected	LOD	Reference
266 nm Nd^{3+}:YAG laser	Air	None	TNT, RDX	2 ppt (TNT), 5 ppt (RDX)	[150]
Secondary electrospray ionisation (SESI)	N_2	KCl	TNT	1 μg L^{-1}	[151]
Thermal ionisation	Air	CCl_4	TNT, RDX , PETN	0.15 ng (TNT reported)	[152]
Ni^{63}	Air	CCl_4	NG, RDX, TNT, PETN	Not reported	[153]
X-ray with Rhodium target	Air	-	Ammonia	30-7500 ppt	[154]
SESI	N_2	-	RDX, PETN, NG, EGDN, TNT	Ppq	[155]

A limitation of IMS is selectivity. False positive responses can occur from samples containing chemical interferents such as perfumes and hand creams. Another issue is that K_0 values can drift as a result of temperature and pressure changes within the drift tube. Collisions between product ions, carrier gas and water molecules in the drift tube can also lead to clustering reactions which can

shift the value of K_0 [156], [157]. False negative responses are also an issue and can arise from ineffective ionisation of analytes of interest in a competitive ionization environment.

2.5 COLORIMETRIC KITS

Colorimetry describes techniques which use colour change to determine the presence of analytes in solution, usually through indicating the presence of specific functional groups. A wide range of applications exists for colorimetric kits [158]–[160] and examples of commercially available kits for ETD are listed in Table 4. Such kits are easy to use, exists in different forms *i.e.* sprays, swabs and pens and provides results in seconds. Thus, colorimetric kits are very useful as a diagnostic tool. As with colorimetric arrays discussed previously, technological advances have seen the integration of colorimetric kits with digital sensors for better colour discrimination. Many commercial systems exist as electronic portable devices which benefit from data storage, automated detection and ruggedness capability. Recent reviews covering luminescent approaches, design and deployment of colorimetric kits for security, are provided by Kangas [94] and Meaney [161].

Table 4: *Examples of commercially available colorimetric kits*

Manufacturer	Product name	Explosives detected	Test time	Detection mode	Reference
Morphix®	TraceX®	Nitroaromatics, nitramines/nitrate esters, inorganic nitrates, chlorates/bromates, peroxides, acids and bases	$<$ 3 minutes	Naked eye	[162]
DetectaChem	SEEKERe	Nitroaromatics, nitramines/nitrate esters, inorganic nitrates, chlorates/perchlorates, peroxides	Seconds	Digital	[163]
BBI Detection	Liquid Explosive Test Kit (LETK)	Nitromethane, hydrazine, nitro-glycerine, fuels, and precursor solvents, peroxides, acids and bases	1-2 minutes	Naked eye	[164]

2.5.1 *Recent developments*

Colorimetric kits exploit luminescence, absorbance and fluorescence phenomena to elicit colour changes. Fluorescence quenching methods remain the most popular technique and an in-depth review can be found by Sun *et. al* [165]. Such methods can be achieved through a variety of materials including: small molecules, metal organic frameworks (MOFs) and polymers and functionalised nanoparticles.

MOFs have received a lot of interest due to their many tunable properties such as: porosity, structure, topology and the variety of mechanisms with which to elicit responses. Several authors report the development of MOF materials capable of multi-target detection [166]–[168]. Conjugated polymers are effective candidates for the detection of nitroaromatic explosives because they are excellent electron donors. One mechanism exploited for ETD is the 'molecular wire' effect, which allows for the conductive quenching of connected polymer molecules on adsorption of a target analyte [169]. Significant enhancement over molecule-based fluorophores can be achieved [170] and this effect has been used to develop 'amplifying fluorescent polymers (AFP)', as seen in the commercially available Fido explosives detectors which have detection limits down to ppt levels [171]–[173].

Due to their unique optical, catalytic and electronic properties, there is continuing interest in the use of nanoparticles to improve the speed, sensitivity and selectivity of colorimetric approaches. Au-Ag nanoparticles functionalised with β–cysteamine were developed by Arshad *et. al* and incorporated onto a paper sensor for the detection of TNT [174]. Tawfik *et. al* used polythiophene coated CdTe QDs to detect TNP. The amphiphilic sensors were coupled with a smartphone to facilitate on–site detection with LOD being 0.56×10^{-9} M [175].

2.6 RAMAN SPECTROSCOPY

Raman spectroscopy involves the collection and analysis of scattered light from a material which can then be used to provide information on molecular vibrations and hence sample identification and quantitation. Raman has been widely used in the counter-terrorism community, with a number of reviews covering Raman [176], [177] and its most common variants; spatially offset Raman spectroscopy (SORS) [178], [179] and surface enhanced Raman spectroscopy (SERS) [180]–[182]. Examples of commercially available Raman systems are listed in Table 5. SORS allows through–barrier analysis of opaque or semi–transparent materials leaving samples intact. This makes the technology desirable for liquid screening and has been realised in the commercially available Agilent Insight and RESOLVE systems, widely used in UK airports. The rest of this section will focus on SERS.

SERS overcomes the low sensitivity of conventional Raman through adsorption of analyte molecules onto a roughened metal surface, resulting in strong enhancement of the analyte's Raman signals. Significant enhancement factors and the capability for single–molecule detection using noble–metal nanostructures [23], [29] makes SERS a promising approach for explosives detection.

Table 5: *Examples of commercially available ETD Raman systems*

Manufacturer	Model	Laser	Excitation wavelength	Technology	Reference
Smiths Detection Inc.	ACE-ID	Diode	785 nm	Raman	[183]
Nuctech	RT1003 series	Diode	830 nm	Raman	[184]
Thermo Fisher Scientific Inc.	Gemini Analyzer	Diode	785 nm	IR and Raman	[185]
Agilent (formerly Cobalt Light Systems)	Insight 100M and 200M	Diode	830 nm	SORS	[186]
Hamamatsu	C13560 spectroscopic module	Diode	785 nm	SERS	[187]

2.6.1 *Recent developments*

LSPR can be tuned by changing the size, morphology and spatial positioning and identity of nanostructures [188], [189]. As such, a range of nanostructures have been developed for explosives detection, including: rods [190], tubes [191], wires [192], prisms [193], [194] and octahedra [195]. Additional examples of SERS substrates can be found in Table 6.

Table 6: *SERS substrates for ETD - recent developments*

Substrate	Nanostructure	Laser λ (nm)	Material detected	LOD	Reference
Borosilicate glass	Au nanocubes	633	DNT, RDX	10^{-15} M (DNT), 10^{-9} M (RDX)	[196]
Klarite	-	785	TATP, TNT	-	[197]
Chemically modified Klarite® containing MIPs	Au nanoparticles	785	TNT	3.0 μM	[198]
Polystyrene	Au nanoparticles	785	TNT	10^{-5} M	[199]
Silicon wafer	Ag nanoparticles decorated with Si nanowires	632	Ammonium Perchlorate	10 μM	[192]
Aluminium	Ag nanoflowers	785	TNT	5 μg	[200]
Reduced graphene oxide	Ag nanoparticles	532	DNT	Nanomolar	[201]
Silicon	Ag/Cu nanoparticles	632	Ammonium nitrate, TNP	5 μM (ammonium nitrate and TNP)	[202]
Graphene nanosheets with Ag nanoparticles	-	514	TNT	5.0×10^{-16} M	[203]
Microscope slide	Cucurbit[7]uril and Au nanoparticles	633	DNT	1 μM	[41]

Work towards exploiting the chemical enhancement to improve explosives detection has led to the development of functionalised nanoparticles, with common linking agents being: APTES (3–aminopropyltriethoxysilane) [204] DACH (trans–1,2–Diaminocyclohexane) [205] and PATP (p–aminothiophenol (PATP) [206]. As with IMS devices, there is a need for convenient sample delivery and separation/pre–concentration of complex sample matrices for Raman–based techniques. Piorek *et al.* developed a microfluidic system with a SERS sensor and showed detection of 2,4–dinitrotoluene (DNT) down to 1 ppb of gaseous phase [207]. The system provides continuous, real-time sample analysis. A large surface-to-volume is achieved using shallow channels of 4-40 μm, enabling pre-concentration of the sample and trace-level detection.

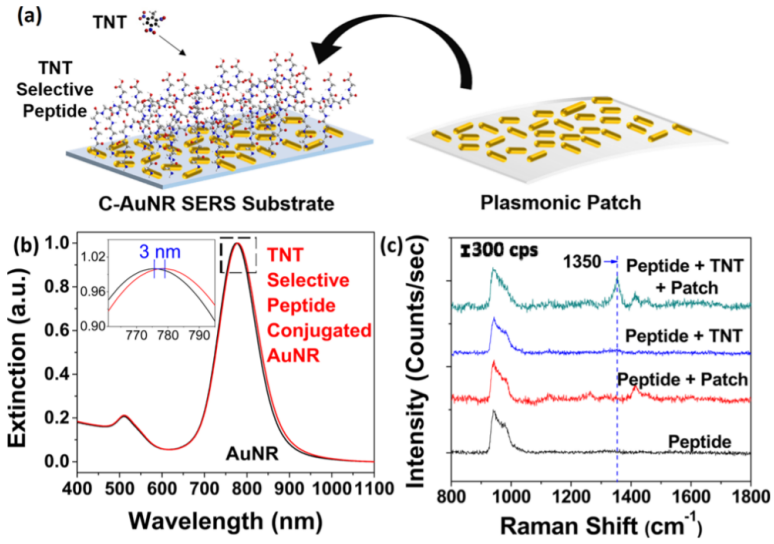

Figure 17: *SERS 'plasmonic patch' for the collection and analysis of explosives as described in ref [208]. A) Schematic representing vapour detection of TNT via peptide-conjugated gold nanorods. B) Characterisation of bare and peptide conjugated gold nanorods using UV-Vis spectroscopy. C) Raman data showing vapor-phase detection of TNT.*

Shi *et al.* report the development of a chemically modified SERS substrate for the detection of inorganic and organic explosives. Silver nanowires were manufactured with diethyl-dithiocarbamate (DDTC) ligands to produce a positively charged system. SERS detection was achieved using an excitation wavelength of 785 nm. The detection of perchlorates (ClO_4^-), chlorates (ClO_3^-), nitrates (NO_3^-) and 2,4–dinitrophenol were reported to be 2, 1.7, 0.1, 45.8, and 36.6 ng, respectively [209]. The flexible substrate can be used as a swab and this is a promising advancement of SERS for operational ETD screening. Other flexible substrates have also been reported. Liyange *et. al* fabricated gold triangular nanoprisms onto an APTES functionalised glass coverslip followed by transfer onto a flexible adhesive tape. The resulting sensor showed detection of TNT down to 900 parts per quadrillion (ppq) and 56 ppq for RDX and PETN, using a commercial off the shelf Raman system [194]. The 'plasmonic patch' developed by Gupta *et. al.* is a transparent

flexible PDMS film decorated with gold nanorods which can be added to different SERS substrates, leading to enhanced sensitivity [208] (Figure 17). Liu *et. al* also report development of a flexible substrate, by immobilising silver nanoparticles onto a composite sponge surface consisting of polyurethane and polydopamine. Perchlorates, chlorates and nitrates were detected at sub-nanogram quantities [210].

Non-plasmonic substrates including graphene and semiconductor materials generally have low enhancement capabilities, however, their strong charge transfer properties [211], [212] have been used effectively with noble nanoparticles for detection of many explosives. Examples include ZnO [213], graphene oxide [214], [215] and TiO_2 [216]. The introduction of oxygen vacancies can improve Raman enhancement of semiconductors and this can be achieved through surface and atomic defects [217]. Ben–Jaber *et al.* report the use of photo-induced SERS (PIERS) for the detection of TNT, DNT, RDX and PETN at concentrations of 7 μg/L, 0.1 μg/L, 2.2 mg/L and 3.2 mg/L, respectively [218] (Figure 18). PIERS signals showed enhancement compared with SERS for all explosives studied, with a 20-fold increase achieved for RDX. Substrate regeneration was achieved using UV-light.

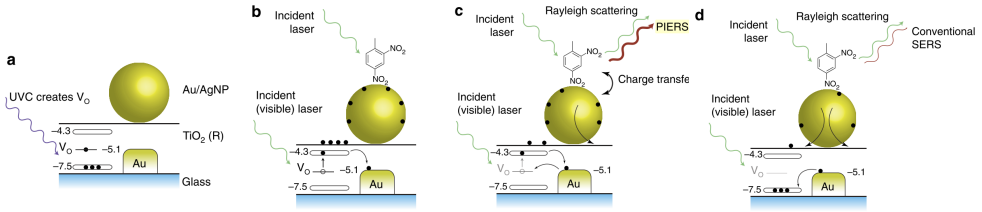

Figure 18: *Proposed PIERS mechanism. UV light is used to increase the availability of electrons in the conduction band of the SERS substrate through the creation of vacancy defects. This results in elevated levels of electron migration from substrate to nanoparticles upon Raman laser illumination. (A) Creation of oxygen vacancies (V_O) in the TiO_2 below the conduction band using ultraviolet C light (UVC).(B) Sample deposition (DNT shown) followed by irradiation with 633 nm Raman laser. This leads to photoexcitation of TiO_2 and increase in charge on the nanoparticles. (C) Charged nano particles lead to PIERS signal enhancement. V_O are replenished upon exposure to air. (D) The PIERS effect gradually disappears as the V_O are completely replenished over time. The substrate can then be cleaned and recharged through exposure to more UVC light absorption [218]. Reproduced from ref [218]. Copyright 2016 Nature.*

Glass *et. al* studied the surface oxygen vacancy states of different metal oxide substrates. Differences in the rates of vacancy formation and healing were correlated to the duration of the PIERS enhancement [219]. Table 7 shows the majority of PIERS studies to date have focused on metal oxides, with particular emphasis on TiO_2. This is due to the similarity in the mechanisms responsible for metal oxide photocatalysis and the PIERS effect. As such, inspiration for new substrates can be drawn from materials with effective photocatalytic properties. Given the UV pre-irradiation step is sample-independent and the proven versatility of SERS in detecting a range of organic and inorganic explosives [220]–[222], development of a reusable multi-target sensor is a possibility and would greatly benefit routine screening in civilian and military environments. These studies indicate potential further applications of established metal oxide SERS materials as PIERS substrates.

Table 7: *Summary of recent developments in PIERS.*

Substrate	Illumination source (λ, irradiation time)	Laser λ (nm)	Analytes detected	SERS/PIERS EF (max.)	Ref.
AuNPs on TiO_2 (rutile)	254 nm, 4 hours	633	R6G, DNT, PETN, RDX, glucose	34.79	[218]
AuNP on ZnO	254 nm, 30 mins	633	Thiophenol	7.52	[223]
AgNPs on $LiNbO_3$	254 nm, 6 mins	-	4-Aminothiophenol	2	[224]
AuNP on TiO_2, WO_3, ZnO thin films	254 nm, 5 mins	633	MBA	2.6	[219]
Tyrosine functionalised AuNPs, TiO_2	Visible light (xenon ozone-free arc lamp through a cut-off filter $\lambda > 400$ nm) 10 mins	785	Tyrosine dimerization	2.1	[225]
AuNPs on WS_2	254 nm	633	MBA	4	[226]
ssDNA functionalised AuNP, AgNPs, TiO_2	365 nm, 30 mins	780	ATP, thrombin, cocaine	4	[227]
Ag-doped TiO_2	Near-IR source, 100 seconds	785	MBA	2.3	[228]
AuNPs on SnO_2	254 nm, 4 hours	785	BPE (trans-1,2-bis-(4-pyridyl) ethylene) and R6G	9.3	[229]
AgNPs, WO_3, TiO_2, ZnO, NiO	254 nm, 1 hour	532	Meso-tetra(N- methyl-4-pyridyl)porphine tetrachloride, methylene blue and nitrophenol	2.5	[230]
AuNPs, TiO_2 (anatase)	254 nm, 1 hour	633	MBA	21.6	[231]
AgNPs, diphenylalanine peptide nanotubes	254 nm, 5-45 mins	532	meso-tetra porphine tetrachloride, rhodamine B, aminothiophenol	4.5	[232]
AgNPs, TiO_2 (anatase)	254 nm, 21 mins	785	Crystal violet, carbaryl, phoxim and thiram	8-fold	[233]
AgNPs, TiO_2 (rutile/anatase heterostructure)	UPB mercury lamp, 24 min	785	Malachite green, crystal violet, R6G, thiram and acephate	27.8	[234]

A limitation of SERS is signal reproducibility, which is affected by the shape and size, as well as the separation, of the nanoparticles used in the substrate. Efforts to overcome these problems have resulted in some commercially available substrates which include: QSERS, RAM-SERS, Klarite^{TM} and SERStrate, which have recently been tested using commercial Raman systems for contraband detection [235]–[238].

2.7 CONCLUSIONS

Table 8 and Figure 19 provide a comparison of each technology, with insight into their analytical performances. Note, a holistic approach has been taken with consideration from literature reviewed here in addition to subjective assessments. Animals remain a benchmark for emerging technologies with key attributes being high selectivity, sensitivity, concurrent detection of multiple analytes and fast screening times. The majority of in-field systems have sampling times within minutes and this has also been observed in many emerging technologies reviewed here. IMS remains a key technology in the field of ETD due to having good overall sensitivity, selectivity and analysis times in seconds.

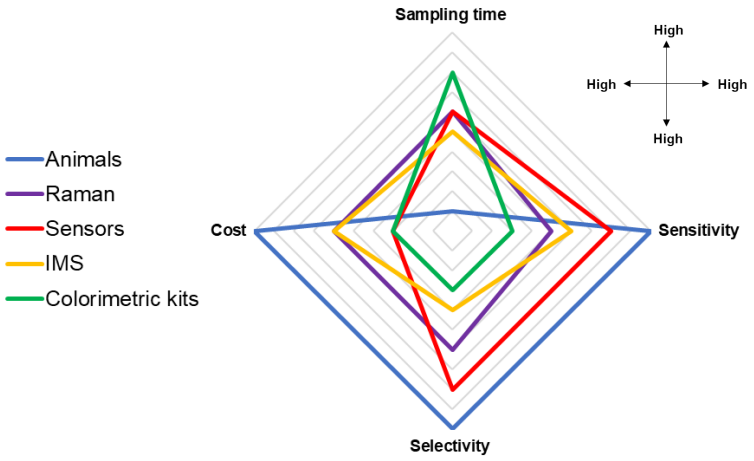

Figure 19: *Visual comparison of ETD technologies based on sampling time, sensitivity, molecular selectivity and cost.*

However, current IMS systems lack molecular selectivity compared with spectroscopic approaches such as Raman and absorption/emission spectroscopy which can provide molecular fingerprinting and functional group information. Ions generated from benign materials with similar mobilities to explosive ions can trigger false positive responses and such interferences in-

Table 8: *Advantages and limitations of ETD technologies*

Techniques	Advantages	Limitations
Animals	concurrent sampling in real-time, wide range of threat materials	high training and maintenance costs, inconsistencies, affected by the environment and surroundings, not always practical in civilian environments
IMS	easy to use, dual vapour and particulate detection in some systems, can be integrated with mass spectrometry, library	expensive, radioactive ionisation source, affected by humidity, temperature and sample composition, destructive, requires rigorous sampling to maximise analyte collection
Raman	portability, non-destructive analysis, sampling through packaging, stand-off detection capability, sampling of solid, liquid and gasses	interference from fluorescent or strongly absorbing materials, small scan area, cannot be used for metals or alloys
Colorimetric kits	easy to use, portability, inexpensive, integration with smart phone technology, small footprint and power requirements	stability/shelf life, may require multiple tests, destructive
Sensors	portability, customisable, multi-modal capability	largely untested in operational environments

clude oils, creams, perfumes and medication. Efforts to improve the selectivity of IMS include: use of dopants, development of chemically modified swabs, understanding the ion chemistry of analytes and integration of IMS with mass spectrometry techniques. Traditional colorimetric reagents are limited by specificity, sensitivity and toxicity of some materials. Development of sensor arrays and use of ratiometric fluorescence approaches overcomes these problems as they probe the chemical properties of analytes, leading to greater selectivity and sensitivity. The use of multiple sensor elements to give a combined response further improves analyte differentiation and selectivity. This has been largely possible through the use of tunable nanomaterials such as MOFs, nanoparticles, quantum dots and conjugated polymers.

SERS is a promising approach with high sensitivity and selectivity and can be used with current desktop and portable Raman systems. However the technique has yet to be adopted in operational environments. As the number of SERS substrates continue to expand, the need to develop standardised tests for assessing detection capability and reproducibility is required. Work towards

reproducible substrates at low cost for commercial use is also important for SERS to be a viable option for operational screening.

2.8 CONCLUDING REMARKS AND PREMISE FOR WORK IN THESIS

It is likely that nanomaterials will play an important role in the development of future ETD technologies. We have seen significant developments made in gas sensing such as graphene and quantum dots, with some systems able to detect multiple classes of explosives at low concentrations. Whilst sensitivity and selectivity remain important goals for ETD systems, consideration of the operational environment is also important for design of future systems as deployment is a balancing act of many considerations. These include, cost, sampling throughput, sampling time, portability and ease of operation.

The potential for SERS and its variants to meet these requirements has prompted the investigations described in this thesis. PIERS has been identified as a promising avenue of research, due to the simplicity of the method and infancy of the research. Whilst many applications have been reported, the range of PIERS substrates is limited to mostly TiO_2 based materials. The duration of the PIERS enhancement can range from minutes to hours, even in substrates of the same material. This limits the use of PIERS as a reliable sensor. In addition, different fabrication methods can alter the properties of materials, making it difficult to compare similar substrates. Another gap identified in current PIERS research is improving selectivity towards analytes of interest.

These observations have been used as the focus of the research described in Chapters 3 and 4. Chapter 3 will first characterise PIERS using commercially available TiO_2 before investigating the effect of a low oxygen environment on the duration of the PIERS enhancement. The properties of semiconductors can

be tuned through introduction of dopants and this approach is used in Chapter 4 to fabricate Ag and Cu doped ZnO. The substrates will be characterised and the PIERS enhancements compared using a common Raman probe molecule.

As seen previously, an abundance of research exists involving colorimetric detection of explosives, with one promising new development being the use of plasmonic nanoparticles with colorimetric agents to produce a SERS assay. This dual detection approach is explored in Chapter 5, using gold nanoparticles functionalised with different molecules. The effectiveness of the assay will be further explored by using the functionalised nanoparticles in PIERS. To explore the practicality of the assay, the use of machine learning and digital colorimetric detection is also explored.

STUDYING PIERS USING PILKINGTON ACTIV™

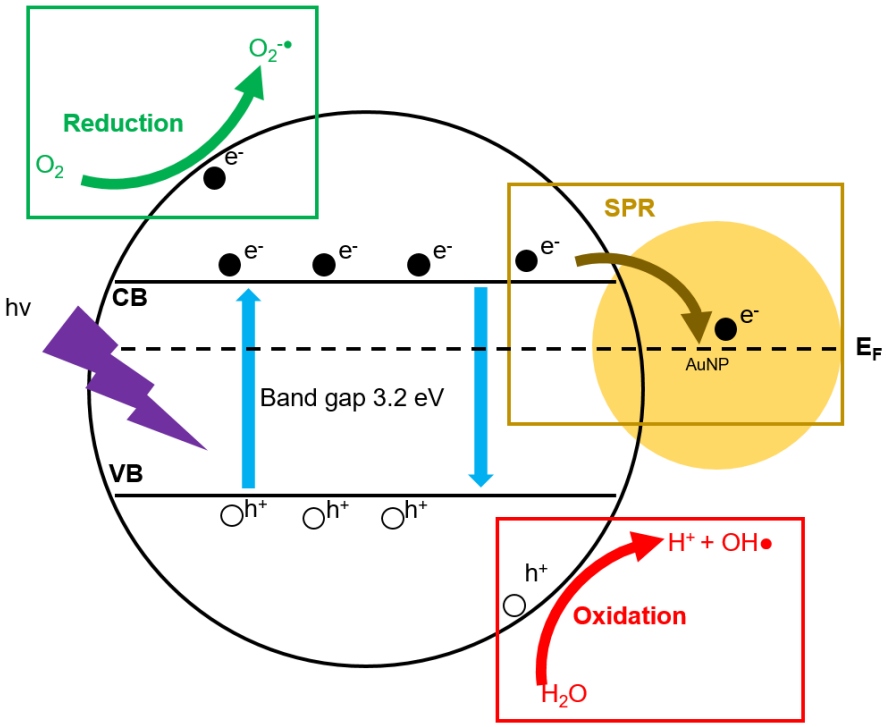

3

STUDYING PIERS USING PILKINGTON ACTIV™

3.1 INTRODUCTION

The SERS effect arises when an analyte molecule adsorbs onto a rough metallic surface, leading to enhancement of the analyte's Raman signal. In practice, this is achieved using nanofabricated surfaces or nanoparticles. Plasmonic metals such as silver and gold have been extensively used as SERS substrates, due to their stability, biocompatibility [11] and ease of control of optical properties [12].

Two main effects contribute to the SERS enhancement and these are the chemical (CE) and electromagnetic (EM) components. The EM enhancement provides the largest contribution [13]–[15] and arises from the electromagnetic interaction of light with the nanomaterial. This leads to collective oscillations of surface conduction electrons on the nanoparticle, called localised surface plasmon resonance (LSPR) [10]. This phenomenon enhances the local electric fields near the metal surface, leading to enhancements of both the incident and Raman-scattered fields. The CE component can be used to describe a number of effects which occur between the molecule and metal, which is dependent on the interactions involved. These include: ground state interactions, resonance Raman effects in the molecule arising from a suitable excitation wavelength and charge transfer (CT) effects between molecule-metal and metal-molecule [22]–[24]. Of these contributions, CT effects are most relevant and describes

the movement of charge between the Fermi energy level of the metal and the HOMO (highest occupied molecular orbital) and LUMO (lowest unoccupied molecular orbital) energy levels of adsorbed molecules.

Semiconductor materials have also been used as non-plasmonic SERS substrates and examples include: TiO_2 [239], ZrO_2 [240], ZnO [241], [242] and Cu_2O [243]. Nonplasmonic substrates generally have low enhancement capabilities; however, their strong charge-transfer properties [211], [212] have been used effectively with noble nanoparticles for SERS.

The introduction of oxygen vacancies can improve Raman enhancement of semiconductors, and this can be achieved through surface and atomic defects [217]. The PIERS approach combines metallic nanoparticles with photoactive semiconductors to produce strong Raman enhancement beyond the normal SERS effect. Band-gap activation of semiconductor materials can induce formation of surface oxygen vacancy defects which enable transfer of photo-excited charge carriers to plasmonic metal nanoparticles, leading to 'photo-induced SERS'.

The formative PIERS study by Ben-Jaber *et. al* used TiO_2 rutile, prepared through atmospheric pressure chemical vapour deposition (APCVD) [218]. Since then, a range of substrates have been reported. Zhang *et. al* prepared TiO_2 anatase through electrochemical anodization of titanium foil. The crystalline films containing arrays of nanopore structures were used with silver nanoparticles (AgNPs) to detect environmental contaminants, including the pesticides carbaryl, phoxim and thiram, achieving detection limits of 10^{-5} M [233]. Man *et. al* constructed a biomolecular recognition platform using TiO_2 and AgNPs, for the detection of adenosine triphosphate, thrombim and cocaine. TiO_2 anatase was prepared using hydrothermal synthesis, resulting in nano-foil and nanorod structures. Detection was achieved by functionalising TiO_2

nanostructures with a sandwich structure consisting of aptamers to achieve specific analyte recognition [227]. Ke *et. al* synthesised composite structures containing TiO_2 rutile and AuNPs [225] to detect tyrosine dimerization, an indicator for oxidative reactivity in inflammatory cells. As such, a wide range of different preparation methods have been used in literature, resulting in different morphologies, size and crystal phases of semiconductor materials. Whilst many applications have also been found, one area of study which has received less attention is improving the current limitations of PIERS. One example is the exponential-like decay of the PIERS enhancement reported in many studies [219], [227] which can vary from 20 minutes to a few hours. The enhancement lifetime is linked to the recombination of photoexcited charge carriers and is a complex process dependent on a number of factors such as: substrate, chemical environment and laser parameters. The time-limited enhancement is not ideal for sensing applications, given there is already variability inherent in SERS. Another limitation is the photo-induced-superhydrophilic effect in semiconductor materials. Whilst favourable in self-cleaning applications, this property can affect the distribution of AuNPs, leading to variability in SERS enhancement.

This chapter describes work to improve the current PIERS method and begins through characterising the PIERS effect using a commercially available TiO_2 material, Pilkington Activ™. A custom-chamber was fabricated to conduct measurements in a low oxygen environment. Two new variants of PIERS were developed with improved enhancements over normal PIERS. To demonstrate the new PIERS techniques, detection studies were carried out using Raman probe molecules MBA and R6G, as well as the pesticide thiram and explosives triacetone triperoxide (TATP), hexamethylene triperoxide diamine(HMTD) and trinitrotoluene (TNT).

3.2 METHODS

Unlike other analytes used in this research, which were used as purchased, the TATP described in this thesis was synthesised as part of a separate project for the Defence Science and Technology Laboratory [244]. Synthesis was carried out using methods adapted from Oxley [245], Pachman [246] and Tomlinson-Philips [247]

Due to the shock, heat and friction sensitive nature of TATP, synthesis should be carried out on a small scale. A thorough risk assessment was carried out and independently reviewed prior to the synthesis. Lab work was carried out with appropriate personal protective equipment (PPE) which included: nitrile gloves (SHIELDskin CHEM™NEO NITRILE™300), chemical resistant splash-proof goggles and labcoat. All laboratory work was carried out in a fumehood. Solid TATP samples was handled using plastic spatulas to mitigate spark ignition. Samples were stored in a fridge, in threadless vials to mitigate ignition events due to heat and friction. Fridge storage also mitigates TATP decomposition, suppresses sublimination and conversion of TATP to DADP. Solutions of TATP were stored in organic solvents such as acetonitrile or methanol to reduce the compound's sensitivity. Prior to disposal, solutions of TATP were diluted with methanol. All unwanted TATP solutions and reagents were stored in separate containers marked for incineration.

Methanol (CAS 67-56-1, HPLC grade, $\geq$ 99.8 %) and HPLC-grade water (CAS 7732-18-5, HPLC grade) were purchased from Sigma-Aldrich. Accustandard explosives reference solutions (TNT, HMTD and TNT) were purchased from Kinesis and diluted as required. 50 nm tris-capped AuNPs were synthesised as described in Chapter 5 which also contains the characterisation data. Pilkington Activ™ was used as supplied by NSG Pilkington. Activ™ consists

of TiO_2 (approx.15 nm in thickness) coated onto 4 mm float glass. Preparation of Activ™ glass involves depositing a precursor gas mixture containing titanium dioxide onto float glass using APCVD [248].

X-ray photoelectron spectroscopy (XPS) was carried out using a Thermo K alpha spectrometer with monochromated Al Kα radiation, a dual beam charge compensation system at a pass energy of 50 eV. Survey scans were performed between 0 and 1200 eV. XPS data was fitted using CasaXPS software with the calibration of C 1s at 284.5 eV. UV-Vis was carried out on a Shimadzu UV-2550 instrument, in absorbance mode and scan range 200-800 nm. Room temperature photoluminescence spectroscopy was carried out using a Renishaw 1000 system, equipped with a He–Cd laser, using a wavelength of 325 nm.

For SERS and PIERS, mixtures of tris-capped AuNP and analytes of interest were mixed (by volume), vortexed for 1 minute before depositing (10-30 μL) onto a substrate (uncoated Pilkington glass or microscope slides). For PIERS, samples were irradiated under UV-C light (254 nm, 2 $\times$ 8W bulbs positioned 13 cm above the substrate) for a minimum of 60 minutes. Both SERS and PIERS analysis were carried out on a Renishaw Raman inVia microscope with a 633 nm He–Ne excitation laser (1.9 mW when operated at 25 % power, spot size approx. 4.4 mm^2). All the spectra were acquired using an exposure time of 10 seconds with 1 accumulation. A minimum of 5 positions were measured for each sample to ensure consistency between locations. The spectra were averaged and baseline correction was carried out using the adjacent-averaging plug-in in Origin.

3.3 RESULTS

3.3.1 *Characterisation of Pilkington Activ™*

Activ™ is the world's first self-cleaning glass and widely used to benchmark the activities of emerging photocatalytic thin film materials [249]. Activ™ was selected to minimise the batch-batch variations which can be apparent in films prepared in-house. Figure 20 shows a typical SEM image of Activ™ which comprises of rounded particles ca. 30 nm diameter. The UV-Vis spectrum of Pilkington Activ™ is shown in Figure 21. Activ™ is slightly coloured compared with plain (uncoated) barrier glass, which can be evident when placed against a white background. The UV-Vis spectrum of barrier glass has an absorption around 310 nm, which is attributed to soda-lime–silicate. In the UV-Vis spectrum of Activ™, a weak absorption around 380 nm is observed, which corresponds to the bandgap energy (E_g) of nanocrystalline titania. The band gap energy of a semiconductor describes the energy needed to excite an electron from the valence band (VB) the conduction band (CB) and can be estimated using absorption spectra and the Tauc method [250]. TiO_2 is an indirect semiconductor and Figure 21 shows the Tauc plot and calculated bandgap of 3.20 eV which agrees with literature [249].

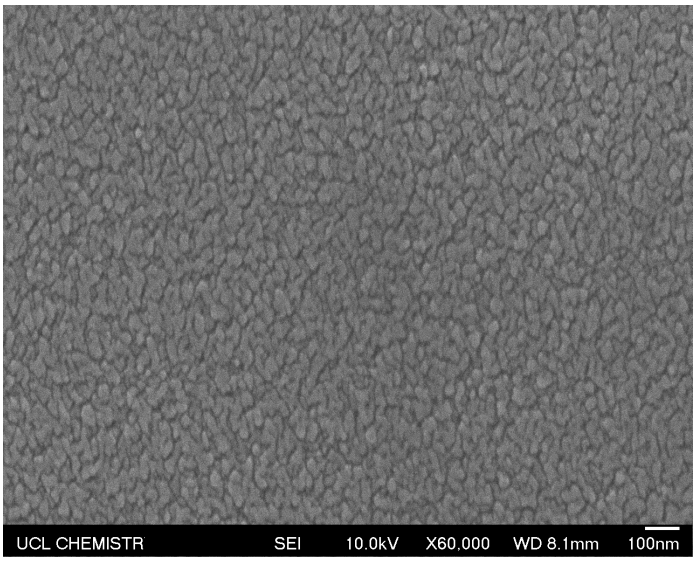

Figure 20: *SEM of Pilkington Activ™.*

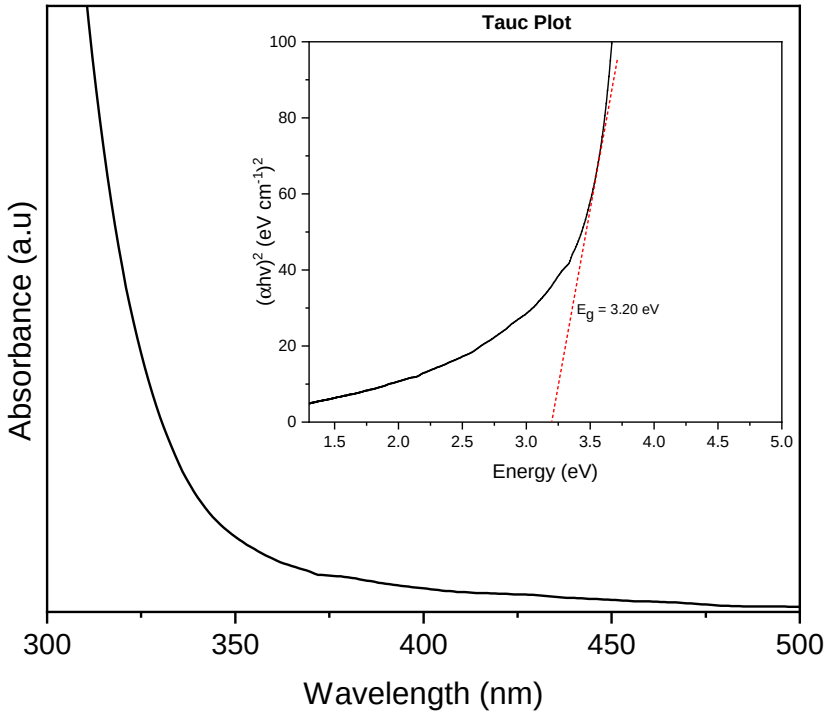

Figure 21: *Determination of bandgap of TiO_2 in Pilkington Activ™.*

To further confirm the identity of TiO_2, surface characterisation methods were carried out using Raman and X-ray photoelectron spectroscopy (XPS). Titanium dioxide occurs as three polymorphs: rutile, anatase and brookite. Activ™ consists of anatase, which is tetragonal, with the space group D_{4h}^{19} ($I4_1/amd$). Raman spectra was collected at room temperature and Figure 22 shows peaks at frequencies of 144, 396, 514 and 641 cm^{-1}, which correspond to the Raman active modes of Eg, B_{1g}, A_{1g}, and Eg modes of anatase, respectively [251], [252].

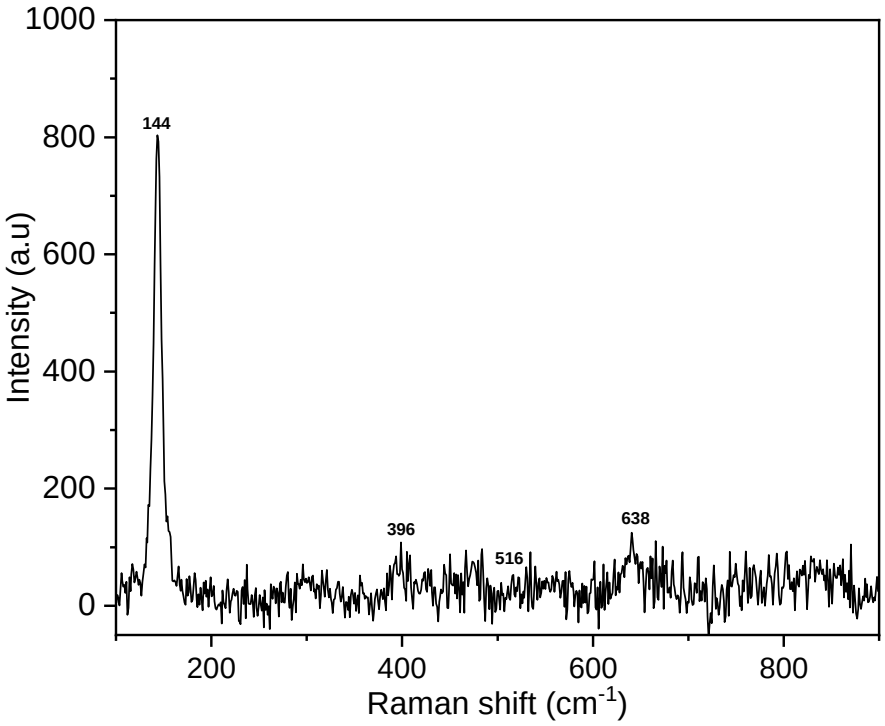

Figure 22: *Raman spectrum of Pilkington Activ™.*

XPS examination (Figure 23) of the Ti 2p core level showed two characteristic peaks due to spin-orbit splitting. The symmetric Ti $2p_{3/2}$ and Ti $2p_{1/2}$ components, have binding energies (BE) of 458.3 eV and 464.0 eV, respectively. The Ti $2p_{1/2}$ - $2p_{3/2}$ splitting value is 5.7 eV, which is consistent with Ti^{4+} in the TiO_2 lattice [253], [254]. The O1s core level spectrum consisted

of three peaks. The peak with BE value of 529.5 eV corresponds to lattice oxygen in Ti-O bonds [253]. The peak with BE of 532.4 eV corresponds to hydroxyl groups chemisorbed on the surface as Ti-OH bonds [255].

The peaks between 531-532 eV is a source of debate within the literature, with some authors assigning the peak oxygen vacancies (V_o) [256]. Other sources attribute the peak to surface adsorption of hydroxyl groups from water [255], [257]. Evidence for the latter was shown by Yamamoto *et al.*, using near-ambient pressure XPS to study the O1s region of TiO_2 films subjected to water and monitored under different temperatures [258]. The authors attributed changes in the O1s peak to surface hydroxyls from the dissociation of adsorbed H_2O molecules. There is also the consideration that it may be more thermodynamically favourable for surface oxygen vacancies to heal under ambient conditions. As such, it is likely the peak observed at 531.3 eV is due to adventitious adsorption of hydroxyls or oxygen onto the TiO_2 surface.

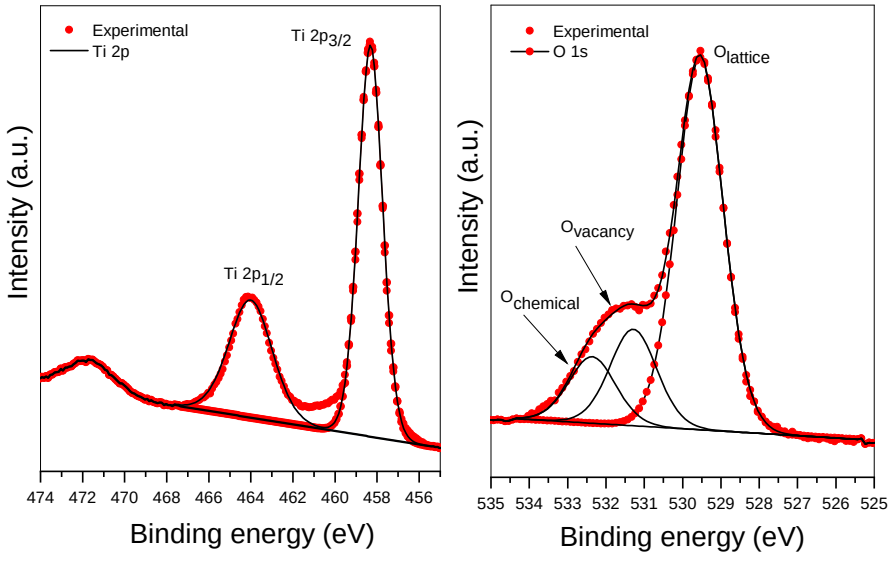

Figure 23: *XPS of Pilkington Activ™.*

3.3.2 *SERS and PIERS measurements of MBA on Activ™*

Figure 24 shows the typical procedure for conducting SERS and PIERS measurements in this study. In SERS, a mixture containing AuNPs and analyte is prepared and thoroughly mixed before depositing onto a substrate. The droplet is allowed to dry before analysis is carried out. PIERS measurements involve the use of a photoactive semiconductor substrate which is pre-irradiated for one hour before immediate deposition of the analyte and AuNP mixture. Since TiO_2 is a photocatalyst, deposition is carried out after irradiation in order to mitigate against analyte degradation from TiO_2 and photodegradation from the UV source.

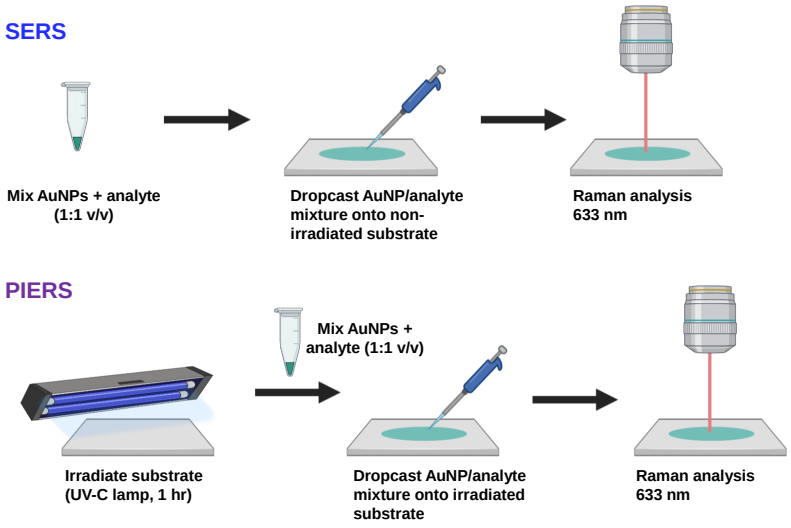

Figure 24: *SERS and PIERS method*

Since the samples are deposited through drop-casting, the 'coffee-ring' effect is evident, whereby differing rates of evaporation between the solvent components can lead to a heterogeneous distribution of analyte and AuNPs. The coffee ring pattern forms due to capillary action and Marangoni flow of the evaporating components [259]–[261]. As such, the effect can impact on the sensitivity and reproducibility of SERS measurements, as nanoparticle clusters

can form, leading to plasmonic hotspots and areas of high SERS enhancement. In order to ascertain an overall level of enhancement, spectra was averaged from from 5-10 different positions.

Figure 25 shows that MBA adsorbed onto AuNPs was strongly enhanced compared to the conventional Raman spectrum for powdered MBA. The characteristic peak at 1075 cm^{-1} can be assigned to the in-plane ring breathing mode coupled with ν(C-S). The peak at 1587 cm^{-1} is attributed to the aromatic ring ν(C-C). The SERS spectrum indicates MBA molecules are orientated at an angle towards the AuNP surface. This is inferred from the presence of the benzene ring out-of-plane bending and ring bending modes at 522 cm^{-1} and 1480 cm^{-1}, respectively [262]. The weak band observed at 1710 cm^{-1} is attributed to the C=O stretching mode and indicates the presence of neutral carboxylic acid groups [263]. Additional peaks for MBA are listed in Table 9. In the SERS spectrum, frequency shifts were observed with respect to the Raman spectrum. This is due to a combination of factors, including the structural deformation of the MBA molecule and change in polarizability of MBA upon formation of the Au-thiolate-bond [264], [265]

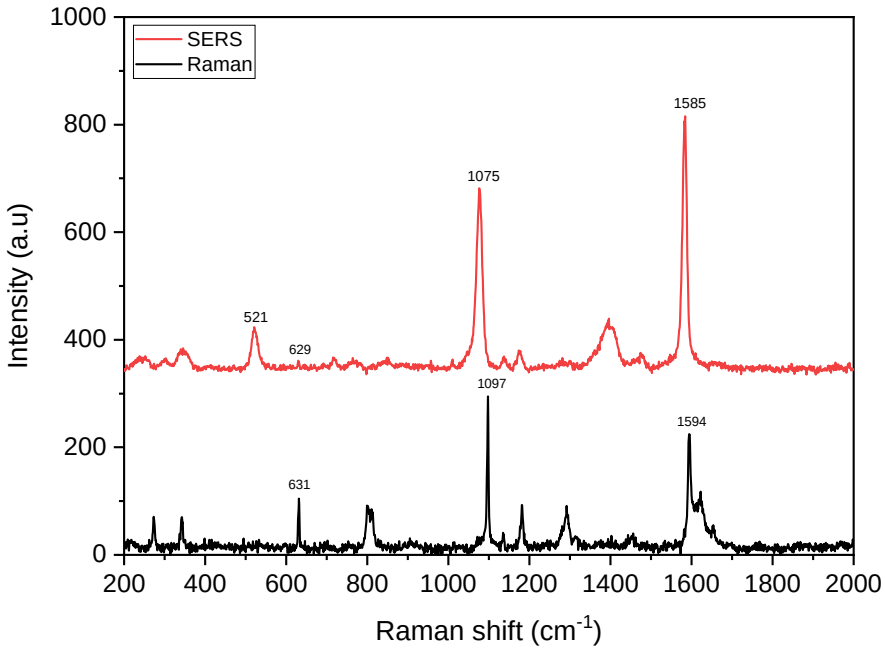

Figure 25: *Raman of MBA powder and SERS collected from a 1 μM MBA solution deposited onto a microscope slide.*

Table 9: *Vibrational modes for MBA. From Michota [263], Ma [262] and Wang [266].*

Raman mode (cm $^{-1}$)	SERS and PIERS modes (cm $^{-1}$)	Assignment
274	340	Au-S
1098	1075	in-plane ring breathing mode, C-O stretching, ν(C-O)
1180	1174	C-H bending
1480	1457	Ring bending
1590	1585	ring breathing axial deformation modes
1617	1707	C-O stretching, ν(C=O)

The enhancement factor for SERS can be calculated using equation 13 [21], [267]. I_{RS} and I_{SERS} refer to selected peaks in the Raman and SERS spectra, respectively. N_{Bulk} and N_{SERS} are the average number of molecules in the scattering area in the Raman and SERS measurements, respectively.

$$EF = \frac{I_{SERS}/N_{SERS}}{I_{RS}/N_{Bulk}} \tag{13}$$

The way in which N_{SERS} and N_{Bulk} is calculated can vary across the literature, depending on the experimental set-up. In this study, these values were calculated as per equations 14 and 15, where C is the concentration of the analyte, V is the deposition volume, N_A is Avogadro's constant, A_{Sub} is the area of the substrate (9 mm^2). The volume of the solid sample can be calculated from the laser spot area, A_{Raman} (351.76 nm^2) and h, the confocal depth (21 μm). M and ρ, are the molecular weights and densities, of the analyte, respectively. The EF factor in PIERS measurements, is compared against SERS.

$$N_{SERS} = \frac{CVN_A A_{Raman}}{A_{Sub}} \tag{14}$$

$$N_{Bulk} = \frac{\rho h N_A A_{Raman}}{M} \tag{15}$$

For MBA with concentration of 10^{-6} M, SERS enhancements of 3.37×10^6 and 5.81×10^6 were observed for the 1075 and 1584 cm^{-1} peaks, respectively, which is within the range reported in literature [262], [263], [266].

The comparison between SERS and PIERS of MBA on Pilkington Activ™ is shown in Figure 26. From the SERS spectrum, Raman peaks attributing to MBA can be seen and the spectral profile is similar to the Raman spectrum collected from powder. From the PIERS spectrum with 1 hr UV irradiation

at 254 nm, an enhancement of the characteristic peaks of MBA is observed (Figure 26A). Taking the 1585 cm^{-1} peak as an example, an enhancement factor of 3.51×10^7 is observed. When compared to the SERS, the increase in enhancement is ≈6 times. Post-PIERS measurements were made by keeping the samples in the dark for over one hour and subsequently collecting spectra from the same region. A decrease in the Raman signal is seen indicating a loss in the PIERS enhancement. This can be attributed to healing of oxygen vacancies on the surface of TiO_2 as the film is exposed to air. To better support the above observations, reference SERS spectra was collected on a piece of Activ™ which had been kept in the dark and without irradiation (Figure 26B). Weak SERS intensities are seen, which indicates a weak EM enhancement. In addition, the SERS spectra collected from samples deposited onto float glass (without TiO_2) also shows a weak enhancement, comparable to Figure 26A. As a further confirmation, Raman spectra collected from MBA deposited onto irradiated Activ™ in the absence of AuNPs does not show any observable peaks (Figure 26C). These observations confirm the additional enhancement originates from a photo-induced effect.

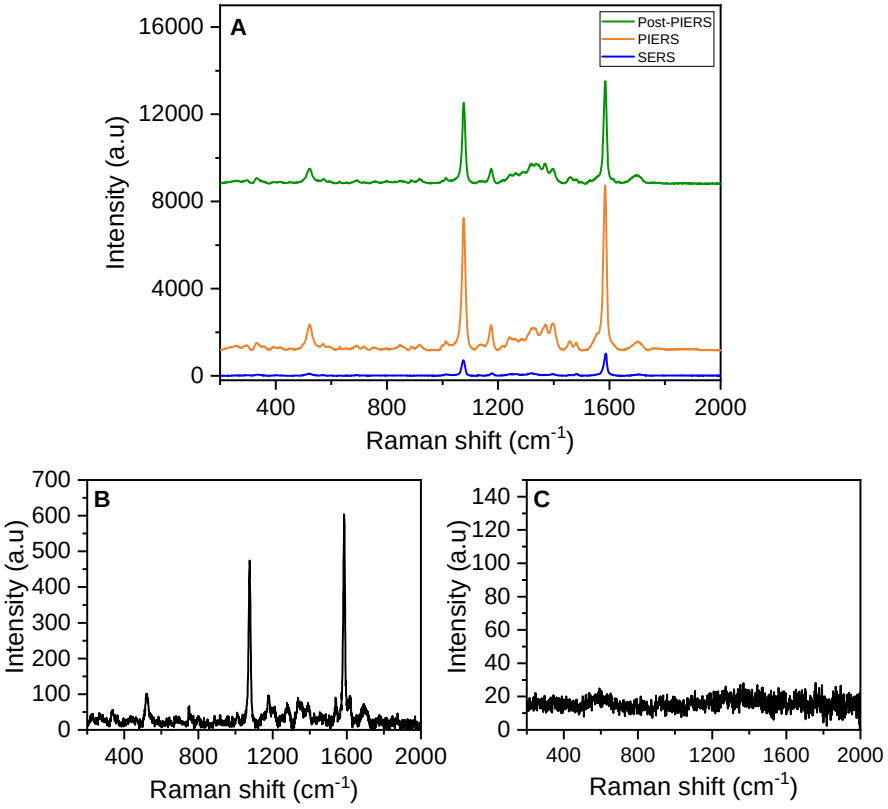

Figure 26: *SERS and PIERS enhancement of MBA (10^{-6} M) solution. A) Comparison between SERS, PIERS and post-PIERS measurements, B) Reference spectrum of MBA deposited onto uncoated float glass and C) Reference spectrum of MBA deposited onto irradiated Activ™.*

The observed additional enhancement can be attributed to the PIERS effect. When semiconductors are exposed to photons with energy above their bandgap, electrons are excited from the valence band (VB) to the conduction band (CB), leaving a hole in the VB. TiO_2 is an n-type semiconductor, which means the charge carriers are electrons. Both the excited electrons and holes can participate in a redox processes and subsequently utilised, for example in photocatalysis or superhydrophilic surfaces. The nature in which photogenerated electron-hole pairs (e^--h^+) migrate towards the surface of TiO_2, will impact on the subsequent redox processes and properties of TiO_2. Oxygen vacancies

(V_O) are point defects which can be induced in a number of ways. Under UV irradiation, reduction of Ti(IV) cations to Ti(III) by electrons and trapping of holes at lattice sites occurs simultaneously, which result in weakening of Ti-O-Ti bonds within the lattice. As oxygen is liberated, V_O are formed. The two electrons formerly bound to the oxygen ion remain in the oxide and populate defect states, typically located inside the bandgap (in-gap states). When these electron donor states lie close to the CB, electrons can delocalize into the CB. The AuNPs acts as a bridge between the semiconductor and molecule, allowing electrons to be injected into the Fermi level (E_F) of AuNPs, under laser excitation. This results in shifting of the AuNP E_F to more negative values, broadening the resonance conditions between the E_F and molecular orbitals of adsobed molecules. As such, more charge-transfer pathways can exist and greater enhancement is observed. In the current system, an excitation laser of 633 nm (1.96 eV) is used. The band gap of TiO_2 anatase is 3.20 eV, the V_O donor states for anatase is reported to be 0.35-1.27 eV below the CB [268], the energy gap of MBA is 4.57 eV [269] and the Fermi level of gold is 5.0 eV (vs. vacuum) [270]. The drop in signal intensity in the post-PIERS measurement is due to healing of the surface oxygen vacancies in the TiO_2 film when exposed to air. The charge-transfer scheme for PIERS is shown in Figure 27.

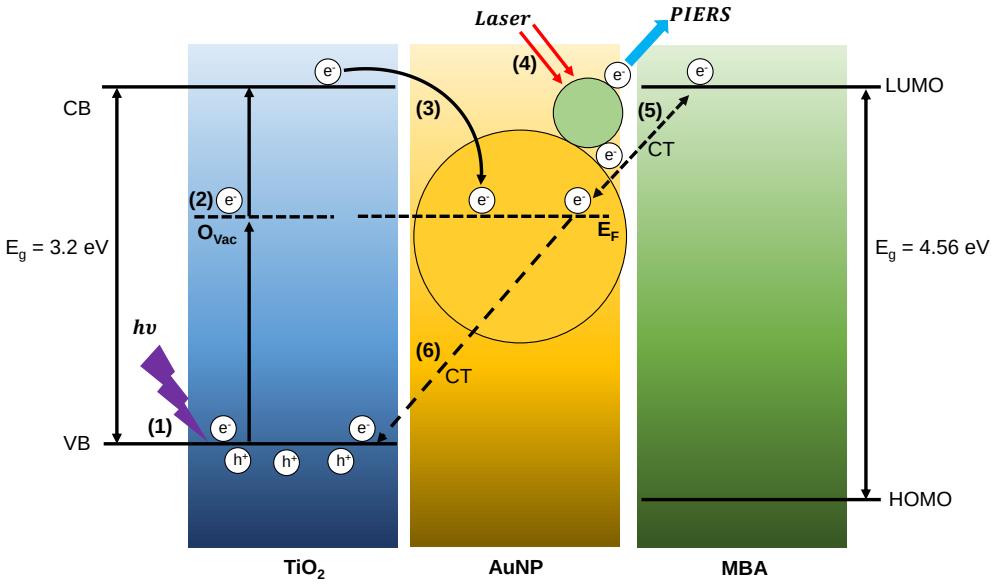

Figure 27: *Stages in the mechanism of charge transfer in PIERS, where E_g is the bandgap, O_{Vac} is the defect level, E_F is the Fermi level, CT denotes charge-transfer processes, LUMO is the lowest occupied molecular orbital and HOMO is the highest occupied molecular orbital. 1) Above-bandgap excitation of TiO_2 using 254 nm UV light, 2) Generation of defect state, 3) Injection of electrons into the Fermi level of AuNPs, 4) Laser irradiation using 633 nm laser, 5) CT between AuNPs and LUMO of MBA molecules, 6) Relaxation of electrons back to VB of TiO_2.*

3.3.3 *Studying the charge-transfer in PIERS using UV-Vis*

To provide evidence of charge injection process in PIERS, UV-Vis was used to monitor changes in the LSPR of AuNPs deposited onto irradiated Activ™. The LSPR of noble metal nanoparticles arises from the coherent oscillation of free electrons on the surface of AuNPs with the incident light. The LSPR is strongly affected by electron density and shifts in the LSPR of nanoparticles can be used to study photogenerated charge carriers at metal-semiconductor interfaces. Whilst resonance shifts can also be attributed to changes in the size, shape and dielectric environment of the AuNPs, a number of studies have used this approach to study charge-transfer (CT) [271]–[273]. Figure 28 shows the absorption spectra of AuNPs deposited onto Activ™ before irradiation and after 1 hrs UV irradiation, with consecutive timepoint measurements over

10 minutes. After irradiation, the LSPR peak blue-shifted by about 7 nm. Consecutive measurements show the change is partially reversible and a 4 nm red-shift is observed after 10 minutes. UV-induced plasmon changes were also observed by Parente *et al.* [272] from TiO_2-AuNP heterostructures and Mulvaney [273].

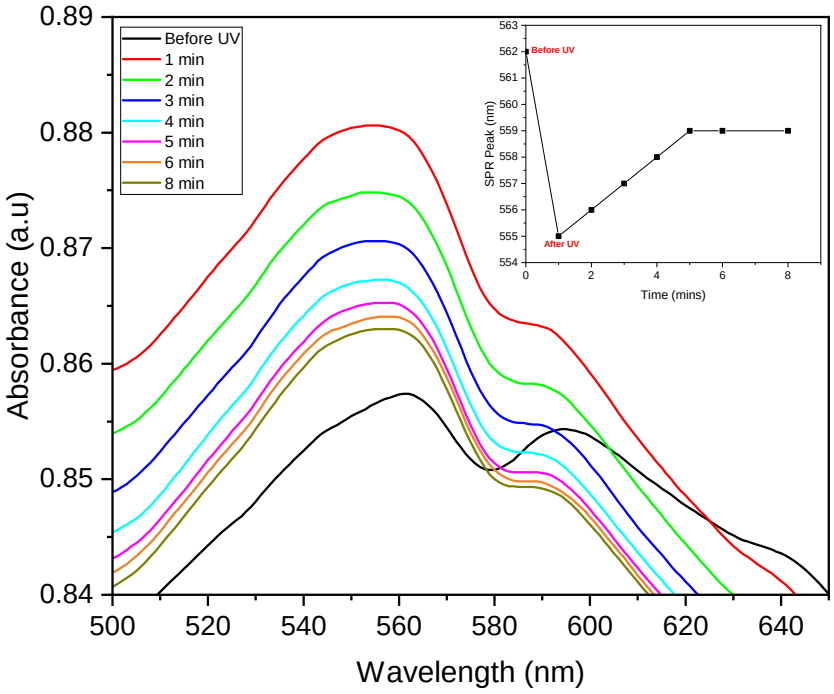

Figure 28: *AuNP LSPR blue-shift on Activ™.*

The injected electron density ($\frac{\Delta N}{N}$) on the AuNPs due to pre-irradiation of TiO_2 can be estimated using Equation 16 [273]. $\Delta\lambda$ is the measured wavelength shift (7 nm) and λ_0 is the initial AuNP plasmon peak position on the TiO_2 substrate (562 nm). From Equation 16, the electron density is 2.5 % upon irradiation.

$$\frac{\Delta N}{N} = -\frac{2\Delta\lambda}{\lambda_0} \tag{16}$$

3.3.4 *Studying the charge-transfer in PIERS using photoluminescence*

The previous section showed one approach to support the charge-transfer effect in PIERS through monitoring the shifts in the AuNP LSPR. In this section, we study the charge transfer behaviour through changes in the fluorescence emission of Rhodamine 6G (R6G). R6G is widely used as a marker and laser dye for its stability, high fluorescence and quantum efficiency. The plasmonic resonance exhibited by metallic nanoparticles can be used to tailor the properties of organic molecules and interactions between dye molecules and noble nanoparticles can be used to study charge transfer effects [274], [275]. Furthermore, the addition of a semiconductor to metallic nanoparticles can create a potential energy barrier for electron migration. The result is the modification of AuNP and/or semiconductor properties.

Mixtures of AuNP and R6G were deposited onto Activ™ and Pilkington glass. Initially, SERS and PIERS measurements for R6G were collected and these are shown for a solution of R6G at 1 µM, in Figure 29, along with the powder Raman spectrum. A list of characteristic peaks for R6G is shown in Table 10. Using the peak at 1357 cm $^{-1}$, the enhancements for SERS and PIERS were 1.10×10^{3} and 4.46×10^{3}, respectively, giving an overall 4 times PIERS enhancement compared to SERS.

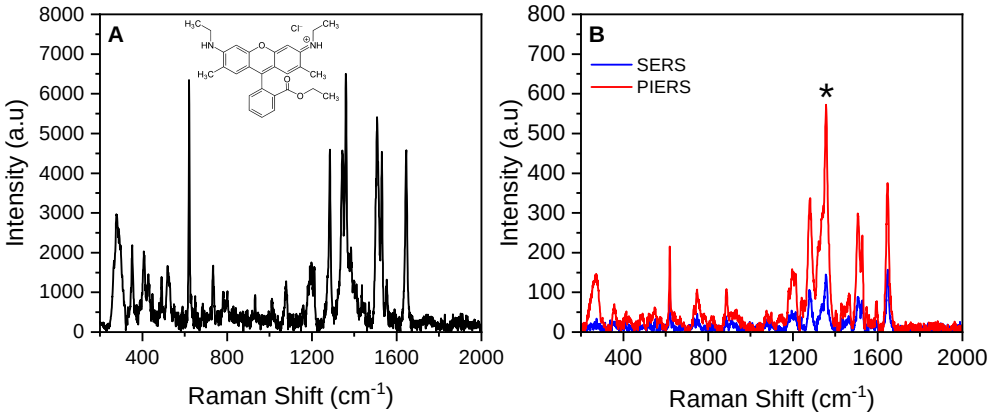

Figure 29: *SERS and PIERS of R6G A) Raman spectrum of R6G powder, B) Comparison between SERS and PIERS of R6G (peak at 1357 cm $^{-1}$ marked with asterisk used in EF calculation). Note, Raman spectrum in A) was collected with higher laser power to ensure clarity of peaks.*

Table 10: *Calculation of SERS and PIERS enhancement factors (EF) for R6G at 1 μM.*

Raman peak (cm $^{-1}$)	Assignment	SERS peak	EF: SERS	EF: PIERS
621	C–C–C ring in-plane vibration [276]	618	1.10×10^3	3.20×10^3
1360	N–H in-plane bending [276]	1357	1.10×10^3	4.46×10^3
1646	aromatic C-C stretching [276]	1648	1.71×10^3	4.07×10^3

For the photoluminescence (PL) studies, samples were kept in the dark overnight before analysis to prevent unwanted photo-activation of the substrate. A 514.5 nm excitation source was used which is below the band gap excitation energy for TiO_2, eliminating PL emission from TiO_2. Figure 30A shows the UV-Vis spectrum of R6G in methanol for reference, with an absorption maximum at 550 nm. There is an overlap between the absorption maximum of the AuNPs at 540-550 nm (as shown in Chapter 5) and the emission of R6G molecules which shows that non-radiative energy transfer between dye

molecules and AuNPs is possible. Figure 30B shows the emission of R6G on each substrate with and without UV irradiation. The fluorescence emission peak for R6G on Pilkington glass is at 576 nm and on Activ™, at 573 nm. These values fall within literature ranges of 550-570 nm and variations can be due to a combination of the dye concentration and the solvent environment, which can affect the dispersion of R6G molecules into its monomer and dimer forms [277]. In the presence of AuNPs, the emission peak is enhanced in both cases and peak position is red-shifted. To observe the effect of photo-active substrates on the fluorescence of R6G, samples containing AuNP and R6G deposited onto Pilkington glass were subjected to 5 minutes of UV-C irradiation followed by PL analysis under 514.5 nm. On Pilkington glass, a small reduction in emission intensity is observed. On Activ™, the intensity is enhanced compared with the sample in the absence of UV irradiation.

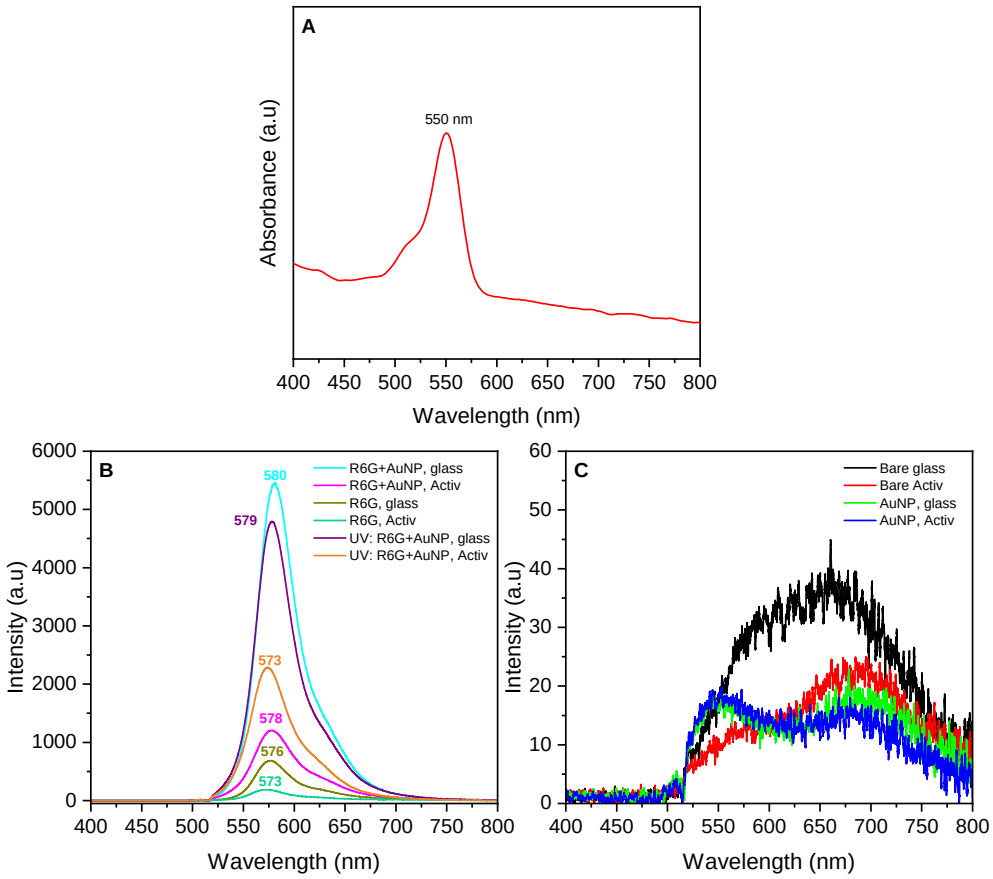

Figure 30: *Photoluminescence (PL) studies to observe charge transfer in PIERS A) Absorption spectrum of R6G in methanol B) PL of R6G and AuNPs on Pilkington glass and Activ™ with and without UV irradiation, C) PL of bare Pilkington glass and Activ™ and with deposition of AuNPs. PL spectra were collected using a 325 nm excitation source.*

Upon excitation, a fluorophore can return to ground state by emitting a photon at a longer wavelength (radiative decay) or without emitting a photon (non-radiative decay). In the vicinity of a metallic structure, both the radiative and non-radiative decay rates can be changed due to interactions with the surface plasmons from the metallic surface. As such, the local field effects can result in fluorescence enhancement or quenching [278]. The distance between nanoparticle-fluorophore can affect fluorescence enhancement or quenching. Studies using AuNPs have shown that at small distances (AuNP radius $\leq$30 nm), surface plasmon-induced resonance energy transfer occurs which results

in quenching of radiative transitions and fluorescence quenching [279]–[281]. Smaller nanoparticles can have a stronger plasmon field which can result in increased dissipation of nonradiative energy transfer between dye molecules and nanoparticles, resulting in a greater fluorescence quenching [282].

However, at longer distances, localised fluorophores can be excited by the nanoparticles, which can enhance the radiative decay rate and lead to fluorescence enhancement [278], [283]. This can be mediated by changing the shape and size of the nanoparticle [284], distance between nanoparticle and dye [285] and the solvent medium [286], with a number of reported examples using different metallic nanoparticles. The enhancement of R6G fluorescence observed in the presence of AuNPs could be due to the large, 50 nm AuNPs used in comparison to the aforementioned literature [279]–[281], resulting in a higher quantum yield [282]. The tris-base capping agent on the surface of AuNPs can also act as a separation layer reducing the nonradiative energy transfer between R6G molecules and AuNPs [285]. Furthermore, samples were analysed as evaporated from a substrate, as opposed to in-solution analysis, where a greater proximity between AuNP and R6G dye molecules can be achieved, as well as greater dimensionality [287]. Similar results were also observed in literature [288]–[290].

The enhancement of the R6G emission under UV light can be explained by the transfer of photogenerated electrons at the Au-TiO_2 interface, where an interfacial charge equilibrium is established. When the TiO_2 is excited by UV light with photon energy greater than its band gap, excitation of electrons from the valence band (VB) to the CB occurs, with simultaneous generation of holes in the VB. At the AuNP-TiO_2 interface, photogenerated electrons are distributed, with some transferred into the Au nanoparticle, resulting in a new interfacial charge equilibrium. The ability of metallic nanoparticles to ‘capture’

photogenerated electrons occurs when the work function of the metal is at a lower energy than the conduction band edge of the semiconductor [271], [291]. The Fermi level of gold is 0.5 V [292] and the conduction band energy of TiO_2 anatase is -0.8 V [293], (versus Normal Hydrogen Electrode, NHE). Upon UV irradiation, electron accumulation increases the Fermi level (Ef) of Au to more negative potentials (Ef*), bringing this closer to the conduction band of TiO_2.

As a control, PL spectra of the substrates with and without AuNP is shown in Figure 30C. Broad peaks can be seen in both Pilkington glass and Activ™, which is likely due to a combination of surface contaminants and slight absorption in the UV-Vis region (Figure 21), which can give rise to weak emission bands in the blue-green spectral area. In the presence of AuNPs, a peak at approximately 530 nm is observed which is likely due to absorption from the tris-capping agent. PL emission arising from the 50 nm AuNPs used in this study is unlikely as this phenomena usually comes from smaller, metal nanoclusters (< 2 nm), which are considered to have discontinuous energy levels, enabling the interaction with light through electronic transitions[294], [295]. As such, the graphs in Figure 30C supports the observed emission peaks arising from R6G.

3.3.5 *Studying the oxygen vacancies of Activ™ using photoluminescence*

This section focuses on studying the influence of deposited AuNP on the PL of TiO_2. The aim of the work is to establish a link between formation of oxygen vacancies and PIERS enhancement. Spectroscopic techniques can be used to study the nature of photogenerated excitons and their role in photocatalysis which subsequently affects the efficacy of applications such as self-cleaning surfaces, gas sensing and PIERS. Photoluminescence can be used

to differentiate between surface and bulk processes, study the separation and recombination of photoinduced charge carriers and contributions of surface oxygen vacancies and defects.

PL has been used to differentiate between anatase and rutile phases of TiO_2. However, the PL processes in TiO_2 are complex, with many mechanisms still under debate. For example, Tang *et. al.* attributed the green PL emission band of anatase to localised distortions in the lattice, resulting in self-trapping of the exciton [296]. On the other hand, Wang *et al.* attributed the green emission band to donor-acceptor recombination, realised through oxygen vacancies and surface hydroxyl groups, respectively [297]. Work by Pallotti *et al.* reported the main contributions to the PL of TiO_2 anatase being due to two characteristic bands. The green emission band (at approximately 495-540 nm) is assigned to surface oxygen vacancies, whereas the red emission band (at approximately 600-650 nm) is due to subsurface oxygen vacancies [298], [299].

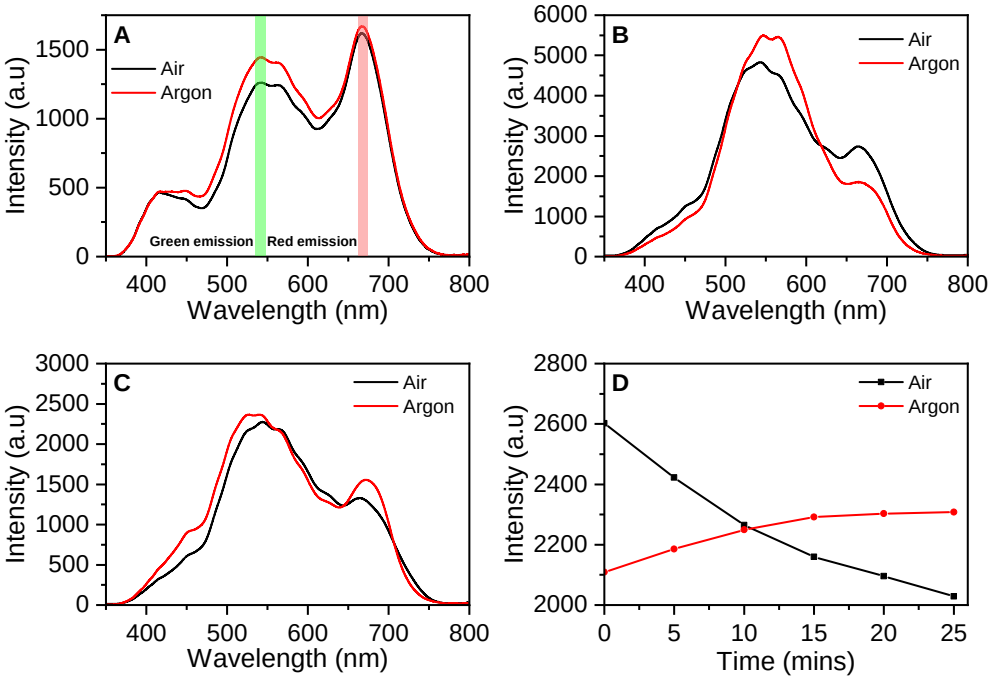

Figure 31: *Studying the PL emission of TiO_2 Activ™ in air and argon. A) Bare TiO_2 without prior UV irradiation B) Bare TiO_2 after 1 hr UV (254 nm) irradiation, C) TiO_2 with AuNP deposited, followed by 1 hr UV (254 nm) irradiation D) Timepoint analysis of Bare TiO_2 samples with deposited AuNPs carried out by observing the PL intensity of the green emission band in air and argon. PL spectra were collected using a 325 nm excitation source.*

Figure 31 shows the PL spectra of TiO_2 Activ™ analysed under air and argon. PL studies were carried out in the custom chamber described in the next section (Figure 32), at room temperature using a 325 nm excitation source. Firstly, the PL of TiO_2 Activ™ was collected in the absence of AuNPs and without additional UV pre-treatment (Figure 31A). The characteristic PL peaks for TiO_2 anatase can be seen. The peak in the UV region, around 390-410 nm, is attributed to the band edge emission and corresponds to the bandgap estimated from the Tauc Plot in Figure 21. The green and red band emisson (henceforth named GBE and RBE, respectively), are positioned around 550 nm and 670 nm, respectively. Samples analysed under argon were placed in the custom chamber under argon flow for one hour before PL collection. Both the GBE and RBE are enhanced under argon flow, with the GBE show-

ing greater enhancement. Figure 31B shows the PL of TiO_2 Activ™ which has been pre-treated by irradiating under UV-C (254 nm) for 1 hour before immediate analysis. Both the GBE and RBE are enhanced compared with samples without UV pre-treatment. Under argon, the GBE is more enhanced compared with the sample in air but the RBE is suppressed. This suggests there are different excitation mechanisms associated with the GBE and RBE. These results correspond to results by Pallotti *et al.*, who observed a higher dominance of the GBE in above-bandgap excitation, and RBE dominance in below-bandgap excitation [298].

There is general agreement in literature that a number of electron and hole traps exist for TiO_2 and various depths have been reported. A number of studies have revealed the GBE is attributed to hole traps arising from oxygen vacancy (V_O) defects, where the recombination of electrons with holes in defect states results in the GBE. This would explain the sensitivity of the GBE towards UV pre-irradiation which increases the concentration of oxygen vacancies, resulting in faster recombination and higher GBE. The adsorption of chemical species on the surface of semiconductors can also affect charge carrier recombination dynamics. V_O can be healed by exposing TiO_2 to O_2 which can decrease the number of luminescent traps and scavenge electrons from the conduction band and shallow traps [300]. Furthermore, photogenerated charge carriers can react with adsorbed O_2 to form superoxide species. As such, at bandgap excitation, photogenerated electrons will react with adsorbed species whilst others will follow a radiative pathway. In a low O_2 environment (as represented when samples are analysed in argon), a greater proportion of photogenerated electrons will be available for radiative decay, resulting in greater GBE.

Figure 31C shows the PL of TiO_2 Activ™ with AuNPs after 1 hr UV-treatment. Both the GBE and RBE are suppressed compared with samples in 31B. It has been reported that AuNPs can capture photoexcited electrons at metal-semiconductor interfaces. This process provides an alternative recombination route for photogenerated electrons, which does not result in PL. As such, the number of electrons which radiatively recombine with holes in TiO_2 are diminished, resulting in a lower emission [301], [302].

A timepoint analysis was carried out using samples with AuNP deposited onto Activ™ (Figure 31D). Both analyses were carried out after 1 hr UV irradiation. The GBE was then measured over a period of 30 minutes, under air and argon. In air, the emission shows an exponential-like decay with time. However, in argon, we observe an increase in emission followed by a plateau, akin to a logistic growth curve. The change in the GBE emission in air further supports the healing of V_O.

It must be noted that in this study samples were irradiated in air before transferring to the chamber under argon flow. Ideally, the chamber would be designed in such a way to include vacuum sealing as well as simultaneous irradiation and filling of the chamber with inert gas. To negate the effect of residual O_2, the chamber was purged with argon at a flowrate of 0.5 L/min for at least 30 minutes. However, the internal atmospheric composition could contain low concentrations of oxygen and could affect the charge carrier recombination dynamics.

This section has studied the PL behaviour of the GBE in TiO_2 which is attributed to the formation of V_O defects. Samples were analysed in a low oxygen environment, with AuNPs and under prolonged UV-C irradiation. The changes in the GBE can be attributed to changes in the pathway of photogenerated charge carriers. These observations correlate with similar studies

carried out in literature. The above results, in addition to the CT experiments discussed earlier, further supports the PIERS mechanism of defect-induced charge transfer.

3.3.6 *PIERS in a low oxygen environment*

This section describes the study into PIERS carried out in low oxygen environments. All experiments were carried out in a custom-built chamber connected to an argon gas flow. A number of iterations were trialled through prototype chambers (to meet size, movement and hermetic requirements) before fabrication of the final design using a 3D printer. The chamber consists of an annulus connected to a stage which is tightened using screws. Gas flow is achieved through syringe needles inserted into the chamber and connected to a gas cylinder. A rubber baffle connects the microscope objective to the chamber and the entire unit can be moved simultaneously with the microscope stage. [1] Figure 32 shows the experimental setup used in this section, along with photographs of the chamber. Note that for experiments described in this section, measurements were carried out using a 785 nm Raman laser due to having to accommodate the chamber with the microscope stage. Measurements were collected from a 50x objective and with a laser power of 4.508 mW (at 25 %), which is higher than that used in previous sections. Due to the difference in laser wavelength and power, SERS and PIERS experiments were repeated to provide appropriate controls.

[1] The author would like to thank the MAPS workshop in the Chemistry Department for advice, design refinement and building of the chamber.

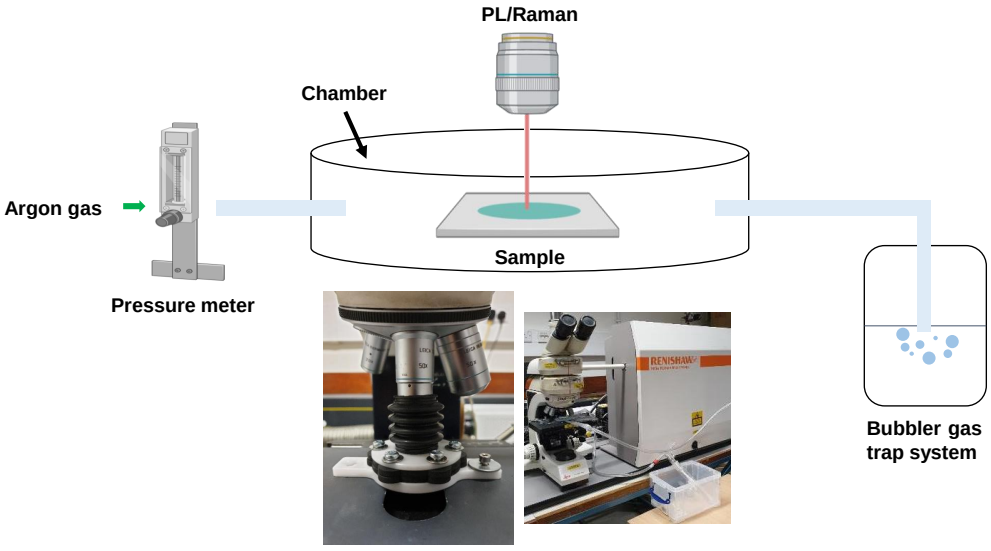

Figure 32: *Custom chamber used to conduct Raman measurements under argon flow.*

Figure 33 shows the PIERS carried out in argon, compared against PIERS carried out in air and normal SERS. When PIERS was carried out in air, a 4.43 $\times$ 10^6 enhancement was observed. When PIERS was carried out under argon flow, a 7.46 $\times$ 10^6 enhancement was observed, giving approximately 2-fold improvement compared with normal SERS (Table 11).

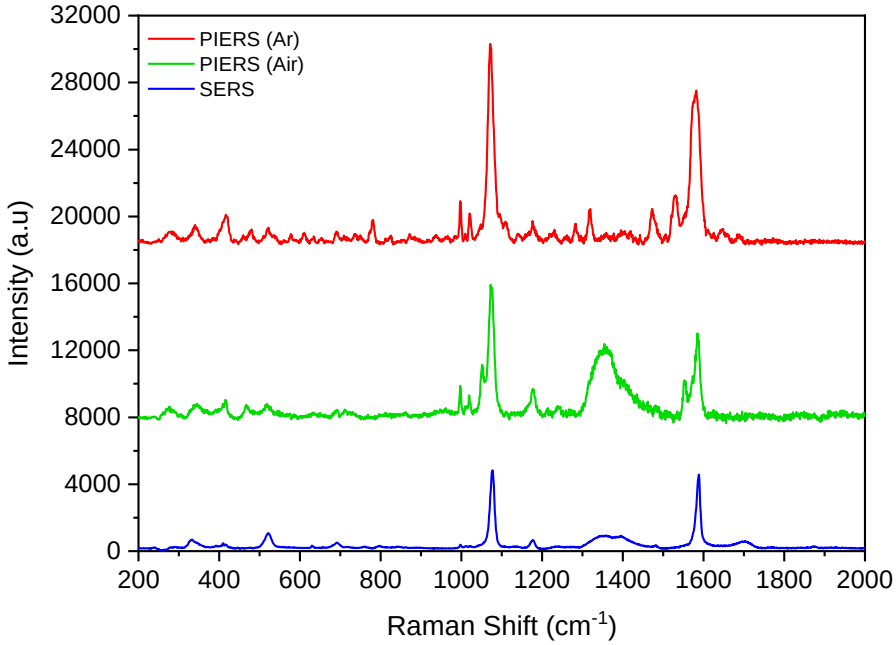

Figure 33: *PIERS carried out in argon and air*

Table 11: *SERS and PIERS enhancement factors under different conditions*

Condition	MBA peak (cm^{-1})	EF:SERS/Raman	EF:PIERS/Raman	Overall EF
Air	1071	1.91×10^6	4.43×10^6	2.31
	1585	2.58×10^6	2.86×10^6	1.11
Argon	1071	1.91×10^6	7.46×10^6	3.90
	1585	2.58×10^6	5.71×10^6	2.22

Additional studies were conducted to monitor the changes in the MBA spectra under argon flow. (Figure 34). In Figure 34A, the spectral profile of MBA was monitored through changes in the intensity of the 1075 cm^{-1} peak over time. As a control, SERS was collected under argon, from a glass substrate for the same time period. When PIERS is observed in air, the enhancement follows a logarithmic-like decay curve. However, when PIERS is carried out under argon flow, a small decay in enhancement is observed initially, after which the enhancement increases over the course of around 40 minutes. Whilst the SERS under argon showed fluctuations in the enhancement, the level of

enhancement remained low and did not reach the levels observed in the PIERS measurements.

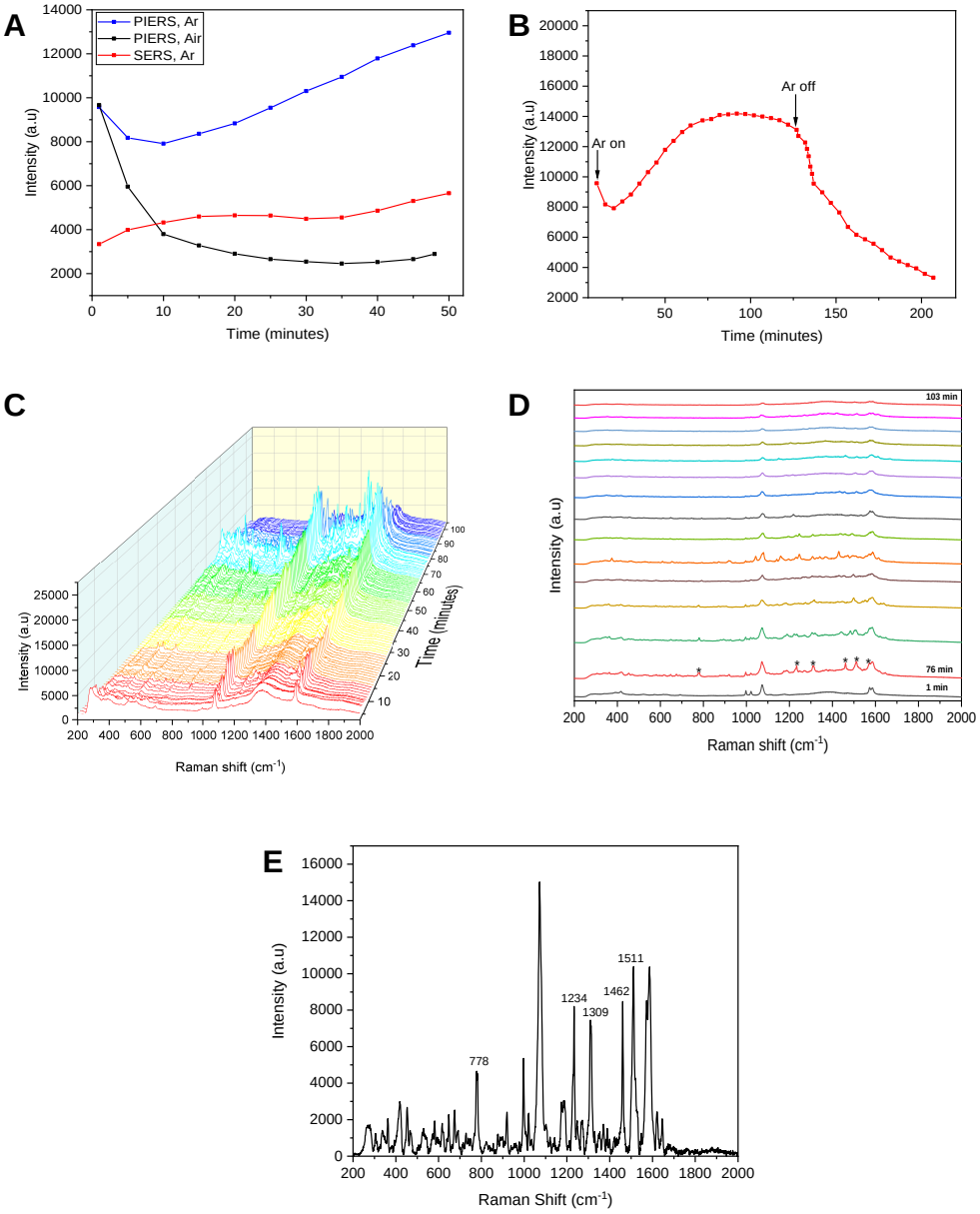

Figure 34: *Studying PIERS under argon. A) Timepoint measurements plotted using the 1075 cm^{-1} peak between SERS and PIERS in air and argon (Ar) carried out over a period of 50 minutes, B) Intensity of the 1075 $^{-1}$ peak monitored when PIERS was carried over 4 hours under argon, C) Waterfall diagram of MBA spectra collected at time points in B), D) Selected spectra from C), at 1 min, 76 min and every 2 minutes thereafter to show the change in the spectral profile. Peaks labelled with an asterisk denote enhanced vibrational modes reported in literature, E) Enlarged view of spectrum at 76 minutes showing additional enhanced modes.*

Figure 34B shows a timepoint measurement carried out over 3 hours, showing a similar trend in which the peak intensity increases over time and reaching a plateau after approximately 75 minutes. The PIERS enhancement remained constant until the argon was switched off and air introduced into the system. The peak intensity can be seen to decrease to levels comparable to those observed in SERS. The corresponding spectra of the extended timepoint measurement is shown in Figure 34C and 34D, which shows an increase in the intensity of MBA peaks and subsequent drop on introduction of air. These observations indicate the chemical environment can affect the resultant PIERS enhancement. Interestingly, the spectrum at the point with the greatest enhancement shows a number of additional peaks not normally observed in SERS or PIERS spectra of MBA (Figure 34E). These peaks can be selectively enhanced vibrational modes of MBA as some match those calculated by Li *et al.* [303].

3.4 MECHANISM OF PIERS IN A LOW-OXYGEN ENVIRONMENT

As seen above, when PIERS is carried out in argon, there is a notable difference in the enhancement and lifetime of the PIERS effect. These results, along with the CT and PL experiments described previously can be explained as due to changes in the interfacial charge-transfer pathways in the TiO_2-AuNP system. The factors affecting PIERS enhancement are closely linked to those affecting the photocatalytic process in metal oxide semiconductors. In n-type semiconductors, photocatalysis is initiated when a material is subjected to photon energy equal to or above its bandgap. Photogenerated excitons in the VB and CB can then migrate to the surface from which redox processes occur. High recombination rates between photogenerated electrons and holes can limit

the effectiveness of a photocatalyst. Excited charge carriers can also become trapped as surface defects, creating oxygen vacancies, which can trap electrons and slow down the recombination rate of photogenerated charge carriers. In the PL experiments, the emission peak attributed to TiO_2 oxygen vacancies O_{vac} was found to be enhanced under prolonged irradiation and when the sample was kept in argon, suggesting these conditions can favour an increase in mobile electrons within the system. This also suggests a link between the PIERS enhancement to the rate of oxygen vacancy healing. Furthermore, this is supported by a recent study linking oxygen vacancies with longer lifetimes to higher photocatalytic activity and greater PIERS enhancement [304].

The presence of AuNPs in the system can provide an alternative pathway for migration of photogenerated electrons. At the TiO_2-AuNP interface, a Schottky barrier is formed due to the overlap between the Fermi level of the metal (Au) and the conduction band of the TiO_2. This allows the transfer of photogenerated electrons across the barrier, and injection onto the AuNP surface. The UV-Vis measurement showed the LSPR of AuNPs was temporarily shifted by 7 nm when subjected to UV irradiation on TiO_2, which indicates a charge-transfer process in place. These observations are supported by similar shifts in AuNP LSPR observed in PIERS studies reported [218], [224], [233]. Charge injection onto AuNPs can increase the lifetimes of the photogenerated carriers. Another outcome is improved resonance conditions between the Fermi level and molecular orbitals of adsorbed species, increasing the number of charge transfer pathways with the adsorbates. This was shown through the PIERS enhancement of R6G as well as an enhanced fluorescence emission in the presence of AuNPs and after a brief exposure to UV irradiation.

As such, factors which affect the properties of semiconductors can also influence normal PIERS (in air). The routes that photogenerated charge carriers

can undertake in the current TiO_2-AuNP system is shown in Figure 35 and it can be seen that numerous pathways exist towards recombination.

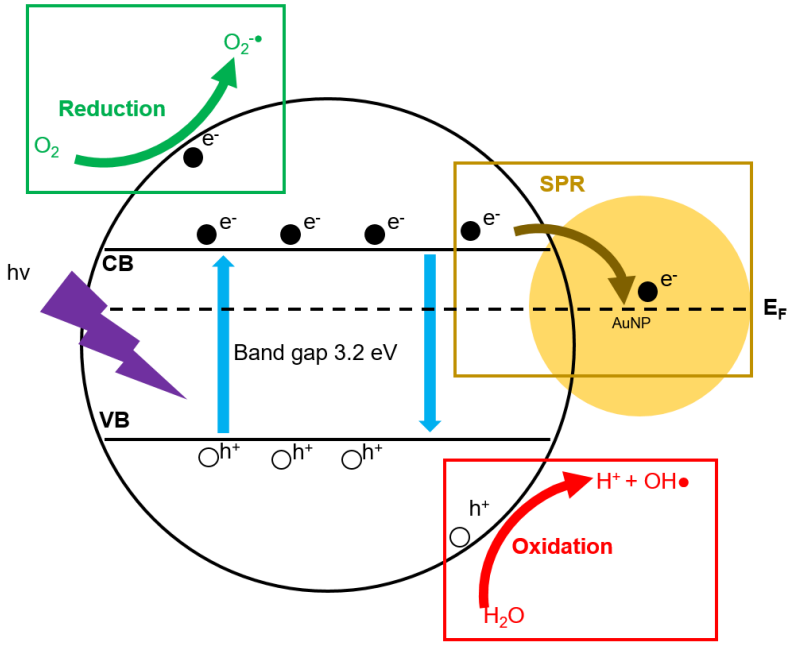

Figure 35: *Processes occurring during PIERS carried out in air.*

In all reported studies to date, PIERS measurements have been carried out in air and an exponential-like decay of the enhancement is observed, after which there is a return to SERS enhancement. When PIERS is carried out in argon, there is a disruption to the aforementioned pathways and a number of events can take place. Firstly, the low-oxygen environment created, disrupts the redox processes, namely suppression of the O_2 reduction pathway. A greater number of electrons become available for the TiO_2 to AuNP pathway, leading to higher electron density on AuNPs, greater charge-transfer contribution enhancement. Secondly, the low-oxygen environment can slow down the rate of oxygen-vacancy healing and so photogenerated electrons remain trapped at defect sites for longer. This further slows down the recombination of charge carriers, possibly allowing for a prolonged transfer of high electron density from TiO_2-AuNP and the longer PIERS lifetime. Evidence of this can be seen

in the time-points analysis plots of the PIERS and the TiO_2 PL spectra (Figures 34A and 31D, respectively). In both cases, an exponential-like decay was observed for measurements in air, whereas in argon, a logistic growth effect was seen. The re-introduction of air into the system restores the reductive pathway and promotes healing of the film, resulting in a drop in the PIERS enhancement to levels similar to SERS.

3.5 OVERCOMING SURFACE WETTING LIMITATIONS OF ACTIV™ FOR USE IN PIERS

This section focuses on practical improvements to using Pilkington Activ™ for PIERS. The 'coffee-ring' effect is widely exploited in SERS measurements and is observed upon deposition of liquid mixtures onto a solid support, forming a droplet. The phenomena occurs due to a combination of evaporation, capillary action and Maragoni flow effects from the solvent, leaving a higher concentration of particles at the periphery of the coffee ring [259], [261]. In SERS (and by extension, PIERS), the enhancement of the local electric field is much stronger in nanogap junctions, which is why AuNPs clustered together (i.e. at the edge of the coffee ring) will give higher EF compared compared with isolated particles. One of the properties which makes Activ™ an attractive material for self-cleaning surfaces is its photo-induced superhydrophillicity. The effect occurs upon formation of surface oxygen vacancies which causes dissociation of adsorbed H_2O molecules and hydroxylation of the TiO_2 surface. Improved surface interactions with H_2O molecules (through H-bonds and Van der waals forces), lowers the contact angle of droplets, increasing wettability.

However, when samples are dropcasted onto UV-irradiated TiO_2, the enhanced hydrophilic surface results in uncontrolled spreading of the droplet,

which largely eliminates the coffee-ring effect, affecting the distribution of AuNPs. This study aimed to improve the enhancement observed in normal PIERS, by controlling the spread of the deposited droplet.

A simple solution was developed whereby a mask was placed over the Activ™ during the irradiation step to create two different areas of wettability. A schematic of the approach is shown in Figure 36A. To confirm there were two areas with different wetting properties, contact angle measurements were carried out using H_2O (Figure 36B). On the masked part of the sample, the contact angle is 55.16° which shows the area is hydrophilic. In the unmasked area, the contact angle is reduced to 21.97°. This shows the surface turned highly hydrophilic after UV irradiation. The result confirms there the two areas with different wetting properties. The effect of the different wetting properties on AuNP distribution was studied using SEM. Figure 36C shows a sample of Activ™ irradiated without the mask. The AuNPs are spread out across the film, dispersed into isolated particles and small clusters. In the masked sample (Figure 36D), the AuNPs form much larger clusters and the boundary between the hydrophilic and highly hydrophilic areas can be seen, as marked by the high density AuNP layer.

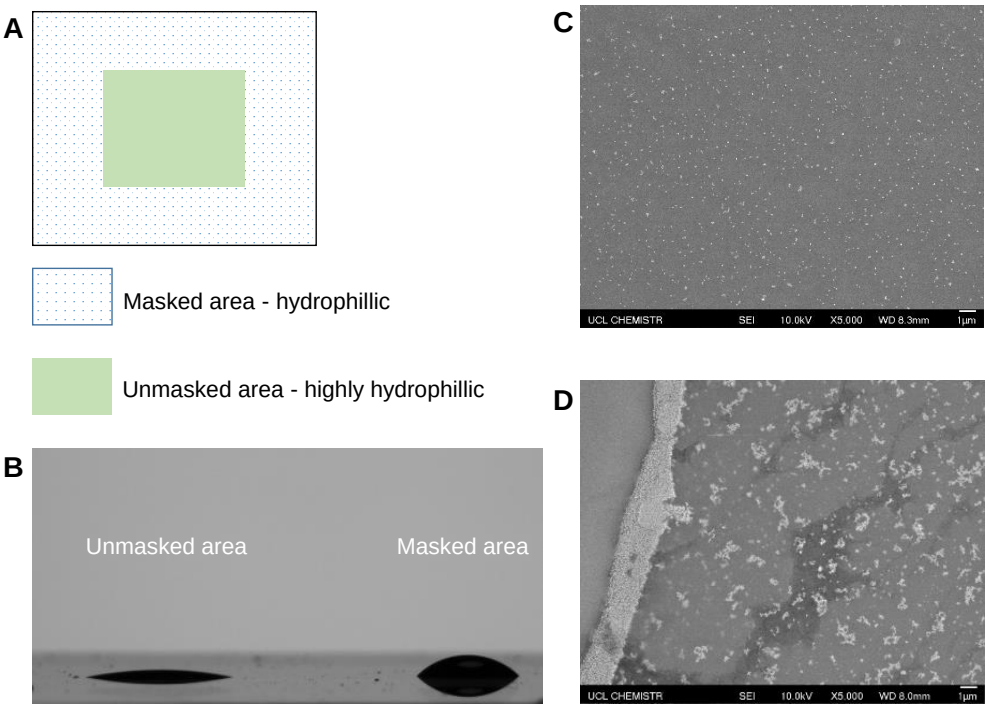

Figure 36: *Characterisation of masked Activ™. A) Schematic of mask outline used. B) Photo showing contact angle measurements taken on a piece of Activ™ with mask and subjected to irradiation. Two areas of different wetting properties are observed. C) SEM image of irradiated unmasked Activ™ and D) SEM image of irradiated masked Activ™, showing the distribution of AuNPs.*

MBA solutions were prepared in methanol at different concentrations (μM - nM) and PIERS was carried out using the masked substrate (henceforth named m-PIERS). The enhancement of characteristic Raman peaks (1098 cm^{-1} and 1595 cm^{-1}) were compared with normal SERS and PIERS (without mask). PIERS was also carried out in argon and the enhancement factors for all conditions can be seen in Table 12. For MBA at 1 nM, all of the PIERS variants showed an improved enhancement compared with SERS. The EF's show there is an increasing level of enhancement which follows the trend: m-PIERS > PIERS (Ar) > PIERS > SERS. Comparing the 1595 cm^{-1} peak, there is approximately 3 times enhancement when PIERS was carried out in argon, compared with SERS. When a mask was used, a 12 times enhancement is seen. This trend is also observed when MBA was tested at different concentrations as

Table 12: *Calculation of SERS and PIERS enhancement factors (EF) for MBA at 1 nM.*

Peak (cm^{-1})	EF: SERS	EF: PIERS	EF: PIERS (Ar)	EF: m-PIERS
1098	3.45×10^7	4.12×10^7	8.63×10^7	3.67×10^8
1595	1.64×10^7	2.15×10^7	4.52×10^7	1.89×10^8

seen in Figure 37A, which shows the logarithmic plot of MBA concentration compared with intensity of the 1075 cm^{-1} peak. There is a good correlation between intensity and concentration (R^2 = 0.92-0.98).

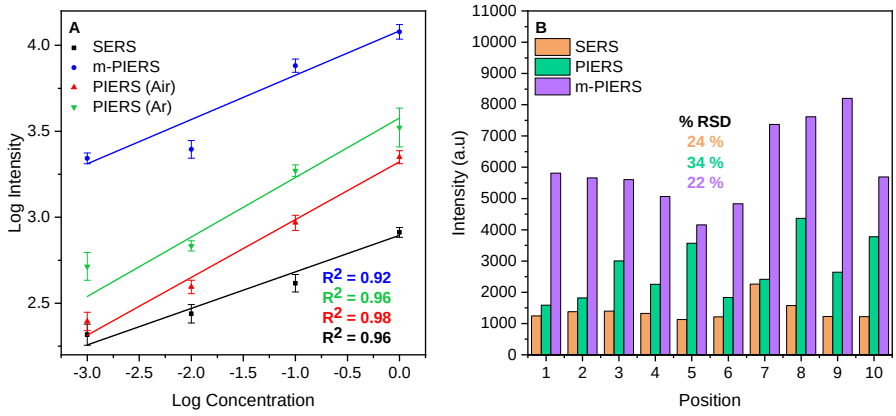

Figure 37: *Comparing m-PIERS with SERS and PIERS using MBA at 1 µM. A) Plot of MBA prepared at concentrations (µM-nM) and intensity of the 1075 cm^{-1} B) Comparing the variation in intensity of 10 random positions. All spectra collected using a 633 nm laser.*

The spectral variability was compared by assessing the intensity of the 1585 cm^{-1} peak across 10 positions (Figure 37B). The fluctuations in intensity is typical of SERS-based measurements where samples are drop-casted onto substrates. The variation can be attributed to a combination of effects in play, which include the Brownian motion of AuNPs in the deposited droplet, Marangoni flow effects from the solvent, solubility of the analyte and interactions between analyte and AuNPs [259], [261], [305]. These factors affect the number of hotspots formed and levels of enhancement observed. Normal PIERS

Table 13: *Relative standard deviation (RSD %) reported in studies for which the reproducibility of the SERS substrate was evaluated.*

Substrate	Analyte	% RSD	Reference
AgNPs	Oxine 720 and Nile Blue A	19 %	[306]
AuNPs	R6G	20 %	[307]
AgNPs	R6G dye	25 %	[308]

showed the highest variation (% RSD = 34 %), and this could be reflected in the time-dependent changes in the hydrophilicity of the film upon irradiation. As observed in the SEM images above, a lower contact angle was observed in the irradiated film, resulting in a smaller droplet with less concentrated AuNPs per unit area. In comparison, using a masked substrate (m-PIERS) showed less variation (% RSD = 22 %). Even though larger clusters of AuNPs are observed, the improvement in % RSD value could be due to a maximum threshold enhancement being reached. These values are comparable to studies with similar deposition methods (Table 13).

This section has shown one way to overcome the issue of photo-induced hydrophilicity when using metal oxide surfaces for PIERS. By applying a mask during photo-irradiation, it was possible to influence the distribution of AuNPs, resulting in greater AuNP clustering compared with normal PIERS. Comparisons between normal SERS, PIERS and m-PIERS using MBA showed the latter to have the greatest enhancement. This can be attributed to two main effects. Firstly, AuNP clusters can harbour more plasmonic junctions and so a greater number of hotspots exist for optimal enhancement. Secondly, the large clusters of AuNPs can cause red-shifting of the LSPR band, and a longer wavelength would result in better alignment with the laser excitation wavelength used. Whilst further studies are required to support this statement,

tentative evidence can be inferred by examining Figures 28 and 36. The extinction spectra, which represents a PIERS experiment, shows the main AuNP LSPR peak to be around 560 nm. The presence of additional peaks at longer wavelengths also suggest there are a range of particle sizes and aggregates. From the SEM image of the m-PIERS sample, AuNP clusters of different sizes can be seen and in greater quantity compared with the PIERS sample and so it can be reasoned that a range of resonances exist which span a broad range of wavelengths, and which mostly likely includes the wavelength of the laser. m-PIERS has been shown to be a simple solution to overcoming weak PIERS signals using Activ™. In principle, the technique can be applied to any surface exhibiting photo-induced hydrophilicity.

3.6 APPLYING PIERS TO THE DETECTION OF OTHER MOLECULES

In this section, the various forms of PIERS described above (PIERS in argon and m-PIERS) is applied to the detection of different molecules of interest in the detection space. Analytes tested include: the fungicide Thiram, peroxide explosives (TATP and HMTD) and a nitroexplosive (TNT).

3.6.1 *Detection of Thiram*

Pesticide residues from agricultural products can cause environmental damage and negatively impact local ecosystems. As such, there is a need to develop effective environmental monitoring processes. Thiram (tetramethylthiram disulfide) is a common fungicide used to preserve crops, fruits and vegetables during storage. One issue with the use of thiram is the ease in which the

material can enter soils, contaminate groundwater and waterways. Due to the risk posed to consumers and workers handling thiram for foliar spraying, as well to wildlife, the EU has recently banned the use and sale of seeds treated with plant protection products containing thiram [309].

Many approaches have been successfully applied to the detection of Thiram. Examples include: colorimetry, mass spectrometry and high-performance liquid chromatography (HPLC) [310]. SERS detection of thiram remains an active area due to the high sensitivity, fast detection time and non-destructive nature of the technique [311] and has been demonstrated using various plasmonic or hybrid (metal/semiconductor) nanostructures [312]–[314]. Here, PIERS has been used to show detection of thiram. Solutions of thiram were prepared at different concentrations (5.03×10^{-4}-5.03×10^{-8} M) and mixed with AuNPs. PIERS measurements were then carried out using Pilkington Activ™ as described previously.

The powdered spectrum of thiram is shown in Figure 38A, along with the SERS, PIERS (air) and PIERS (Ar) spectra at different concentrations (38B-D, respectively). In both the SERS and PIERS, spectra, there are small shifts in the wavenumbers compared with the solid sample. Thiram has a disulfide bond which spontaneously breaks upon exposure to AuNPs and binds to the nanoparticles through the Au–S bond, gold thiolate bond. This is confirmed in the change observed in the 557 cm^{-1} peak, which is the dominant peak in the Raman spectra and attributed to the S-S stretch. The decrease in intensity of the 557 cm^{-1} band in observed in the SERS and PIERS spectra can be attributed to molecular cleavage of the disulphide bond upon adsorption on the metal surface [315]. The strongest peak in the SERS and PIERS spectra is seen at 1382 cm^{-1}, attributed to C-N stretching and symmetric CH_3 deformation. This peak was selected for the subsequent quantitative analysis. Figure 38E

shows the logarithmic plot of thiram concentration compared with intensity of the 1382 cm^{-1} peak. There is a good correlation between intensity and concentration in both SERS and PIERS measurements (R^2 = 0.91-0.99)

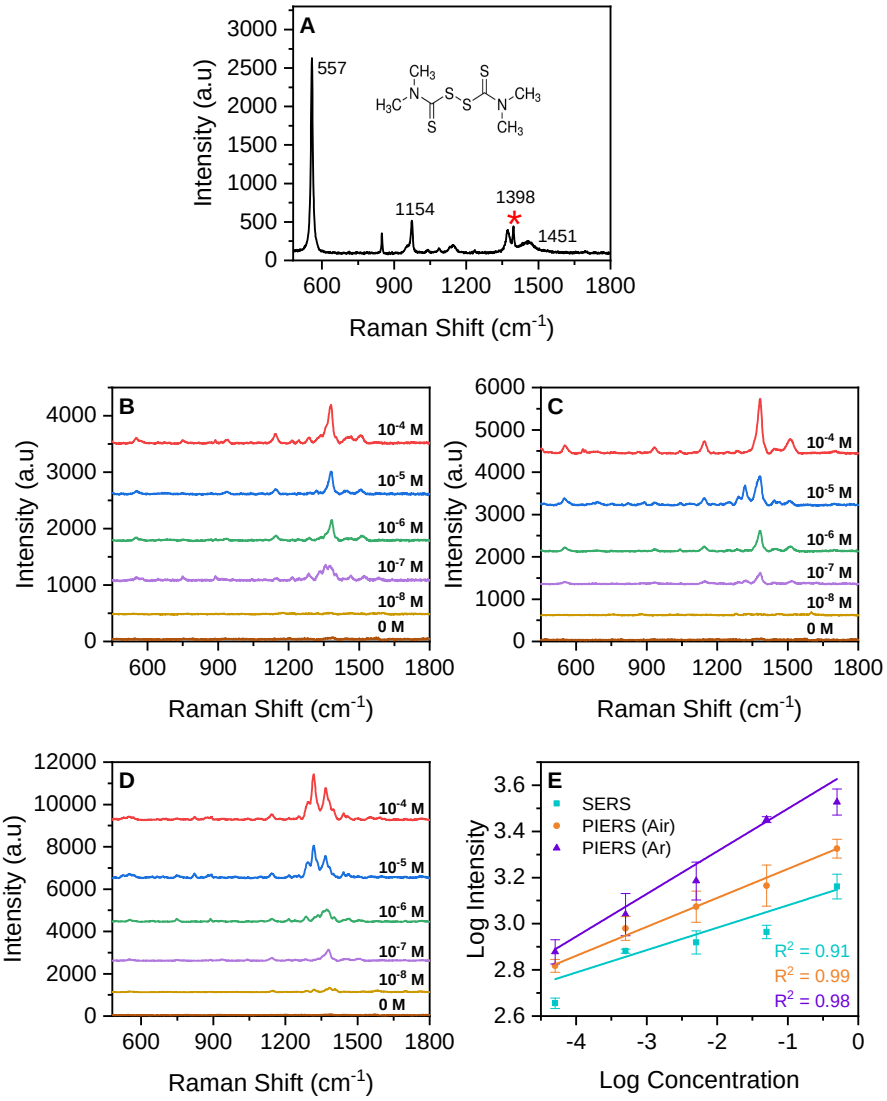

Figure 38: *SERS and PIERS detection of Thiram using Activ™. A) Raman spectrum of powdered Thiram (the 1382 cm^{-1} peak marked with an asterisk is the main peak used for plot E) and in EF calculations mentioned in-text), B) SERS, C) PIERS (in air) and D) PIERS (in argon) spectra of Thiram at different concentrations (averaged across a minimum of 3 positions), E) Plot of SERS and PIERS intensity of the main Thiram peak against concentration in the range 10^{-2} M - 10^{-8} M. Logarithmic fittings were performed to reveal correlation between SERS and PIERS intensity and Thiram concentration. Spectra have been baseline-corrected and offset for clarity.*

Other peaks attributable to thiram are listed in Table 14, along with their respective EF's. The different EF's observed can be the result of different orientations from each vibrational mode with respect to the AuNP surface. This, along with the small shifts in wavenumber are characteristic of the chemical enhancement in SERS [27], [316]. It was possible to detect thiram at a concentration of 10^{-8} M using normal PIERS and PIERS in argon. PIERS showed a 2-fold enhancement and for PIERS in argon, a 3-fold enhancement was observed, with respect to conventional SERS. The greatest enhancement is observed for PIERS (Ar), followed by normal PIERS and then SERS, which correlates with earlier observations using MBA.

Table 14: *Calculation of SERS and PIERS enhancement factors (EF) for Thiram at a concentration of* 5.03×10^{-5} *M.*

Raman peak (cm^{-1})	Assignment	SERS peak	EF: SERS	EF: PIERS	EF: PIERS (Ar)
557	S-S stretching	550	3.47×10^{2}	9.58×10^{2}	1.10×10^{3}
1154	N-CH_3 stretching, CH_3 rocking	1142	7.75×10^{3}	1.39×10^{4}	1.83×10^{4}
1398	CH_3, CN stretching,	1382	1.78×10^{4}	3.02×10^{4}	4.64×10^{4}
1451	CH_3 symmetric and asymmetric deformation	1443	4.55×10^{3}	8.52×10^{3}	1.98×10^{4}

3.6.2 *Detection of triacetone triperoxide (TATP)*

The TATP described in this thesis was synthesised as part of a separate project for the Defence Science and Technology Laboratory [244]. Details of this project are not covered in this thesis, and the following paragraphs have been included mainly to show the identity of the product. Synthesis was carried out using methods adapted from Oxley [245], Pachman [246] and Tomlinson-

Philips [247] to lower the theoretical yield but maintain high recovery. Figure 39 shows different stages of the synthesis process.

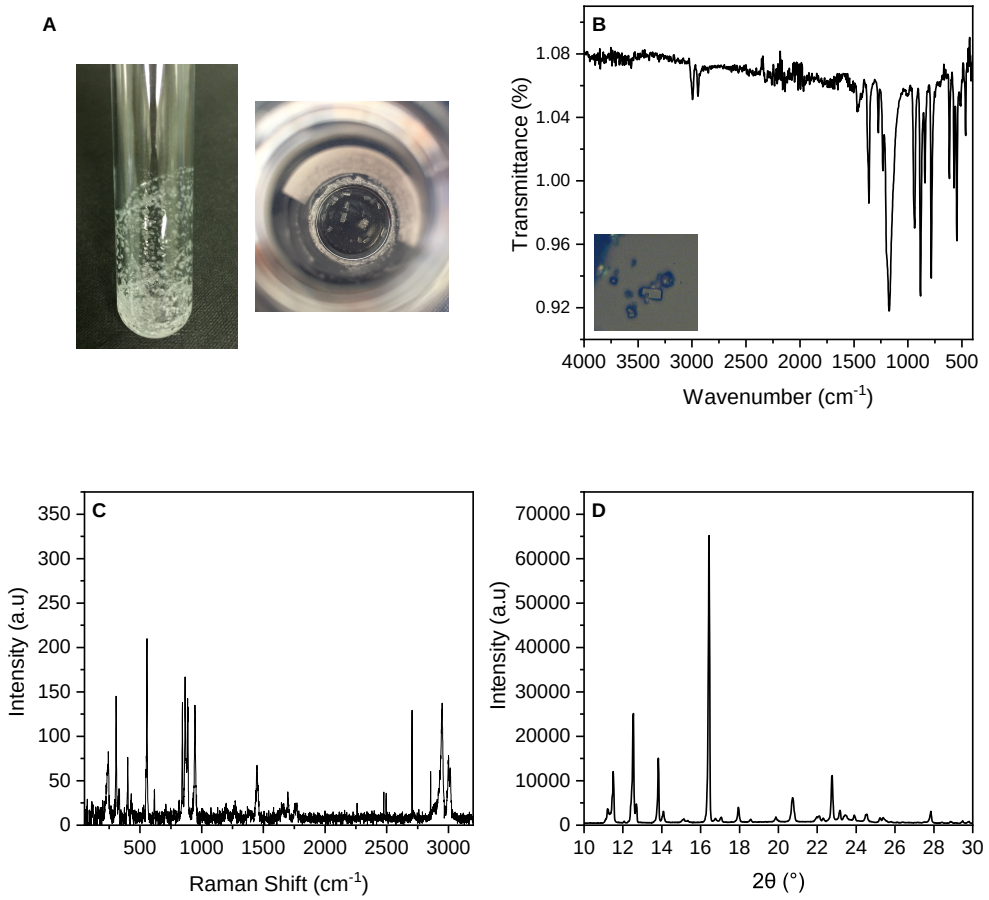

Figure 39: *Characterisation of TATP: A) Synthesis steps showing formation in solution and after crystallisation, B) IR analysis of recrystallised product. Inset image shows close-up of slab-like crystals under microscope, C) Long scan Raman analysis of recrystallised product and D) Powder XRD pattern.*

IR and Raman spectroscopy was used to to identify functional groups specific to TATP. As seen in Fig 39B, the majority of peaks lie in the 'fingerprint' region of 500-1500 cm^{-1}. The O-O peroxide bond, being symmetrical, does not induce great changes in dipole moment and would normally be expected to have low intensity peaks, but interference from the polar C-O vibration modes means these groups of peaks dominate in vibrational spectra. These vibrations appear between 800-1100 cm^{-1} in the Raman spectra. The C-C stretch ap-

pears at 1400 cm^{-1}. Microscopy analysis of the recrystallised product showed opaque crystals which appeared as needles or slabs and with dimensions of approximately 4 mm × 1 mm (Figure 39B (inset)). The melting point of TATP was determined over 4 replicates and showed a temperature range between 87-92 °C, which is in agreement with literature [245], [317], and indicated the presence of more than one compound in the mixture.

XRD can be used to identify an individual polymorphic form or a mixture of polymorphs. As different polymorphs produce unique diffraction patterns, the atomic spacing can be determined using Bragg's Law, as a function of 2θ. Samples of product were carefully ground and analysed using XRD (Figure 39D). Comparisons were made with the calculated and experimental patterns by Reany *et al.* who predicted the existence of 6 polymorphs [318]. Similarities were observed for peaks at 11.5°, 12.5°, 14° and 16.4°, with the latter being the most intense peak. A slight shift in the peaks was observed, which, in part, can be explained by the fact that the single crystal XRD data reported by Reany was collected at 180-200 K, whereas the XRD data was collected at 298 K. Furthermore, shouldering can be seen for peaks at 11.5°, 12.5° and 14°. Taken in consideration with the wide range of melting points observed, this further suggests there is a mixture of different polymorphs present.

3.6.3 *PIERS detection of TATP*

Figure 40 shows the SERS and PIERS detection of TATP. As mentioned above, the most important bands appear in the region between 800-1100 cm^{-1} and these correspond to the O-O and C-O stretching modes in the peroxide ring. The observed peaks at 998 cm^{-1} (O-O symmetric stretching) and 1022 cm^{-1} (C-O symmetric stretching) are in reasonable agreement with literature [220],

[245]. TATP is highly volatile and can sublime at room temperature which made prolonged measurements from the same sample difficult. Although a 1.4 times PIERS enhancement was observed in TATP compared with conventional SERS, detection of TATP was challenging and it was not possible to detect TATP at concentrations lower than 1 mM.

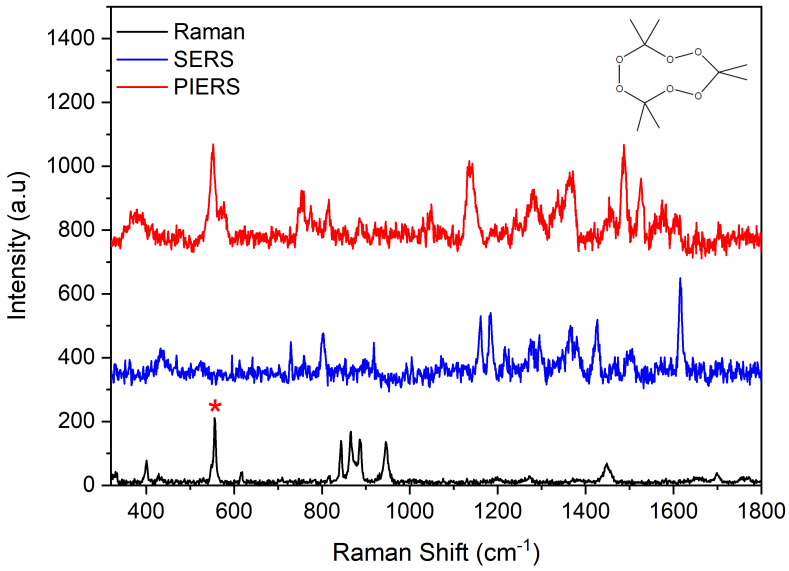

Figure 40: *Comparing the SERS and PIERS detection of TATP at 1 mM. The peak at 555 cm^{-1}, marked with an asterisk, denotes the peak used to calculate the enhancement factor.*

3.6.4 *Detection of trinitrotoluene (TNT)*

The Raman spectrum of powdered TNT is shown in Figure 41A, along with stacked plots showing the SERS, PIERS and m-PIERS spectra (Figure 41B). In all plots, the dominant peak is at 1350 cm^{-1}, which is attributed to the NO_2 symmetric stretch. The peak observed at 1540 cm^{-1} is attributed to the NO_2 asymmetric stretch and the peak at 1218 cm^{-1} is attributed to the ring breathing/bending vibrational mode. Using the 1350 cm^{-1} peak, the

enhancements observed for SERS, PIERS and m-PIERS were, 2.04×10^3, 2.18×10^3 and 9.54×10^3, respectively.

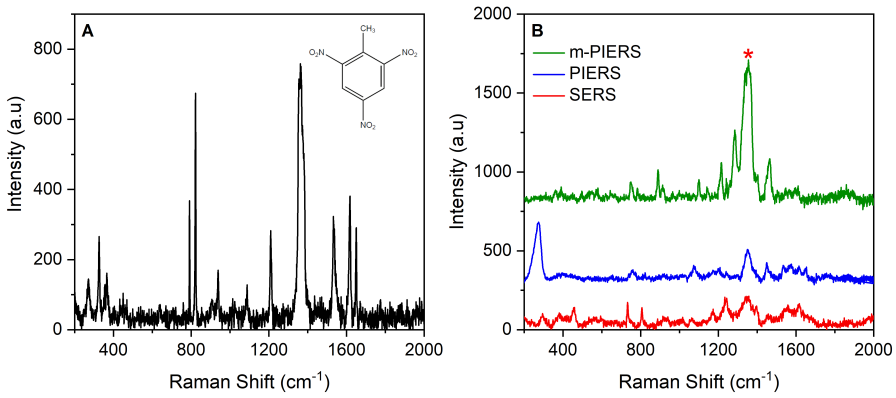

Figure 41: *SERS and PIERS detection of TNT. A) Raman spectra of powdered TNT, B) SERS, PIERS (air) and m-PIERS using 1.1 mM TNT. The peak at 1350 cm^{-1}, marked with an asterisk, denotes the peak used to calculate the enhancement factor.*

3.6.5 *Detection of hexamethylene triperoxide diamine (HMTD)*

Similar to TATP, the main Raman features in hexamethylene triperoxide diamine (HMTD) are attributed to vibrations in the peroxide ring, with the main peaks in the Raman spectrum (Figure 42A) being the O-O stretch at approximately 750 cm^{-1} and the C-O band at 950 cm^{-1} [245], [319]. Both peaks are observed in the SERS and PIERS spectra, with the former (marked with an asterisk) being more dominant (Figure 42B). A cluster of peaks between 1200-1400 cm^{-1} can also be seen to dominate in all SERS and PIERS spectra, with the most intense positioned at 1354 cm $^{-1}$. These peaks have been attributed to breakdown products by Chang and Ko [320], [321]. This could be particularly pertinent in the current system, given the fragility of peroxide compounds and with the use of a photocatalytic substrate. Cleavage points at the weak

O-O and C-N bonds could give rise to a series of fragmented products such as NHCO and HCN which have positions in the observed range [320]. Table 15 shows the assignment and EF's of the other identified HMTD peaks. The SERS (Figure 42C) and PIERS (Figure 42D) detection of HMTD at different concentrations (10^{-5}-10^{-8} M) shows good consistency of the spectral profile and Figure 42E shows the equivalent logarithmic plot of HMTD concentration compared with intensity, using the 1382 cm^{-1} peak. There is a good correlation between intensity and concentration in both SERS and PIERS measurements (R^2 = 0.98).

The known HMTD peak at 747 cm^{-1} was used for quantitative analysis. For a concentration of 2.4× 10^{-7} M, 1.5 and 5 times enhancements were observed for PIERS and m-PIERS, respectively, when compared to conventional SERS. For the 1341 cm^{-1} peak, 5 and 11 times enhancements were observed for PIERS and m-PIERS, respectively (Table 15).

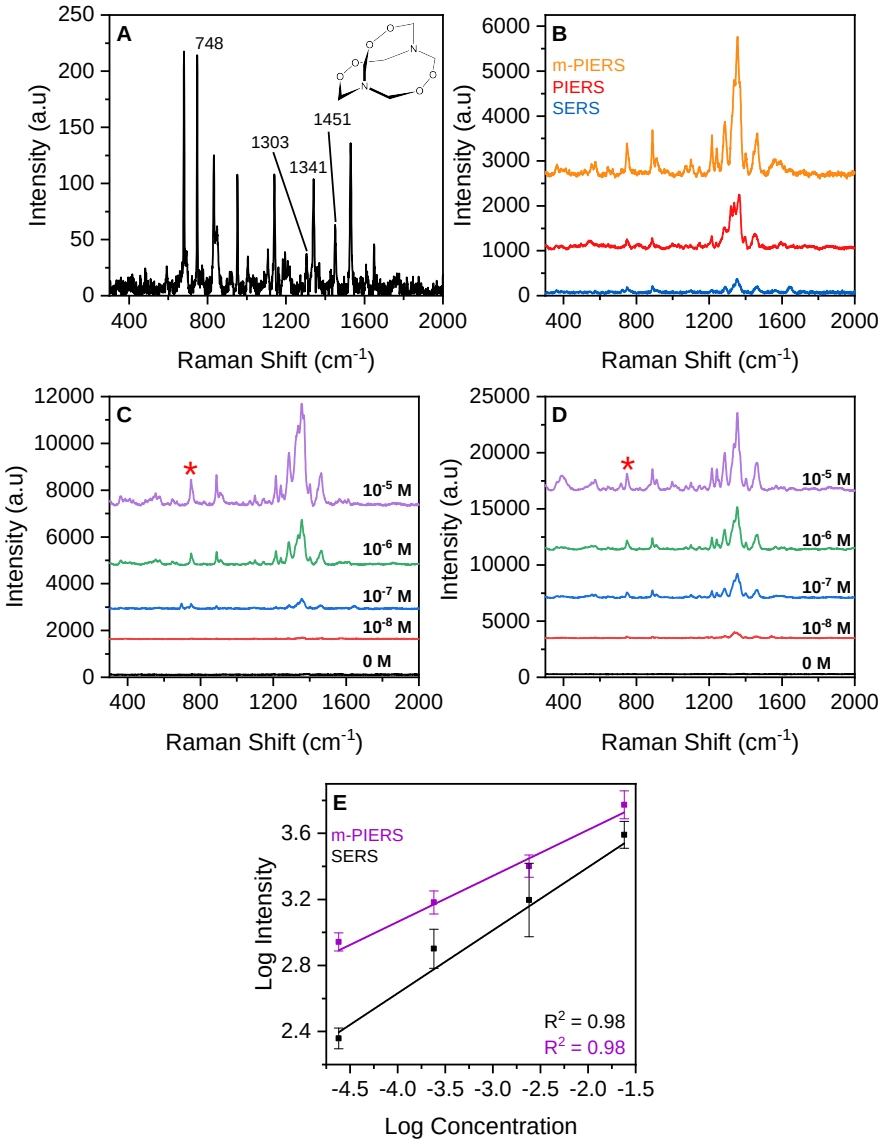

Figure 42: *Detection of HMTD using SERS and PIERS. B) SERS, PIERS and m-PIERS of HMTD at 2.4 × 10^{-7} M, C) SERS and D) m-PIERS spectra of HMTD detection at different concentrations (10^{-5}-10^{-8} M). Peak marked with an asterisk denote main HMTD peak E) Plot of SERS and m-PIERS intensity of the main HMTD peak against HMTD concentration in the range 10^{-5}-10^{-8} M. Logarithmic fittings were performed to reveal correlation between SERS and m-PIERS intensity and HMTD concentration. Spectra has been baseline-corrected and offset for clarity.*

Table 15: *Calculation of SERS and PIERS enhancement factors (EF) for HMTD at 2.40×10^{-7} M.*

Raman peak (cm^{-1})	Assignment	SERS peak	EF: SERS	EF: PIERS	EF: m-PIERS
748	C-O and O-O stretch [320]	748	2.37×10^5	3.48×10^5	1.21×10^6
1303	CH_2 twist [322]	1290	8.94×10^5	2.98×10^6	7.23×10^6
1341	C-N stretching [320]	1333	5.23×10^5	2.75×10^6	5.70×10^6
1451	CH_2 scissor [322]	1465	6.53×10^5	1.39×10^6	3.33×10^6

3.7 CONCLUSIONS

This chapter has demonstrated the PIERS effect using a commercially available TiO_2 substrate, Pilkington Activ™. A PIERS lifetime of approximately 15 minutes was determined and detection was carried out on Raman probe molecules MBA, and R6G as well as the pesticide thiram and explosives: TATP, HMTD and TNT.

The PIERS effect was also characterised through studying the charge-transfer in the system and changes in oxygen vacancy formation. A custom-chamber was built to enable measurements to be made in a low-oxygen environment. These studies are the first to be performed for a PIERS substrate. Charge-transfer studies involved looking at changes in the AuNP LSPR and fluorescence enhancement in the TiO_2-AuNP system. LSPR blue to red shifts were attributed to changes in the electron density on AuNPs. This was supported by the enhancement in the fluorescence of R6G. Furthermore, PL studies using the oxygen vacancy peak for TiO_2 showed enhancement of the O_{vac} peak when TiO_2 was exposed to UV irradiation and argon, suggesting these factors can increase the mobile electrons within the system. These observa-

tions also suggest the PIERS effect is linked to the lifetime of the induced O_{vac} and healing of O_{vac} can reduce the PIERS enhancement. Building on these observations, PIERS studies were carried out in argon. An increased PIERS enhancement was observed as well as increased enhancement lifetime compared with studies in air. These results suggests a possible way to overcome the exponential-like decay of the PIERS effect. To demonstrate the applicability of this approach, PIERS (Ar) was carried out on thiram and an 2 times improvement was observed for PIERS (Ar) compared with normal PIERS.

A simple solution was developed to overcome the UV-induced superhydrophilic effect observed in Activ™ by employing a mask during sample irradiation. Termed 'm-PIERS', this approach has the benefit of facilitating the formation of AuNP clusters and generating more plasmonic hotspots. The result is greater enhancement than normal PIERS and this has been shown using MBA, TNT and HMTD. In summary, this chapter has introduced two new variants of PIERS which show improvements to SERS and conventional PIERS. This has been evidenced through the Raman probe MBA as well as explosives and pesticide molecules. Further understanding of the PIERS mechanism has also been achieved through PL and CT studies.

One area of future work could involve examining the plasmonic hotspots formed in the SERS and PIERS experiments to improve the signal intensity and reproducibility. This can be achieved through examining the widths of the nanogaps, mass of the nanoclusters, as well as morphology and optical extinction properties which could inform more optimal selection of the laser excitation wavelength to align with the LSPR band. Whilst the drop-cast method used in this study is facile and widely used, the approach does not allow precise control of plasmonic hotspot formation. Template-based ap-

proaches can be used to engineer hotspots with defined geometric and optical properties. Examples reported using metal-semiconductor systems could be investigated for PIERS [323]. Alternatively, colloidal SERS approaches can provide homogenous sample analysis whilst enabling monitoring of aggregation kinetics and control of AuNP cluster formation. Furthermore, the use of metal-semiconductor core-shell nanoparticles would be one approach to carry out colloidal PIERS [324].

PIERS USING ZINC OXIDE DECORATED WITH GOLD NANOPARTICLES

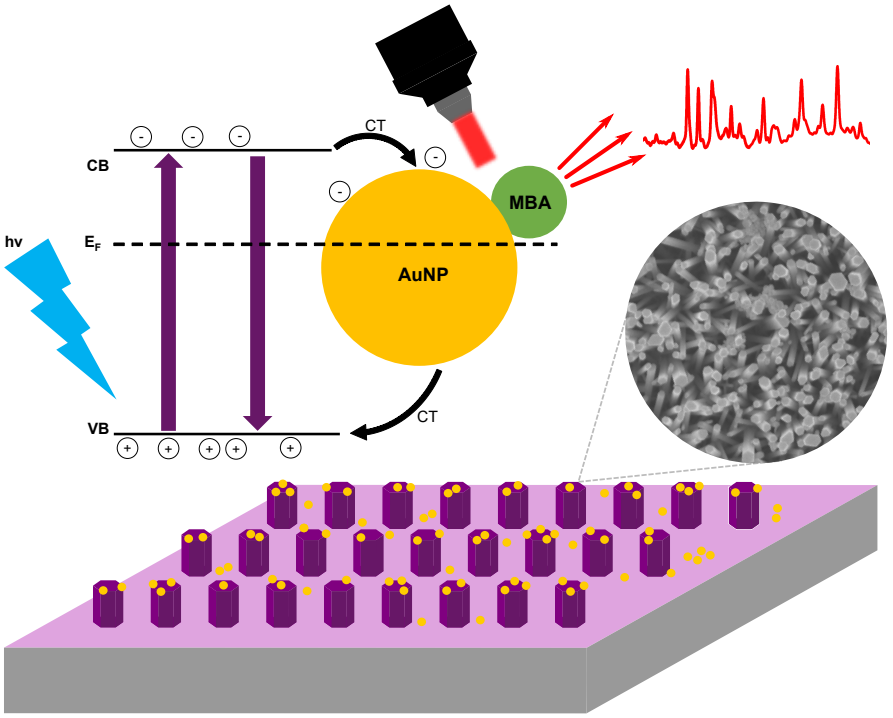

4

PIERS USING ZINC OXIDE DECORATED WITH GOLD NANOPARTICLES

4.1 INTRODUCTION

In recent years, there has been an growing interest in developing facile and low-cost SERS substrates with high enhancement factors for sensing applications. In addition to traditional metallic substrates, metal oxide semiconductors have also been explored, due to their biocompatibility, tunable properties and ease in which they can be scaled up for manufacture. A wide range of fabrication methods exist for the synthesis of semiconductors and some examples include chemical vapour deposition (CVD), spin coating, dip coating, and sol-gel. Chemical bath deposition (CBD) is a traditional aqueous deposition method which remains popular for its simplicity and effectiveness in producing films with controllable properties. Advantages of CBD include: facile synthesis, low-cost, versatility over a range of substrates and reactions can be carried out at low temperatures (< 100 °C). A large number of CBD methods exist for the fabrication of semiconductors for SERS applications, including; CdS [325], MoO_3 [326] and ZnO, the latter for which methods exist for tunable morphologies, such as; nanotubes [327], nanosheets [328], nanorods [329] exist.

SERS enhancement from semiconductors arises from a number of effects, including light absorption and trapping, photo-induced charge transfer and

optical resonance between the semiconductor and analyte molecule [330]. However, the enhancements seen in semiconductors are generally quite low and typically in the range 10^3-10^5 [45]. One strategy to overcome this problem is the introduction of defects, such as vacancies, atom substitutions, and interstitial atoms into the crystal lattice [331], [332]. This can be achieved during synthesis, through post-treatment methods such as annealing [47], [49], or photo-induced defect formation. The latter approach is used in Photo-induced enhanced Raman spectroscopy (PIERS), which is carried out in the presence of metallic nanoparticles. Doping is another method used to introduce defects in semiconductors and to change the bandgap energy. The result is usually the creation of more efficient charge transfer pathways and this has been exploited in SERS for chemical sensing [333], [334].

ZnO is a known n-type semiconductor with a wide band-gap (3.20-3.30 eV) [335], [336] and is a promising material for a range of applications including electronics, optoelectronics and sensors [242]. The large exciton binding energy in ZnO (60 meV) makes ZnO an efficient light emitter. Other favourable properties include high conductivity and transparency, which has driven many studies into tuning optical and electronic properties for various applications. For photocatalysis, ZnO is widely considered to be a suitable alternative for TiO_2, due the similarity in bandgap energy. Currently, only three studies have reported the use of ZnO for PIERS. Work by Fularz, showed that annealing ZnO samples in O_2 improved SERS enhancement, and when combined with PIERS, a 2.5-fold enhancement was observed compared to normal PIERS [230]. The effectiveness of this combinatorial is likely due to the introduction of different defects such as oxygen interstitials and oxygen vacancies which manifests in creation of acceptor levels in the band gap, and reduction in the bandgap energy, improving the transfer of photoexcited charge carriers in the

system. The formation and healing rates of oxygen vacancies were studied by Glass and Barbillon, and in both studies, ZnO was prepared through vapour deposition methods [312], [337]. The effect of doped ZnO on PIERS has not been studied, but is worth investigating given the improvements seen in many SERS studies.

The previous chapter introduced the PIERS technique and demonstrated the use of PIERS to detect a range of explosives and relevant molecules at trace concentrations. This chapter reports the design, synthesis, and comparison of PIERS substrates decorated with Au nanoparticles. A facile method employing CBD was used to prepare ZnO thin films in addition to Ag and Cu doped ZnO films. The chapter begins with characterisation of the crystalline ZnO samples in order to confirm identity and morphology of the nanostructures. The PIERS activity was compared using MBA and it was found that doped ZnO provided greater enhancement than the undoped samples. The relative PIERS enhancement for ZnO was compared with similar studies in literature using highly crystalline ZnO films. Mechanisms for the SERS and PIERS behaviour are proposed to explain the differences in enhancement, with the main factors due to high defect density, photo-induced charged transfer and LSPR charge injection.

4.2 METHODS

4.2.1 *General methods and chemicals*

Zinc nitrate hexahydrate 98 % ($Zn(NO_3)_2.6H_2O$, CAS 10196-18-6), hexamethylenetetramine (HMTA, CAS 100-97-0), copper(II) nitrate trihydrate ($Cu(NO_3)_2.3H_2O$, CAS 13778-31-9) and water (CAS 7732-18-5, HPLC grade)

were purchased from Sigma-Aldrich. Silver nitrate 99.9 % ($AgNO_3$, CAS 7761-88-8) was purchased from Fisher Scientific.

Diffuse reflectance spectroscopy was carried out using a Shimadzu system with an integrating sphere (Labsphere) and illuminated using a white light source (KI-120 Koehler Illuminator, Labsphere). Reflection measurements were taken at 8°off normal incidence. Light levels were measured using a fiber-coupled spectrometer (QEPro, Ocean Optics) and calibrated against a diffuse reflectance standard, barium sulphate. The morphology and thickness of the ZnO samples were studied through top- and side-view analysis using a JEOL 6301 scanning electron microscope (SEM), using a beam current of 10 kV. Energy dispersive X-ray spectroscopy (EDX) was carried out using an Oxford Instruments Energy Dispersive Spectroscopy (EDS) detector. Room temperature photoluminescence spectroscopy was carried out using a Renishaw 1000 system, equipped with a He–Cd laser, using a wavelength of 325 nm. X-ray diffraction (XRD) analysis was performed using a Bruker-Axs D8 (GADDS) diffractometer. The instrument operated with a monochromated Cu X-ray source with Cu Kα1 (λ = 1.54056 Å) and Cu Kα2 radiation (λ = 1.54439 Å) emitted with an intensity ratio of 2:1 and a 2D area X-ray detector with a resolution of 0.01°. Films were analyzed with a glancing incident angle (θ) of 1°. The diffraction patterns obtained were compared with standard patterns from the Inorganic Crystal Structure Database (ICSD). X-ray photoelectron spectroscopy (XPS) was carried out using a Thermo K alpha spectrometer with monochromated Al Kα radiation, a dual beam charge compensation system at a pass energy of 50 eV. Survey scans were performed between 0 and 1200 eV. XPS data was fitted using CasaXPS software with the calibration of C 1s at 284.5 eV. UV-Vis was carried out on a Shimadzu UV-2550 instrument, in absorbance mode and scan range 200-800 nm.

SERS and PIERS measurements were carried out using a Renishaw Raman inVia microscope with a 633 nm He–Ne excitation laser (1.9 mW when operated at 25 % power). A fresh batch of AuNPs were synthesised for this study using the method described in Chapter 5, which also shows the optical and morphological characterisation of the AuNPs. Mixtures of tris-capped AuNP and analytes of interest were mixed (by volume), vortexed for 1 minute before depositing (10-30 μL) onto a substrate. For PIERS, the ZnO samples were irradiated under UV-C light (254 nm) for 30 minutes before deposition of the AuNP and analyte mixture. Spectra was collected from at least 5 positions to provide a representative level of enhancement for each sample.

4.2.2 *Synthesis of ZnO nanorods*

ZnO seeds were prepared on silicon substrates using ALD. Diethyl zinc and water were cycled alternately at 150 °C. ZnO nanorod growth was carried out through immersion of ZnO seed substrates in $Zn(NO_3)_2.6H_2O$ and HMTA at 90 °C for 4.5 hours. The films were subsequently rinsed with distilled water and air dried at room temperature.

The mole quantity of copper and silver precusor were kept the same for the synthesis of the doped samples. For the Cu-ZnO sample, 46.7 mg of $Cu(NO_3)_2.3H_2O$ was dissolved in HPLC-grade H_2O to produce a 38.60 mM stock solution. 64.77 µL of stock solution was then added to the reaction mixture, which gives 2.5×10^{-6} moles of $Cu(NO_3)_2$. For the Ag-doped samples, a stock solution of 32.83 mM $AgNO_3$ was prepared and 76.15 µL of solution added to the reaction mixture to give 2.5×10^{-6} moles of $AgNO_3$. Stock solutions were prepared fresh for each new synthesis.

4.3 RESULTS

4.3.1 *Synthesis and characterisation of ZnO nanorods*

Chemical bath deposition is a popular method which uses a precursor aqueous solution to produce thin films. Here, the technique was used to fabricate vertically aligned ZnO nanorods from a silicon substrate containing ZnO seeds. The approach involves two main steps, nucleation on a substrate followed by growth to form a solid phase from a solution. [338] To better control the lattice properties of the nanorods, a seed layer was deposited onto the substrate before inducing the growth phase. ZnO seeds were prepared onto a silicon substrate using ALD and each piece measured (1 cm $\times$ 1 cm $\times$ 0.1 cm) [1]. The substrates were then immersed vertically in aqueous solutions of zinc nitrate and HMTA to induce growth of the nanorods. The synthesis can be represented by the following chemical reactions below.

$$C_6H_{12}N_4 + 6\,H_2O \rightleftharpoons 4NH_3 + 6HCHO \quad (1)$$

$$NH_3 + H_2O \rightleftharpoons NH_4^+ + OH \quad (2)$$

$$Zn^{2+} + 4NH_3 \rightleftharpoons [Zn(NH_3)_4]^{2+} \quad (3)$$

$$Zn^{2+} + 2OH \rightleftharpoons Zn(OH) \quad (4)$$

$$Zn(OH_2) \rightleftharpoons \text{ZnO nanorods} + H_2O \quad (5)$$

Figure 43: *Synthesis of ZnO nanorods using $Zn(NO_3)_2.6H_2O$ and $C_6H_{12}N_4$ (HMTA).*

$Zn(NO_3)_2$ and HMTA were used as the source of zinc and OH^-, respectively. Upon mixing $Zn(NO_3)_2$ and HMTA ($C_6H_{12}N_4$) and with an increase in

[1] The author would like to thank Dr. John Chapman-Fortune for preparing the ALD substrates.

temperature, HMTA was decomposed into ammonia, resulting in the formation of Zinc hydroxide. Dehydration of Zinc hydroxide enables Zn^{2+} to form. The seed layer can act as nucleation sites for the formation of ZnO nanorods. Bottom-up approaches, such as CBD, can generally provide better control of morphology during synthesis and uniform deposition can be easily achieved since the process occurs through ion-by-ion growth. $Zn(NO_3)_2$ and HMTA precursors are also commonly used in a 1:1 ratio [242], [339]. A schematic of the nanorod synthesis process is shown in Figure 44.

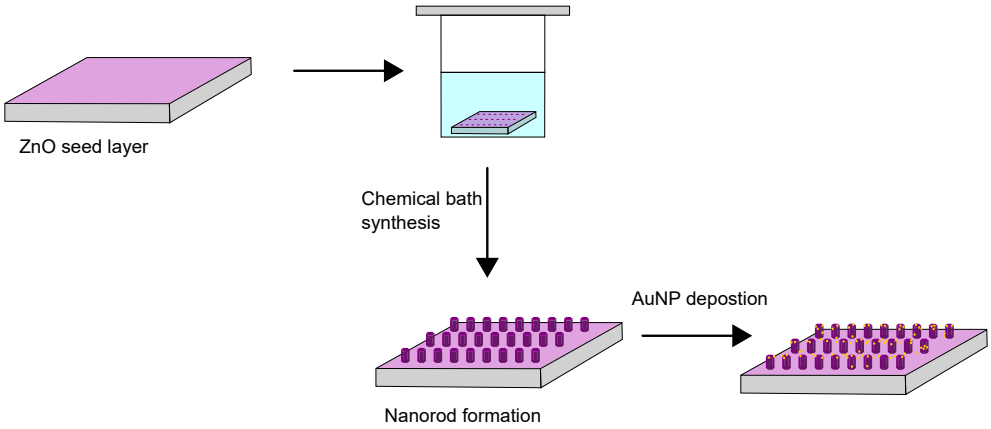

Figure 44: *Scheme showing the fabrication process for AuNP decorated ZnO nanorods.*

4.3.2 *XRD analysis*

The growth of the ZnO seeds to rods can be seen in the XRD patterns shown in Figure 45A. A number of small peaks showing reflections at (010), (002) and (101) indicate the seeds have low crystallinity and multi-directional growth. The XRD of the synthesised nanorods all show diffraction peaks which correspond to the presence of ZnO wurtzite phase (with reference to ICSD: 26170). In all samples, the dominant peak is in the (002) plane, indicating the preferential growth of the ZnO nanorods was oriented along the c-axis, which is

attributed to the ZnO polar surface, and is more energetically favoured due to having low internal stress and minimum surface free energy. In the Ag-ZnO sample, an additional reflection angle was observed at 38.15°(2θ) which was indexed to the (111) peak associated with the face-centred-cubic (fcc) phase of metallic Ag (ICSD: 22434).

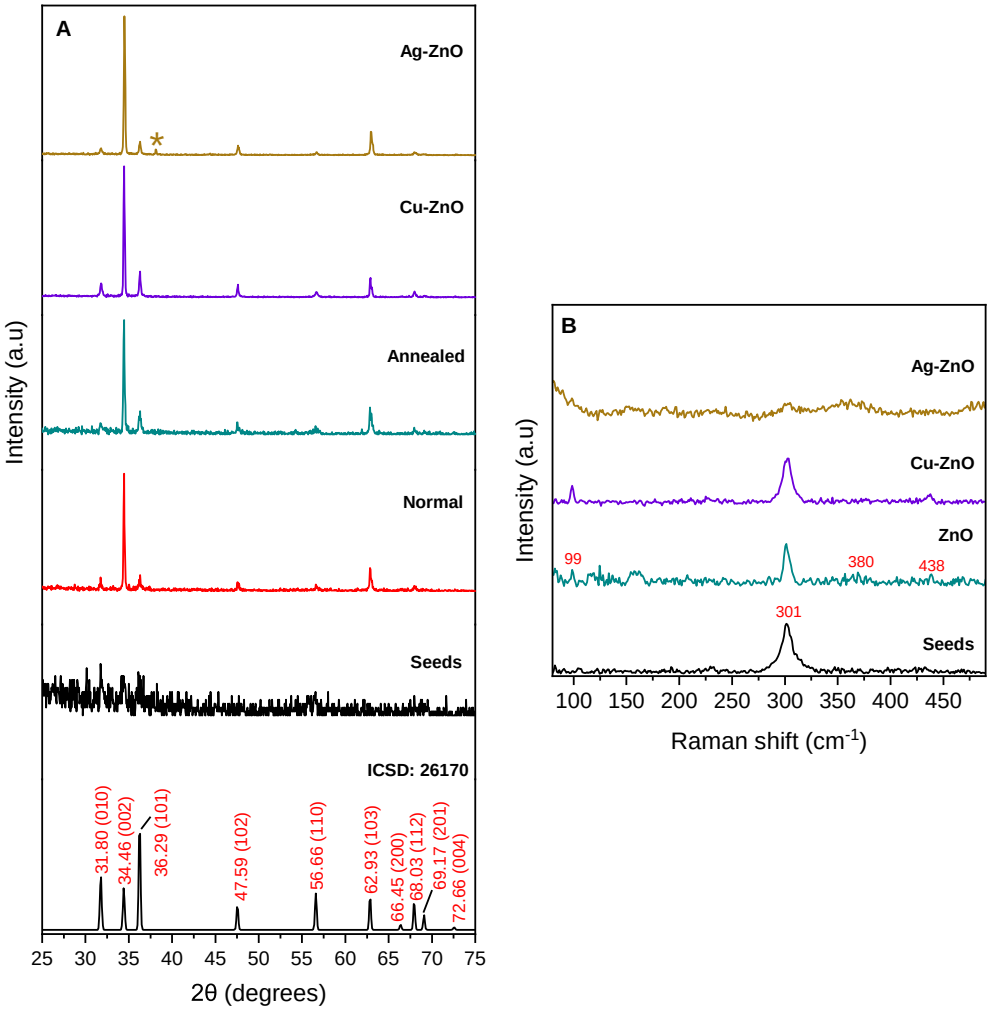

Figure 45: *XRD and Raman analysis of ZnO films: A) XRD diffraction patterns compared with reference pattern acquired from the Inorganic Crystal Structure Database (ICSD), B) Room temperature Raman spectra.*

The crystallite size was estimated using the Scherrer formula (Equation 17) [340], where λ is the wave length of the X-ray beam, K is the Scherrer constant, β is the Full width at half maximum (FWHM) of the peak in radians

and θ is the Bragg angle. The (002) diffraction peak was used to calculate the crystallite size for each sample and is shown in Table 16.

$$D = \frac{\lambda K}{\beta \cos\theta} \tag{17}$$

The results showed a decrease in the FWHM after annealing at 300 °C, which suggests higher crystallinity in the annealed sample. The crystallite size was also found to increase from 21.4 nm to 32.3 nm after annealing, suggesting high temperature treatment resulted in better coalescence of ZnO grains to form larger particles.

Table 16: *Calculation of the crystallite, lattice parameters and unit cell volume for ZnO, Cu-ZnO and Ag-ZnO samples.*

	Crystallite parameters		Lattice parameters		
Sample	FWHM	Crystallite size (nm)	a (Å)	c (Å)	Unit cell volume (Å^3)
ZnO	0.386	21.4	3.2513	5.2085	47.68
ZnO (annealed)	0.257	32.3	3.2579	5.2163	47.95
Cu-ZnO	0.285	29.1	3.2534	5.2139	47.79
Ag-ZnO	0.301	27.5	3.2560	5.2073	47.81

The lattice parameters and unit cell volume for hexagonal ZnO was calculated for all samples and is reported in Table 16. The increase in lattice parameter between as-synthesised and annealed ZnO indicates a change in the crystal morphology, which is expected from the annealing process inducing thermal expansion of the unit cell. The lattice parameter and unit cell volume for the Ag-ZnO sample increased with respect to the as-synthesised ZnO. Ag has been previously reported to exhibit amphoteric dopant behaviour, in which Ag^+ can occupy in the lattice and at interstitial sites [341]. Furthermore, the radius of Ag^+ (1.15 Å) is larger than Zn^{2+} (0.74 Å), and so the increase in unit cell volume seen in the Ag-ZnO sample further supports the substitution of Ag

into the lattice of ZnO. The presence of metallic silver in the XRD pattern also suggests the formation of Ag clusters which can reside on the surface of the ZnO or through out diffusion of substitutional Ag ions [342]. This is due to the radius of Ag^{+} (115 pm) or Ag^{2+} (97 pm) being larger than that of Zn^{2+}(74 pm) [343], and thus some lattice defects and the distortion of the crystal lattice can be induced when Ag atoms substitute Zn atoms in the ZnO lattice, which inhibits the c-axis preferred orientation of the ZnO film. A similar observation is made for the radius of Cu^{2+} (0.73 Å) with corresponding increase in the unit cell volume, however, no peaks were observed in the XRD patterns for metallic or oxides of Cu metal.

4.3.3 *Raman analysis*

Room temperature Raman spectra was collected from the substrate before synthesis, annealed ZnO, Cu-ZnO and Ag-ZnO (Figure 45B). The dominant peak observed at 301 cm^{-1} is attributed to scattering from the silicon substrate [344]. ZnO (wurtzite) belongs to the C4 6v (P63mc) space group. According to the group theory analysis, only A_1, E_1, and E_2 vibrational modes are Raman active phonons [345]. The presence of ZnO in the ZnO Ag-ZnO and Cu-ZnO samples is evidenced by the dominant peaks located at 99 cm^{-1} and 438 cm^{-1}, which correspond to the E_{2L}, and E_{2H} fundamental phonon modes of hexagonal ZnO, respectively and are an indicator of the crystallinity of the ZnO nanorods. The peak at 380 cm^{-1} can be attributed to the A_1(TO) mode. There is negligible difference between the Cu-ZnO and ZnO samples. The intensity of the E_2 high and low phonon modes (E_{2H} and E_{2L}, respectively) decreased in the Ag-ZnO sample compared to the ZnO sample. These observations could be due to the incorporation of Ag into the ZnO lattice, which would induce

changes in the translational symmetry of the crystal [346], [347]. This could arise from lattice defects such as vacancies and interstitials and such changes in the crystal structure could manifest in changes to the local vibrational modes. The 301 cm^{-1} peak in Ag-ZnO is also significantly reduced in intensity, which could be due to the formation of a thicker film.

4.3.4 *Diffuse reflectance spectroscopy*

Diffuse reflectance spectra was carried out on ZnO, Cu-ZnO and Ag-ZnO. All samples revealed a characteristic absorption edge near 380 nm, which corresponds to the optical bandgap of ZnO. A slight red-shift was observed in the Ag and Cu incorporated samples in addition to a reduction in the reflectance. This could be due to changes in the surface morphology of Cu-ZnO and Ag-ZnO samples. As observed in the XRD and Raman data, incorporation of Ag into ZnO was found to result in changes to the ZnO lattice, leading to larger crystallite sizes compared with normal ZnO. The lower diffuse reflectance could result from a more textured surface and greater light scattering. Figure 46 shows the Kubelka–Munk plots used to estimate the band gap energy for each sample. The bandgap for ZnO, Cu-ZnO and Ag-ZnO were found to be 3.30 eV, 3.24 ev and 3.28 eV, respectively. The change in bandgap observed in the Ag-ZnO and Cu-ZnO samples further supports the successful incorporation of dopants into the ZnO lattice. Similar observations have been made using Co [348], Ag [349] and Cu-doped ZnO [350]. One reason for this could be the change in the band structure resulting from substitution at the Zn^{2+} sites.

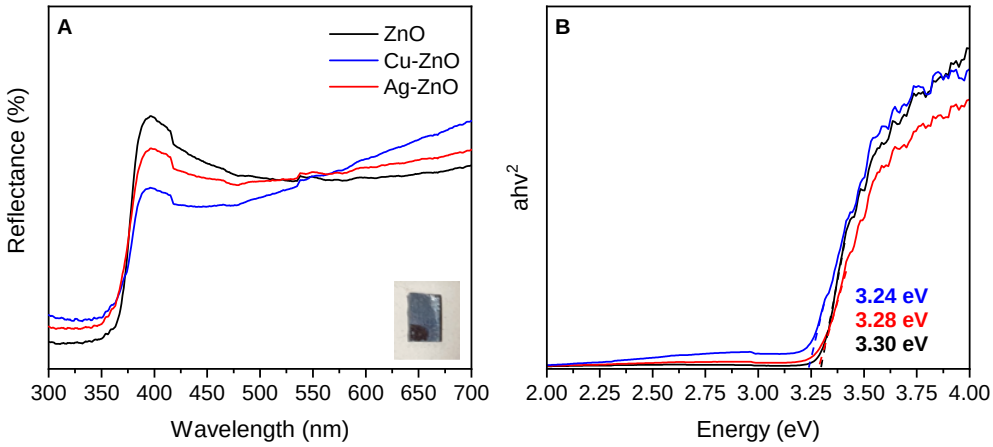

Figure 46: *Determination of bandgap of ZnO and doped ZnO films using diffuse reflectance spectroscopy: A) Diffuse reflectance spectra of each film. Inset image shows typical ZnO film. The black region shows bare silicon substrate (ZnO seed layer) whilst the silver region contains the ZnO nanorods, B) Bandgap determination using Kubelka-Munk function.*

4.3.5 *SEM*

Figure 47A-C shows the SEM of the ZnO, Cu-ZnO and Ag-ZnO samples. From the images, nanorods can be clearly seen and no obvious change was observed in the morphology or size of the nanorods in each of the samples. Each sample consisted of vertically oriented nanorods. ImageJ was used to measure the average diameter from 70 rods, which was found to be 95 nm, 86 nm and 146 nm for ZnO, Ag-ZnO and Cu-ZnO, respectively. The films were also visualised using SEM before and after annealing, with no obvious changes in topology (images not shown). Elemental analysis was carried out using EDX (Figures 47D-F) and identified Zn, O and Si in all three samples. Ag was detected in the Ag-ZnO sample, however, Cu was not detected. The atomic weight % of Ag was determined to be 1.15 % from elemental analysis.

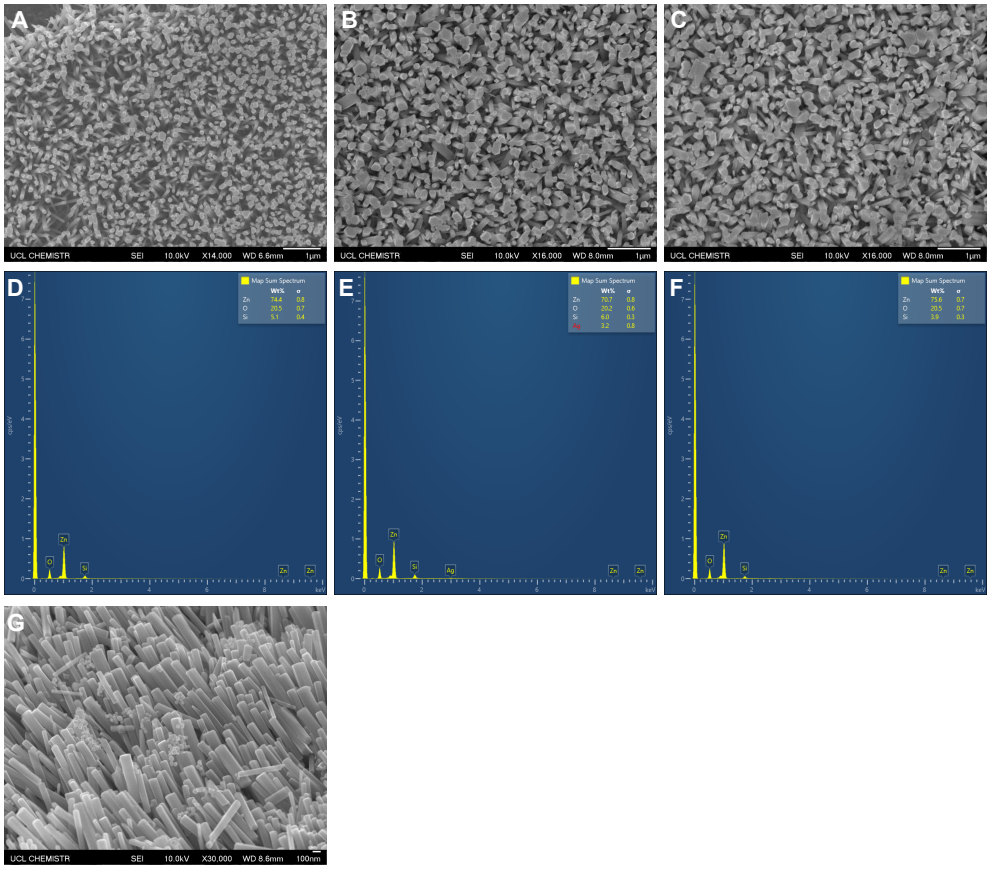

Figure 47: *SEM and corresponding elemental analysis of ZnO films: A) and D) ZnO, B) and E) Ag-ZnO, C) and F) Cu-ZnO. The side-on SEM for sample ZnO is shown at magnification of 30,000 in G).*

4.3.6 *XPS analysis*

The chemical composition of the ZnO samples was further studied using X-ray photoelectron spectroscopy (XPS). The core-shell level XPS spectra of ZnO is shown in Figure 48. Symmetrical doublet peaks were observed in the Zn 2p spectra (Figure 48A), due to spin-orbit coupling. The position of the peaks are located at 1045.1 eV and 1022.0 eV, which correspond to the Zn $2p_{1/2}$ and Zn $2p_{3/2}$ lines, respectively. The 23.1 eV energy difference observed between the two doublet peaks corresponds to Zn being in the Zn^{2+} oxidation state. A similar trend was also observed in the Cu-ZnO and Ag-ZnO samples (Figure

49A and D). Furthermore, the position of the Zn $2p_{1/2}$ and Zn $2p_{3/2}$ peaks in both the Cu-ZnO and Ag-ZnO samples shifted to lower binding energy.

The peak deconvolution of the XPS O 1s region (Figure 48B) shows three components contributing to the spectral shape as a function of photon energy, suggesting the O exists in three chemical environments. The three components are located at 530.5 eV, 531.9 eV and 532.9 eV. The low binding component at 530.5 eV is attributed to the O^{2-} ions in wurtzite structure of a hexagonal Zn^{2+} ion array. The peak at 531.9 eV is usually attributed to O^{2-} in the oxygen deficient regions with the matrix of ZnO [351]. A number of sources also report the intensity of this peak is connected to the variations in the concentration of oxygen vacancies [352], [353]. The high binding component at 532.9 eV is usually attributed to the presence of loosely bound oxygen on the surface of ZnO.

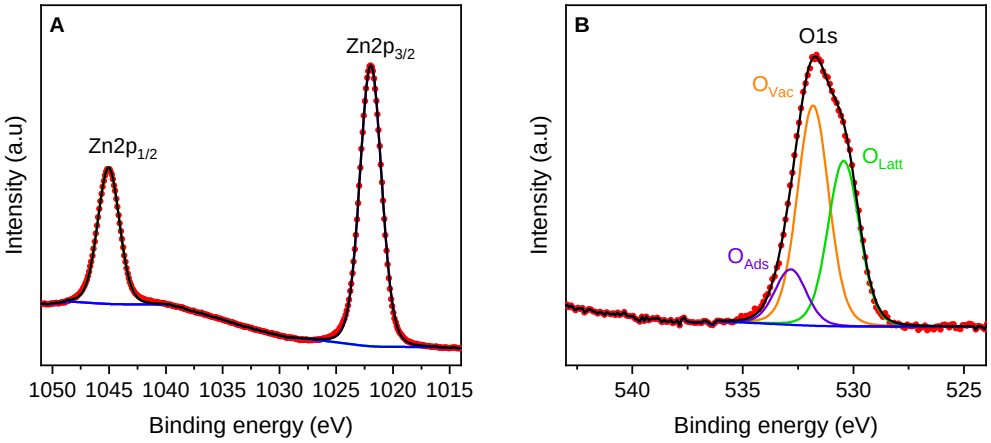

Figure 48: *X-ray photoelectron spectroscopy of ZnO films.*

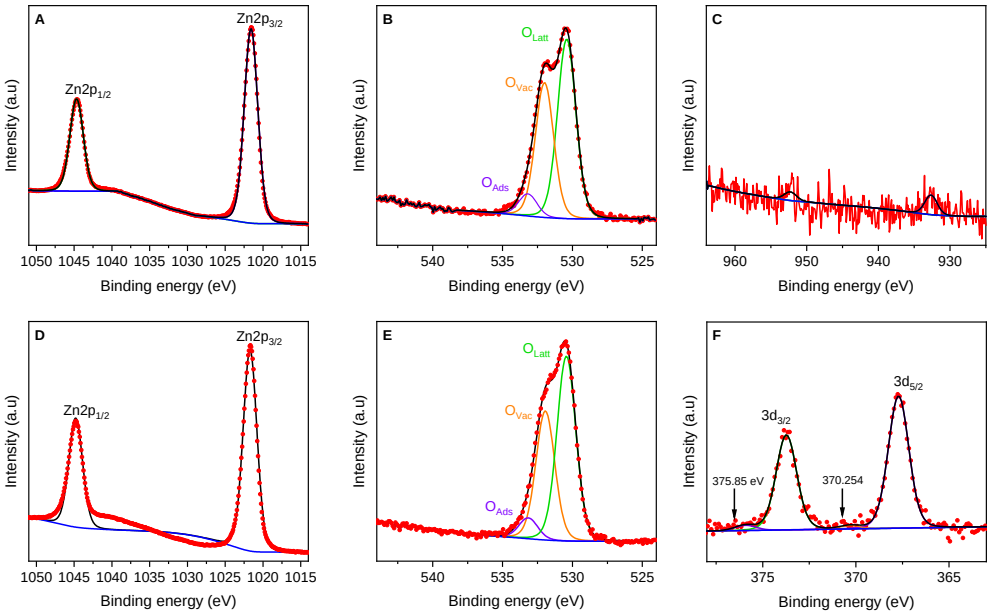

Figure 49: *X-ray photoelectron spectroscopy of copper (A-C) and silver (D-F) doped ZnO films.*

Determination of the Cu species using XPS was difficult due to the low intensities observed. Figure 49C shows the Cu 2p core-level region. Weak doublet peaks were observed at 932.7 eV and 952.4 eV and can tentatively be assigned to the Cu $2p_{3/2}$ and $2p_{1/2}$, respectively. The positions of these two peaks agree with literature references for Cu [354]. Cu surface oxidation can occur resulting in the formation of copper oxide, which can exist in two phases, cupric oxide (CuO) and cuprous oxide (Cu_2O). Identifying the Cu valence state is normally achieved through identifying characteristic satellite peaks, typically located at 943 eV and 945 eV, which are difficult to identify from the current XPS spectra.

Figure 49F shows the XPS of Ag 3d spectra. The doublet bands representing Ag $3d_{5/2}$ and Ag $3d_{3/2}$ are located at 367.8 eV and 373.8, respectively. An energy difference of 6.0 eV indicates the presence if metallic Ag [355]. Satellite regions identified at higher binding energy with respect to the Ag $3d_{5/2}$ and Ag $3d_{3/2}$ lines suggest the possible existence of silver oxide species.

From the XRD and XPS, it can be inferred the majority component of Ag in the Ag-ZnO sample is likely to be metallic silver. The energy values of the Zn, Cu and Ag peaks mentioned are summarised in Table 17.

Table 17: *XPS peak positions for the Zn, Cu and Ag orbitals. Binding energy values are reported in eV.*

	Zn parameters		Ag parameters		Cu parameters	
Sample	Zn $2p_{1/2}$	Zn $2p_{3/2}$	Ag $3d_{3/2}$	Ag $3d_{5/2}$	Cu $2p_{1/2}$	Cu $2p_{3/2}$
ZnO	1045.1	1022.0	-	-	-	-
Cu-ZnO	1044.7	1021.6	-	-	952.4	932.7
Ag-ZnO	1044.8	1021.8	373.8	367.8	-	-

4.3.7 *Photoluminescence*

The typical photoluminescence spectra of ZnO is characterised by two emission bands. The first is located around 380-400 nm and is referred to as the near-band edge (NBE). The second, is a broad emission band in the visible region located between 500-680 nm [356]. The visible emission band usually consists of a number of overlapping peaks, pertaining to multicomponent emissions from various defect states in ZnO which include: substitutions, interstitials and vacancies. The emission band can be broadly subdivided into three main regions; the green band (spanning the spectral region 510-570 nm), yellow (590 nm) and red-orange (640-680 nm) [356], [357].

Room temperature PL spectra of the ZnO samples are presented in Figure 50. An excitation wavelength of 325 nm was used. This is higher than the bandgap energy of ZnO and allows for the promotion of electrons from the VB to the CB. In the PL spectrum of the ZnO seed layer (Figure 50A), the dominant UV emission band is clearly seen around 390 nm. A low intensity

peak in the visible region with a centre around 570 nm can be seen which indicates the ZnO seed layer has low defect density.

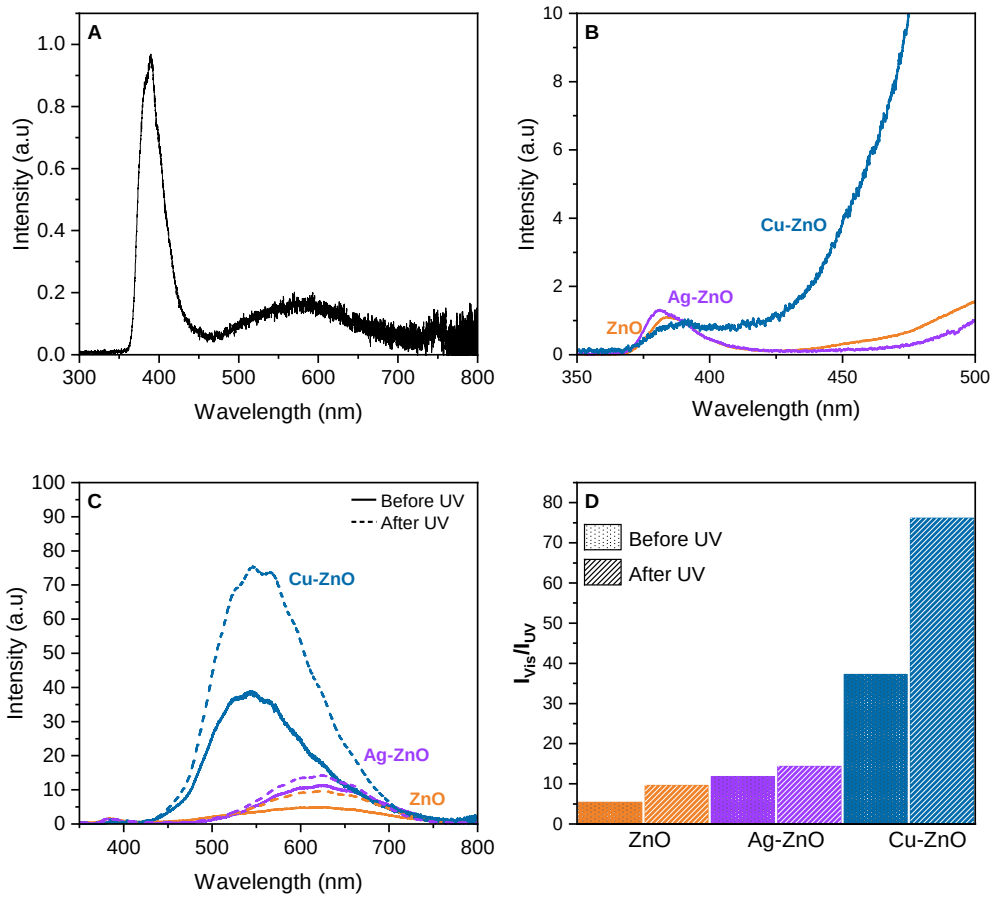

Figure 50: *Characterisation of ZnO samples using photoluminescence spectroscopy: A) PL of ZnO seeded layer, B) Close-up view of the NBE, C) Normalised PL spectra (with respect to the UV emission band) of ZnO, Ag and Cu-ZnO samples with and without prior UV irradiation, D) Plot showing the intensity ratio between UV and emission bands for each sample before and after UV irradiation. PL spectra were collected using a 325 nm excitation source.*

The normalised PL spectra of ZnO, Ag-ZnO and Cu-ZnO is shown in Figure 50C. The PL of each sample was measured before and after UV irradiation. In all samples, a small UV emission band was observed between 380-390 nm which is in agreement with the bandgap calculations reported previously (Figure 46). A close-up of the NBE is shown in Figure 50B. In the Ag-ZnO sample, a slightly enhanced peak was observed compared with the ZnO sample.

This suggests that a higher density of electrons were detected in the Ag-ZnO sample. As inferred from the XRD analysis, metallic Ag was detected which suggests the presence of AgNPs in the sample. As such, the enhanced NBE peak could be due to resonance interaction between the localized SPR on the AgNPs and the NBE in ZnO, resulting in the injection of electrons from the AgNPs into the conduction band of ZnO. In the Cu-ZnO sample, a decrease in the NBE was observed in addition to a red shift. The incorporation of Cu ions into the ZnO lattice can introduce additional defects which can act as electron traps. Cu substitution into Zn sites exhibit an energy level 0.45 eV above the VB [358] which can result in narrowing of the ZnO bandgap. In both the Ag-ZnO and Cu-ZnO samples, there is asymmetry in the NBE peaks, which implies the dopants exhibit an energy level within the ZnO bandgap which can affect the peak position and asymmetry.

Figure 50C shows the full range PL spectra of each sample. The ZnO and Ag-ZnO samples share a similar spectral profile with a dominant peak residing in the visible region with centre around 625 nm. In comparison, the Cu-ZnO sample showed a much broader visible emission peak, with centre around 550 nm and overlapping the ZnO and Ag-ZnO samples. Shifts in the emission spectra of ZnO can be due to different types and concentrations of defects, as well as nanostructure morphology, and these in turn are determined by fabrication conditions [359]. With reference to the SEM images shown in Figure 47, a qualitative analysis shows the nanorods in the ZnO and Ag-ZnO samples are thinner and more needle-like compared with the Cu-ZnO samples which could explain the dominance of the red emission in the PL spectra [356].

Samples were subjected to UV irradiation to observe changes in the electronic properties of the ZnO samples. This consisted of 0.25 hrs of illumination under a 254 nm light source, followed by immediate analysis. In all samples,

a higher intensity was observed after UV irradiation. The intensity ratio of UV to visible emission $\frac{I_{\text{Vis}}}{I_{\text{UV}}}$ is commonly used as an indicator of crystal quality and estimate the concentration of oxygen vacancies [360]–[362]. Figure 50D shows the intensity ratio of the UV and visible emission peaks between each sample. The graph shows the Ag and Cu incorporated ZnO samples have a higher concentration of defects compared with the normal ZnO sample. Samples subjected to UV irradiation showed a higher defect concentration compared with non-irradiated samples. This is in agreement with the rationale that above-bandgap irradiation of metal oxide semiconductors can induce oxygen vacancy formation.

4.3.8 *SERS and PIERS of ZnO samples*

The enhancement of the ZnO samples were tested using MBA. To show the contribution of ZnO to the SERS enhancement, spectra was collected from a mixture of AuNPs and MBA deposited onto glass. Figure 51A-C shows the typical spectra for each ZnO sample, averaged across ten positions and normalised to the Si peak of the substrate, at 520 cm^{-1}. Figure 51E shows the conventional SERS spectrum collected on glass. All ZnO samples showed a greater SERS enhancement compared with samples on glass, which suggest the presence of ZnO improves upon conventional SERS. For the PIERS measurements, each sample was irradiated under a 254 nm UV-C lamp for 15 minutes before depositing a mixture of AuNP and MBA at a concentration of 1 µM.

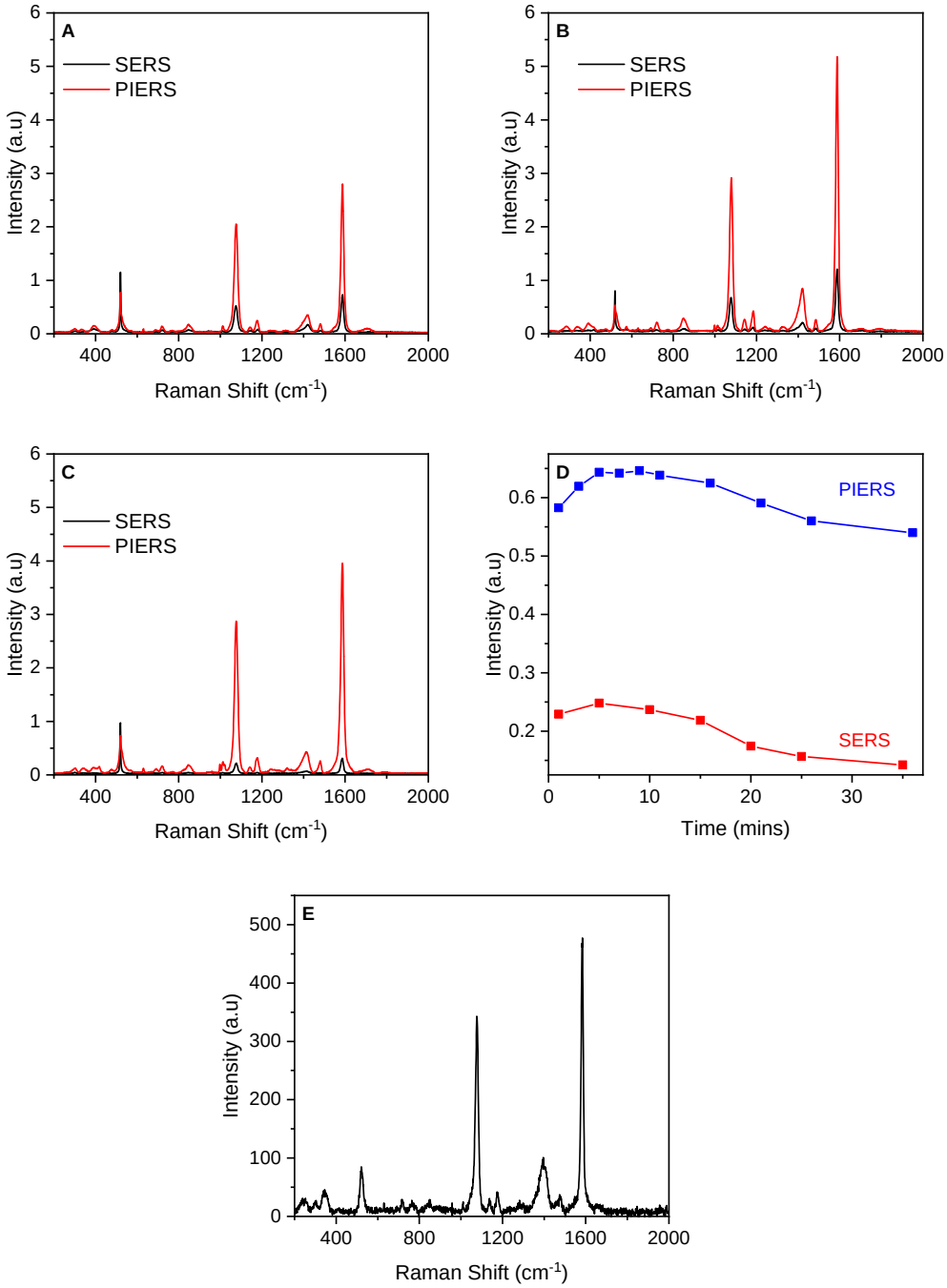

Figure 51: *PIERS analysis of ZnO samples using MBA (1 µM): A) ZnO, B) Ag-ZnO, C) Cu-ZnO, D) Analysis of the 1075 cm $^{-1}$ peak in sample ZnO over 40 minutes, E) Typical SERS spectrum of MBA on glass.*

Figure 51D shows a time-point analysis carried out using the ZnO sample, in which the PIERS intensity of 1075 peak was monitored over approximately 40 minutes. As a control, the SERS spectra was collected on a separate

sample which had been kept in the dark prior to analysis. Each plot has been normalised to the highest peak. The results show a similar trend in both plots, whereby the intensity of the 1075 cm^{-1} peak increased in the first 5 minutes, after which an a gradual decrease was observed. The PIERS graph shows a higher initial intensity and a broader peak indicating the level of enhancement was more prolonged compared with the SERS, where only a shallow peak was observed. From the timepoint analysis, the PIERS lifetime of the ZnO sample is roughly 25 minutes.

Enhancement factors were calculated for three characteristic peaks of MBA and these are shown in Table 18. For all of the peaks shown, similar trends can be seen for SERS and PIERS, with enhancements generally being higher for the doped samples compared with ZnO and glass.

Table 18: *SERS and PIERS enhancement factors for MBA at 1 μM for ZnO, Ag-ZnO and Cu-ZnO samples.*

Sample	Peak (cm^{-1})	EF: SERS/Raman	EF: PIERS/Raman	SERS/PIERS
Glass	1071	3.17×10^{6}	-	-
	1490	8.40×10^{6}	-	-
	1585	6.27×10^{5}	-	-
ZnO	1071	1.09×10^{7}	4.42×10^{7}	4.06
	1490	4.03×10^{7}	2.10×10^{8}	5.22
	1585	2.01×10^{7}	7.97×10^{8}	3.96
Ag-ZnO	1071	1.19×10^{7}	1.08×10^{8}	9.09
	1490	7.99×10^{7}	5.36×10^{8}	6.70
	1585	2.99×10^{7}	2.38×10^{8}	7.95
Cu-ZnO	1071	5.15×10^{6}	8.50×10^{7}	16.51
	1490	2.12×10^{7}	4.09×10^{8}	19.32
	1585	1.11×10^{6}	2.01×10^{7}	18.07

4.3.9 *Degree of charge transfer in ZnO samples*

The use of metallic nanoparticles and a metal oxide substrate can provide greater SERS enhancement compared with the individual components alone. This effect arises due to the creation of an interfacial charge transfer system which increases the number of pathways and density of charge carriers leading to enhanced Raman signals. One way to show this is by comparing the b_2 (non-totally symmetric) and a_1 (totally symmetric) vibrational modes of a probe molecule such as MBA. This approach can provide an indication of new CT processes in the semiconductor-metal-analyte system. According to the CT model proposed by Lombardi, the Franck–Condon principle is responsible for enhancement of solely the totally symmetric vibrational modes of a probe molecule, while the Herzberg–Teller effect can enhance both totally and non-totally symmetric vibrational modes [363]. The degree of charge transfer (p_{CT}) can be calculated using Equation 18, shown below.

$$p_{\mathrm{CT}} = \frac{I^{\mathrm{k}}(CT) - I^{\mathrm{k}}(SPR)}{I^{\mathrm{k}}(CT) + I^{0}(SPR)} \tag{18}$$

Here, k is an index for identifying individual Raman bands. I^k(CT) is the intensity of the Raman bands affected by the CT resonance. I^k(SPR) is the intensity of the localised SPR. Equation 18 can be simplified by taking the intensities of selected a_1 and b_2 lines using the equation below.

$$p_{\mathrm{CT}} = \frac{\dfrac{I_{\mathrm{b_2}}}{I_{\mathrm{a_1}}}}{1 + \dfrac{I_{\mathrm{b_2}}}{I_{\mathrm{a_1}}}} \tag{19}$$

Previous studies have assigned the MBA bands at 998 cm^{-1} and 1178 cm^{-1} as non-totally symmetrical and totally symmetrical bands, respectively [269], [364], [365]. These bands were used to qualitatively evaluate the p_{CT} for each sample. The samples were compared with AuNP-MBA deposited onto glass and the values for the the p_{CT} can be found in Table 19. In the sample where AuNP-MBA was deposited onto glass, the p_{CT} is low. On introduction of ZnO, Ag-ZnO and Cu-ZnO samples, the p_{CT} is increased. This indicates the presence of ZnO provides a new CT path in which the excited electrons generated at the Fermi level of Au transfers to the CB level of ZnO. As such, the results here can be tentatively used to show the introduction of ZnO improves the SERS enhancement of MBA.

Table 19: *Degree of charge transfer for ZnO, Ag-ZnO and Cu-ZnO samples.*

Sample	Peak (cm^{-1})	Intensity (a.u)	R	p_{CT}
Glass	998 (b_2) 1178 (a_1)	18.59 34.34	0.54	0.35
ZnO	998 (b_2) 1178 (a_1)	402.86 508.14	1.79	0.44
Ag-ZnO	998 (b_2) 1178 (a_1)	257.98 306.19	1.84	0.46
Cu-ZnO	998 (b_2) 1178 (a_1)	255.68 286.49	1.89	0.47

4.3.10 *Enhancement mechanism in ZnO samples*

For SERS, metallic nanoclusters are an effective means to generate large enhancements. Naogap junctions between particles give rise to plasmonic 'hotspots' within which extremely localised EM fields exist due to LSPR. The differences in SERS enhancement between the ZnO samples can be explained

by the structural properties described previously which suggest the samples facilitate numerous pathways for the migration of excited charge carriers between the AuNPs and MBA. This is possible due to the overlap between the bandgap energy of the ZnO, fermi energy of the Au and the HOMO/LUMO of the MBA. The band gap of the ZnO samples are between 3.18-3.30 eV. The energy gap of MBA is 4.57 eV [269] and the Fermi level of gold is 5.0 eV (vs. vacuum) [270]. As shown in the PL analysis, numerous defect states exist within the band gap of ZnO which reside at different levels. For example, the energy levels of defect states originating from oxygen vacancies are located at 1.62 eV below the conduction band [357], [366]. In the current system, an excitation laser of 633 nm (1.96 eV) was used. Under Raman excitation, electrons from the VB of ZnO can be excited to the defect level where they can be trapped. A charge transfer pathway can occur whereby electrons from the defect states can migrate to the EF of Au, leading to an increase in electron density on the Au surface. Another pathway can be envisioned with CT from the defect state to the molecule. As such, the defect-driven SERS enhancement could explain the higher levels of enhancement observed in the ZnO samples compared with glass.

XRD and XPS analysis of the Ag-ZnO sample showed lattice doping and the presence of metallic Ag, likely in the form of nanoparticles, which would explain the higher enhancement observed from the Ag-ZnO sample. The LSPR level of Ag nanoparticles can induce charge injection into the NBE of ZnO. From the PL spectra, the observed emission bands were at a similar wavelength range to the ZnO sample. The normalised PL spectra showed a greater concentration of defects in the Ag-ZnO sample. A higher abundance of defect states can improve electron transition from the semiconductor along the pathways towards the Au and MBA molecule. The enhancement of the NBE

of Ag-ZnO under UV (as seen in Figure 50B) suggests there is charge injection in the form of hot electrons from the LSPR of AgNPs into the conduction band of ZnO. This implies the greater SERS enhancement observed in the Ag-ZnO sample, compared with normal ZnO, can be attributed to a combination of high defect and charge injection, resulting in greater overall CT in the system. Figure 52 shows the possible mechanism for defect-driven (A) and charge injection induced (B) SERS.

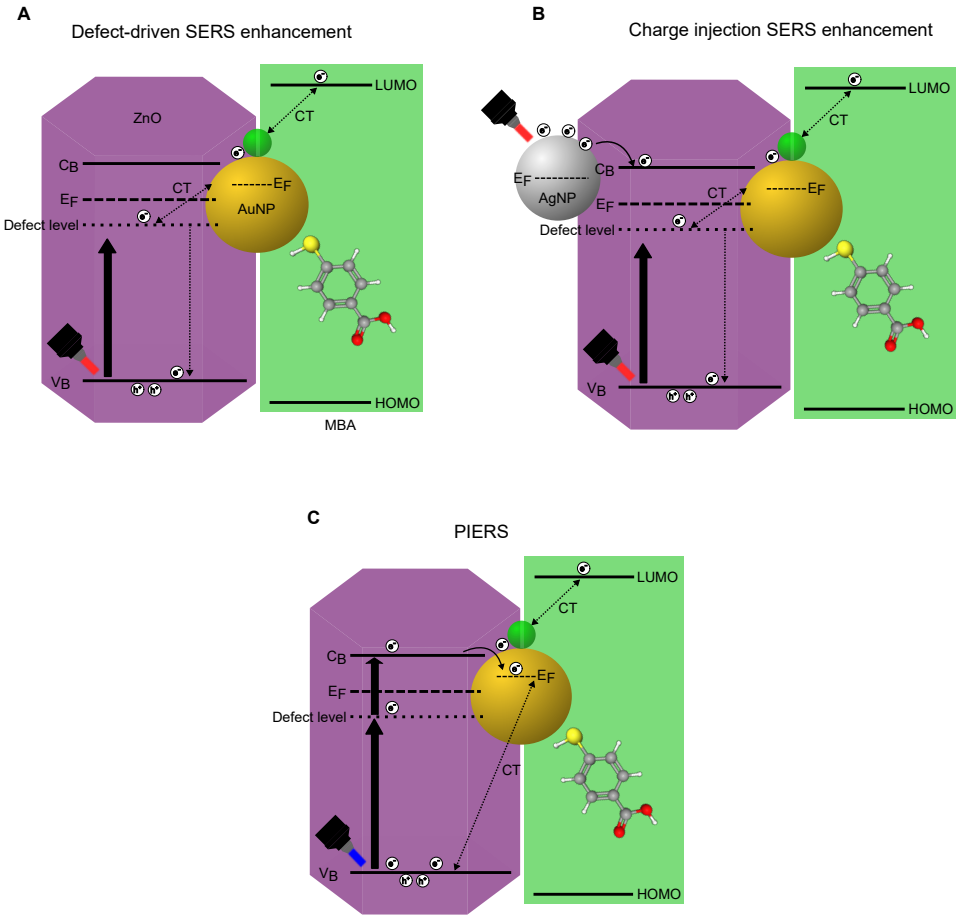

Figure 52: *Photoinduced charge-transfer processes responsible for the SERS and PIERS enhancements observed in the ZnO samples. EF is the Fermi level, CT denotes charge-transfer processes, LUMO is the lowest occupied molecular orbital and HOMO is the highest occupied molecular orbital. A) Charge-transfer from ZnO to AuNP due to trapping of photoexcited electrons at defect sites within the ZnO bandgap from Raman 633 nm laser, B) LSPR charge injection from AgNP particles into the conduction band of ZnO, C) Excitation of ZnO using 254 nm UV light resulting in electron and hole separation and formation of defect state. The overlap between the CB of ZnO and E_F of Au leads to injection of electrons into the E_F of Au AuNPs and CT between AuNPs and LUMO of MBA molecules.*

SERS signals can be further improved through PIERS, where a semiconductor substrate can provide additional chemical enhancement through photo-induced charge transfer. In the PIERS measurements, samples were irradiated with energy greater than the bandgap of ZnO (Figure 52C), creating electron-hole pairs which migrate to the surface of ZnO. UV irradiation can also induce surface defect states, such as oxygen vacancies which form an

impurity level between the CB and VB of ZnO and act as traps for electrons or holes. Since oxygen vacancies can exist as singly, doubly or neutral states, the trapped electrons impede the recombination of the electron-hole pairs. As such, a greater number of electrons are made available for interfacial charge transfer leading to higher electron density on the AuNP and greater enhancement of the Raman signals. The incorporation of dopants resulted in higher PIERS signals compared with undoped ZnO. The higher concentration of native defects in the Cu-ZnO and Ag-ZnO samples can further add to the trapping of charge carriers and delay the e^-/h^+ recombination process. The presence of AgNPs can also improve charge transfer in two ways; as a source of charge injection and as recombination centres, reducing the concentration of free excitons. A similar explanation can be made for Cu-ZnO, where presence of Cu near the surface, as copper oxide, lattice-embedded nanoparticles or a mixture of both, can further contribute to charge trapping and charge transfer to the Raman signal.

4.3.11 *Comparison with other studies*

This study has shown the use of Ag-doped ZnO can produce a higher PIERS enhancement compared with undoped ZnO. A similar observation was observed in a study by Zhou *et al.*, using Ag-doped TiO_2 decorated with AgNPs. With varying concentrations of dopant, the authors found the optimal dopant concentration resulted in a 6-fold improvement in enhancement compared with the use of AgNPs alone. A time-dependent enhancement effect was also observed and the authors attributed these observations to a combination of higher crystallinity of Ag/Ag-doped TiO_2 substrate, photo-induced charge transfer and charge-induced molecular reorientation [228].

Two similar studies involved the use of ZnO for PIERS. Glass *et al.*, prepared films using chemical vapour deposition under a N_2 environment without annealing [337]. Films prepared by Barbillon *et al.* used pulsed laser deposition and were annealed under O_2 [223]. The microstructure and crystallinity plays an important role in the properties of metal oxides and it is widely acknowledged the PIERS effect is influenced by the concentration and lifetime of induced oxygen vacancies. Comparison of the relative PIERS enhancement showed the highly crystalline films used by Barbillon to have greater enhancement. The highest relative PIERS enhancement reported for undoped ZnO in this study (5.22) and those reported by Barbillon (7.52), are both higher than values reported by Glass (3.16). One reason for the contrasting enhancements is likely to be differences in the crystallinity of the films. In both the current study and the one by Barbillon, crystalline ZnO was observed, with preferential growth along the polar plane and a high proportion of defects including oxygen vacancies. ZnO with majority polar planes tend to contain more oxygen vacancies due to a greater ability to remove either OH or H_2O groups form the surface [367] and this property has been utilised to produce films with higher photocatalytic activity [368]. Since oxygen vacancies can act as electron traps, and increase the electron density in the ZnO-AuNP system through interfacial charge transfer, films with higher crystallinity are likely to be better PIERS substrates. Annealing at high temperatures is a common way to improve the crystallinity of metal oxide films. However, use of high temperatures has also been shown to diminish oxygen vacancy concentrations due to inducing formation of larger crystallite size. This highlights the importance of tuning the synthesis conditions in order to achieve optimal balance between crystallinity and oxygen vacancy concentration, which is congruent to the application.

It is also worth comparing the results described here with the PIERS studies in Chapter 3, using Pilkington Activ™. From the PIERS enhancement values, it can be seen that the ZnO samples produced much greater enhancement compared with Activ™ (2.31). This can be explained from the proposed mechanisms whereby the superior enhancement comes from a combination of the high defect density, photo-induced charged transfer and LSPR charge injection. Another factor could be due to the differences in energy of the metal-oxygen bond in ZnO and TiO_2. It is widely reported the Ti-O bond has a higher energy compared with Zn-O [369], which can result in the formation of a higher concentration of defect states in ZnO.

4.4 CONCLUSIONS

This work demonstrates a simple approach to develop ZnO substrates decorated with Au nanoparticles which can be used as PIERS substrates affording high enhancement. Low temperature CBD was used to prepare Ag and Cu doped ZnO thin films followed by annealing at low temperature. Structural and chemical analysis was carried out using XPS, Raman and SEM and showed the ZnO to be hexagonal wurtzite structured and in the form of nanorods between 100-150 nm in diameter. Successful incorporation of Ag and Cu dopants into the ZnO lattice was confirmed through XRD. In the Ag-ZnO sample, metallic Ag was also detected which indicated the presence of Ag nanoparticles. PL analysis showed a high degree of defects in all samples. The SERS and PIERS enhancement was studied using Raman probe molecule MBA. All samples showed a greater enhancement compared with conventional SERS carried out on a glass substrate. Differences in the SERS enhancement for ZnO, Ag-ZnO

and Cu-ZnO were attributed to structural differences, which suggest different mechanisms at play contributing to the different enhancement behaviours.

As seen in the previous chapter, drop-cast deposition results in the formation of AuNP clusters which can produce large SERS enhancements due to proximity of nanoparticles creating nanogap junctions. However, drop-casting also results in nanoclusters of different sizes which can cause shifting of the LSPR band and spectral misalignment with the wavelength of Raman laser. Improvements to the current SERS and PIERS protocol could involve studying the size of the nanoclusters, widths of the nanogaps and relating this to absorbance measurements in order to guide selection of the laser wavelength. These measurements are also important to characterise the LSPR contributions from additional plasmonic nanostructures such as CuNPs and AgNPs. In order to fully utilise the highest SERS enhancements, control of the nanogap junction is required. This can be achieved through physical means such as lithography and sputter deposition, or through chemical-mediated aggregation methods [323], [370].

DUAL DETECTION OF NITROAROMATIC EXPLOSIVES

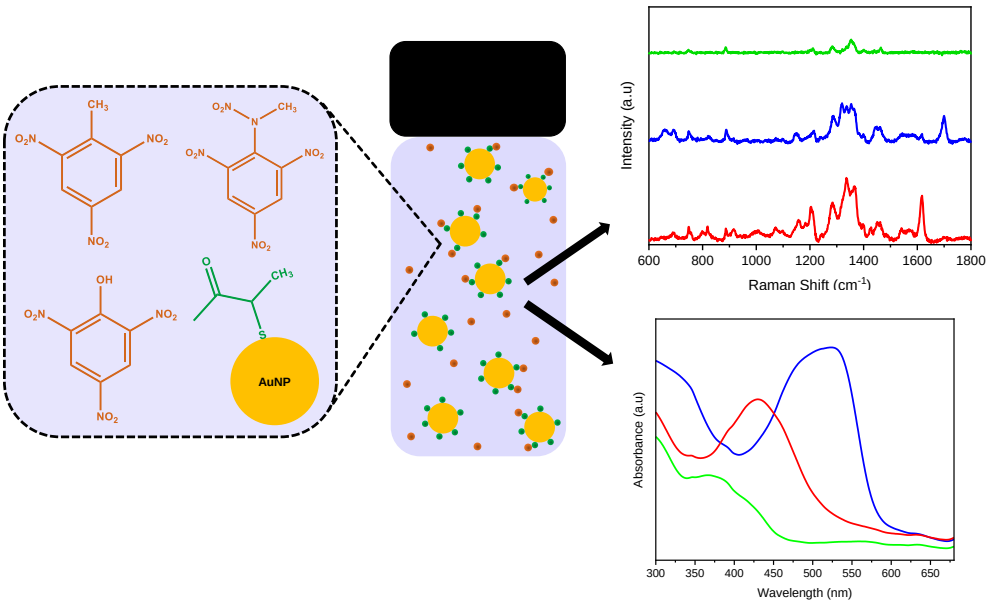

5

DUAL DETECTION OF NITROAROMATIC EXPLOSIVES

5.1 INTRODUCTION

Many nitroaromatic explosives contain an electron deficient centre and this property is exploited in many colorimetric sensors which function by observing a reaction between a nucleophilic reagent and explosive, giving rise to brightly coloured complex. This behaviour within nitroaromatic compounds was first observed by Janovsky [371] who found that acetone treated with an alkaline medium added to dinitrobenzene derivatives gave an intense violet colour. Similar results were also observed using aldehydes and with trinitrobenzene derivatives. The mechanism was later determined through efforts by Meisenheimer, Jackson and Earle [372]. Studies by Jackon *et al.* using methanolic 1,3,5-trinitrobenzene (TNB) and KOH led to the proposal of a quinoid structure, later confirmed by Meisenheimer *et al.*, through studies using trinitro derivatives (2,4,6-trinitrophenetole and trinitrianiline) and potassium alkoxides (potassium ethoxide and potassium methoxide). As such, the adducts of nucleophiles to polynitroaromatic compounds are commonly called Meisenheimer or Jackson-Meisenheimer complexes. A subtle difference exists between Meisenheimer and Janovsky complexes. Whilst both proceed through the addition of a nucleophile to an aromatic substrate, Meisenheimer complexes involve O/N-nucleophiles and Janovsky complexes, C-nucleophiles [373], [374]. Janovsky

reactions are typically carried out in non-aqueous or partially aqueous systems [375]. And finally, Meisenheimer complexes are typically formed by attack of the nucleophile at a position occupied by a leaving group or hydrogen, whereas for Janovsky reactions, the attack occurs at unsubstituted ring-positions and adjacent to a nitro group [376].

One of the first commercial test kits for detection of TNT was developed by the EnSys and designed for the analysis of soil samples [377]. More recent kits are capable of multi-analyte detection, such as the 'SEEKERe' by DetectaChem, which uses a camera to provide digital colour discrimination [163], [164]. Many developments have focused on fluorescence quenching sensors and such methods can be achieved through a variety of materials including small molecules, MOFs, polymers, and functionalized nanoparticles [378]. Qian *et al.* developed a two-component composite sensor using 3- mercaptopropionic acid-capped SiO_2 spheres and L-cysteine-capped CdTe QDs [379]. Choodum *et al.* developed several test kits for TNT by trapping different colorimetric reagents (tetramethylammonium hydroxide, ethylenediamine, and potassium hydroxide) in poly(vinyl alcohol) or polyvinyl chloride hydrogels. Quantitative data from the resultant colored Meisenheimer complexes is provided through a conventional smartphone camera [91], [93]. Whilst colorimetric methods provide fast analysis times, many reagents are limited by sensitivity, suffer from false-positives and can be toxic for users and the environment.

As mentioned previously in this thesis, Surface enhanced Raman spectroscopy (SERS) is a highly sensitive technique which has been widely used in trace detection. One developing area is the use of SERS assays which combine plasmonic nanoparticles with colorimetric agents. The coloured derivatives indicate presence of the analyte which can be further confirmed using SERS.

For example, Dasary *et al.* used cysteine-functionalised AuNPs for selective detection of TNT, achieving detection limits of 2 picomolar (pM) and 50 pM in aqueous solution and SERS, respectively [380]. The assay exploited the selective Meisenheimer complex formed between TNT and cysteine, enabling discrimination against 2,4 -dinitrotoluene and nitrophenol. A similar approach was undertaken by Arshad *et al.*, which involved use of β-cysteamine-capped Au@Ag core-shell nanoparticles. The assay achieved detection limits of 0.35 µg/mL and could be coated onto a paper substrate for use as a facile sensor [174].

The aim of this study is to develop a dual detection method for nitroaromatic explosives, utilising colorimetry and SERS. This chapter begins with the synthesis and characterisation of AuNPs. A passivated Turkevich method was used to produce monodispersed quasi-spherical 50 nm particles. SERS signals can be enhanced when analyte molecules are in close proximity to plasmonic hotspots. To facilitate this, AuNPs were functionalised through two different methods: using para-aminothiphenol (p-ATP) and 3-mercapto-2-butanone (3M2B), before being used as assays for the detection of nitroaromatic explosives, including TNT, tetryl and PA. A paper-based colorimetric assay was developed with detection achieved using a smartphone and open-source software. SERS spectra was also used to train a machine learning model to enable differentiation between the nitroexplosives tested.

5.2 METHODS

5.2.1 *Chemicals and Materials*

Gold (III) chloride trihydrate ($HAuCl_4.3H_2O$, CAS 27988-77-8), was purchased from Fisher Scientific. 1,8-diazabicyclo[5.4.0]undec-7-ene (DBU CAS 6674-22-2), 3-mercapto-2-butanone (3M2B, CAS 40789-98-8), 4-Aminothiophenol (p-ATP, CAS 1193-02-8), NaOH (CAS 1310-73-2), Tris base (CAS 77-86-1, Trizma® base, $\geq$ 99 %) H_2O_2 (CAS 7722-84-1, 30 wt % in H_2O, ACS reagent), citric acid monohydrate (CAS 5949-29-1, ACS reagent grade $\geq$ 99.0 %) and water (CAS 7732-18-5, HPLC grade) were purchased from Sigma-Aldrich, UK. Accustandard explosives reference solutions Trinitroluene (TNT), tetryl, and picric acid (PA) (1 mg/mL in acetonitrile) were purchased from Kinesis.

5.2.2 *Synthesis and characterisation of AuNPs*

AuNPs were synthesised using a two-stage seed-mediated approach, adapted from [231]. Briefly, Au seeds were prepared by adding NaOH (320 µL, 2 M) to a solution of $HAuCl_4$ (25 mM) in 570 320 µL of HPLC-grade water, giving a working stock solution of 8 mM. From the $HAuCl_4$ working stock solution, a 0.2 M solution was prepared by addition to pre-heated HPLC-grade water to 90 °C. The mixture was stirred for 2 minutes before addition of citric acid (72 mM, 0.2 mM), followed by a further 5 minutes of mixing before transfer to quench on ice. The growth stage was carried out at room temperature. 0.5 mL of seed solution was added to 8.8 mL of water, followed by addition of Tris stock solution (250 µL, 0.1 M). $HAuCl_4$ (25 mM, 250 µL) was then added, followed

by 1 minute of stirring and then addition of H_2O_2 (30 % wt v/v, 200 µL). The reaction mixture is allowed to mix for 30 minutes before use. Transmission electron microscopy (TEM) was carried out using a Jeol JEM-100CX II with a beam current of 70-100 kV. Samples were deposited onto holey carbon films (HC300Cu, EM Resolutions), allowed to dry and subjected for analysis.

5.2.3 *p-ATP and DBU-3M2B Assays*

UV-Vis analysis was carried out on a Shimadzu UV-2550 instrument, in absorbance mode and scan range 200-1000 nm. Analysis was carried out using 2 mL solutions added to a quartz cuvette. Solutions of p-ATP at various concentrations were prepared from serial dilutions from a 2 mM stock solution using methanol. p-ATP functionalised AuNPs were prepared by adding p-ATP at various concentrations to stock solutions of AuNPs in a 1:1 ratio (v/v).The mixtures were allowed to mix for a minimum of 1 hour-overnight. DBU-3M2B assays were prepared by first mixing DBU (10 mM, acetonitrile) and 3M2B (10 mM, acetonitrile) in a 1:1 ratio (v/v). The mixture was allowed to stir for 10 minutes before addition of explosive solutions. A colour change indicating the formation of the Janowsky complex was observed within 1 minute with full intensity reached within 5 minutes. For TNT the colour change progressed from pale yellow to red/purple and finally salmon pink. For tetryl the colour progressed from pale yellow to increasing intensity.

5.2.4 *Machine learning*

The data analysis was performed using Python and the Scikit-learn library was used for all machine learning [381]. The dataset consisted of 217 spectra from samples containing TNT (n=135) and tetryl (n=72). All the spectra were pre-processed as follows; first by applying linear interpolation to standardise the wavenumber axis for all the measurements [382]. The spectra was then truncated to contain only the regions of interest. In this study, measurements with Raman shifts below 225 cm^{-1} and above 1750 cm^{-1} were removed. Following this, asymmetric least squares (ALS) baseline correction was applied to remove background fluorescence [383]. Finally, standard normal variate normalisation was performed to give each spectrum a mean intensity of 0 and a standard deviation of 1 [384], [385]. The dataset was randomly split into training (70 %) and test (30 %) datasets [1]. To evaluate the performance of the models, the subset accuracy was calculated for the predictions made from the test dataset. The subset accuracy is defined the fraction of samples that have all their labels correctly classified. To minimise variation due to the spectra present in the test dataset, the accuracy of the various models was calculated for 1000 randomly selected training and test datasets and the mean prediction accuracy was determined.

[1] The author would like to thank Tabitha Jones for help with conducting the ML tests.

5.3 RESULTS

5.3.1 *Synthesis and characterisation of AuNPs*

One of the most common methods for the synthesis of AuNPs is the Turkevich method. In this one-pot process, AuNPs are formed using citrate reduction of a gold precursor in water at temperatures between 70-100 °C [386]. Highly monodisperse nanoparticles between 10-20 nm can be obtained, with larger particles achieved through subsequent growth stages. The passivated Turkevich method used in this study was initially developed for use in flow synthesis to prevent fouling of the reactor [231]. The method has been used in this study, with minimal changes, as a facile approach to synthesise 50 nm AuNPs with high stability.

The synthesis proceeds through three stages, beginning with the passivation of the $HAuCl_4$ using NaOH, producing a hydroxylated precursor [387]. This was then used in the growth of Au seeds and subsequently larger AuNPs. Tris base was used as the capping agent which stabilises the AuNPs as well as regulating the pH and H_2O_2 was used to control morphology of the synthesised particles [388]. UV-Vis analysis carried out on the seed solution shows an absorption peak at 530 nm. During the particle growth stage, an absorption peak at 553 nm was observed which shifts to 548 nm following overnight stirring (Figure 53A). The observed peaks are attributed to the localised surface plasmon resonance (LSPR) of spherical AuNPs [389]. As particles become bigger, scattering events become more significant and this is shown in the evolution and red-shift of the 530 nm peak. Upon formation of Au seeds, a growth phase proceeds whereby the final size is obtained. Different mechanisms have been proposed for particle growth. One approach is where nucleated

particles induce formation of short-lived aggregates which break apart during the synthesis [390]. This is one rationale which could explain the gradual shift of the 553 nm peak towards lower wavelengths which was also observed in earlier studies [231], [387].

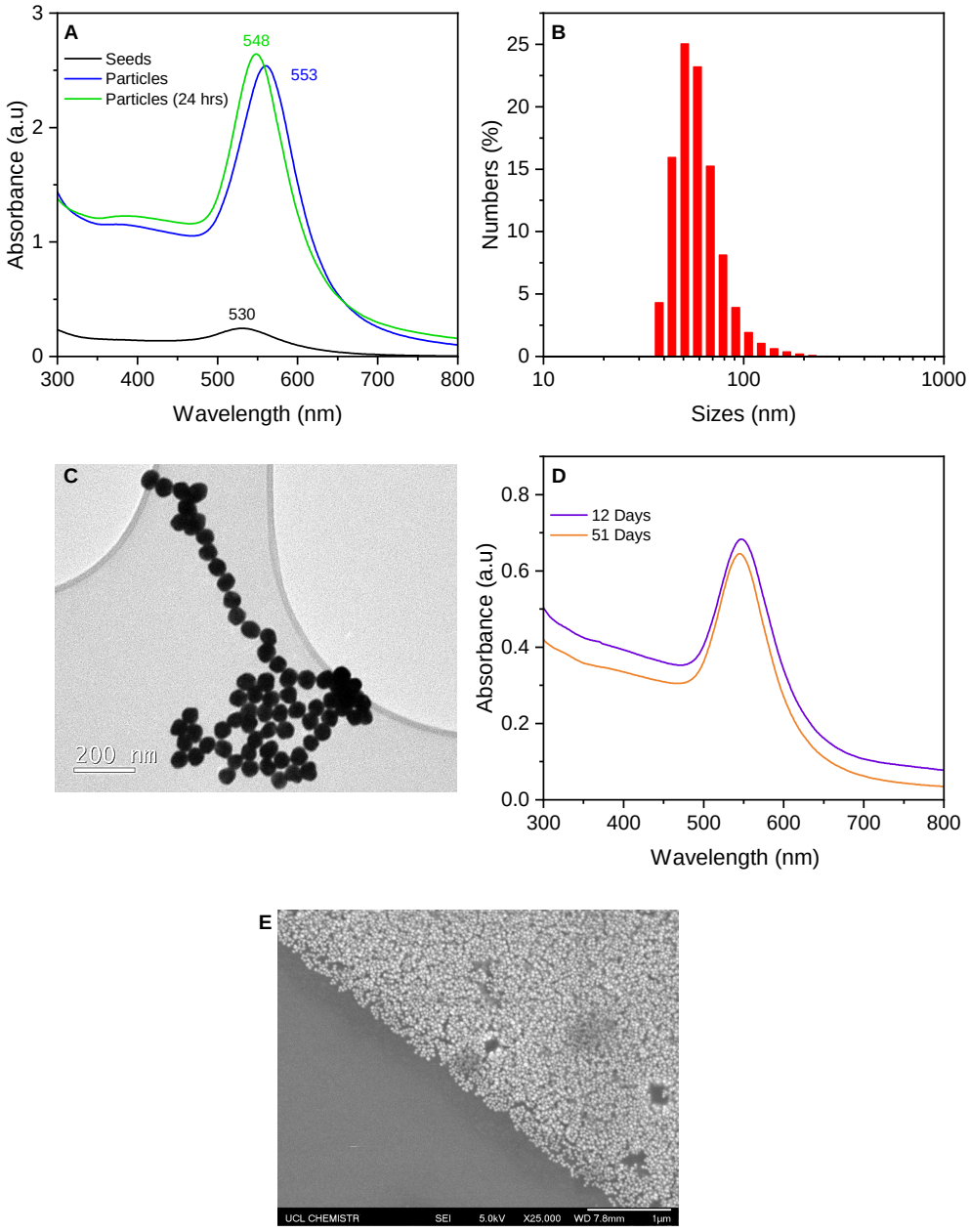

Figure 53: *Characterisation of AuNPs. A) Absorption spectra of seeds and particles, B) DLS analysis of synthesised AuNPs showing size distribution. Particle size shown in logarithmic scale for ease of comparison, C) TEM image of AuNPs, D) Stability study of AuNPs at 12 and 51 days post-synthesis, E) SEM of AuNPs deposited onto microscope slide, imaged at 1 µm scale and 25,000 magnification.*

The symmetrical nature of the 553 nm peak and low baseline indicate good monodispersity and size distribution, which is confirmed through particle analysis using dynamic light scattering (DLS) (Figure 53B), TEM (Figure 53C) and SEM (Figure 53E). The average particle diameter measured by DLS was between 51-59 nm. The particle size was also determined through TEM images using the commercially available software ImageJ. The average particle size was found to be 55.6 nm (RSD = 8 %), from an analysis of 126 particles. The slightly larger size recorded in DLS could be due to differences in measurement approach - DLS is carried out in solution and measures the hydrodynamic radius of particles which could give an overestimation of the size. TEM and SEM images show the AuNPs are mono-dispersed and quasi-spherical. AuNP stability was monitored using UV-Vis after 12 and 51 days. From Figure 53D, the absorption maximum is at 548 nm and remains constant with a minor drop in absorbance intensity. Note the difference in magnitude of intensity compared with Figure 53A is due to the use of a diluted sample which was aliquoted from the completed reaction and kept for the stability study.

The concentration of the seeds (N_{seed}) can be estimated using Equation 20 [391], where C_{Au} is the known initial concentration of gold, M, the atomic weight of gold (197 g mol^{-1}), ρ_{Au} is the density of gold (19.3 g cm^{-1}) and d_{seed} is the average particle diameter (in nm). Assuming spherical particles and complete conversion of the Au precursor in this study, the initial concentration of gold is 8 mM and the average seed diameter is 12 nm, which gives a value of 1.35×10^{13} particles in 0.15 mL for N_{seed}.

$$N_{seed} = \frac{6 \cdot 10^{21} \cdot C_{Au} \cdot M}{\pi \cdot \rho_{Au} \cdot d_{seed}^{3}} \tag{20}$$

For seed-mediated Turkevich synthesis, the final total number of AuNPs is determined by the number of seed particles first generated in the early stages of the synthesis. Since no further particles are formed during the growth steps, the final total number of AuNPs is equivalent to the number of seed particles [392]–[394]. The number density of AuNPs (N_{AuNP}) can be calculated using Equation 21 [391], by dividing N_{seed} the total volume of the AuNP solution (V). For a 0.5 mL volume, this gives a value of 2.71×10^{13} particles which is similar to the original seed particles.

$$N_{AuNP} = \frac{N_{seed}}{V} \tag{21}$$

The molar concentration of the AuNP solutions was then calculated by dividing the number density of particles by Avogadro's constant (6.022×10^{23}), giving a concentration of approximately 9×10^{-8} M.

5.3.2 *Detection of TNT using p-ATP functionalised AuNPs*

The electron-withdrawing nitro groups in TNT can decrease the electron density in the aromatic centre, conferring Lewis-acid behaviour. In the presence of a Lewis-base such as p-ATP, the amino group on p-ATP can deprotonate TNT at the methyl group, resulting in the formation of a TNT anion, where the negative charge is re-distributed throughout the molecule through resonance stabilization from the electron-withdrawing nitro groups [395], [396]. The p-ATP cation interacts with the TNT anion, forming a cation-anion pair. This is one way in which TNT and p-ATP can interact (Figure 54A). The electron-rich amino group of p-ATP can also serve as a nucleophile, participating in nucleophilic addition into the methyl group moiety of TNT and forming a

Meisenheimer complex (Figure 54B). Such complexes are brightly coloured and have been exploited for use as assays for detecting nitro explosives. Examples of nucleophiles used in literature include cysteine and APTES [111], [395]. Another possible interaction is between the π-systems in p-ATP and TNT, which can serve as π-donor and π-acceptor species, respectively (Figure 54C) [397]. There is also the possibility of weak Hydrogen-bond formation between the amine nitrogen in p-ATP and the nitro group oxygen in TNT (Figure 54D). As such, p-ATP can complex with TNT through various means and these interactions are used in the assay to capture TNT molecules for use in SERS. The thiol moiety in p-ATP also allows covalent attachment to the surface of AuNPs through a thiolate bond and the relatively small p-ATP molecule facilitates close proximity between captured TNT molecules and the AuNP surface. Overall, these factors can improve the SERS enhancement of TNT.

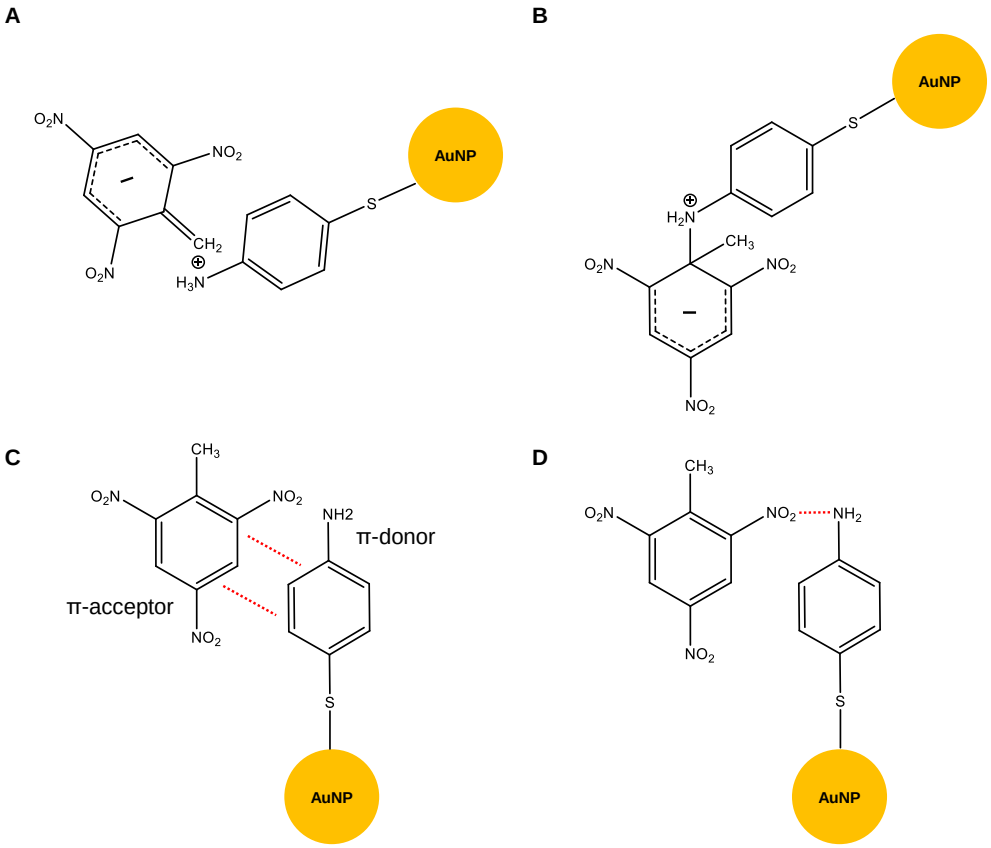

Figure 54: *Different types of interactions between TNT and p-ATP: A) Anion-cation pair, B) Meisenheimer complex, C) π-donor–acceptor interactions, D) H-bonding.*

5.3.3 *UV-Vis analysis of p-ATP functionalised AuNPs and TNT*

To show the interaction between p-ATP and TNT, reference absorption spectra of TNT and p-ATP were collected and compared with a solution containing both TNT and p-ATP. As shown in Figure 55A, peaks at 470 nm and 530 nm can be seen in the mixture, which can indicate the formation of complexes between p-ATP and TNT [398]. For development of the assay, initial work was carried out to find concentrations of p-ATP compatible for use with the AuNPs. This is important for two reasons; first, to avoid interference in the SERS spectra from p-ATP molecules and secondly, to enable the formation of a self-assembled layer on the AuNPs with capability to complex with TNT.

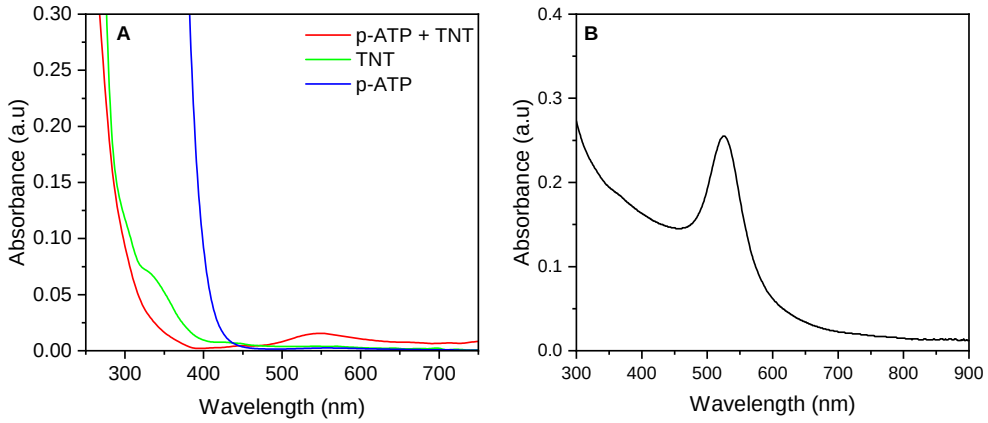

Figure 55: *UV-Vis absorption spectra showing A) TNT (0.44 mM), p-ATP (5.11 mM) and mixture of TNT and p-ATP, B) AuNPs diluted in methanol.*

The absorption spectrum of non-functionalised AuNPs is shown in Figure 55B for reference. Solutions of AuNPs were diluted to the same concentration and functionalised using p-ATP at concentrations of 4.73 µM, 10.17 µM, 113 µM and 1.1 mM (henceforth named p-ATP-4.73, p-ATP-10.17, p-ATP-113 and p-ATP-1.1m, respectively). Figure 56A shows the resultant absorption spectra. p-ATP-4.73 and p-ATP-10.17 show an absorption peak at 530 nm, indicating negligible changes in the absorption spectra compared with the AuNP solution. However, p-ATP-113 showed a peak around 650 nm and further increase in p-ATP concentration to 1.1 mM showed a more distinct and broader peak around 700 nm. There is also a reduction in the intensity and broadening of the 530 nm peak. Compared to the control spectra of AuNP and colourless p-ATP (Figures 55 A and B), this suggests the higher concentrations of p-ATP induced AuNP aggregation, and these trends are comparable to similar studies in literature [399]. Solutions of p-ATP-4.73 and p-ATP-10.17 were further mixed for four hours and the absorption spectra shows no aggregation (Figure 56B).

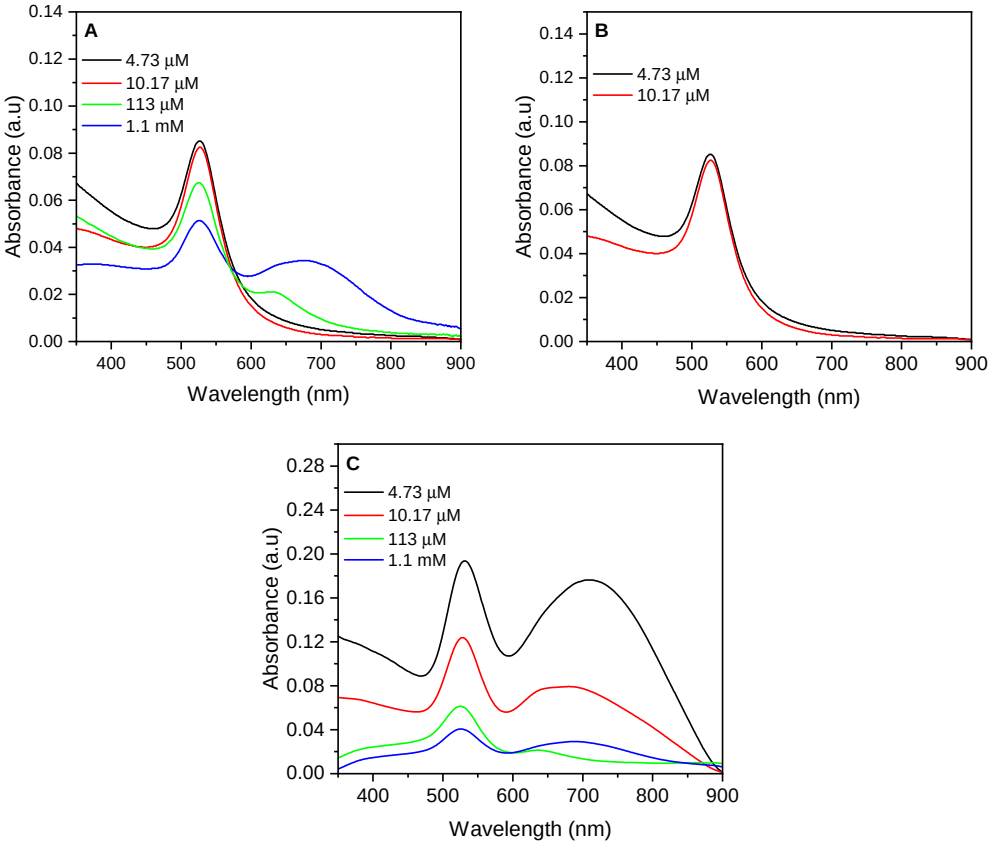

Figure 56: *Detection of TNT using p-ATP-AuNPs: A) Absorption spectra of AuNPs functionalised using different concentrations of p-ATP, B) Absorption spectra of functionalised AuNP solutions after 4 hours of stirring, C) Absorption spectra of assays corresponding to the concentration of p-ATP used in A) on addition of 20.15 µM TNT.*

The p-ATP functionalised AuNPs were tested by mixing an aliquot of each solution with 20.15 µM TNT. Figure 56C shows the absorption spectra of each assay. For p-ATP-AuNP-4.73 and p-ATP-AuNP-10.17, a new peak emerged at 670 and 730 nm, respectively. For the assays prepared p-ATP-113 and p-ATP-1.1m, the addition of TNT caused flattening of the second peak. From the absorption spectra, it can be inferred that addition of TNT caused p-ATP-AuNPs to undergo aggregation. From Figure 54, it can be seen that one TNT molecule can interact with multiple p-ATP molecules through the π-donor and π-acceptor system. This would bring AuNPs closer together, changing the scattering properties of the clustered AuNPs resulting in the additional peak

in the absorption spectra. These results show TNT can induce changes in the absorption spectra of p-ATP-AuNPs and an optimal concentration of p-ATP is required.

5.3.4 *SERS analysis of p-ATP functionalised AuNPs and TNT*

Figure 57 shows the SERS analysis of TNT assays. For the SERS analysis, samples were prepared by drop-casting 3 µL of assay solution onto microscope slides followed by Raman analysis of the dried sample. Spectra was averaged from a minimum of 5 positions to ascertain an overall level of enhancement. For reference, the Raman spectra of TNT and p-ATP powder is shown in 57A and B, respectively. The Raman spectrum of p-ATP shows three dominant peaks. The peak at 380 cm^{-1} is attributed to the C-S vibration. The peak at 1085 cm^{-1} is attributed to the C-H bending mode and the peak at 1589 cm^{-1} is due to the ring stretching modes.

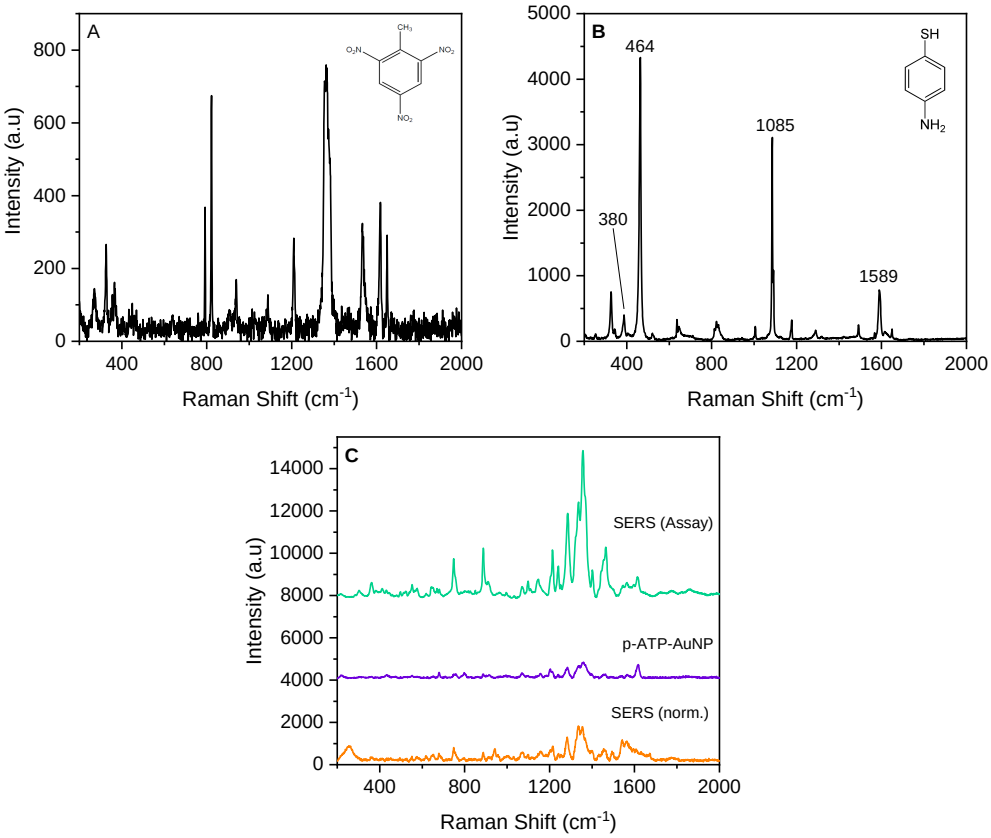

Figure 57: *Detection of TNT using p-ATP-AuNPs: A) Raman spectrum of TNT powder, B) Raman spectrum of p-ATP powder, C) SERS spectra comparing a TNT assay with controls whereby functionalised AuNPs were tested in the absence of TNT and where non-functionalised AuNPs were tested with TNT (normal SERS). TNT and p-ATP concentrations were 25 μM and 4.73 μM, respectively.*

Figure 57C shows the SERS spectra of TNT using the p-ATP functionalised AuNPs (Assay, green), compared with the normal SERS controls, without p-ATP (orange) and without TNT (purple). There is a noticeable difference between the Raman spectrum of p-ATP to that of the p-ATP functionalised AuNP, with a number of new broad peaks around 1200 cm^{-1} and 1350-1400 cm^{-1}. Aromatic amines can be catalytically oxidized to their corresponding azo-compounds in the presence of noble metal catalysts and a study by Wu *et al.* showed that p-ATP molecules adsorbed onto rough nanostructured surfaces of noble metals can undergo a coupling reaction to produce the paired structure, p,p'-dimercaptoazobenzene (DMAB) [400]. A number of studies using both

gold and silver nanostructures have also reported the presence of DMAB [206], [396], [398]. The characteristic peaks for DMAB at 1142 cm^{-1}, 1390 cm^{-1}, and 1435 cm^{-1} are attributed to the N=N vibrational modes and these are seen in the spectra of the p-ATP functionalised AuNPs, indicating the presence of DMAB.

In both the normal and assay SERS spectra, 20.15 μM TNT was used. As can be seen in the figure, the addition of TNT to the DMAB-functionalised AuNPs resulted in a change in the spectral profile and intensity of peaks. The assay spectrum contains features from both the functionalized AuNPs and TNT bands, as well as additional peaks, which indicate strong spectral changes in both species and the possible formation of a DMAB-TNT complex. A number of TNT peaks are present. The peak around 1230 cm^{-1} is attributed to the ring breathing modes and the peaks at 1357 cm^{-1} and 1544 cm^{-1}, attributed to the NO_2 symmetric and asymmetric stretching vibrations, respectively. These peaks are in agreement with similar studies using p-ATP functionalised nanostructures for TNT detection [380], [397].

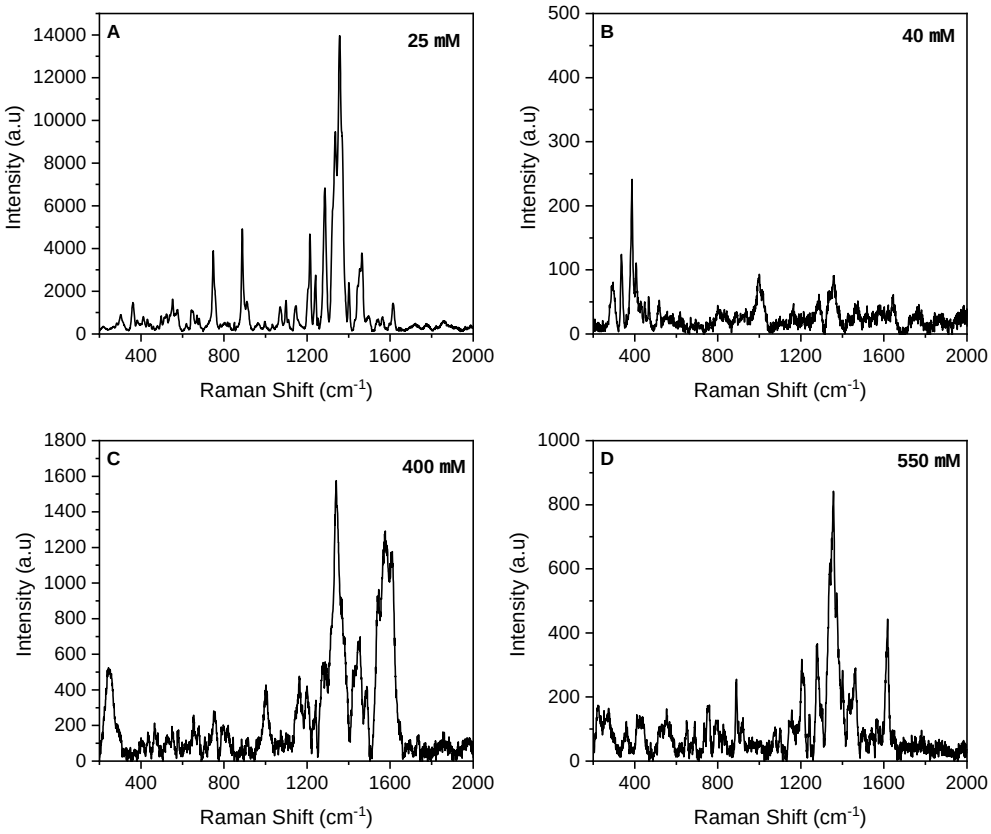

Figure 58: *SERS assays using different concentrations of TNT: A) 25 μM, B) 40 μM, C) 400 μM and D) 550 μM.*

Figure 58 shows the assay spectra collected using the same concentration of p-ATP (5 μM) with varying concentrations of TNT (25-550 μM). Whilst the peaks at 1230 cm^{-1}, 1357 cm^{-1} and 1544 cm^{-1} are visible, there are noticeable differences in the spectral profile. In Figure 58B, the dominant peaks are clustered around 400 cm^{-1} and in Figure 58C, there is a cluster of peaks around 1600 cm^{-1}. These differences could represent a number of competing interactions between DMAB, p-ATP and TNT. Figure 59 shows a possible way in which p-ATP enables chemical enhancement of TNT Raman signals through the formation of a TNT-DMAB complex, whereby the orientation of the p-ATP molecules are perpendicular to the AuNP surface.

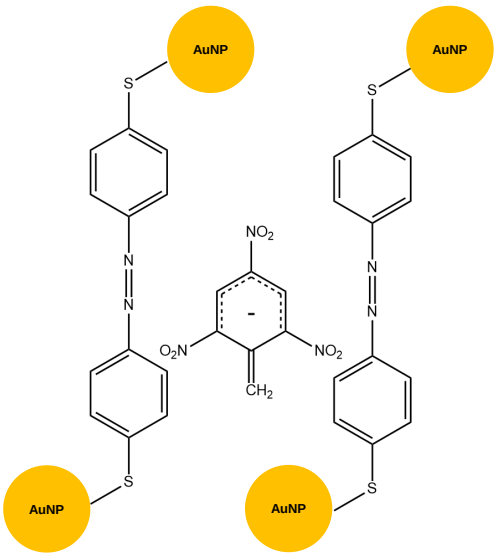

Figure 59: *Possible interaction between TNT and p-ATP through a TNT-DMAB complex.*

Whilst it is possible to infer the presence of DMAB from the SERS spectra, it was not possible to determine the extent of p-ATP catalytic coupling and hence whether all p-ATP was converted into DMAB. As such, the assay spectra likely represents vibrational modes arising from the interactions between normal p-ATP and TNT as well as DMAB and TNT. Another point to consider is the addition of TNT to functionalised AuNPs occurred in solution and so complex formation would be subject to reaching absorption equilibrium conditions. Furthermore, a number of other interactions can also exist between p-ATP and TNT, as described earlier in Figure 54.

Different levels of enhancement are seen in the SERS spectra which does not correlate with the different TNT concentrations used. One reason for the varied enhancement could be due to the aggregation effect seen on the AuNPs when TNT is added. As observed in the absorption spectra above (Figure 56C), the presence of TNT caused broadening of the AuNP LSPR peak. An additional peak is also seen around 750 nm. These characteristics indicate the formation of aggregated AuNP structures which would subsequently affect

the SERS enhancement. This suggests the current assay may only be suitable for TNT concentrations lower than the ones tested. The drastic changes in the properties of the AuNPs limits the effectiveness of the colorimetric detection. Further optimisation of the method could lead to a more effective assay, however this was not carried out due to a more successful approach found, which is described in the following section.

5.3.5 *Detection of nitro explosives using Janovsky complex*

In the previous section, the detection of TNT was demonstrated using different gold nanostructures functionalised with p-ATP. The rationale being to exploit the known interactions between p-ATP and TNT in order to concentrate TNT molecules onto the surface of gold nanostructures. This section describes a similar approach whereby nitro-explosives are detected through the formation of Janovsky complexes, using the molecule 3-mercapto-2-butanone (3M2B). Detection was achieved by monitoring the change in UV-Vis absorption and SERS spectra. Figure 60 illustrates the detection principle.

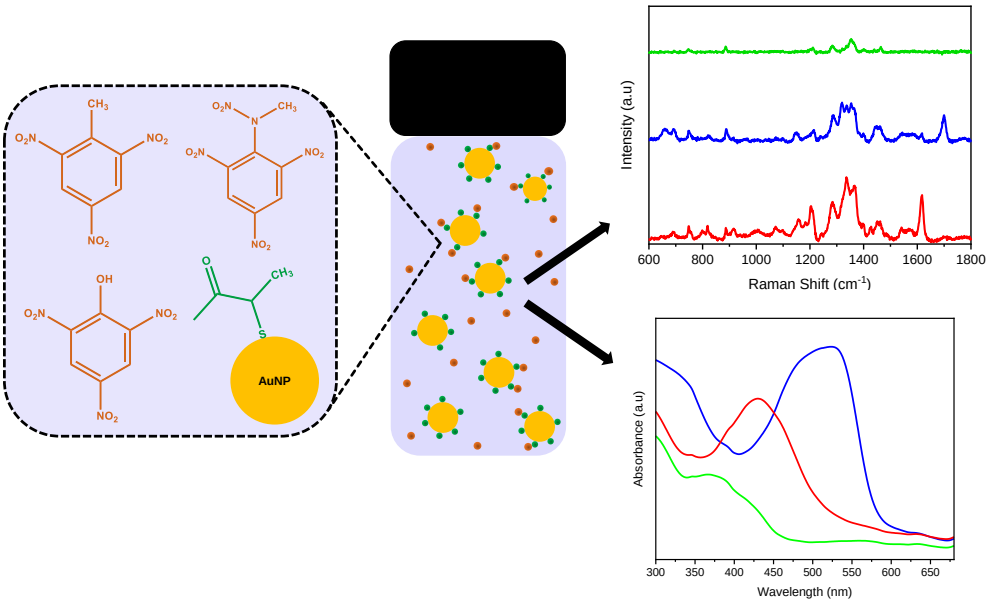

Figure 60: *Diagram showing principle of DBU-3M2B assays and subsequent dual detection of nitroexplosives using SERS (top panel) and colorimetry (bottom panel).*

The nucleophilic addition of 3M2B to nitroaromatic compounds can be achieved by deprotonation of 3M2B. 1,8-Diazabicyclo[5.4.0]undec-7-ene (DBU) is an amidine base widely used in organic synthesis due to its advantages of being large in size, having a low cation symmetry and strong delocalized charge on the cation formed from the DBU [401]. DBU is a non-nucleophilic and strong base which can react with 3M2B to produce an enolate ion, and which can subsequently attack the electron-deficient nitroaromatic compounds. This results in the formation of a Janovsky complex. Figure 61 shows the possible reaction scheme using TNT as an example. In addition to its role in adduct formation, 3M2B was also selected as it contains a thiol group which can form a thiolate bond with AuNPs. The relatively small 3M2B molecule facilitates close proximity between captured TNT molecules and the AuNP surface and so overall, these factors can improve the SERS enhancement of TNT.

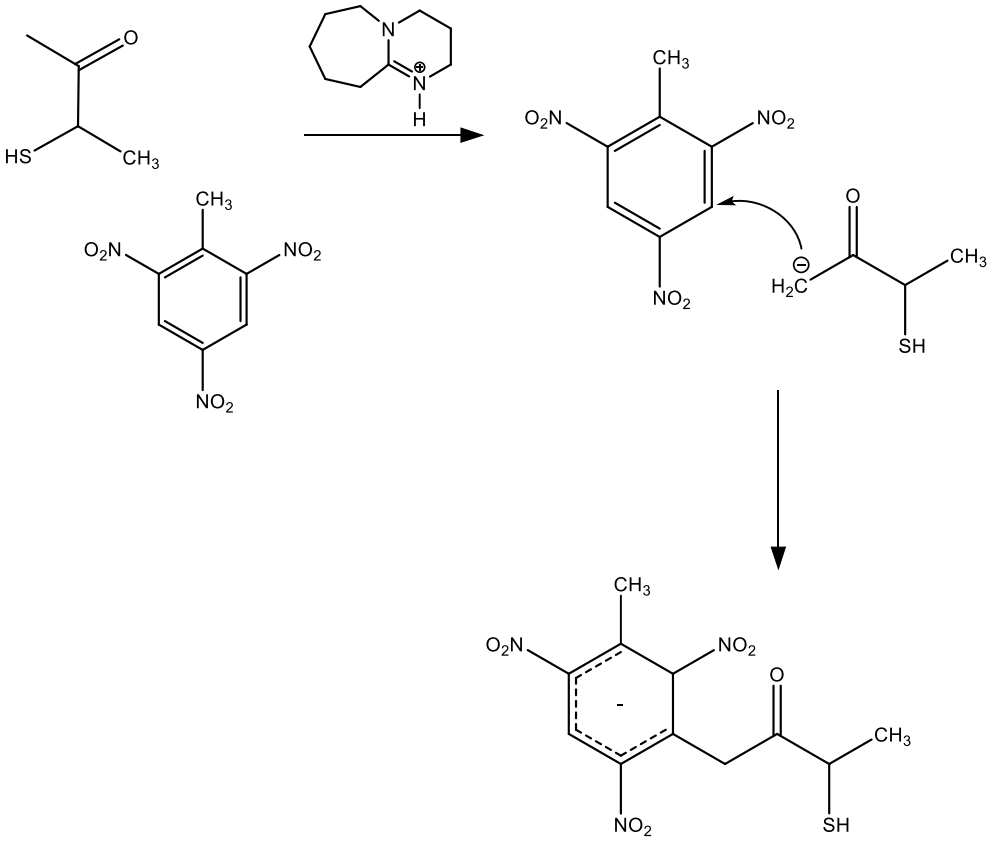

Figure 61: *Scheme showing the formation of Janovsky complex using DBU, 3M2B and TNT.*

5.3.6 *Absorption spectra of DBU-3M2B assays with explosives*

Figure 62 shows the absorption spectra of the DBU-3M2B assay with TNT. The assay was prepared by mixing 0.01 M of DBU and 3M2B prior to the addition of TNT. This mixture was then further mixed for 5 minutes before analysis. As seen in Figure 62A, the UV-Vis absorption of TNT at 0.11 mM shows a minor peak at 425 nm. DBU is a colourless solution and 3M2B is pale yellow. When TNT is added to DBU-3M2B, the solution turned from a pale yellow colour to salmon pink, and a peak around 515 nm was observed. This suggests the addition of DBU to 3M2B resulted in the formation of an enolate-carbanion derived from 3M2B to give a Janovsky adduct with TNT. A solution

containing DBU and TNT, prepared to the equivalent assay concentrations was tested and shows two main peaks, one at 525 nm and another at 650 nm. This suggests a possible reaction between TNT and DBU giving rise to competing products. This rationale can be drawn from works by Ainscough and Bernasconi, who conducted kinetic studies on the reactions of TNT with bases [402], [403]. By conducting experiments in different solvents and with base in excess to TNT, the authors reported that TNT and similar nitrotoluene derivatives can undergo free-radical reactions in basic solution, with solvent composition in the reaction mixture one factor which can affect the species formed.

It is known that DBU is a non-nucleophilic and hindered base. In the mixture containing DBU and TNT, DBU is in excess to TNT and in a mixed solvent system containing methanol. Considering DBU's strong basicity, methoxide anions can be generated which can participate in nucleophilic attack of the methyl group on TNT. Subsequent deprotonation of the methyl group could lead to the formation of a benzyl carbanion, such as the 2,4,6-trinitrobenzyl anion, as observed by the peak at 650 nm. The reaction of the 2,4,6-trinitrobenzyl anion with a second molecule of TNT could form a pseudo-Janovsky complex, observed from the peak at 525 nm. In the presence of 3M2B (assay), nucleophilic attack comes from the enolate ion formed from 3M2B, which is a more favourable pathway as evidenced by the single peak in the absorption spectra.

The assay with TNT was further studied by monitoring the absorption profile over a period of 20 minutes (Figure 62B). Upon addition of TNT to the DBU and 3M2B mixture (at time = 0 minutes), the absorbance of the 515 nm peak increased, representing the formation of the Janovsky complex. The peak at 650 nm also increased but reached a maximum absorbance within 3

minutes, after which the absorbance gradually decreased to its initial level. By monitoring the evolution of the 515 nm peak, it can be seen the reaction is complete within 5 minutes (Figure 62C).

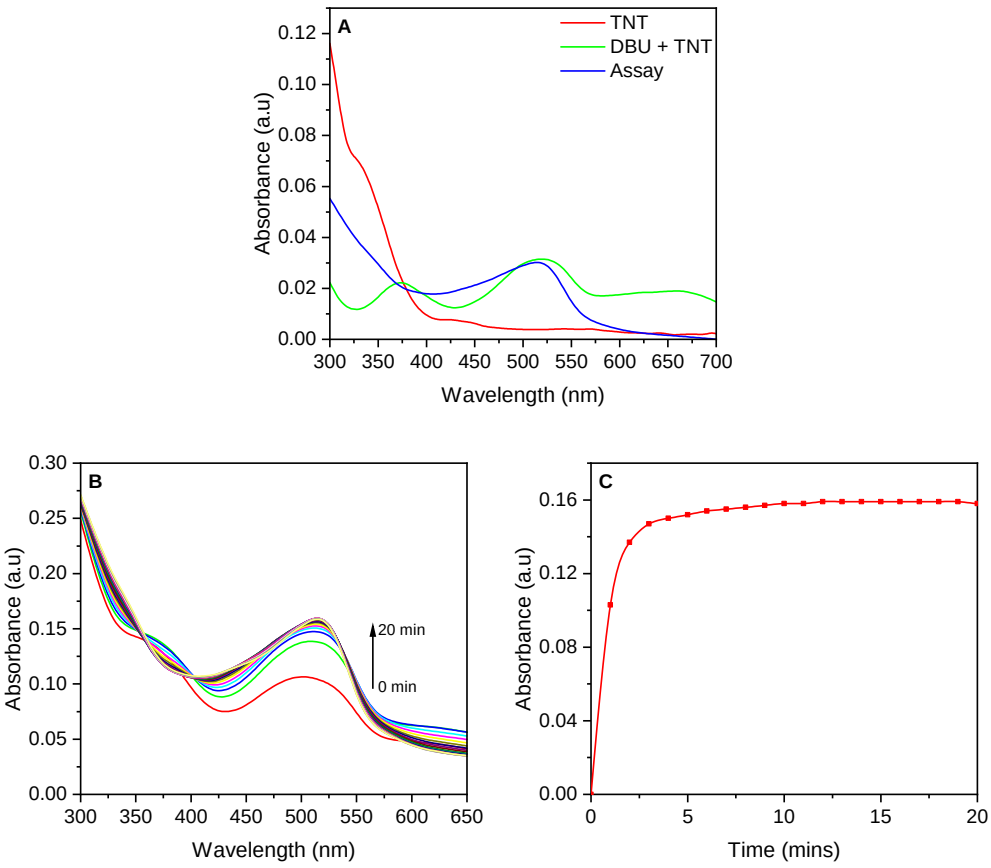

Figure 62: *Absorption spectra of DBU-3M2B assay with TNT: A) Comparison between controls and assay, B) Timepoint analysis of reaction over 20 minutes upon addition of TNT to DBU and 3M2B. Arrow indicates progress of reaction from 0 minutes, C) Analysis of 514 nm peak over 20 minutes.*

Figure 63 shows the absorption spectra of the DBU-3M2B assay with tetryl. The assay was prepared as mentioned above, by pre-mixing DBU and 3M2B before addition of tetryl. When tetryl was added to the assay, a faint pink colour was observed which gradually turned yellow. The absorption spectra of the assay (Figure 63A) shows a single broad peak at 475 nm. The spectrum containing only DBU and tetryl shows two peaks, at 430 nm and 510 nm. From the spectrum, it appears tetryl reacts in a similar way to TNT. In the absence

of 3M2B, there appears to be formation of a pseudo-Janovsky complex. In monosubstituted 2,4,6-trinitroaromatic compounds such as TNT and tetryl, nucleophilic attack can occur at different positions on the aromatic ring, leading to different Meisenheimer complexes [404]. Taking the same analogy, it is possible there exists several pseudo-Janovsky complexes giving rise to the doublet-peak character seen. The assay with tetryl was further studied by monitoring the absorption profile over a period of 20 minutes (Figure 63B). From the addition of tetryl to DBU and 3M2B (at time = 0 minutes), the 475 nm peak gradually increased, representing the formation of the Janovsky complex. The absorption spectra of TNT, tetryl, PA and DBU-3M2B is shown together in Figure 64. As mentioned above, each spectral profile is different and so the absorption spectra can be used to differentiate between the explosives.

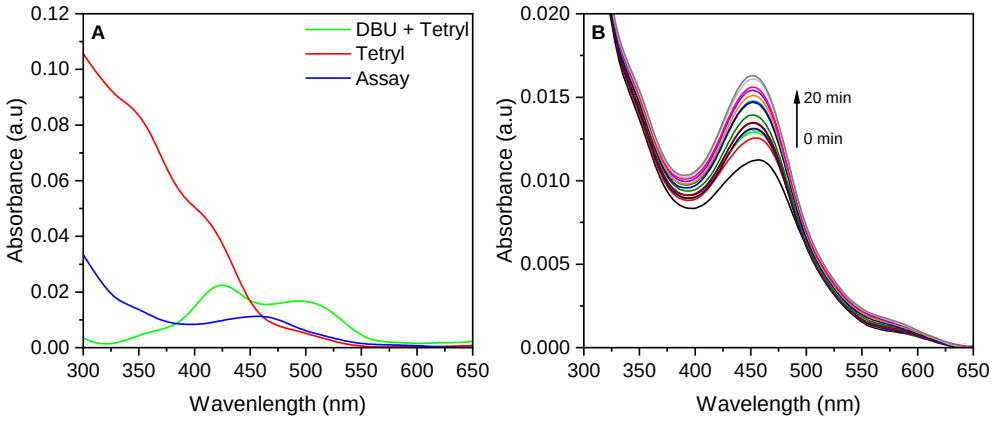

Figure 63: *Absorption spectra of DBU-3M2B assay with Tetryl: A) Comparison between controls and assay, B) Timepoint analysis of reaction over 20 minutes upon addition of Tetryl to DBU and 3M2B. Arrow indicates progress of reaction from 0 minutes.*

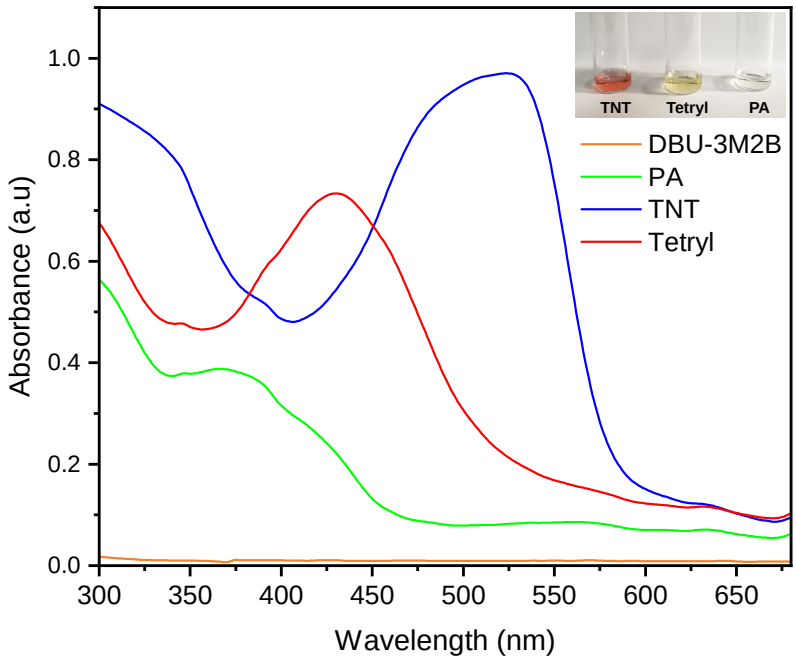

Figure 64: *UV-Vis spectra of DBU-3M2B assays with explosives.*

5.3.7 *Possible reaction products formed in the DBU-3M2B assays with nitroexplosives*

Figure 65 shows the possible reaction products in the DBU-3M2B assay with TNT, tetryl and PA. Results from the UV-Vis absorption spectra shows that different complexes are likely to be formed between each explosive and the 3M2B enolate ion. One assumption made regarding the assays is complete conversion of 3M2B to its enolate ion prior to addition of the explosive. Control studies carried out between DBU and each explosive showed DBU can complex with TNT and tetryl. However, different peaks are observed compared with reactions with the 3M2B enolate ion, suggesting different reaction mechanisms.

The three electron-withdrawing NO_2 in TNT produces an electron-deficient toluene ring which can encourage the covalent addition of nucleophiles to a ring carbon atom. Depending on the reactants in the system, coloured complexes

can form as TNT undergoes different mechanisms of nucleophilic attack. Meisenheimer complexes are formed on reaction with a strong base. Janovsky complexes are typically formed on reaction with acetone treated with a base [405], [406]. A carbanion derived from the ketone can proceed with addition to the polynitro compound, resulting in a Janovsky complex. In the current study, acetone has been replaced with 3M2B and DBU is used as a strong non-nucleophilic base. The generation of the 3M2B enolate ion forms the attacking nucleophile. Due to the strong electron affinity of NO_2 groups, positions 1, 3, and 5 on the TNT molecule would be electron deficient and be the most likely position for electron donation and subsequent addition of the enolate ion. The resulting complex absorbs in the visible region, as seen by the salmon pink colour formed.

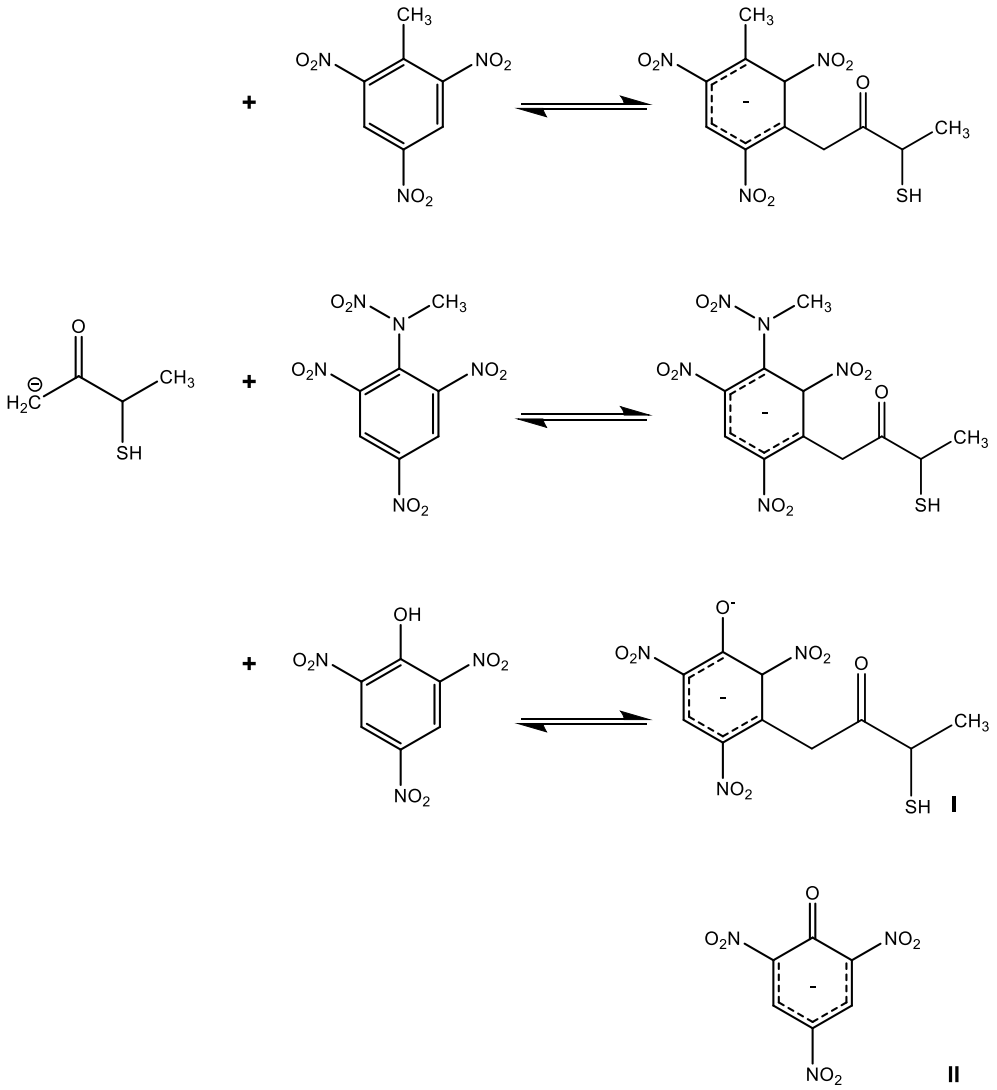

Figure 65: *Possible reaction products between between nitroaromatic explosives (TNT, tetryl and PA) and 3M2B enolate ion, formed from reaction with DBU (not shown). I and II shows two possible products from the reaction with PA.*

Tetryl has a similar structure to TNT and is substituted at one of the ortho positions by a nitramine nitro group. Tetryl is known to easily form Meisenheimer complexes, with studies reporting the use of NaOH [407] and methanol [404]. The strong electron withdrawing groups at the ortho and para positions makes tetryl open to nucleophilic attack at multiple positions. Similar to TNT, a Janovsky complex can form through addition of the enolate ion.

The reaction between PA and ketones is well documented, with one example being the reaction between PA and creatinine which is commonly used in the Jaffé reaction [408]. In alkaline conditions, abstraction of a proton from the ketone results in a carbanion, which can attack the PA at electron deficient positions, forming a Janovsky complex [408], [409]. A similar approach is proposed here with attack coming from the enolate ion of 3M2B. A reaction between unreacted DBU and PA is also possible, resulting in the formation of a phenolate ion. The three NO_2 groups in PA can stabilise the phenolate ion by resonance electron withdrawal, allowing the negative charge to be moved to an electronegative oxygen atom in the NO_2 group. Since there are three NO_2 groups, a highly acidic phenol is produced and as such, it may be possible for an acid-base reaction to occur between the PA and enolate ion.

5.3.8 *SERS spectra of DBU-3M2B assays with TNT*

Figure 66 shows the SERS plots of each assay tested using TNT, tetryl and PA, at concentrations of 23 µM, 130 µM and 15 µM, respectively. Each SERS sample was prepared by mixing an aliquot of assay solution with AuNPs. The mixture was then allowed to stir overnight before deposition onto a microscope slide for SERS. The SERS spectrum of DBU (0.01 M) and 3M2B (0.01 M) mixed with AuNP is also provided as a reference to show the differences in

the spectral profiles are attributed to analyte peaks. SERS analysis was carried out using a 633 nm laser and each spectra shows an average of 5-10 positions.

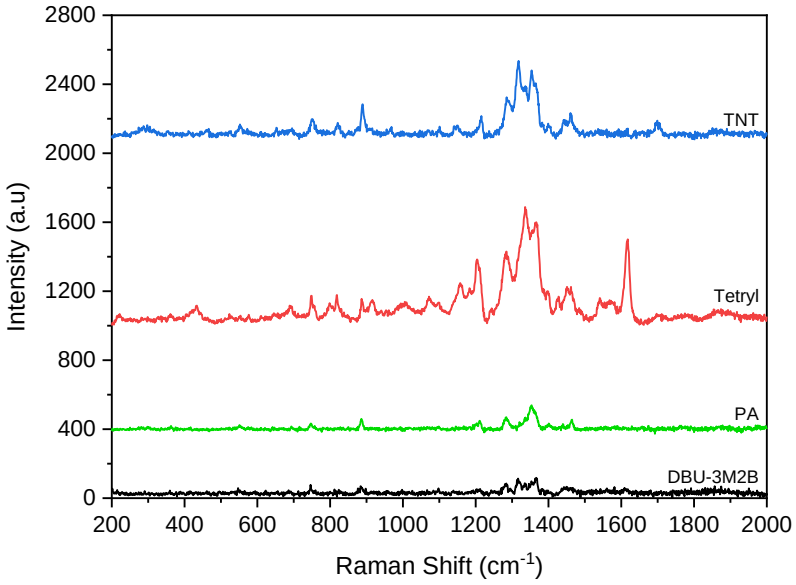

Figure 66: *SERS spectra of DBU-3M2B assays with explosives.*

In the SERS spectrum of DBU-3M2B and AuNP, only a small number of peaks are observed with low intensity. These are positioned at approximately 746 cm^{-1}, 887 cm^{-1} and the region between 1317-1366 cm^{-1}. On addition of TNT to DBU-3M2B, a number of peaks were observed which indicate the formation of a Janovsky complex between TNT and the enolate ion of 3M2B. The SERS spectrum of the TNT Janovsky complex shows a dominant cluster of peaks between 1300-1350 cm^{-1}. The peak at 1350 cm^{-1} can be assigned to the NO_2 symmetrical stretching mode of TNT. The peak at 830 $^{-1}$ is attributed to the NO_2 scissoring mode. The peak present at 1218 cm^{-1} is attributed to the ring breathing/bending vibrational mode.

Tetryl shares a similar structure to TNT, with the addition of a methylnitramine and nitro group. As such, there are similarities in the SERS spectrum of the tetryl and TNT Janovsky complexes. The dominant peak in the tetryl spectrum is at 1360 cm^{-1} and can be assigned to the NO_2 symmetrical stretch,

whereas the peak at 1541 cm^{-1} can be assigned to the NO_2 asymmetric stretch. For nitramine compounds, the peak between 760 and 767 cm^{-1} is attributed to the out-of-plane deformation of the nitro group [410] and for tetryl, this can be seen with the peak positioned at 760 cm^{-1}. All observed peaks lie very close to SERS studies reported in literature [180], [220], [221], [411], [412].

In the assay with PA, the SERS spectrum was absent of characteristic peaks. These results support the rationale that both TNT and tetryl formed Janovsky complexes with the 3M2B enolate ion. For PA, the phenolic hydroxyl group does not participate in substitution/elimination reactions and as such no complex was formed between PA and the 3M2B enolate ion. The weak to little affinity between PA and the AuNPs resulted in low SERS enhancement. This would explain the lack of peaks observed in the SERS spectra for PA. The peaks that are present, closely resemble the control SERS spectrum of DBU and 3M2B.

The SERS assay with TNT was compared with the conventional Raman and SERS spectra of TNT, in the absence of DBU and 3M2B (Figures 67A). In general, the Raman and SERS spectra of molecules (collected under the same excitation wavelength) should be quite similar, with the main characteristic peaks identifiable in both. However, differences between the Raman and SERS spectra can occur and be due to a number of factors, such as changes in resonance conditions and surface selection rules [10]. Whilst Raman spectra shows only contributions from the vibrational modes in a molecule, SERS spectra also contains contributions from the interaction between adsorbed molecule and substrate. The effect on spectral profile can include peak shift and broadening, as well as emergence or disappearance of peaks [10]. These effects are the result of the chemical enhancement effect. In the current work, additional complexity is likely from the formation of Janovsky complexes.

This will further contribute to differences observed in spectral profile between the Raman and SERS spectra.

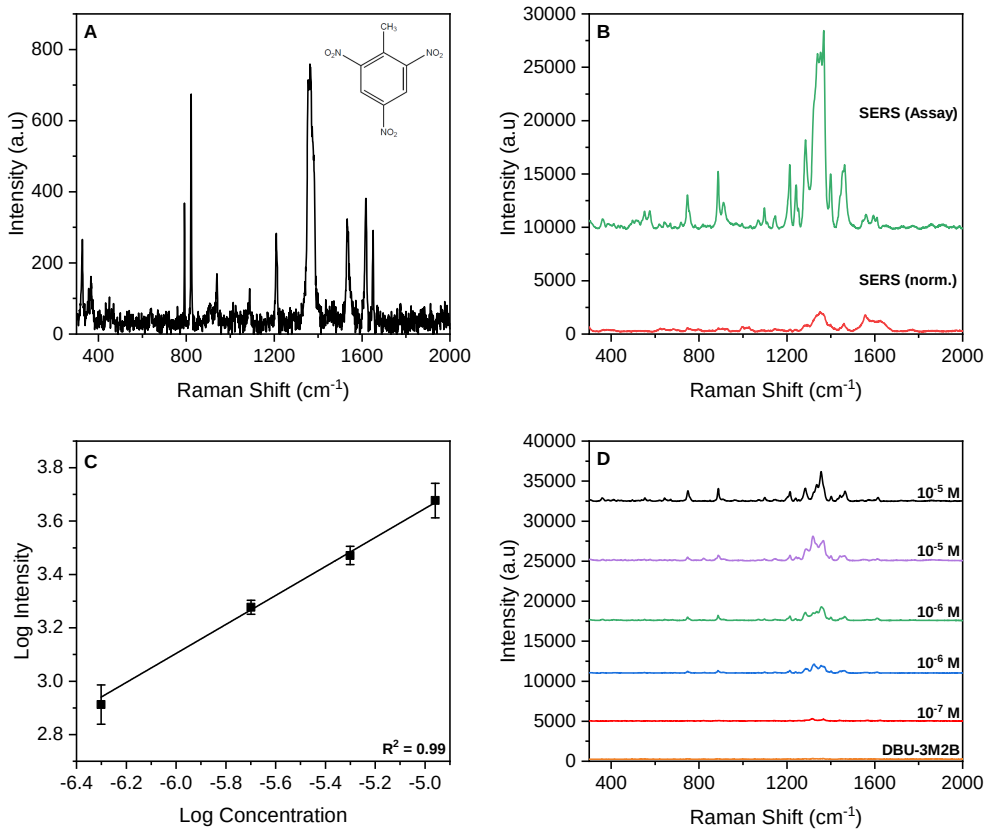

Figure 67: *Detection of TNT using DBU-3M2B assays: A) Raman spectrum of solid TNT for reference, B) DBU-3M2B assay using TNT, compared with SERS using AuNP and TNT (both at mM TNT concentrations), C) Plot of SERS intensity of the main TNT peak in each assay, against concentration in the range 10^{-5} M - 10^{-7} M. Logarithmic fittings were performed to reveal the correlation between SERS intensity and concentration. Spectra have been baseline-corrected and offset for clarity, D) SERS spectra of assays tested, including those shown in C).*

A similar rationale can be applied for the comparison between the assay and conventional SERS spectra (without DBU-3M2B), both collected using mM concentration of TNT (Figure 67B). In the conventional SERS spectrum, broad peaks can be seen around 1350 cm^{-1}, 1550 cm^{-1} and 1600 cm^{-1}, regions attributed to the NO_2 symmetrical and asymmetrical modes, respectively. In comparison, the same regions for the assay spectrum shows a number of sharp peaks, with the dominant peaks in the 1350 cm^{-1} region. An increased

intensity is also apparent. One explanation could be due to the ability of the assay to 'capture' TNT molecules bringing them to closer to the surface of the AuNPs. Another possibility could be due to electrostatic interaction between the Janovsky complex AuNPs, leading to the formation of small clusters of AuNP 'hotspots'. In SERS, the plasmonic coupling between nanoparticles in close proximity can result in large electromagnetic field enhancements, which can explain why AuNPs clustered together will give higher enhancements compared with isolated particles. The enhancement of TNT at 1.46 mM was compared between the normal and assay SERS. Using the 1350 cm^{-1} peak, an enhancement factor of 2.29×10^4 was calculated for TNT under normal SERS conditions. The enhancement in the assay SERS was 2.03×10^5.

To show the relationship between the SERS response and TNT concentration, a range of TNT solutions prepared at different concentrations (1.1×10^{-5} M to 5×10^{-7} M) were added to assay solutions containing DBU and 3M2B. Figure 67C shows the resultant calibration graph plotted using the NO_2 symmetrical mode. The graph shows the intensity of the 1350 cm^{-1} peak increased with increasing TNT concentration. A linear relationship was observed over the concentrations tested with a correlation coefficient value of $R^2 = 0.99$. The corresponding spectra of all concentrations tested are shown in Figure 67D.

5.3.9 *SERS spectra of DBU-3M2B assays with Tetryl*

The DBU-3M2B assay with tetryl was also studied in a similar fashion (Figure 68). The assay spectrum was compared with the Raman and normal SERS (without DBU-3M2B) and this is shown in Figure 68A. The Raman spectrum was collected from recrystallised reference solution. Due to the low quantities of material recovered, a weak spectrum was seen. However the main peaks

were observed at 799 cm^{-1}, 825 cm^{-1}, 1360 cm^{-1} and 1616 cm^{-1}. The most intense peak is attributed to the NO_2 symmetrical mode at 1360 cm^{-1}. These peaks were also observed in the conventional SERS spectrum (without DBU-3M2B). Overall, there is good agreement between the between the Raman and both SERS (normal and DBU-3M2B) spectra, which supports the detection of tetryl. The enhancement of tetryl was compared between the normal and assay SERS and is shown in Table 20.

Table 20: *Calculation of SERS enhancement factors (EF) for tetryl at 1.34 $\times 10^{-4}$ M.*

Raman peak (cm^{-1})	Assignment	SERS peak	EF: SERS (normal)	EF: SERS (assay)
1360	NO_2, sym	1373	8.43×10^3	1.27×10^4
1616	NO_2, asym	1616	6.53×10^3	2.38×10^4

Due to the limited Raman data available for tetryl, a sample of powdered tetryl was analysed using ATR-IR in order to provide confidence in the identity of the peaks observed (Figure 68D). The peak at 1073 cm^{-1} is attributed to the C-N and ring stretching modes. The peaks at 1340 cm^{-1} and 1540 cm^{-1} are attributed to the symmetric and asymmetric NO_2 modes, respectively. The peak around 1611 cm^{-1} is attributed to the aromatic conjugated system. The peak at 3086 cm^{-1} and adjacent shouldering could be due to a combination of CH_3 and CH stretches. These peaks are in good agreement with those reported by Puiu *et al.* [413]. Both the NO_2 and C=C aromatic stretches appear in the SERS spectra which indicate these modes are IR and Raman active. The difference in the position of symetric NO_2 mode between TNT and tetryl could be to the presence of the amine group exhibiting a small electron-withdrawing effect as well as steric effects from the methyl groups acting on the proximal nitro groups.

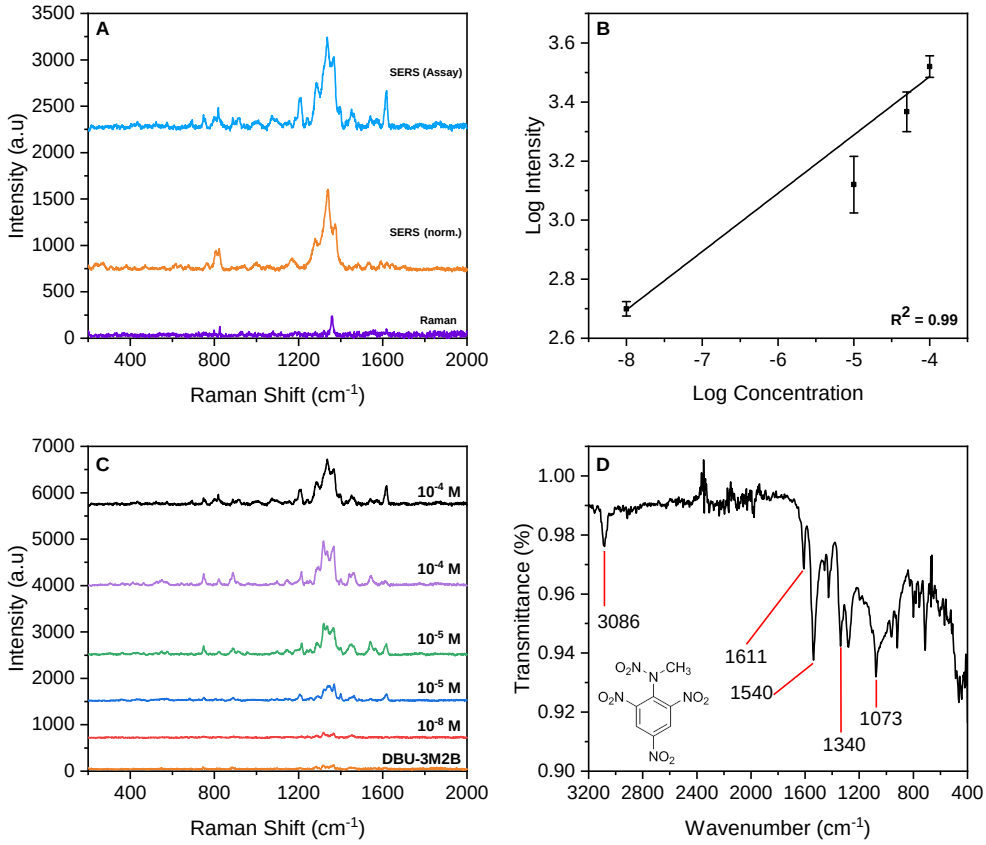

Figure 68: *Detection of tetryl using DBU-3M2B assays: A) DBU-3M2B assay using tetryl (1.30 × 10^{-4} M), compared with SERS using AuNP and tetryl (1.74 mM, without DBU-3M2B) and the Raman of solid tetryl, B) Plot of SERS intensity of the main tetryl peak in each assay, against concentration in the range 10^{-4} M - 10^{-8} M. Logarithmic fittings were performed to reveal the correlation between SERS intensity and concentration, C) SERS spectra of assays tested, including those shown in B), D) ATR-IR spectrum of solid tetryl. Red lines show the main peaks attributed to tetryl. Spectra have been baseline-corrected and offset for clarity*

To show the relationship between the SERS response and tetryl concentration, a range of tetryl solutions prepared at different concentrations (1.0 × 10^{-4} M to 1 × 10^{-8} M) were added to assay solutions containing DBU and 3M2B. Figure 68B shows the resultant calibration graph plotted using the NO_2 symmetrical mode. The graph shows the intensity of the 1350 cm^{-1} peak increases with increasing tetryl concentration. A linear relationship was observed over the concentrations tested with a correlation coefficient value of R^2 = 0.99. The corresponding spectra of all concentrations tested are shown in

Figure 68C and it can be seen there was good spectral consistency across all concentrations tested.

The ability of DBU to form methoxide ions from methanol can lead to subsequent reactions with nitrocompounds. This reaction pathway is similar to the conditions required for a Meisenheimer reaction, which involves attack of the arene species by a nucleophile. As such, it is possible that a competition reaction exists in the current system whereby both Janovsky and Meisenheimer reactions are taking place resulting in a number of Janovsky and pseudo-Janovsky/Meisenheimer complexes. However, the quantity of methanol in the current system is small, and so it is likely the Janovsky reaction takes precedence. Identification of Meisenheimer complexes through Raman spectroscopy have typically reported peaks around 2900 cm^{-1}, which are attributed to the due to the NH_2^+ symmetric stretching, C–H stretching and CH_2 asymmetric stretching modes [380], [414], [415], however, limited data is available for Janovsky complexes. The long scan of each assay, in the range 2000-3000 cm^{-1}, is shown in Figure 69. For TNT (Figure 69A), two peaks can be seen, at 2625 cm^{-1} and 2927 cm^{-1}. These peaks are absent in the normal SERS spectra of TNT (without DBU-3M2B), collected at a higher concentration of 2.2 mM. This further indicates the formation of a complex between TNT and 3M2B enolate ion. Peaks at the same position are observed only weakly for the tetryl assay and in the PA assay, only the peak at 2927 cm^{-1} is observed (Figure 69B). The SERS sample containing only DBU and 3M2B does not show any peaks. These results support the above UV-Vis and SERS data in that TNT and tetryl can form a Janovsky complex with 3M2B, whereas PA does not.

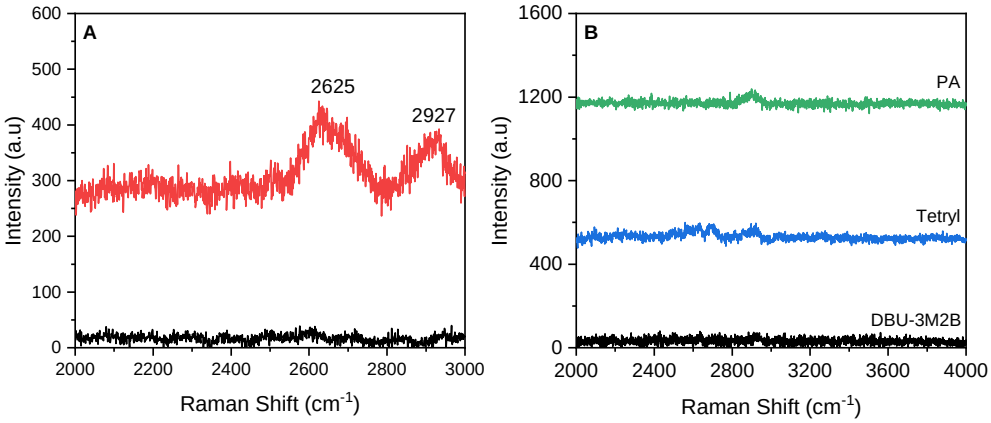

Figure 69: *Long scan SERS spectra showing possible identification peak for TNT Janovsky complex: A) DBU-3M2B assay SERS spectrum (red) compared with the normal SERS spectrum containing only AuNP and TNT (black). In both cases, the concentration of TNT was 67 µL, B) Longscan SERS of the DBU-3M2B assays for tetryl and PA, compared with the SERS of DBU-3M2B.*

5.3.10 *Applying DBU-3M2B assay to PIERS*

The above results have demonstrated the use of 3M2B functionalised AuNPs for SERS detection of nitroaromatic explosives. The nanoparticles were functionalised using the thiol moiety of 3M2B which can subsequently interact with TNT and tetryl through its enolate ion, forming Janovsky complexes. An added advantage of using functionalised nanoparticles for detection is the ability to bring analyte molecules closer to the surface of the nanoparticle, thus enabling greater enhancement. Comparison with non-functionalised AuNPs showed approximately 9 times enhancement of the Raman signal for TNT. Building on this work, the functionalised AuNPs were tested using PIERS. As previously described in Chapter 3, PIERS can be considered as 'photo-induced SERS' and involves the use of a photoactivated substrate which affords enhancement through charge-transfer effects from the substrates to AuNPs. An improved approach to PIERS was also developed, called m-PIERS, which involves the use of a 'mask', placed over the photoactive material during irradiation. This

produces two areas with different wetting properties and has the effect of overcoming photo-induced superhydrophilic behaviour, a property inherent in metal oxide semiconductors under certain conditions. This is useful for controlling the spread of the deposited droplet, ensuring a greater number of AuNPs over a smaller area and increasing the chance of hotspots.

In this section, the DBU-3M2B assay was carried out using TNT at μM concentrations. m-PIERS was compared against SERS with all samples deposited onto Pilkington Activ™ (TiO_2) as the photoactive substrate. Following m-PIERS, the sample was kept in the dark in air for 1 hour before re-analysis (post-PIERS). The results are shown in Figure 70, with each spectra representing an average of five positions. A clear PIERS enhancement can be seen and the characteristic NO_2 stretch at 1350 cm^{-1} is seen in all three spectra. However the dominant peak in all three spectra is at 1320 cm^{-1} and it appears this peak is dominant over the 1350 cm^{-1} peak when TNT concentrations are low. This trend was also seen previously, in Figures 67B and D. The post-PIERS spectra was collected from the same area after leaving the sample in air in the dark. A reduction in the intensity of the peaks can be seen and this suggests a loss in PIERS enhancement which is due to the TiO_2 healing. Using the NO_2 symmetrical mode of TNT, the calculated enhancement factor for SERS and PIERS was 5.16×10^6 and 1.43×10^7, respectively. This shows there's approximately 3 times enhancement achieved using the functionalised AuNPs.

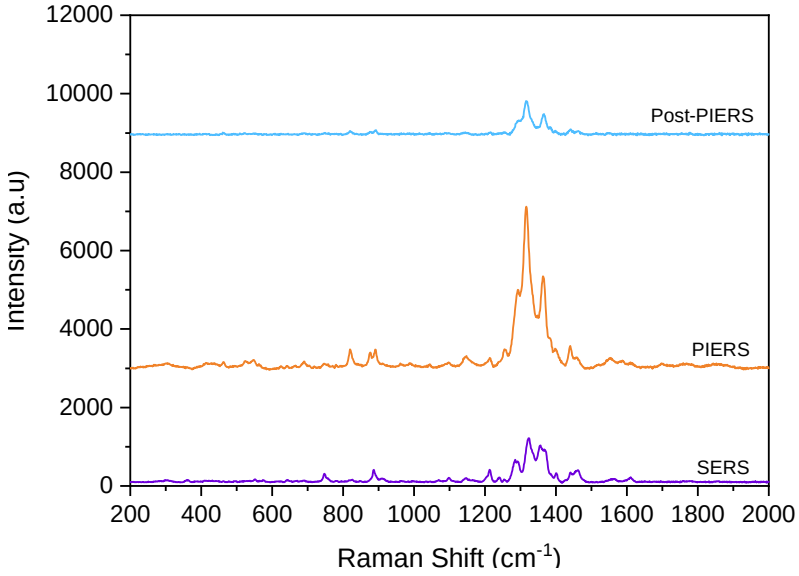

Figure 70: *PIERS using DBU-3M2B and TNT (67 μM) using Pilkington Activ™.*

The SERS results in this study agree with the work by Milligan *et al.* [416] who used 3M2B to functionalise AgNPs. Similar spectral features were observed for TNT, with the characteristic NO_2 peak at 1300 cm^{-1}. In the study by Milligan, the NO_2 peak appears asymmetric, possibly suggesting the broadened peak harbouring a number of overlapping peaks. This is also evident in the current study, where a number of peaks are seen between 1300-1350 cm^{-1} (Figure 67B and 67D). Overall, enhancement of SERS signals were observed for TNT and tetryl. The enhancement factor varies between molecules and between peaks within the same molecule. This trait is common in SERS and is due to the different coexisting mechanisms leading to chemical enhancement [22], [415], [417].

5.3.11 *Detection of TNT and tetryl using machine learning*

Machine learning (ML) is a branch of artificial intelligence which uses algorithms to extract patterns and features within data in order to make decisions.

ML is becoming increasingly popular due to its ability to handle large data sets. Spectral profiles from SERS can be complex to interpret and can be further complicated due to orientation effects of molecules with respect to the substrate. There has been interest towards applying ML to Raman and SERS data in many fields [418], [419]. However, in explosive trace detection, ML has mainly been applied to: ion mobility spectrometry (IMS)[420], colorimetry [98] and mass spectrometry [421] data. Some examples of ML approaches towards SERS data include work by Kalasung *et al.*, who used Principle Component Analysis (PCA) analysis for the detection of PETN using ZnO nanorod arrays decorated AuNP substrates, achieving an accuracy of 56 % [335]. Büttner et al. fabricated SERS substrates using UV-Nanoimprint-Lithography to produce a silicon pillar array which was subsequently coated in gold. Principal components were identified through singular value decomposition (SVD) and shown to be able to differentiate TNT from perfume musks [422].

In this section, the SERS spectra from the DBU-3M2B assays was used with common ML approaches to identify explosives. Partial Least Squares-Discriminant Analysis (PLS-DA) was used, also known as Projection of Latent Structures-Discriminant Analysis. PLS-DA is a well-established multivariate classification technique [423], [424] and is particularly suited to noisy data which contains many collinear predictor variables and one or more response variables. This has led to its popularity in chemometrics. In PLS-DA, the dimensionality of the predictor (X) variables is reduced by finding new latent variables which best describe the variation in the response (Y) variables. In this way, it can be understood as a "supervised" version of PCA.

A commonly used tool to assess the performance of ML classification model is an N x N confusion matrix. Here, 'N' is the number of target classes and the matrix compares the actual target values with those predicted by the

machine learning model. The mean prediction accuracy of the PCA-LDA classifier is 0.965 and the confusion matrix is shown in Figure 71. In addition, high prediction accuracies can be seen for TNT (0.972) and tetryl (0.955) with low levels of misclassification. The initial results show a successful application of ML to differentiate two explosives with similar SERS profiles.

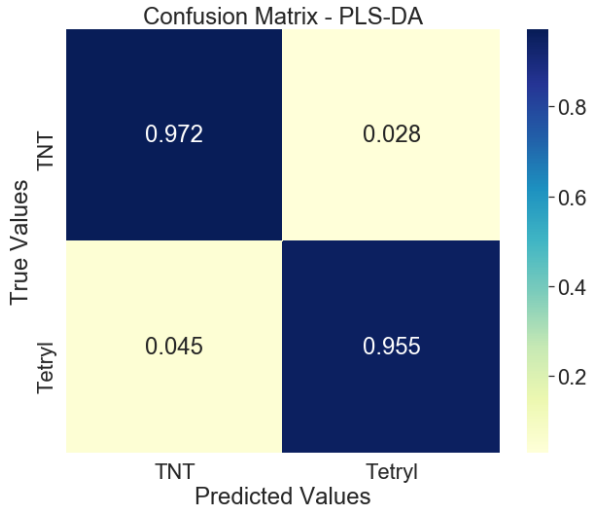

Figure 71: *Confusion matrix for the PLS-DA classifier. The numbers in the cells correspond to the fraction of spectra that were correctly classified (diagonal) or misclassified (off-diagonal).*

5.3.12 *Paper sensor*

One important factor when transitioning an in-house sensor into a real-world application is the ease in which analysis can be carried out in the field where there might be limited access to specialist equipment. To demonstrate the practicality of the colorimetric assay described in this section, a paper sensor was developed with analysis carried out using a smart phone camera and commercially available colour recognition software (Figure 72). There are a number of reasons for this approach. Firstly, the paper substrate demonstrates the assay can function on a lightweight medium, replacing the need for cuvettes and

minimising volumes of liquid involved. Secondly, the widespread availability of smartphones is utilised here to carry out colorimetric analysis. And finally, freely available software is used to demonstrate the versatility of the approach.

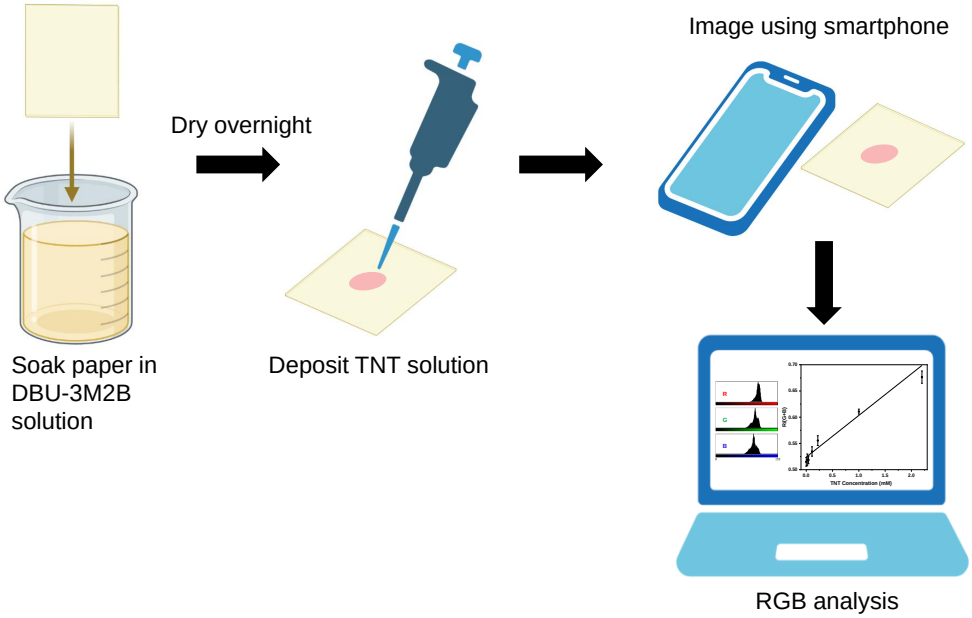

Figure 72: *DBU-3M2B assays using paper sensor: A) Deposition of TNT, PA and tetryl onto filter paper pre-soaked with DBU-3M2B solution, B) Deposition of TNT at different concentrations (0-2.2 mM) onto filter paper pre-soaked with 0.1 M DBU-3M2B solution.*

The sensor was prepared by first immersing filter paper in 0.1 M solutions of DBU and 3M2B overnight. The filter paper was then allowed to dry in a desiccator. To confirm the selectivity of the test as observed in the previous section, 5 uL of TNT, tetryl and PA at µM concentrations, were deposited on different areas of the filter paper. The results are shown in Figure 73A. Colour changes were observed for TNT and tetryl which agree with the observations in the UV-Vis measurements.

A second test was carried out whereby TNT at concentrations 0.02 - 2.2 mM were deposited onto strips of filter paper pre-soaked in DBU-3M2B. To each dried piece of filter paper, 6 μL of TNT solution was pipetted and allowed to dry. Colour change on the paper was observed almost immediately

and complete within 2 minutes. As can be seen in Figure 73B, the range of concentrations studied can easily be interpreted by eye. The tests were photographed using a smartphone and the image processed using commercially available software, ImageJ [425]. ImageJ, a freely available Java-based image processing program, was used to process the digital images into colour intensity values in the red (R), green (G), and blue (B) channels. This was possible through the pre-installed colour histogram plugin. The image processing steps required for colour evaluation were minimal and involved cropping out the background so as to present only the droplet for analysis. All samples were imaged under identical lighting conditions to ensure consistent image analysis. From triplicate experiments and extraction of the RGB profiles, a linear relationship can be seen between the averaged R/(G+B) value and TNT concentration ($R^2 = 0.96$) for concentrations in the range 0.02 - 2.2 mM (Figure 73C)

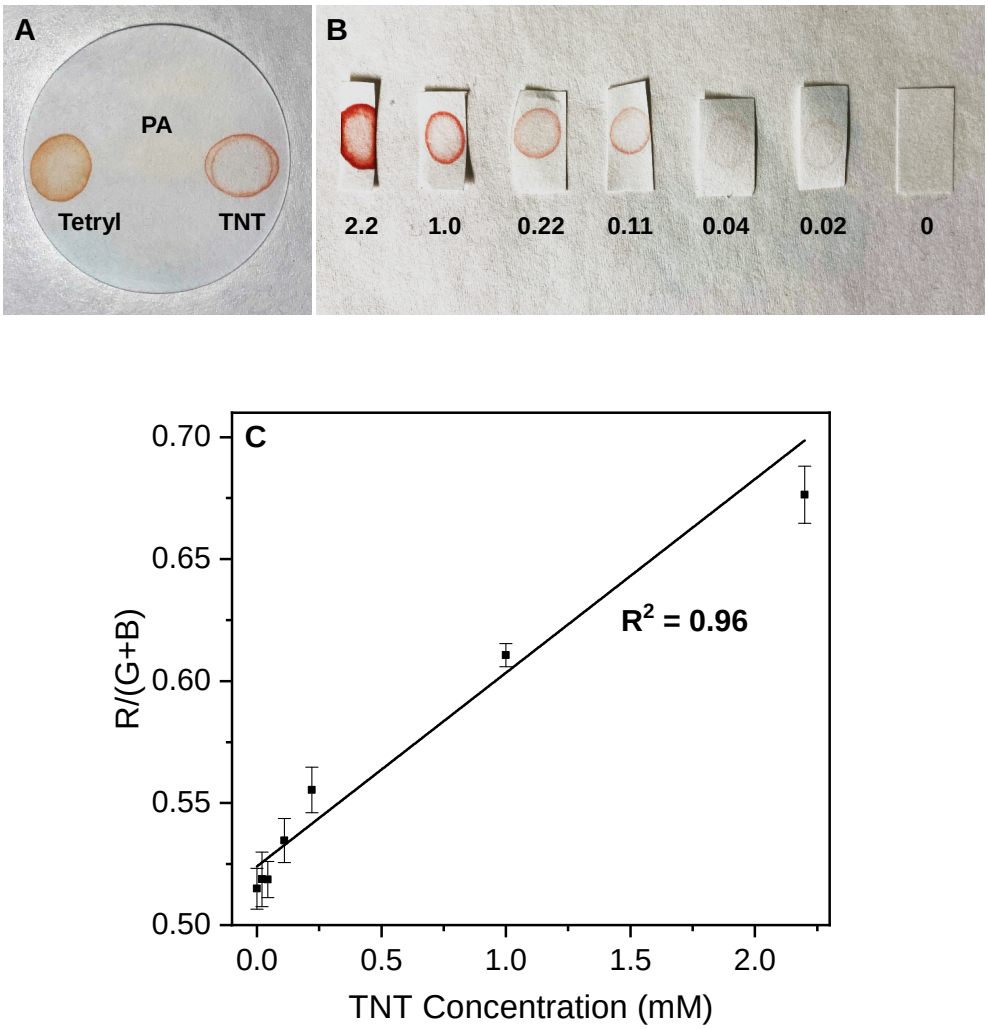

Figure 73: *DBU-3M2B assays using paper sensor: A) Deposition of TNT, PA and tetryl onto filter paper pre-soaked with DBU-3M2B solution, B) Deposition of TNT at different concentrations (0-2.2 mM) onto filter paper pre-soaked with 0.1 M DBU-3M2B solution.*

This section has demonstrated the DBU-3M2B assay can be fashioned into an inexpensive sensor and interpreted with ease. The assay was applied to a paper substrate for facile recognition of TNT without use of analytical instrument. Whilst colour differentiation was visible using the naked eye, analysis was also carried out by using a smartphone and ImageJ software to process the digital images. By analysing the RGB output, it was possible to detect TNT in the range 0.02-2.2 mM. The results demonstrate the potential

for in-field use of the DBU-3M2B assay for explosives detection. With further streamlining of the image processing steps, it is highly feasible that an auto image-processing algorithm capable of quantitative detection can be achieved.

5.4 CONCLUSIONS

This chapter has reported work using modified AuNPs to detect nitro explosives. In the first half of the chapter, p-ATP was used to functionalise AuNPs for the detection of TNT. Characteristic peaks for TNT were identified in the SERS spectra due to the complex formed between DMAB and TNT. However, the SERS enhancement was found to be inconsistent with respect to increasing levels of TNT concentration. One reason could be due to the changes in the absorption spectra observed on addition of TNT, which resulted in broadening of the LSPR peak and the emergence of a secondary peak. This indicated there was a change in the scattering properties of the AuNPs and likely a change in the dispersity of the AuNPs due to aggregation induced by the interaction between TNT and p-ATP.

In the second part of the chapter, an alternative approach to functionalisation of AunPs was taken. In this two-step approach, a non-nucleophilic base (DBU) was reacted with 3M2B to produce the equivalent enolate ion. Addition of nitro explosives then led to the formation of a Janovsky complex. A colour change was observed for TNT and tetryl. In the resultant SERS spectra, characteristic peaks for each explosive were seen. In addition, peaks were observed in the longscan of TNT and tetryl spectra but not in the PA spectra which could indicate the Janovsky complexes for these two explosives.

The SERS spectra of the assay showed an improved enhancement of TNT compared with normal SERS (without DBU-3M2B) and this is likely

to be due to the formation of the Janovsky complex and the ability of the assay to 'capture' TNT molecules, bringing them closer to the surface of the AuNPs. The DBU-3M2B assay was applied to PIERS and the results showed the combined use of functionalised AuNPs and PIERS to have a greater enhancement effect compared to normal SERS and PIERS. This is the first reported use of modified AuNPs in PIERS for the detection of explosives. The SERS data was then used to train a a supervised classification method and the results showed it was possible to achieve ≈ 97 % prediction accuracy, with only ≈ 200 spectra. These results show a good proof of concept in applying machine learning to SERS data. Finally, a colorimetric paper sensor was developed using the DBU-3M2B assay. Identification of TNT and tetryl was easily visible via the naked eye. TNT was deposited at different concentrations and detection was achieved digitally by combining a smartphone and freely available software. This is the first demonstration of a paper sensor using the DBU-3M2B assay and the result provides a promising design for in-field use.

It is evident the 3M2B assay provides a better approach for detection of explosives. Whilst the two approaches have not been compared like-for-like, some general observations can be made on the mechanisms involved. In DBU-3M2B assay, the nucleophile is an enolate ion whereas in typical meisenheimer complex (as proposed in the use of p-ATP), the nucleophile originates from the amine functional group of a neutral molecule. Since nucleophilicity increases with respect to density of the negative charge, the enolate ion may induce more successful attachment into the aromatic ring of TNT compared with p-ATP. Also, the enolate ion could have preferential attachment at one of the positions away from the methyl group of TNT, in which case bypassing the steric hindrance which could affect the ease in which the complex is formed.

These factors could facilitate a stronger complex and more distinctive SERS spectra.

The DBU-3M2B assay has shown a promising approach for the detection of nitroaromatic explosives. The current study is the first to report the functionalisation of AuNPs using the DBU-3M2B pair and also the first study to apply functionalised AuNPs for explosives detection using PIERS. Preliminary results shown in the paper sensor shows the ease in which the assay can be developed into a low-cost device without the need for expensive analysis equipment. Automated detection can also be envisioned, as demonstrated by simply using a smartphone for colour identification, as well as through open source ML methods for SERS analysis. The latter has also shown the potential of ML in identifying molecules with similar SERS profiles. Collectively, these results shows the advantages of using SERS as a detection method for multi-analyte detection of explosives.

A natural progression of this work would include testing of additional nitroexplosives. Confirmation of the Janovsky complex through mass spectrometry or nuclear magnetic resonance (NMR)-based approaches, would also provide better mechanistic understanding. If evidence of Meisenheimer complexes in the assay is also proven, this could enable the assay to be optimised to target wider range of nitroaromatic explosives. Building a more extensive SERS spectral library would significantly enhance the capabilities of the ML tool and enable multi-analyte detection.

6

CONCLUSIONS

6.1 CONCLUSIONS

The overall goal of the research in this thesis was to develop new methods for the analysis of energetic materials using enhanced Raman spectroscopy approaches. SERS and PIERS were chosen due to their potential for rapid and non-destructive analysis at trace levels. The research was guided through an initial literature review to survey current developments in SERS and PIERS and which also enabled comparison with other techniques used in ETD. Three workstreams were then identified, which focused on better understanding of PIERS, developing a new PIERS substrate and developing a dual detection assay for nitroaromatic explosives. The following sections summarise each results chapter, detailing the highlights, relevance of the work and future work.

6.1.1 *Studying PIERS using Pilkington Activ™*

The aim of this chapter was to study the PIERS effect with the goal of improving the technique for trace analysis. Previous studies have reported numerous PIERS active substrates and work towards understanding the mechanism has included studying the lifetime of oxygen vacancies in different materials and correlating the PIERS enhancement to photocatalytic activity. In the conventional PIERS method, the enhancement decreases over time, showing an

exponential-like decay. This is due to the healing of the metal oxide substrate and the result is limiting for detection applications. Another limitation is the light induced superhydrophilic property which is observed in some metal oxide substrates. This is a problem because the activated film surface causes droplets to spread across its surface which reduces the density of AuNPs and decreases the number of hotspots which are crucial for high enhancement. In this workstream, commercially available TiO_2 (Pilkington Activ™) was selected as a model substrate.

Initial studies were carried out to confirm the PIERS effect by studying the charge transfer between TiO_2 and AuNP post irradiation. A characteristic blue-shift was observed in the LSPR of AuNPs after UV irradiation followed by red-shift back to a position close to the original LSPR position. This supports the PIERS enhancement originating from TiO_2 to AuNPs and the CT process is temporary. The CT mechanism was further supported by introducing a fluorescent dye, R6G, into the system. The Raman spectrum of R6G was enhanced under PIERS. The fluorescence emission of R6G was shown to be greatest when R6G, AuNPs and TiO_2 were subjected to UV irradiation compared with the fluorescence emission of R6G on each constituent component. Next, PL was used to study the role of oxygen vacancies by observing the change in the green emission peak in TiO_2, associated with the formation of oxygen vacancies in TiO_2. Subjecting the sample to UV irradiation prior to PL analysis resulted in enhancement of the green emission peak. To reduce the healing rate of oxygen vacancies, samples were placed in a custom-built chamber flushed with argon. Analysis under these conditions also showed an enhancement of the green emission peak. These observations indicate the role of oxygen vacancies to be important in the PIERS enhancement. PIERS studies carried out using MBA under argon not only showed a significant

enhancement compared with normal PIERS in air, but also the lifetime of the enhancement can be extended for over 1 hour.

To overcome the light-induced superhydrophilic effect, a mask was placed over the TiO_2 substrate during UV irradiation to create two areas with different wetting properties. This approach, termed 'm-PIERS', gave significant enhancement over normal PIERS and is due to the higher AuNP density on the film leading to greater number of hotspots for PIERS. To demonstrate the new PIERS techniques, detection studies were carried out using Raman probe molecules MBA and R6G, as well as the pesticide thiram and explosives triacetone triperoxide (TATP), hexamethylene triperoxide diamine (HMTD) and trinitrotoluene (TNT), showing superior enhancements compared with conventional SERS and PIERS.

6.1.2 *PIERS using ZnO decorated with gold nanoparticles*

The aim of this chapter was to demonstrate the PIERS effect using doped ZnO as a novel substrate. Previous work reported in literature showed better enhancement with the use of crystalline ZnO. In this study, ZnO thin films were prepared on a silicon substrate using CBD to produce uniform nanorod structures with high crystallinity. Ag and Cu doped ZnO samples were prepared to compare the effect of doping on PIERS activity. Samples were characterised on a structural and elemental level using XRD, XPS EDX, Raman and PL. The PIERS enhancement was compared using MBA and it was shown the doped ZnO samples produced a higher level of enhancement compared with undoped ZnO. The differences in the SERS and PIERS enhancement observed is likely due to the subtle structural differences and possible mechanisms for the enhancement were proposed. When compared with the two reports of ZnO

PIERS substrates currently in literature, the enhancements seen in this study are much higher. These observations can be attributed to a combination of effects including: a crystalline film with polar preferential growth, high defect concentration and presence of nanoparticles as sources of hot electrons.

6.1.3 *Dual detection of nitroaromatic explosives*

The aim of this chapter was to develop a dual detection method for explosives using colorimetry and SERS which could then be used in PIERS. Initially, a widely-cited approach was adopted, using p-ATP as the functionalising ligand for AuNPs. However, the SERS enhancement was found to vary with increasing TNT concentration, indicating inefficiency in the binding between ligand and TNT. In addition, the properties of the AuNPs were altered on addition of TNT which resulted in aggregation of the AuNPs. This limited the effectiveness of the assay.

The use of an enolate ion was found to be more effective at adduct formation, resulting in a coloured Janovsky complex. The assay showed it was easy to differentiate between TNT and tetryl through the naked eye and clear differences could be seen in the SERS spectra. The use of functionalised AuNPs was also found to result in better PIERS enhancement compared to the use of non-functionalised AuNPs. Real-world applications were demonstrated by incorporating data from the assay to successfully train a machine-learning algorithm and being able to conduct the colorimetric analysis using a smartphone camera and freely available image analysis software.

6.1.4 *Summary of main successes*

- Preliminary studies show it may be possible to extend the PIERS lifetime by keeping the substrate in a low oxygen environment during analysis.
- A method has been developed to mitigate the effect of light-induced superhydrophillicity by applying a mask to the substrate during irradiation.
- Preliminary studies show Ag and Cu doped ZnO to produce higher levels of PIERS enhancement compared with undoped ZnO.
- First demonstrated use of functionalised AuNPs for PIERS for explosives detection.
- Development of a colorimetric SERS assay for the detection of nitroaromatic explosives.
- Successful demonstration of ML to identify explosives using collected SERS assay data, which is a promising indicator for the development of a SERS sensor.
- Development of a colorimetric sensor using smartphone and freely available software.

6.1.5 *Future work*

As seen in the current work, drop-cast deposition results in the formation of nanoclusters of different sizes. Improvements to the current SERS and PIERS protocol could involve studying the arrangement of the AuNP nanoclusters in order to tune the excitation laser wavelength to improve the resonance condi-

tions and enhancement. This can be achieved by examining the morphology, mass and optical properties. Further improvements could involve strategies to control formation of the nanoclusters and engineering plasmonic hotspots with well-controlled gaps.

The results seen in the current work and in literature shows the PIERS lifetime varies between materials. A useful area of future research would be to correlate the lifetime of the photoexcited charge carriers with the differences reported between PIERS substrates. This can be achieved using sensitive techniques such as Transient Absorption Spectroscopy (TAS). A longer lifetime would extend the 'usefulness' of PIERS as a sensor. A better approach would be to eliminate the PIERS lifetime entirely. The PIERS lifetime and enhancement can be improved by conducting experiments under a low oxygen environment, indicating the environment can affect the PIERS activity. Further development of this work should consider not only analysis, but irradiation under a vacuum or inert environment. This would isolate effects from residual oxygen and better inform the contribution of environment on PIERS. As eluded to previously, the development of better PIERS substrates requires understanding of the factors affecting PIERS and future PIERS work should also draw inspiration from advances made in the development of photocatalytic materials. Whilst many photocatalytic research focuses on improving the photocatalytic activity of materials, there are many similarities in terms of the materials and mechanism of action with PIERS.

Concomitant to overcoming the limitations of conventional PIERS, there is also a need to optimise and develop new substrates. Further investigations relating to the ZnO work could be understanding the effect of dopant concentration on the PIERS enhancement. As seen in the mechanism proposed for the Ag-ZnO sample, and evidence from XPS and XRD, the presence of Ag

nanoparticles can further enhance PIERS due to the LSPR contributions. The LSPR properties of the AgNPs were not characterised in this study but it would be pertinent to identify the size, shape and optical properties. Varying the concentration of dopant used in the synthesis, could also allow optimisation of the size and/or shape of the Ag nanoparticles and further improve enhancement. Better design of the ZnO thin films could lead to improvements in PIERS enhancement and examples of modifications include: different patterns (nanoparticles, nanosheets, nanoneedles etc...), surface modifications and use of composite materials. Future work should also include testing the ZnO films on non-conventional Raman probes.

The preliminary work describing the DBU-3M2B assay has opened up many routes for further research. One prominent direction is applying the assay to more nitro-based explosives and using the SERS data to build a more extensive ML library. Focus can also be given to developing an ML approach to read colorimetric data. This is highly feasible given the many solutions reported in literature. Being able to use ML for both SERS and colorimetric data would be highly advantageous and would form the basis of a detection system.

7

APPENDICES

7.1 PUBLISHED PAPERS

The work in this thesis, in addition to related work not discussed, has been published in several peer reviewed papers, listed below.

1. **To, K. C.**, Ben-Jaber, S., Parkin, I. P., Recent Developments in the Field of Explosive Trace Detection, ACS Nano, 14, 9, 10804-10833, 2020.

2. Panariello, L.; **To, K. C.**; Khan, Z.; Wu. G.; Gkogkos, G.; Damilos, S.; Parkin, I. P.; Gavriilidis, A. Kinetics-based design of a flow platform for highly reproducible on demand synthesis of gold nanoparticles with controlled size between 50-150 nm and their application in SERS and PIERS sensing. Chemical Engineering Journal 2021, 37, 129069.

3. Promdet, P.; Sathasivam, S.; **To, K. C.**; Dixon, S.; Guo, J.; Kafizas, A.; Carmalt, C. J.; Parkin, I. P. Photocatalytic behavior of Zinc gallate and N-doped Zinc gallate thin films. Materials Advances (submitted).

4. **To, K. C.**, *et al.*, Detection of explosives using enhanced Raman spectroscopy approaches and machine-learning (manuscript in progress).

5. Promdet, P.; Cui, F.; Quesada-Cabrera; **To, K. C.**; Hwang, G. B.; Shin Juhun.; Carmalt, C. J.; Parkin, I. P. Cu nanoparticle embedded-ZnO

nanoplate thin film for photocatalytic hydrogen production (manuscript in progress).

6. **To, K. C.**, *et al.*, Dual detection of nitroaromatic explosives using colorimetry and SERS (manuscript in progress).

7. **To, K. C.**, *et al.*, Characterisation of the PIERS effect using Pilkington Activ™ (manuscript in progress).

BIBLIOGRAPHY

[1] C. V. Raman and K. S. Krishnan, 'A new type of secondary radiation,' *Nature*, vol. 121, no. 3048, pp. 501–502, 1928, ISSN: 00280836. DOI: 10.1038/121501c0.

[2] A. Y. Hirakawa and M. Tsuboi, 'Molecular geometry in an excited electronic state and a preresonance Raman effect,' *Science (80-.).*, vol. 188, no. 4186, pp. 359–361, 1975, ISSN: 00368075. DOI: 10.1126/science.188.4186.359.

[3] D. Strommen and K. Nakamoto, 'Resonance Raman spectroscopy,' *J. Chem. Educ.*, vol. 8, pp. 474–478, 1977, ISSN: 10643745. DOI: 10.1007/978-1-4939-0452-5_15.

[4] L. Nagli, M. Gaft, Y. Fleger and M. Rosenbluh, 'Absolute Raman cross-sections of some explosives: Trend to UV,' *Opt. Mater. (Amst).*, vol. 30, no. 11, pp. 1747–1754, 2008, ISSN: 09253467. DOI: 10.1016/j.optmat.2007.11.019.

[5] E. D. Emmons, J. A. Guicheteau, A. W. Fountain and S. D. Christesen, 'Comparison of visible and near-infrared Raman cross-sections of explosives in solution and in the solid state,' *Appl. Spectrosc.*, vol. 66, no. 6, pp. 636–643, 2012, ISSN: 00037028. DOI: 10.1366/11-06549.

[6] K. L. Wustholz, C. L. Brosseau, F. Casadio and R. P. Van Duyne, 'Surface-enhanced Raman spectroscopy of dyes: from single molecules to the artists' canvas,' *Phys. Chem. Chem. Phys.*, vol. 11, no. 34,

p. 7350, 2009, ISSN: 1463-9076. DOI: 10.1039/b904733f. [Online]. Available: http://xlink.rsc.org/?DOI=b913171jhttp://xlink.rsc.org/?DOI=b904733f.

[7] M. Fleischmann, P. J. Hendra and A. J. McQuillan, 'Raman spectra of pyridine adsorbed at a silver electrode,' *Chem. Phys. Lett.*, vol. 26, no. 2, pp. 163–166, 1974, ISSN: 00092614. DOI: 10.1016/0009-2614(74)85388-1.

[8] D. L. Jeanmaire and R. P. V. Duyne, 'Surface Raman Spectroelectrochemistry Part1. Heterocyclic,' *J. Electroanal Chem.*, vol. 84, p. 1, 1977.

[9] M. G. Albrecht and J. A. Creighton, 'Anomalously Intense Raman Spectra of Pyridine at a Silver Electrode,' *J. Am. Chem. Soc.*, vol. 99, no. 15, pp. 5215–5217, 1977, ISSN: 15205126. DOI: 10.1021/ja00457a071.

[10] E. Le Ru and E. Pablo, *Principles of Surface Enhanced Raman Spectroscopy and related plasmonic effects*, First edit. Wellington: Elsevier, 2009, ISBN: 9780444527790.

[11] J. Kneipp, H. Kneipp, B. Wittig and K. Kneipp, 'Novel optical nanosensors for probing and imaging live cells,' *Nanomedicine Nanotechnology, Biol. Med.*, vol. 6, no. 2, pp. 214–226, 2010, ISSN: 15499634. DOI: 10.1016/j.nano.2009.07.009. [Online]. Available: http://dx.doi.org/10.1016/j.nano.2009.07.009.

[12] Z. Starowicz, R. Wojnarowska-Nowak, P. Ozga and E. M. Sheregii, 'The tuning of the plasmon resonance of the metal nanoparticles in terms of the SERS effect,' *Colloid Polym. Sci.*, vol. 296, no. 6, pp. 1029–1037, 2018, ISSN: 14351536. DOI: 10.1007/s00396-018-4308-9.

[13] J. A. Creighton, C. G. Blatchford and M. G. Albrecht, 'Plasma resonance enhancement of Raman scattering by pyridine adsorbed on silver or gold sol particles of size comparable to the excitation wavelength,' *J. Chem. Soc. Faraday Trans. 2 Mol. Chem. Phys.*, vol. 75, pp. 790–798, 1979, ISSN: 03009238. DOI: 10.1039/F29797500790.

[14] E. C. Le Ru, E. Blackie, M. Meyer and P. G. Etchegoint, 'Surface enhanced raman scattering enhancement factors: A comprehensive study,' *J. Phys. Chem. C*, vol. 111, no. 37, pp. 13 794–13 803, 2007, ISSN: 19327447. DOI: 10.1021/jp0687908.

[15] M. Moskovits, 'Surface-enhanced spectroscopy,' *Rev. Mod. Phys.*, vol. 57, no. 783, pp. 783–826, 1985.

[16] G. Mie, 'Beiträge zur Optik trüber Medien, speziell kolloidaler Metallösungen,' *Ann. Phys.*, vol. 330, no. 3, pp. 377–445, 1908, ISSN: 00033804. DOI: 10.1002/andp.19083300302. [Online]. Available: https://onlinelibrary.wiley.com/doi/10.1002/andp.19083300302.

[17] M. G. Blaber, M. D. Arnold and M. J. Ford, 'A review of the optical properties of alloys and intermetallics for plasmonics,' *J. Phys. Condens. Matter*, vol. 22, no. 14, 2010, ISSN: 09538984. DOI: 10.1088/0953-8984/22/14/143201.

[18] V. Amendola, R. Pilot, M. Frasconi, O. M. Maragò and M. A. Iatì, 'Surface plasmon resonance in gold nanoparticles: A review,' *J. Phys. Condens. Matter*, vol. 29, no. 20, 2017, ISSN: 1361648X. DOI: 10.1088/1361-648X/aa60f3.

[19] S. Y. Ding, J. Yi, J. F. Li, B. Ren, D. Y. Wu, R. Panneerselvam and Z. Q. Tian, 'Nanostructure-based plasmon-enhanced Raman spectroscopy

for surface analysis of materials,' *Nat. Rev. Mater.*, vol. 1, no. 6, 2016, ISSN: 20588437. DOI: 10.1038/natrevmats.2016.21.

[20] Y. S. Yamamoto, Y. Ozaki and T. Itoh, 'Recent progress and frontiers in the electromagnetic mechanism of surface-enhanced Raman scattering,' *J. Photochem. Photobiol. C Photochem. Rev.*, vol. 21, pp. 81–104, 2014, ISSN: 13895567. DOI: 10.1016/j.jphotochemrev.2014.10.001. [Online]. Available: http://dx.doi.org/10.1016/j.jphotochemrev.2014.10.001.

[21] E. C. Le Ru and P. G. Etchegoin, 'Rigorous justification of the |E|4 enhancement factor in Surface Enhanced Raman Spectroscopy,' *Chem. Phys. Lett.*, vol. 423, no. 1-3, pp. 63–66, 2006, ISSN: 00092614. DOI: 10.1016/j.cplett.2006.03.042.

[22] L. Jensen, C. M. Aikens and G. C. Schatz, 'Electronic structure methods for studying surface-enhanced Raman scattering,' *Chem. Soc. Rev.*, vol. 37, no. 5, pp. 1061–1073, 2008, ISSN: 03060012. DOI: 10.1039/b706023h.

[23] E. C. Le Ru and P. G. Etchegoin, 'Single-Molecule Surface-Enhanced Raman Spectroscopy,' *Annu. Rev. Phys. Chem.*, vol. 63, no. 1, pp. 65–87, 2012, ISSN: 0066-426X. DOI: 10.1146/annurev-physchem-032511-143757. [Online]. Available: http://www.annualreviews.org/doi/10.1146/annurev-physchem-032511-143757.

[24] D. Cialla, A. März, R. Böhme, F. Theil, K. Weber, M. Schmitt and J. Popp, 'Surface-Enhanced Raman spectroscopy (SERS): Progress and trends,' *Anal. Bioanal. Chem.*, vol. 403, no. 1, pp. 27–54, 2012, ISSN: 16182642. DOI: 10.1007/s00216-011-5631-x.

[25] J. R. Lombardi, R. L. Birke, T. Lu and J. Xu, 'Charge-Transfer Theory of Surface Enhanced Raman Spectroscopy: Herzberg-Teller Contributions,' *J. Chem. Phys.*, vol. 84, no. 8, pp. 4174–4180, 1986, ISSN: 00219606. DOI: 10.1063/1.450037.

[26] A. Campion, J. E. Ivanecky, C. M. Child and M. Foster, 'On the Mechanism of Chemical Enhancement in Surface-Enhanced Raman Scattering,' *J. Am. Chem. Soc.*, vol. 117, no. 47, pp. 11 807–11 808, 1995, ISSN: 15205126. DOI: 10.1021/ja00152a024.

[27] A. Otto, 'The 'Chemical' (Electronic) Contribution to Surface-Enhanced Raman Scattering,' *J. Raman Spectrosc.*, vol. 36, no. 6-7, pp. 497–509, 2005, ISSN: 03770486. DOI: 10.1002/jrs.1355.

[28] R. Pilot, R. Signorini, C. Durante, L. Orian, M. Bhamidipati and L. Fabris, 'A review on surface-enhanced Raman scattering,' *Biosensors*, vol. 9, no. 2, 2019, ISSN: 20796374. DOI: 10.3390/bios9020057.

[29] P. L. Stiles, J. A. Dieringer, N. C. Shah and R. P. V. Duyne, 'Surface-Enhanced Raman Spectroscopy,' *Annu. Rev. Anal. Chem.*, vol. 1, no. 1, pp. 601–626, 2008, ISSN: 09718044. [Online]. Available: https://doi.org/10.1146/annurev.anchem.1.031207.112814.

[30] Z.-q. Tian and X.-m. Zhang, 'Early History , Principles , Methods ,' in *Dev. Electrochem. Sci. Inspired by Martin Fleischmann*, John Wiley & Sons, Ltd, 1973, pp. 113–131.

[31] C. Zong, M. Xu, L. J. Xu, T. Wei, X. Ma, X. S. Zheng, R. Hu and B. Ren, 'Surface-Enhanced Raman Spectroscopy for Bioanalysis: Reliability and Challenges,' *Chem. Rev.*, vol. 118, no. 10, pp. 4946–4980, 2018, ISSN: 15206890. DOI: 10.1021/acs.chemrev.7b00668.

[32] D. M. Solís, J. M. Taboada, F. Obelleiro, L. M. Liz-Marzán and F. J. García De Abajo, 'Optimization of Nanoparticle-Based SERS Substrates through Large-Scale Realistic Simulations,' *ACS Photonics*, vol. 4, no. 2, pp. 329–337, 2017, ISSN: 23304022. DOI: 10.1021/acsphotonics.6b00786.

[33] E. C. Le Ru, C. Galloway and P. G. Etchegoin, 'On the connection between optical absorption/extinction and SERS enhancements,' *Phys. Chem. Chem. Phys.*, vol. 8, no. 26, pp. 3083–3087, 2006, ISSN: 14639076. DOI: 10.1039/b605292d.

[34] L. Qin, S. Zou, C. Xue, A. Atkinson, G. C. Schatz and C. A. Mirkin, 'Designing, fabricating, and imaging Raman hot spots,' *Proc. Natl. Acad. Sci. U. S. A.*, vol. 103, no. 36, pp. 13 300–13 303, 2006, ISSN: 00278424. DOI: 10.1073/pnas.0605889103.

[35] E. Petryayeva and U. J. Krull, 'Localized surface plasmon resonance: Nanostructures, bioassays and biosensing-A review,' *Anal. Chim. Acta*, vol. 706, no. 1, pp. 8–24, 2011, ISSN: 00032670. DOI: 10.1016/j.aca.2011.08.020. [Online]. Available: http://dx.doi.org/10.1016/j.aca.2011.08.020.

[36] H. Wei, S. M. Hossein Abtahi and P. J. Vikesland, 'Plasmonic colorimetric and SERS sensors for environmental analysis,' *Environ. Sci. Nano*, vol. 2, no. 2, pp. 120–135, 2015, ISSN: 20518161. DOI: 10.1039/c4en00211c.

[37] S. L. Kleinman, R. R. Frontiera, A. I. Henry, J. A. Dieringer and R. P. Van Duyne, 'Creating, characterizing, and controlling chemistry with SERS hot spots,' *Phys. Chem. Chem. Phys.*, vol. 15, no. 1, pp. 21–36, 2013, ISSN: 14639076. DOI: 10.1039/c2cp42598j.

[38] Y. Wang and J. Irudayaraj, 'A SERS DNAzyme biosensor for lead ion detection,' *Chem. Commun.*, vol. 47, no. 15, pp. 4394–4396, 2011, ISSN: 1364548X. DOI: 10.1039/c0cc04140h.

[39] S. Mahajan, T. C. Lee, F. Biedermann, J. T. Hugall, J. J. Baumberg and O. A. Scherman, 'Raman and SERS spectroscopy of cucurbit[n]urils,' *Phys. Chem. Chem. Phys.*, vol. 12, no. 35, pp. 10 429–10 433, 2010, ISSN: 14639076. DOI: 10.1039/c0cp00071j.

[40] C. Zhong, C. Hu, R. Kumar, V. Trouillet, F. Biedermann and M. Hirtz, 'Cucurbit[n]uril-Immobilized Sensor Arrays for Indicator-Displacement Assays of Small Bioactive Metabolites,' *ACS Appl. Nano Mater.*, vol. 4, no. 5, pp. 4676–4687, 2021, ISSN: 25740970. DOI: 10.1021/acsanm.1c00293.

[41] W. I. Chio, W. J. Peveler, K. I. Assaf, S. Moorthy, W. M. Nau, I. P. Parkin, M. Olivo and T. C. Lee, 'Selective Detection of Nitroexplosives Using Molecular Recognition within Self-Assembled Plasmonic Nanojunctions,' *J. Phys. Chem. C*, vol. 123, no. 25, pp. 15 769–15 776, 2019, ISSN: 19327455. DOI: 10.1021/acs.jpcc.9b02363.

[42] X. Shi, W. Gu, C. Zhang, L. Zhao, L. Li, W. Peng and Y. Xian, 'Construction of a Graphene/Au-Nanoparticles/Cucurbit[7]uril-Based Sensor for Pb2+ Sensing,' *Chem. - A Eur. J.*, vol. 22, no. 16, pp. 5643–5648, 2016, ISSN: 15213765. DOI: 10.1002/chem.201505034.

[43] A. I. Pérez-Jiménez, D. Lyu, Z. Lu, G. Liu and B. Ren, 'Surface-enhanced Raman spectroscopy: Benefits, trade-offs and future developments,' *Chem. Sci.*, vol. 11, no. 18, pp. 4563–4577, 2020, ISSN: 20416539. DOI: 10.1039/d0sc00809e.

[44] X. Wang and L. Guo, 'SERS Activity of Semiconductors: Crystalline and Amorphous Nanomaterials,' *Angew. Chemie - Int. Ed.*, vol. 59, no. 11, pp. 4231–4239, 2020, ISSN: 15213773. DOI: 10.1002/anie.201913375.

[45] X. X. Han, W. Ji, B. Zhao and Y. Ozaki, 'Semiconductor-enhanced Raman scattering: Active nanomaterials and applications,' *Nanoscale*, vol. 9, no. 15, pp. 4847–4861, 2017, ISSN: 20403372. DOI: 10.1039/c6nr08693d.

[46] H. Zhang, R. An, X. Ji, Y. Dong, F. Pan, C. Liu and X. Lu, 'Effects of nitrogen doping on surface-enhanced Raman scattering (SERS) performance of bicrystalline TiO2 nanofibres,' *Chinese J. Chem. Eng.*, vol. 26, no. 3, pp. 642–647, 2018, ISSN: 10049541. DOI: 10.1016/j.cjche.2017.05.020. [Online]. Available: https://doi.org/10.1016/j.cjche.2017.05.020.

[47] Z. Zheng, S. Cong, W. Gong, J. Xuan, G. Li, W. Lu, F. Geng and Z. Zhao, 'Semiconductor SERS enhancement enabled by oxygen incorporation,' *Nat. Commun.*, vol. 8, no. 1, pp. 2–11, 2017, ISSN: 20411723. DOI: 10.1038/s41467-017-02166-z. [Online]. Available: http://dx.doi.org/10.1038/s41467-017-02166-z.

[48] G. Song, W. Gong, S. Cong and Z. Zhao, 'Ultrathin Two-Dimensional Nanostructures: Surface Defects for Morphology-Driven Enhanced Semiconductor SERS,' *Angew. Chemie - Int. Ed.*, vol. 60, no. 10, pp. 5505–5511, 2021, ISSN: 15213773. DOI: 10.1002/anie.202015306.

[49] S. Cong, Y. Yuan, Z. Chen, J. Hou, M. Yang, Y. Su, Y. Zhang, L. Li, Q. Li, F. Geng and Z. Zhao, 'Noble metal-comparable SERS enhancement from semiconducting metal oxides by making oxygen vacancies,' *Nat.*

Commun., vol. 6, pp. 1–7, 2015, ISSN: 20411723. DOI: 10.1038/ncomms8800.

[50] Z. Mao, W. Song, X. Xue, W. Ji, L. Chen, J. R. Lombardi and B. Zhao, 'Multiphonon resonant Raman scattering and photoinduced charge-transfer effects at ZnO-molecule interfaces,' *J. Phys. Chem. C*, vol. 116, no. 51, pp. 26 908–26 918, 2012, ISSN: 19327447. DOI: 10.1021/jp3092573.

[51] X. Zhang, Z. Yu, W. Ji, H. Sui, Q. Cong, X. Wang and B. Zhao, 'Charge-Transfer Effect on Surface-Enhanced Raman Scattering (SERS) in an Ordered Ag NPs/4-Mercaptobenzoic Acid/TiO2 System,' *J. Phys. Chem. C*, vol. 119, no. 39, pp. 22 439–22 444, 2015, ISSN: 19327455. DOI: 10.1021/acs.jpcc.5b06001.

[52] X. Jiang, X. Li, X. Jia, G. Li, X. Wang, G. Wang, Z. Li, L. Yang and B. Zhao, 'Surface-enhanced Raman scattering from synergistic contribution of metal and semiconductor in TiO 2/MBA/Ag(Au) and Ag(Au)/MBA/TiO 2 assemblies,' *J. Phys. Chem. C*, vol. 116, no. 27, pp. 14 650–14 655, 2012, ISSN: 19327447. DOI: 10.1021/jp302139e.

[53] J. Akhavan, *The chemistry of explosives*, 3rd New ed. Cambridge: Royal Society of Chemistry, 2011, p. 193.

[54] F. Dubnikova, R. Kosloff, J. Almog, Y. Zeiri, R. Boese, H. Itzhaky, A. Alt and E. Keinan, 'Decomposition of triacetone triperoxide is an entropic explosion,' *J. Am. Chem. Soc.*, vol. 127, no. 4, pp. 1146–1159, 2005, ISSN: 00027863. DOI: 10.1021/ja0464903.

[55] P. Dutta, S. Chakravarty and N. S. Sarma, 'Detection of Nitroaromatic Explosives Using π-Electron Rich Luminescent Polymeric Nanocom-

posites,' *RSC Adv.*, vol. 6, no. 5, pp. 3680–3689, 2016, ISSN: 20462069. DOI: 10.1039/c5ra20347c.

[56] 'Convention on the marking of plastic explosives for the purpose of detection,' ICAO Doc 9571, 1 March 1991.

[57] R. Boschan, R. T. Merrow and R. W. van Dolah, 'The Chemistry of Nitrate Esters,' *Chem. Rev.*, vol. 55, no. 3, pp. 485–510, 1955, ISSN: 0009-2665. DOI: 10.1021/cr50003a001.

[58] R. G. Ewing, M. J. Waltman, D. A. Atkinson, J. W. Grate and P. J. Hotchkiss, 'The Vapor Pressures of Explosives,' *TrAC - Trends Anal. Chem.*, vol. 42, pp. 35–48, 2013, ISSN: 18793142. DOI: 10.1016/j.trac.2012.09.010.

[59] A. Fainberg, 'Explosives Detection for Aviation Security,' *Science (80-.).*, vol. 255, no. 5051, pp. 1531–1537, 1992, ISSN: 0036-8075. DOI: 10.1126/science.255.5051.1531. [Online]. Available: http://www.sciencemag.org/cgi/doi/10.1126/science.255.5051.1531.

[60] K. J. Albert and D. R. Walt, 'High-Speed Fluorescence Detection of Explosives-Like Vapors,' *Anal. Chem.*, vol. 72, no. 9, pp. 1947–1955, 2000, ISSN: 0003-2700. DOI: 10.1021/ac991397w. [Online]. Available: https://pubs.acs.org/doi/10.1021/ac991397w.

[61] N. C. Murray, R. Lacey and P. Mason, 'Exploitation of X-Ray Technology for the Detection of Contraband-Aviation Security Applications,' *Eur. Conf. Secur. Detect.*, no. 437, pp. 13–18, 1997, ISSN: 0537-9989. DOI: 10.1049/cp:19970411.

[62] A. Buffler, 'Contraband Detection with Fast Neutrons,' *Radiat. Phys. Chem.*, vol. 71, no. 3-4, pp. 853–861, 2004, ISSN: 0969806X. DOI: 10.1016/j.radphyschem.2004.04.110.

[63] H. Östmark, S. Wallin and H. G. Ang, 'Vapor Pressure of Explosives: A Critical Review,' *Propellants, Explos. Pyrotech.*, vol. 37, no. 1, pp. 12–23, 2012, ISSN: 07213115. DOI: 10.1002/prep.201100083.

[64] E. H. Camara, P. Breuil, D. Briand, N. F. de Rooij and C. Pijolat, 'A Micro Gas Preconcentrator with Improved Performance for Pollution Monitoring and Explosives Detection,' *Anal. Chim. Acta*, vol. 688, no. 2, pp. 175–182, 2011, ISSN: 00032670. DOI: 10.1016/j.aca.2010.12.039. [Online]. Available: http://dx.doi.org/10.1016/j.aca.2010.12.039.

[65] G. L. McEneff, B. Murphy, T. Webb, D. Wood, R. Irlam, J. Mills, D. Green and L. P. Barron, 'Sorbent Film-Coated Passive Samplers for Explosives Vapour Detection Part A: Materials Optimisation and Integration with Analytical Technologies,' *Sci. Rep.*, vol. 8, no. 1, pp. 1–13, 2018, ISSN: 20452322. DOI: 10.1038/s41598-018-24244-y. [Online]. Available: http://dx.doi.org/10.1038/s41598-018-24244-y.

[66] A. Lichtenstein, E. Havivi, R. Shacham, E. Hahamy, R. Leibovich, A. Pevzner, V. Krivitsky, G. Davivi, I. Presman, R. Elnathan, Y. Engel, E. Flaxer and F. Patolsky, 'Supersensitive Fingerprinting of Explosives by Chemically Modified Nanosensors Arrays,' *Nat. Commun.*, vol. 5, no. May, 2014, ISSN: 20411723. DOI: 10.1038/ncomms5195.

[67] S. Hughes, S. S. Dasary, S. Begum, N. Williams and H. Yu, 'Meisenheimer Complex between 2,4,6-Trinitrotoluene and 3-Aminopropyltriethoxysilane

and Its Use for a Paper-Based Sensor,' *Sens. Bio-Sensing Res.*, vol. 5, no. 6188, pp. 37–41, 2015, ISSN: 22141804. DOI: 10.1016/j.sbsr.2015.06.003. [Online]. Available: https://linkinghub.elsevier.com/retrieve/pii/S2214180415300015.

[68] M. A. Zwijnenburg, E. Berardo, W. J. Peveler and K. E. Jelfs, 'Amine Molecular Cages as Supramolecular Fluorescent Explosive Sensors: A Computational Perspective,' *J. Phys. Chem. B*, vol. 120, no. 22, pp. 5063–5072, 2016, ISSN: 15205207. DOI: 10.1021/acs.jpcb.6b03059.

[69] K. Sablok, V. Bhalla, P. Sharma, R. Kaushal, S. Chaudhary and C. R. Suri, 'Amine Functionalized Graphene Oxide/CNT Nanocomposite for Ultrasensitive Eelectrochemical Detection of Trinitrotoluene,' *J. Hazard. Mater.*, vol. 248-249, no. 1, pp. 322–328, 2013, ISSN: 03043894. DOI: 10.1016/j.jhazmat.2013.01.022. [Online]. Available: http://dx.doi.org/10.1016/j.jhazmat.2013.01.022.

[70] S. S. Dasary, D. Senapati, A. K. Singh, Y. Anjaneyulu, H. Yu and P. C. Ray, 'Highly Sensitive and Selective Dynamic Light-Scattering Assay for TNT Detection Using p-ATP Attached Gold Nanoparticle,' *ACS Appl. Mater. Interfaces*, vol. 2, no. 12, pp. 3455–3460, 2010, ISSN: 19448244. DOI: 10.1021/am1005139.

[71] M. R. Eslami and N. Alizadeh, 'Ultrasensitive and Selective QCM Sensor for Detection of Trace Amounts of Nitroexplosive Vapors in Ambient Air Based on Polypyrrole-Bromophenol Blue Nanostructure,' *Sensors Actuators, B Chem.*, vol. 278, no. April 2018, pp. 55–63, 2019, ISSN: 09254005. DOI: 10.1016/j.snb.2018.09.060. [Online]. Available: https://doi.org/10.1016/j.snb.2018.09.060.

[72] F. Dubnikova, R. Kosloff, Y. Zeiri and Z. Karpas, 'Novel Approach to the Detection of Triacetone Triperoxide (TATP): Its Structure and Its Complexes with Ions,' *J. Phys. Chem. A*, vol. 106, no. 19, pp. 4951–4956, 2002, ISSN: 10895639. DOI: 10.1021/jp014189s.

[73] R. S. Ray, B. Sarma, S. Mohanty and M. Misra, 'Theoretical and Experimental Study of Sensing Triacetone Triperoxide (TATP) Explosive through Nanostructured TiO2 Substrate,' *Talanta*, vol. 118, pp. 304–311, 2014, ISSN: 00399140. DOI: 10.1016/j.talanta.2013.09.057. [Online]. Available: http://dx.doi.org/10.1016/j.talanta.2013.09.057.

[74] F. Dubnikova, R. Kosloff, J. C. Oxley, J. L. Smith and Y. Zeiri, 'Role of Metal Ions in the Destruction of TATP: Theoretical Considerations,' *J. Phys. Chem. A*, vol. 115, no. 38, pp. 10 565–10 575, 2011, ISSN: 10895639. DOI: 10.1021/jp2021616.

[75] S. Banerjee, S. K. Mohapatra, M. Misra and I. B. Mishra, 'The Detection of Improvised Nonmilitary Peroxide Based Explosives Using a Titania Nanotube Array Sensor,' *Nanotechnology*, vol. 20, no. 7, 2009, ISSN: 09574484. DOI: 10.1088/0957-4484/20/7/075502.

[76] M. Amani, Y. Chu, K. L. Waterman, C. M. Hurley, M. J. Platek and O. J. Gregory, 'Detection of Triacetone Triperoxide (TATP) Using a Thermodynamic Based Gas Sensor,' *Sensors Actuators, B Chem.*, vol. 162, no. 1, pp. 7–13, 2012, ISSN: 09254005. DOI: 10.1016/j.snb.2011.11.019. [Online]. Available: http://dx.doi.org/10.1016/j.snb.2011.11.019.

[77] A. S. Rossi, P. Ricci and O. J. Gregory, 'Trace Detection of Explosives Using Metal Oxide Catalysts,' *IEEE Sens. J.*, vol. 19, no. 13, pp. 4773–4780, 2019, ISSN: 15581748. DOI: 10.1109/JSEN.2019.2904246.

[78] P. Wen, M. Amin, W. D. Herzog and R. R. Kunz, 'Key Challenges and Prospects for Optical Standoff Trace Detection of Explosives,' *TrAC - Trends Anal. Chem.*, vol. 100, pp. 136–144, 2018, ISSN: 18793142. DOI: 10.1016/j.trac.2017.12.014. [Online]. Available: https://doi.org/10.1016/j.trac.2017.12.014.

[79] S. Venugopal Rao, S. Abdul Kalam and M. S. S. Bharathi, 'Photonics for Explosives Detection,' *Digit. Encycl. Appl. Phys.*, no. February, pp. 1–31, 2019. DOI: 10.1002/3527600434.eap826.

[80] S. Zubedat, S. Aga-Mizrachi, A. Cymerblit-Sabba, J. Shwartz, J. F. Leon, S. Rozen, I. Varkovitzky, Y. Eshed, D. Grinstein and A. Avital, 'Human-Animal Interface: The Effects of Handler's Stress on the Performance of Canines in an Explosive Detection Task,' *Appl. Anim. Behav. Sci.*, vol. 158, pp. 69–75, 2014, ISSN: 01681591. DOI: 10.1016/j.applanim.2014.05.004.

[81] I. Gazit and J. Terkel, 'Explosives Detection by Sniffer Dogs following Strenuous Physical Activity,' *Appl. Anim. Behav. Sci.*, vol. 81, no. 2, pp. 149–161, 2003, ISSN: 01681591. DOI: 10.1016/S0168-1591(02)00274-5.

[82] A. Poling, B. Weetjens, C. Cox, N. W. Beyene, H. Bach and A. Sully, 'Using Trained Pouched Rats to Detect Land Mines: Another Victory for Operant Conditioning,' *J. Appl. Behav. Anal.*, vol. 44, no. 2, pp. 351–355, 2011, ISSN: 0021-8855. DOI: 10.1901/jaba.2011.44-351.

[83] J. J. Bromenshenk, C. B. Henderson, R. A. Seccomb, P. M. Welch, S. E. Debnam and D. R. Firth, 'Bees as Biosensors: Chemosensory Ability, Honey Bee Monitoring Systems, and Emergent Sensor Technologies Derived from the Pollinator Syndrome,' *Biosensors*, vol. 5, no. 4, pp. 678–711, 2015, ISSN: 20796374. DOI: 10.3390/bios5040678.

[84] R. Bogue, 'Detecting Explosives and Chemical Weapons: A Review of Recent Developments,' *Sens. Rev.*, vol. 35, no. 3, pp. 237–243, 2015, ISSN: 0260-2288. DOI: 10.1108/SR-12-2014-0754.

[85] *Biological Method (BEES) for Explosives Detection*, (visited on 21-07-2020). [Online]. Available: https://www.sps-bees4exp.com/project-bees-for-explosive-detection.

[86] R. N. Gillanders, 'Bees for Explosive Detection,' in *Proceedings of Mine Action 2018*, Slano, Croatia, 9 April 2018, pp. 42–44.

[87] R. N. Gillanders, J. M. Glackin, J. Filipi, N. Kezic, I. D. Samuel and G. A. Turnbull, 'Preconcentration Techniques for Trace Explosive Sensing,' *Sci. Total Environ.*, vol. 658, pp. 650–658, 2019, ISSN: 18791026. DOI: 10.1016/j.scitotenv.2018.12.160. [Online]. Available: https://doi.org/10.1016/j.scitotenv.2018.12.160.

[88] K. Persaud and G. Dodd, 'Analysis of Discrimination Mechanisms in the Mammalian Olfactory System Using a Model Nose,' *Nature*, vol. 299, no. 5881, pp. 352–355, 1982, ISSN: 00280836. DOI: 10.1038/299352a0. arXiv: 1011.1669.

[89] W. Hu, L. Wan, Y. Jian, C. Ren, K. Jin, X. Su, X. Bai, H. Haick, M. Yao and W. Wu, 'Electronic Noses: From Advanced Materials to Sensors

Aided with Data Processing,' *Adv. Mater. Technol.*, vol. 4, no. 2, pp. 1–38, 2019, ISSN: 2365709X. DOI: 10.1002/admt.201800488.

[90] L. F. Capitán-Vallvey, N. López-Ruiz, A. Martínez-Olmos, M. M. Erenas and A. J. Palma, 'Recent Developments in Computer Vision-Based Analytical Chemistry: A Tutorial Review,' *Anal. Chim. Acta*, vol. 899, pp. 23–56, 2015, ISSN: 18734324. DOI: 10.1016/j.aca.2015.10.009.

[91] A. Choodum, K. Malathong, N. NicDaeid, W. Limsakul and W. Wongniramaikul, 'A Cost Effective Hydrogel Test Kit for Pre and Post Blast Trinitrotoluene,' *Forensic Sci. Int.*, vol. 266, pp. 202–208, 2016, ISSN: 18726283. DOI: 10.1016/j.forsciint.2016.05.036.

[92] A. Choodum, P. Kanatharana, W. Wongniramaikul and N. Nicdaeid, 'Poly Vinyl Alcohol Cryogel as a Selective Test Kit for Pre and Post Blast Trinitrotoluene,' *Sensors Actuators, B Chem.*, vol. 222, pp. 654–662, 2016, ISSN: 09254005. DOI: 10.1016/j.snb.2015.08.115.

[93] A. Choodum, J. Keson, P. Kanatharana, W. Limsakul and W. Wongniramaikul, 'Selective Pre and Post Blast Trinitrotoluene Detection with a Novel Ethylenediamine Entrapped Thin Polymer Film and Digital Image Colorimetry,' *Sensors Actuators, B Chem.*, vol. 252, pp. 463–469, 2017, ISSN: 09254005. DOI: 10.1016/j.snb.2017.06.030.

[94] M. J. Kangas, R. M. Burks, J. Atwater, R. M. Lukowicz, P. Williams and A. E. Holmes, 'Colorimetric Sensor Arrays for the Detection and Identification of Chemical Weapons and Explosives,' *Crit. Rev. Anal. Chem.*, vol. 47, no. 2, pp. 138–153, 2017, ISSN: 15476510. DOI: 10.1080/10408347.2016.1233805.

[95] A. K. Yetisen, J. L. Martinez-Hurtado, A. Garcia-Melendrez, F. Da Cruz Vasconcellos and C. R. Lowe, 'A Smartphone Algorithm with Inter-Phone Repeatability for the Analysis of Colorimetric Tests,' *Sensors Actuators, B Chem.*, vol. 196, pp. 156–160, 2014, ISSN: 09254005. DOI: 10.1016/j.snb.2014.01.077.

[96] J. R. Askim, M. Mahmoudi and K. S. Suslick, 'Optical Sensor Arrays for Chemical Sensing: The Optoelectronic Nose,' *Chem. Soc. Rev.*, vol. 42, no. 22, p. 8649, 2013, ISSN: 0306-0012. DOI: 10.1039/c3cs60179j.

[97] M. O. Okuom and A. E. Holmes, 'Developing a Color-Based Molecular Sensing Device: DETECHIP,' *Sensors & Transducers*, vol. 183, no. 12, pp. 30–33, 2014.

[98] L. L. Mølgaard, O. T. Buus, J. Larsen, H. Babamoradi, I. L. Thygesen, M. Laustsen, J. K. Munk, E. Dossi, C. O'Keeffe, L. Lässig, S. Tatlow, L. Sandström and M. H. Jakobsen, 'Improved Detection of Chemical Substances from Colorimetric Sensor Data Using Probabilistic Machine Learning,' *Chem. Biol. Radiol. Nucl. Explos. Sens. XVIII*, vol. 10183, no. May 2017, p. 1 018 307, 2017. DOI: 10.1117/12.2262468.

[99] J. K. Munk, O. T. Buus, J. Larsen, E. Dossi, S. Tatlow and M. H. Jakobsen, 'CRIM-TRACK: Sensor System for Detection of Criminal Chemical Substances,' *Proc. SPIE*, vol. 9652, pp. 965 208–965208–5, 2015, ISSN: 1996756X. DOI: 10.1117/12.2194915.

[100] N Bolse, R Eckstein, M Schend, A Habermehl, C Eschenbaum, G Hernandez-Sosa and U Lemmer, 'A Digitally Printed Optoelectronic Nose for the Selective Trace Detection of Nitroaromatic Explosive Vapours Using Fluorescence Quenching,' *Flex. Print. Electron.*, vol. 2,

no. 2, p. 024 001, 2017, ISSN: 2058-8585. DOI: 10.1088/2058-8585/aa6601.

[101] N. Bolse, R. Eckstein, A. Habermehl, G. Hernandez-Sosa, C. Eschenbaum and U. Lemmer, 'Reliability of Aerosol Jet Printed Fluorescence Quenching Sensor Arrays for the Identification and Quantification of Explosive Vapors,' *ACS Omega*, vol. 2, no. 10, pp. 6500–6505, 2017, ISSN: 24701343. DOI: 10.1021/acsomega.7b01263.

[102] A. Üzer, U. Yalçın, Z. Can, E. Erçağ and R. Apak, 'Indirect Determination of Pentaerythritol Tetranitrate (PETN) with a Gold Nanoparticles-Based Colorimetric Sensor,' *Talanta*, vol. 175, no. February, pp. 243–249, 2017, ISSN: 00399140. DOI: 10.1016/j.talanta.2017.06.049. [Online]. Available: https://linkinghub.elsevier.com/retrieve/pii/S0039914017306847.

[103] V. Krivitsky, B. Filanovsky, V. Naddaka and F. Patolsky, 'Direct and Selective Electrochemical Vapor Trace Detection of Organic Peroxide Explosives *via* Surface Decoration,' *Anal. Chem.*, vol. 91, no. 8, pp. 5323–5330, 2019, ISSN: 0003-2700. DOI: 10.1021/acs.analchem.9b00257. [Online]. Available: http://pubs.acs.org/doi/10.1021/acs.analchem.9b00257.

[104] Y. Zhang, Y. Ma and L. Wang, 'Simple Copper Nanoparticle/Polyfurfural Film Modified Electrode for the Determination of 2, 4, 6-Trinitrotoluene (TNT),' *Anal. Lett.*, vol. 2719, pp. 1–14, 2020, ISSN: 0003-2719. DOI: 10.1080/00032719.2020.1751182.

[105] M. Procek, A. Stolarczyk, T. Pustelny and E. Maciak, 'A Study of a QCM Sensor Based on TiO2 Nanostructures for the Detection of NO2

and Explosives Vapours in Air,' *Sensors (Switzerland)*, vol. 15, no. 4, pp. 9563–9581, 2015, ISSN: 14248220. DOI: 10.3390/s150409563.

[106] X. Lü, P. Hao, G. Xie, J. Duan, L. Gao and B. Liu, 'A Sensor Array Realized by a Single Flexible TiO2/POMs Film to Contactless Detection of Triacetone Triperoxide,' *Sensors (Switzerland)*, vol. 19, no. 4, 2019, ISSN: 14248220. DOI: 10.3390/s19040915.

[107] W. H. Zhang, W. D. Zhang and L. Y. Chen, 'Highly Sensitive Detection of Explosive Triacetone Triperoxide by an In2O3 Sensor,' *Nanotechnology*, vol. 21, no. 31, pp. 1–6, 2010, ISSN: 09574484. DOI: 10.1088/0957-4484/21/31/315502.

[108] L. A. Horsfall, D. C. Pugh, C. S. Blackman and I. P. Parkin, 'An Array of WO 3 and CTO Heterojunction Semiconducting Metal Oxide Gas Sensors Used as a Tool for Explosive Detection,' *J. Mater. Chem. A*, vol. 5, no. 5, pp. 2172–2179, 2017, ISSN: 2050-7488. DOI: 10.1039/C6TA08253J.

[109] W. Qi, H. He, Y. Fu, M. Zhao, L. Qi, L. Hu, C. Liu and R. Li, 'Water-Dispersed Fluorescent Silicon Nanodots as Probes for Fluorometric Determination of Picric Acid *via* Energy Transfer,' *Microchim. Acta*, vol. 186, no. 1, p. 18, 2019, ISSN: 0026-3672. DOI: 10.1007/s00604-018-3135-5. [Online]. Available: http://link.springer.com/10.1007/s00604-018-3135-5.

[110] V. Srinivasan, M. Asha Jhonsi, M. Kathiresan and A. Kathiravan, 'Nanostructured Graphene Oxide Dots: Synthesis, Characterization, Photoinduced Electron Transfer Studies, and Detection of Explosives/Biomolecules,' *ACS Omega*, vol. 3, no. 8, pp. 9096–9104, 2018, ISSN: 24701343. DOI: 10.1021/acsomega.8b01180.

[111] H. Wang, C. Chen, Y. Liu, Y. Wu, Y. Yuan and Q. Zhou, 'A Highly Sensitive and Selective Chemosensor for 2,4, 6-Trinitrophenol Based on L-Cysteine-Coated Cadmium Sulfide Quantum Dots,' *Talanta*, vol. 198, no. November 2018, pp. 242–248, 2019, ISSN: 00399140. DOI: 10.1016/j.talanta.2019.02.016. [Online]. Available: https://doi.org/10.1016/j.talanta.2019.02.016.

[112] T. Alizadeh, F. Atashi and M. R. Ganjali, 'Molecularly Imprinted Polymer Nano-Sphere/Multi-Walled Carbon Nanotube Coated Glassy Carbon Electrode as an Ultra-Sensitive Voltammetric Sensor for Picomolar Level Determination of RDX,' *Talanta*, vol. 194, no. August 2018, pp. 415–421, 2019, ISSN: 00399140. DOI: 10.1016/j.talanta.2018.10.040. [Online]. Available: https://doi.org/10.1016/j.talanta.2018.10.040.

[113] J. Wang, S. Du, T. Onodera, R. Yatabe, M. Tanaka, M. Okochi and K. Toko, 'An SPR Sensor Chip Based on Peptide-Modified Single-Walled Carbon Nanotubes with Enhanced Sensitivity and Selectivity in the Detection of 2,4, 6-Trinitrotoluene Explosives,' *Sensors (Switzerland)*, vol. 18, no. 12, pp. 4–9, 2018, ISSN: 14248220. DOI: 10.3390/s18124461.

[114] A. Dettlaff, P. Jakóbczyk, M. Ficek, B. Wilk, M. Szala, J. Wojtas, T. Ossowski and R. Bogdanowicz, 'Electrochemical Determination of Nitroaromatic Explosives at Boron-Doped Diamond/Graphene Nanowall Electrodes: 2,4, 6-Trinitrotoluene and 2,4, 6-Trinitroanisole in Liquid Effluents,' *J. Hazard. Mater.*, vol. 387, no. November 2019, p. 121 672, 2020, ISSN: 18733336. DOI: 10.1016/j.jhazmat.2019.121672.

[Online]. Available: https://doi.org/10.1016/j.jhazmat.2019.121672.

[115] S. J. Patil, N. Duragkar and V. R. Rao, 'An Ultra-Sensitive Piezoresistive Polymer Nano-Composite Microcantilever Sensor Electronic Nose Platform for Explosive Vapor Detection,' *Sensors Actuators, B Chem.*, vol. 192, pp. 444–451, 2014, ISSN: 09254005. DOI: 10.1016/j.snb.2013.10.111.

[116] Q. Sun, Z. Wu, H. Duan and D. Jia, 'Detection of Triacetone Triperoxide (TATP) Precursors with an Array of Sensors Based on MoS 2 /RGO Composites,' *Sensors (Switzerland)*, vol. 19, no. 6, 2019, ISSN: 14248220. DOI: 10.3390/s19061281.

[117] Z. Li, H. Li, Z. Wu, M. Wang, J. Luo, H. Torun, P. Hu, C. Yang, M. Grundmann, X. Liu and Y. Fu, 'Advances in Designs and Mechanisms of Semiconducting Metal Oxide Nanostructures for High-Precision Gas Sensors Operated at Room Temperature,' *Mater. Horizons*, vol. 6, no. 3, pp. 470–506, 2019, ISSN: 20516355. DOI: 10.1039/c8mh01365a.

[118] A. Mirzaei, K. Janghorban, B. Hashemi and G. Neri, 'Metal-Core@metal Oxide-Shell Nanomaterials for Gas-Sensing Applications: A Review,' *J. Nanoparticle Res.*, vol. 17, no. 9, pp. 1–36, 2015, ISSN: 1572896X. DOI: 10.1007/s11051-015-3164-5.

[119] C. Lin, W. Xu, Q. Yao and X. Wang, *Nanotechnology on Toxic Gas Detection and Treatment*. Elsevier, Oxford, 2018, pp. 275–297, ISBN: 9780128144985. DOI: 10.1016/B978-0-12-814497-8.00009-6. [Online]. Available: http://dx.doi.org/10.1016/B978-0-12-814497-8.00009-6.

[120] H. Ji, W. Zeng and Y. Li, 'Gas Sensing Mechanisms of Metal Oxide Semiconductors: A Focus Review,' *Nanoscale*, vol. 11, no. 47, pp. 22 664–22 684, 2019, ISSN: 20403372. DOI: 10.1039/c9nr07699a.

[121] W. E. Asher, P. Colosimo, E. I. Thorsos and A. Yao, 'On Sensing Nitro-Group Containing Compounds Using Thin Planar Arrays of Titanium Dioxide Nanowires,' *IEEE Sens. J.*, vol. 18, no. 17, pp. 6927–6936, 2018, ISSN: 1530437X. DOI: 10.1109/JSEN.2018.2855110.

[122] Y. Cao, X. Zou, X. Wang, J. Qian, N. Bai and G. D. Li, 'Effective Detection of Trace Amount of Explosive Nitro-Compounds by ZnO Nanofibers with Hollow Structure,' *Sensors Actuators, B Chem.*, vol. 232, pp. 564–570, 2016, ISSN: 09254005. DOI: 10.1016/j.snb.2016.04.012. [Online]. Available: http://dx.doi.org/10.1016/j.snb.2016.04.012.

[123] B. Omijeh and A. Okemeka Machiavelli, 'Optimizing a Sensor to Detect Ammonium Nitrate Based IEDS in Vehicles Using Artificial Neural Networks,' *Am. J. Neural Networks Appl.*, vol. 5, no. 1, p. 1, 2019, ISSN: 2469-7400. DOI: 10.11648/j.ajnna.20190501.11.

[124] N. Ratchapakorn and Y. Ariyakul, 'Development of a Low-Cost Explosive Vapor Detector Using Metal Oxide Gas Sensors,' *ICSEC 2017 - 21st Int. Comput. Sci. Eng. Conf. 2017, Proceeding*, vol. 6, pp. 316–319, 2018. DOI: 10.1109/ICSEC.2017.8443830.

[125] S. James, B. Chishti, S. A. Ansari, O. Y. Alothman, H. Fouad, Z. A. Ansari and S. G. Ansari, 'Nanostructured Cuprous-Oxide-Based Screen-Printed Electrode for Electrochemical Sensing of Picric Acid,' *J. Electron. Mater.*, vol. 47, no. 12, pp. 7505–7513, 2018, ISSN: 03615235. DOI: 10.1007/s11664-018-6692-9.

[126] V. E. Bochenkov and G. B. Sergeev, 'Sensitivity, Selectivity, and Stability of Gas-Sensitive Metal-Oxide Nanostructures,' *Met. oxide nanostructures their Appl.*, vol. 3, pp. 31–52, 2010.

[127] A. Marchisio and J.-M. Tulliani, 'Semiconducting Metal Oxides Nanocomposites for Enhanced Detection of Explosive Vapors,' *Ceramics*, vol. 1, no. 1, pp. 98–119, 2018, ISSN: 2571-6131. DOI: 10.3390/ceramics1010009.

[128] J. Warmer, P. Wagner, M. J. Schöning and P. Kaul, 'Detection of Triacetone Triperoxide Using Temperature Cycled Metal-Oxide Semiconductor Gas Sensors,' *Phys. Status Solidi Appl. Mater. Sci.*, vol. 212, no. 6, pp. 1289–1298, 2015, ISSN: 18626319. DOI: 10.1002/pssa.201431882.

[129] F. Patolsky, R. Shacham, A. Lichtenstein, E. Havivi and H. Modiln, *Systems and Methods for Identifying Explosives*, Patent number WO 2014111944 A8, 24 July 2014.

[130] *Tracense - explosives detection*, (visited on 14-01-2019). [Online]. Available: http://www.tracense.com/?page{_}id=714.

[131] A. P. Alivisatos, 'Semiconductor Clusters, Nanocrystals, and Quantum Dots,' *Science (80-.).*, vol. 271, no. 5251, pp. 933–937, 1996, ISSN: 0036-8075. DOI: 10.1126/science.271.5251.933. [Online]. Available: https://www.sciencemag.org/lookup/doi/10.1126/science.271.5251.933.

[132] Z. M. Khan, S. Saifi, Shumaila, Z. Aslam, S. A. Khan and M. Zulfequar, 'A Facile One Step Hydrothermal Synthesis of Carbon Quantum Dots for Label -Free Fluorescence Sensing Approach to Detect Picric Acid in Aqueous Solution,' *J. Photochem. Photobiol. A Chem.*, vol. 388,

no. November 2019, 2020, ISSN: 10106030. DOI: 10.1016/j.jphotochem.2019.112201.

[133] M. Ganiga and J. Cyriac, 'Detection of PETN and RDX Using a FRET-Based Fluorescence Sensor System,' *Anal. Methods*, vol. 7, no. 13, pp. 5412–5418, 2015, ISSN: 17599679. DOI: 10.1039/c5ay00416k.

[134] K. F. Chou and A. M. Dennis, 'Förster Resonance Energy Transfer between Quantum Dot Donors and Quantum Dot Acceptors,' *Sensors (Switzerland)*, vol. 15, no. 6, pp. 13 288–13 325, 2015, ISSN: 14248220. DOI: 10.3390/s150613288.

[135] S. Wang, N. Li, W. Pan and B. Tang, 'Advances in Functional Fluorescent and Luminescent Probes for Imaging Intracellular Small-Molecule Reactive Species,' *TrAC - Trends Anal. Chem.*, vol. 39, pp. 3–37, 2012, ISSN: 01659936. DOI: 10.1016/j.trac.2012.07.010.

[136] *European Civil Aviation Conference*, https://www.ecac-ceac.org/cep, (visited on 14-08-2018). [Online]. Available: https://www.ecac-ceac.org/cep.

[137] T. Keller, A. Keller, E. Tutsch-Bauer and F. Monticelli, 'Application of Ion Mobility Spectrometry in Cases of Forensic Interest,' *Forensic Sci. Int.*, vol. 161, no. 2-3, pp. 130–140, 2006, ISSN: 03790738. DOI: 10.1016/j.forsciint.2006.03.032.

[138] J. Puton and J. Namieśnik, 'Ion Mobility Spectrometry: Current Status and Application for Chemical Warfare Agents Detection,' *TrAC - Trends Anal. Chem.*, vol. 85, pp. 10–20, 2016, ISSN: 18793142. DOI: 10.1016/j.trac.2016.06.002.

[139] *Bruker DE-tector*, (visited on 24-01-2019). [Online]. Available: https://www.bruker.com/products/cbrne-detection/ims/detector/overview.html.

[140] *L3 B220^{TM} Desktop Trace Detector*, (visited on 24-01-2019). [Online]. Available: http://www.sds.l3t.com/etd/B220-desktop-ETD.htm.

[141] *Smiths Detection Ionscan 600*, (visited on 24-01-2019). [Online]. Available: https://www.smithsdetection.com/products/ionscan-600/.

[142] *Thermo Fisher Scientific EGIS Defender*, (visited on 24-01-2019). [Online]. Available: https://assets.thermofisher.com/TFS-Assets/LSG/Specification-Sheets/D17430~.pdf.

[143] J. Yinon, J. E. Mcclellan and R. A. Yost, 'Electrospray Ionization Tandem Mass Spectrometry Collision-induced Dissociation Study of Explosives in an Ion Trap Mass Spectrometer,' *Oct. Rapid Commun. Mass Spectrom*, vol. 11, pp. 1961–1970, 1997. DOI: 10.1002/(SICI)1097-0231(199712)11:18<1961::AID-RCM99>3.0.CO;2-K.

[144] S.-S. Choi and C. E. Son, 'Analytical Method for the Estimation of Transfer and Detection Efficiencies of Solid State Explosives Using Ion Mobility Spectrometry and Smear Matrix,' *Anal. Methods*, vol. 9, no. 17, pp. 2505–2510, 2017, ISSN: 1759-9660. DOI: 10.1039/C7AY00529F.

[145] W. Chouyyok, J. T. Bays, A. A. Gerasimenko, A. D. Cinson, R. G. Ewing, D. A. Atkinson and R. S. Addleman, 'Improved Explosive Collection and Detection with Rationally Assembled Surface Sampling

Materials,' *RSC Adv.*, vol. 6, no. 97, pp. 94 476–94 485, 2016, ISSN: 2046-2069. DOI: 10.1039/C6RA20157A.

[146] J. Kozole, J. R. Stairs, I. Cho, J. D. Harper, S. R. Lukow, R. T. Lareau, R. Debono and F. Kuja, 'Interfacing an Ion Mobility Spectrometry Based Explosive Trace Detector to a Triple Quadrupole Mass Spectrometer,' *Anal. Chem.*, vol. 83, no. 22, pp. 8596–8603, 2011, ISSN: 00032700. DOI: 10.1021/ac201999a.

[147] R. G. Ewing, M. J. Waltman and D. A. Atkinson, 'Characterization of Triacetone Triperoxide by Ion Mobility Spectrometry and Mass Spectrometry following Atmospheric Pressure Chemical Ionization,' *Anal. Chem.*, vol. 83, no. 12, pp. 4838–4844, 2011, ISSN: 00032700. DOI: 10.1021/ac200466v.

[148] C. K. Hilton, C. A. Krueger, A. J. Midey, M. Osgood, J. Wu and C. Wu, 'Improved Analysis of Explosives Samples with Electrospray Ionization-High Resolution Ion Mobility Spectrometry (ESI-HRIMS),' *Int. J. Mass Spectrom.*, vol. 298, no. 1-3, pp. 64–71, 2010, ISSN: 13873806. DOI: 10.1016/j.ijms.2010.08.011.

[149] *Excellims ESI-IMS GA-2100*, (visited on 08-05-2019). [Online]. Available: https://pdfs.semanticscholar.org/802b/ac96dbe15fb2e5b0e2e18060c82011c pdf.

[150] A. E. Akmalov, A. A. Chistyakov, G. E. Kotkovskii, I. L. Martynov and E. M. Spitsin, 'Laser Ion Mobility Spectrometry in the Detection of Ultra-Low Quantities of Explosives,' *Eur. J. Mass Spectrom.*, vol. 23, no. 4, pp. 140–145, 2017, ISSN: 17516838. DOI: 10.1177/1469066717721696.

[151] A. R. Jafari Horestani, M. T. Jafari, E. Jazan and M. Mossaddegh, 'Effect of Halide Ions on Secondary Electrospray Ionization-Ion Mobility Spectrometry for the Determination of TNT Extracted by Dispersive Liquid-Liquid Microextraction,' *Int. J. Mass Spectrom.*, vol. 433, pp. 19–24, 2018, ISSN: 13873806. DOI: 10.1016/j.ijms.2018.08.006. [Online]. Available: https://doi.org/10.1016/j.ijms.2018.08.006.

[152] H. Shahraki, M. Tabrizchi and H. Farrokhpor, 'Detection of Explosives Using Negative Ion Mobility Spectrometry in Air Based on Dopant-Assisted Thermal Ionization,' *J. Hazard. Mater.*, vol. 357, no. December 2017, pp. 1–9, 2018, ISSN: 18733336. DOI: 10.1016/j.jhazmat.2018.05.054. [Online]. Available: https://doi.org/10.1016/j.jhazmat.2018.05.054.

[153] U. Chiluwal, G. Lee, M. Y. Rajapakse, T. Willy, S. Lukow, H. Schmidt and G. A. Eiceman, 'Tandem Ion Mobility Spectrometry at Ambient Pressure and Field Decomposition of Mobility Selected Ions of Explosives and Interferences,' *Analyst*, 2019, ISSN: 0003-2654. DOI: 10.1039/C8AN02041H. [Online]. Available: http://xlink.rsc.org/?DOI=C8AN02041H.

[154] E. Bunert, T. Reinecke, A. T. Kirk, A. Bohnhorst and S. Zimmermann, 'Ion Mobility Spectrometer with Orthogonal X-Ray Source for Increased Sensitivity,' *Talanta*, vol. 185, no. February, pp. 537–541, 2018, ISSN: 00399140. DOI: 10.1016/j.talanta.2018.04.035. [Online]. Available: https://doi.org/10.1016/j.talanta.2018.04.035.

[155] M. Amo-González, S. Pérez, R. Delgado, G. Arranz and I. Carnicero, 'Tandem Ion Mobility Spectrometry for the Detection of Traces of

Explosives in Cargo at Concentrations of Parts per Quadrillion,' *Anal. Chem.*, vol. 91, no. 21, pp. 14 009–14 018, 2019, ISSN: 15206882. DOI: 10.1021/acs.analchem.9b03589.

[156] G. A. Eiceman, E. G. Nazarov and J. A. Stone, 'Chemical standards in ion mobility spectrometry,' *Anal. Chim. Acta*, vol. 493, no. 2, pp. 185–194, 2003, ISSN: 00032670. DOI: 10.1016/S0003-2670(03)00762-1.

[157] M. Tabrizchi and F. Rouholahnejad, 'Comparing the effect of pressure and temperature on ion mobilities,' *J. Phys. D. Appl. Phys.*, vol. 38, no. 6, pp. 857–862, 2005, ISSN: 00223727. DOI: 10.1088/0022-3727/38/6/012.

[158] A. Namera, M. Kawamura, A. Nakamoto, T. Saito and M. Nagao, 'Comprehensive Review of the Detection Methods for Synthetic Cannabinoids and Cathinones,' *Forensic Toxicol.*, vol. 33, no. 2, pp. 175–194, 2015, ISSN: 18608973. DOI: 10.1007/s11419-015-0270-0.

[159] A. Roda, E. Michelini, M. Zangheri, M. Di Fusco, D. Calabria and P. Simoni, 'Smartphone-Based Biosensors: A Critical Review and Perspectives,' *TrAC - Trends Anal. Chem.*, vol. 79, pp. 317–325, 2016, ISSN: 18793142. DOI: 10.1016/j.trac.2015.10.019. [Online]. Available: http://dx.doi.org/10.1016/j.trac.2015.10.019.

[160] W. R. de Araujo, T. M. Cardoso, R. G. da Rocha, M. H. Santana, R. A. Muñoz, E. M. Richter, T. R. Paixão and W. K. Coltro, 'Portable Analytical Platforms for Forensic Chemistry: A Review,' *Anal. Chim. Acta*, vol. 1034, pp. 1–21, 2018, ISSN: 18734324. DOI: 10.1016/j.aca.2018.06.014.

[161] M. S. Meaney and V. L. McGuffin, 'Luminescence-Based Methods for Sensing and Detection of Explosives,' *Anal. Bioanal. Chem.*, vol. 391, no. 7, pp. 2557–2576, 2008, ISSN: 1618-2642. DOI: 10.1007/s00216-008-2194-6.

[162] *Morphix TraceX*, (visited on 23-01-2019). [Online]. Available: https://www.morphtec.com/tracex/.

[163] *DetectaChem*, (visited on 23-01-2019). [Online]. Available: https://www.detectachem.com/worldwide/seekere.

[164] *BBI Detection*, (visited on 23-01-2019). [Online]. Available: http://www.bbidetection.com/distributor-hub/core-text-s2-threat-detk-letkv1draft/.

[165] X. Sun, Y. Wang and Y. Lei, 'Fluorescence Based Explosive Detection: From Mechanisms to Sensory Materials,' *Chem. Soc. Rev.*, vol. 44, no. 22, pp. 8019–8061, 2015, ISSN: 0306-0012. DOI: 10.1039/C5CS00496A.

[166] C. Wang, L. Tian, W. Zhu, S. Wang, P. Wang, Y. Liang, W. Zhang, H. Zhao and G. Li, 'Dye@bio-MOF-1 Composite as a Dual-Emitting Platform for Enhanced Detection of a Wide Range of Explosive Molecules,' *ACS Appl. Mater. Interfaces*, vol. 9, no. 23, pp. 20 076–20 085, 2017, ISSN: 19448252. DOI: 10.1021/acsami.7b04172.

[167] H. R. Fu, L. B. Yan, N. T. Wu, L. F. Ma and S. Q. Zang, 'Dual-Emission MOF Dye Sensor for Ratiometric Fluorescence Recognition of RDX and Detection of a Broad Class of Nitro-Compounds,' *J. Mater. Chem. A*, vol. 6, no. 19, pp. 9183–9191, 2018, ISSN: 20507496. DOI: 10.1039/c8ta02857e.

[168] M. Jurcic, W. J. Peveler, C. N. Savory, D.-K. Bučar, A. J. Kenyon, D. O. Scanlon and I. P. Parkin, 'Sensing and Discrimination of Explosives at Variable Concentrations with a Large-Pore MOF as Part of a Luminescent Array,' *ACS Appl. Mater. Interfaces*, vol. 11, no. 12, pp. 11 618–11 626, 2019, ISSN: 1944-8244. DOI: 10.1021/acsami.8b22385. [Online]. Available: http://pubs.acs.org/doi/10.1021/acsami.8b22385.

[169] Q. Zhou and T. M. Swager, 'Fluorescent Chemosensors Based on Energy Migration in Conjugated Polymers: The Molecular Wire Approach to Increased Sensitivity,' *J. Am. Chem. Soc.*, vol. 117, no. 50, pp. 12 593–12 602, 1995, ISSN: 15205126. DOI: 10.1021/ja00155a023.

[170] J. S. Yang and T. M. Swager, 'Porous Shape Persistent Fluorescent Polymer Films: An Approach to TNT Sensory Materials,' *J. Am. Chem. Soc.*, vol. 120, no. 21, pp. 5321–5322, 1998, ISSN: 00027863. DOI: 10.1021/ja9742996.

[171] S. W. Thomas, G. D. Joly and T. M. Swager, 'Chemical Sensors Based on Amplifying Fluorescent Conjugated Polymers,' *Chem. Rev.*, vol. 107, no. 4, pp. 1339–1386, 2007, ISSN: 00092665. DOI: 10.1021/cr0501339.

[172] *FLIR - Fido X2*, (visited on 29-04-2019). [Online]. Available: https://www.flir.co.uk/products/fido-x2/.

[173] C. A. Aker, C. J. Cumming, M. E. Fisher, M. J. Fox, M. La Grone, D. K. Reust, M. G. Rockley and E. S. Towers, *Vapor Sensing Instrument for Ultra Trace Chemical Detection*, Patent number US006558626B1, 6 May 2003.

[174] A. Arshad, H. Wang, X. Bai, R. Jiang, S. Xu and L. Wang, 'Colorimetric Paper Sensor for Sensitive Detection of Explosive Nitroaromatics Based on Au@Ag Nanoparticles,' *Spectrochim. Acta - Part A Mol. Biomol. Spectrosc.*, vol. 206, pp. 16–22, 2019, ISSN: 13861425. DOI: 10.1016/j.saa.2018.07.095. [Online]. Available: https://doi.org/10.1016/j.saa.2018.07.095.

[175] S. M. Tawfik, M. Sharipov, S. Kakhkhorov, M. R. Elmasry and Y. I. Lee, 'Multiple Emitting Amphiphilic Conjugated Polythiophenes-Coated CdTe QDs for Picogram Detection of Trinitrophenol Explosive and Application Using Chitosan Film and Paper-Based Sensor Coupled with Smartphone,' *Adv. Sci.*, vol. 6, no. 2, 2019, ISSN: 21983844. DOI: 10.1002/advs.201801467.

[176] M. López-López and C. García-Ruiz, 'Infrared and Raman Spectroscopy Techniques Applied to Identification of Explosives,' *TrAC - Trends Anal. Chem.*, vol. 54, pp. 36–44, 2014, ISSN: 18793142. DOI: 10.1016/j.trac.2013.10.011.

[177] Z. Chen, C. Xiao, W. Xiao, M. Qin and X. Liu, 'A Review on Several Key Problems of Standoff Trace Explosives Detection by Optical-Related Technology,' in *Int. Conf. Optoelectron. Microelectron. Technol. Appl.*, vol. 10244, 2017, 102440H, ISBN: 9781510609891. DOI: 10.1117/12.2258372.

[178] J. Guicheteau and R. Hopkins, 'Applications of Spatially Offset Raman Spectroscopy to Defense and Security,' *Proc. SPIE.*, vol. 9824, pp. 76 –85, 2016. DOI: 10.1117/12.2229157. [Online]. Available: https://doi.org/10.1117/12.2229157.

[179] Q. Liu and X. Zhang, 'Study and Application of New Raman Spectroscopy,' *Proc. SPIE.*, vol. 10255, pp. 1–8, 2016. DOI: 10.1117/12.2267516.

[180] F. Zapata, M. López-López and C. García-Ruiz, 'Detection and Identification of Explosives by Surface Enhanced Raman Scattering,' *Appl. Spectrosc. Rev.*, vol. 51, no. 3, pp. 207–242, 2016, ISSN: 1520569X. DOI: 10.1080/05704928.2015.1118637.

[181] A. Hakonen, P. O. Andersson, M. Stenbæk Schmidt, T. Rindzevicius and M. Käll, 'Explosive and Chemical Threat Detection by Surface-Enhanced Raman Scattering: A Review,' *Anal. Chim. Acta*, vol. 893, pp. 1–13, 2015, ISSN: 00032670. DOI: 10.1016/j.aca.2015.04.010. [Online]. Available: https://linkinghub.elsevier.com/retrieve/pii/S0003267015004754.

[182] R. Gillibert, J. Q. Huang, Y. Zhang, W. L. Fu and M. Lamy de la Chapelle, 'Explosive Detection by Surface Enhanced Raman Scattering,' *TrAC - Trends Anal. Chem.*, vol. 105, pp. 166–172, 2018, ISSN: 18793142. DOI: 10.1016/j.trac.2018.03.018.

[183] *Smiths Detection ACE-ID*, (visited on 24-01-2019). [Online]. Available: https://www.smithsdetection.com/products/ace-id/.

[184] *Nuchtech - RT1003*, (visited on 23-01-2019). [Online]. Available: http://www.nuctechwarsaw.com/SitePages/ThDetailPage.aspx?nk=PAS{\&}k=EIFBGB.

[185] *Thermo Fisher Scientific Gemini Analyzer*, (visited on 24-01-2019). [Online]. Available: https://www.thermofisher.com/order/catalog/product/GEMINI#/GEMINI.

[186] *Agilent Insight100M and Insight200M*, (visited on 24-01-2019). [Online]. Available: https://www.agilent.com/en/products/raman-spectroscopy/raman-spectroscopy-systems/aviation-security.

[187] *Hamamatsu - SERS Detection Module*, (visited on 19-04-2019). [Online]. Available: https://www.hamamatsu.com/jp/en/product/type/C13560/index.html.

[188] C. L. Haynes and R. P. Van Duyne, ‘ Plasmon-Sampled Surface-Enhanced Raman Excitation Spectroscopy,’ *J. Phys. Chem. B*, vol. 107, no. 30, pp. 7426–7433, 2003, ISSN: 1520-6106. DOI: 10.1021/jp027749b.

[189] A. D. McFarland, M. A. Young, J. A. Dieringer and R. P. V. Duyne, ‘Wavelength-Scanned Surface-Enhanced Raman Excitation Spectroscopy,’ *J. Phys. Chem. C*, vol. 109, pp. 11 279–11 285, 2005, ISSN: 19327447. [Online]. Available: https://pubs.acs.org/doi/pdf/10.1021/jp050508u.

[190] B. Samransuksamer, M. Horprathum, T. Jutarosaga, A. Kopwitthaya, S. Limwichean, N. Nuntawong, C. Chananonnawathorn, V. Patthanasettakul, P. Muthitamongkol, A. Treetong, A. Klamchuen, A. Leelapojanaporn, C. Thanachayanont and P. Eiamchai, ‘Facile Method for Decorations of Au Nanoparticles on TiO2 Nanorod Arrays toward High-Performance Recyclable SERS Substrates,’ *Sensors Actuators, B Chem.*, vol. 277, no. September, pp. 102–113, 2018, ISSN: 09254005. DOI: 10.1016/j.snb.2018.08.136. [Online]. Available: https://doi.org/10.1016/j.snb.2018.08.136.

[191] H. Zhou, Z. Zhang, C. Jiang, G. Guan, K. Zhang, Q. Mei, R. Liu and S. Wang, 'Trinitrotoluene Explosive Lights Up Ultrahigh Raman Scattering of Nonresonant Molecule on a Top-Closed Silver Nanotube Array,' *Anal. Chem.*, vol. 83, no. 18, pp. 6913–6917, 2011, ISSN: 00032700. DOI: 10.1021/ac201407z.

[192] V. S. Vendamani, S. V. Nageswara Rao, S. Venugopal Rao, D. Kanjilal and A. P. Pathak, 'Three-Dimensional Hybrid Silicon Nanostructures for Surface Enhanced Raman Spectroscopy Based Molecular Detection,' *J. Appl. Phys.*, vol. 123, no. 1, 2018, ISSN: 10897550. DOI: 10.1063/1.5000994.

[193] J. Y. Xu, J. Wang, L. T. Kong, G. C. Zheng, Z. Guo and J. H. Liu, 'SERS Detection of Explosive Agent by Macrocyclic Compound Functionalized Triangular Gold Nanoprisms,' *J. Raman Spectrosc.*, vol. 42, no. 9, pp. 1728–1735, 2011, ISSN: 03770486. DOI: 10.1002/jrs.2932.

[194] T. Liyanage, A. Rael, S. Shaffer, S. Zaidi, J. V. Goodpaster and R. Sardar, 'Fabrication of a Self-Assembled and Flexible SERS Nanosensor for Explosive Detection at Parts-per-Quadrillion Levels from Fingerprints,' *Analyst*, vol. 143, no. 9, pp. 2012–2022, 2018, ISSN: 13645528. DOI: 10.1039/c8an00008e.

[195] X. Liu, L. Zhao, H. Shen, H. Xu and L. Lu, 'Ordered Gold Nanoparticle Arrays as Surface-Enhanced Raman Spectroscopy Substrates for Label-Free Detection of Nitroexplosives,' *Talanta*, vol. 83, no. 3, pp. 1023–1029, 2011, ISSN: 00399140. DOI: 10.1016/j.talanta.2010.11.015.

[196] S. Ben-Jaber, W. J. Peveler, R. Quesada-Cabrera, C. W. Sol, I. Papakonstantinou and I. P. Parkin, 'Sensitive and Specific Detection of Explos-

ives in Solution and Vapour by Surface-Enhanced Raman Spectroscopy on Silver Nanocubes,' *Nanoscale*, vol. 9, no. 42, pp. 16 459–16 466, 2017, ISSN: 20403372. DOI: 10.1039/c7nr05057g.

[197] H. Wackerbarth, C. Salb, L. Gundrum, M. Niederkrüger, K. Christou, V. Beushausen and W. Viöl, 'Detection of Explosives Based on Surface-Enhanced Raman Spectroscopy,' *Appl. Opt.*, vol. 49, no. 23, p. 4362, 2010, ISSN: 0003-6935. DOI: 10.1364/AO.49.004362.

[198] E. L. Holthoff, D. N. Stratis-Cullum and M. E. Hankus, 'A Nanosensor for TNT Detection Based on Molecularly Imprinted Polymers and Surface Enhanced Raman Scattering,' *Sensors*, vol. 11, no. 3, pp. 2700–2714, 2011, ISSN: 14248220. DOI: 10.3390/s110302700.

[199] Y. Xu, Z. Ye, C. Li, H. McCabe, J. Kelly and S. E. Bell, 'Pressing Solids Directly Into Sheets of Plasmonic Nanojunctions Enables Solvent-Free Surface-Enhanced Raman Spectroscopy,' *Appl. Mater. Today*, vol. 13, pp. 352–358, 2018, ISSN: 23529407. DOI: 10.1016/j.apmt.2018.09.014. [Online]. Available: https://doi.org/10.1016/j.apmt.2018.09.014.

[200] F. Gao, W. F. Liu, Z. H. Meng, P. F. Su, Z. X. Li and M. H. Wang, 'A Rapid and Sensitive Quantitative Analysis Method for TNT Using Raman Spectroscopy,' *Propellants, Explos. Pyrotech.*, vol. 44, pp. 1–9, 2019, ISSN: 07213115. DOI: 10.1002/prep.201800281. [Online]. Available: http://doi.wiley.com/10.1002/prep.201800281.

[201] T. K. Naqvi, A. K. Srivastava, M. M. Kulkarni, A. M. Siddiqui and P. K. Dwivedi, 'Silver Nanoparticles Decorated Reduced Graphene Oxide (rGO) SERS Sensor for Multiple Analytes,' *Appl. Surf. Sci.*, vol. 478, no. November 2018, pp. 887–895, 2019, ISSN: 01694332.

DOI: 10.1016/j.apsusc.2019.02.026. [Online]. Available: https://doi.org/10.1016/j.apsusc.2019.02.026.

[202] M. S. Satya Bharati, B. Chandu and S. V. Rao, 'Explosives Sensing Using Ag-Cu Alloy Nanoparticles Synthesized by Femtosecond Laser Ablation and Irradiation,' *RSC Adv.*, vol. 9, no. 3, pp. 1517–1525, 2019, ISSN: 20462069. DOI: 10.1039/C8RA08462A.

[203] M. Liu and W. Chen, 'Graphene Nanosheets-Supported Ag Nanoparticles for Ultrasensitive Detection of TNT by Surface-Enhanced Raman Spectroscopy,' *Biosens. Bioelectron.*, vol. 46, pp. 68–73, 2013, ISSN: 09565663. DOI: 10.1016/j.bios.2013.01.073.

[204] N. Idros, M. Y. Ho, M. Pivnenko, M. M. Qasim, H. Xu, Z. Gu and D. Chu, 'Colorimetric-Based Detection of TNT Explosives Using Functionalized Silica Nanoparticles,' *Sensors (Switzerland)*, vol. 15, no. 6, pp. 12 891–12 905, 2015, ISSN: 14248220. DOI: 10.3390/s150612891.

[205] N. Ular, A. Üzer, S. Durmazel, E. Erçağ and R. Apak, 'Diaminocyclohexane-Functionalized/Thioglycolic Acid-Modified Gold Nanoparticle-Based Colorimetric Sensing of Trinitrotoluene and Tetryl,' *ACS Sensors*, vol. 3, no. 11, pp. 2335–2342, 2018, ISSN: 23793694. DOI: 10.1021/acssensors.8b00709.

[206] L. Yang, L. Ma, G. Chen, J. Liu and Z. Q. Tian, 'Ultrasensitive SERS Detection of TNT by Imprinting Molecular Recognition Using a New Type of Stable Substrate,' *Chem. - A Eur. J.*, vol. 16, no. 42, pp. 12 683–12 693, 2010, ISSN: 09476539. DOI: 10.1002/chem.201001053.

[207] B. D. Piorek, S. J. Lee, M. Moskovits and C. D. Meinhart, 'Free-Surface Microfluidics/Surface-Enhanced Raman Spectroscopy for Real-

Time Trace Vapor Detection of Explosives,' *Anal. Chem.*, vol. 84, no. 22, pp. 9700–9705, 2012, ISSN: 00032700. DOI: 10.1021/ac302497y.

[208] P. Gupta, J. Luan, Z. Wang, S. Cao, S. H. Bae, R. R. Naik and S. Singamaneni, 'On-Demand Electromagnetic Hotspot Generation in Surface-Enhanced Raman Scattering Substrates *via* "Add-On" Plasmonic Patch,' *ACS Appl. Mater. Interfaces*, vol. 11, no. 41, pp. 37 939–37 946, 2019, ISSN: 19448252. DOI: 10.1021/acsami.9b12402.

[209] Y. e. Shi, W. Wang and J. Zhan, 'A Positively Charged Silver Nanowire Membrane for Rapid On-Site Swabbing Extraction and Detection of Trace Inorganic Explosives Using a Portable Raman Spectrometer,' *Nano Res.*, vol. 9, no. 8, pp. 2487–2497, 2016, ISSN: 19980000. DOI: 10.1007/s12274-016-1135-5.

[210] J. Liu, T. Si and Z. Zhang, 'Mussel-Inspired Immobilization of Silver Nanoparticles toward Sponge for Rapid Swabbing Extraction and SERS Detection of Trace Inorganic Explosives,' *Talanta*, vol. 204, no. May, pp. 189–197, 2019, ISSN: 00399140. DOI: 10.1016/j.talanta.2019.05.110. [Online]. Available: https://doi.org/10.1016/j.talanta.2019.05.110.

[211] I. Alessandri, 'Enhancing Raman Scattering without Plasmons: Unprecedented Sensitivity Achieved by TiO2 Shell-Based Resonators,' *J. Am. Chem. Soc.*, vol. 135, no. 15, pp. 5541–5544, 2013, ISSN: 00027863. DOI: 10.1021/ja401666p.

[212] J. R. Lombardi and R. L. Birke, 'Theory of Surface-Enhanced Raman Scattering in Semiconductors,' *J. Phys. Chem. C*, vol. 118, no. 20, pp. 11 120–11 130, 2014, ISSN: 19327455. DOI: 10.1021/jp5020675.

[213] U. P. Shaik, S. Hamad, M. A. Mohiddon, V. R. Soma and M. Ghanashyam Krishna, 'Morphologically Manipulated Ag/ZnO Nanostructures as Surface Enhanced Raman Scattering Probes for Explosives Detection,' *J. Appl. Phys.*, vol. 119, no. 9, 2016, ISSN: 10897550. DOI: 10.1063/1.4943034.

[214] P. Garg, Bharti, R. K. Soni and R. Raman, 'Graphene Oxide-Silver Nanocomposite SERS Substrate for Sensitive Detection of Nitro Explosives,' *J. Mater. Sci. Mater. Electron.*, no. 0123456789, 2019, ISSN: 1573482X. DOI: 10.1007/s10854-019-02621-1. [Online]. Available: https://doi.org/10.1007/s10854-019-02621-1.

[215] R. Kanchanapally, S. S. Sinha, Z. Fan, M. Dubey, E. Zakar and P. C. Ray, 'Graphene Oxide-Gold Nanocage Hybrid Platform for Trace Level Identification of Nitro Explosives Using a Raman Fingerprint,' *J. Phys. Chem. C*, vol. 118, no. 13, pp. 7070–7075, 2014, ISSN: 19327447. DOI: 10.1021/jp5015548.

[216] E. De La Cruz-Montoya, J. I. Jeréz, M. Balaguera-Gelves, T. Luna-Pineda, M. E. Castro and S. P. Hernández-Rivera, 'Enhanced Raman Spectroscopy of 2,4, 6-TNT in Anatase and Rutile Titania Nanocrystals,' no. May 2006, p. 62030X, 2006, ISSN: 0277786X. DOI: 10.1117/12.666129. [Online]. Available: http://proceedings.spiedigitallibrary.org/proceeding.aspx?doi=10.1117/12.666129.

[217] P. Dharmalingam, K. Venkatakrishnan and B. Tan, 'An Atomic-Defect Enhanced Raman Scattering (DERS)quantum Probe for Molecular Level Detection - Breaking the SERS Barrier,' *Appl. Mater. Today*, vol. 16, pp. 28–41, 2019, ISSN: 23529407. DOI: 10.1016/j.apmt.

2019.04.016. [Online]. Available: https://doi.org/10.1016/j.apmt.2019.04.016.

[218] S. Ben-Jaber, W. J. Peveler, R. Quesada-Cabrera, E. Cortés, C. Sotelo-Vazquez, N. Abdul-Karim, S. A. Maier and I. P. Parkin, 'Photo-Induced Enhanced Raman Spectroscopy for Universal Ultra-Trace Detection of Explosives, Pollutants and Biomolecules,' *Nat. Commun.*, vol. 7, no. May, pp. 1–6, 2016, ISSN: 20411723. DOI: 10.1038/ncomms12189.

[219] D. Glass, E. Cortés, S. Ben-Jaber, T. Brick, W. J. Peveler, C. S. Blackman, C. R. Howle, R. Quesada-Cabrera, I. P. Parkin and S. A. Maier, 'Dynamics of Photo-Induced Surface Oxygen Vacancies in Metal-Oxide Semiconductors Studied Under Ambient Conditions,' *Adv. Sci.*, vol. 6, no. 22, 2019, ISSN: 21983844. DOI: 10.1002/advs.201901841.

[220] S. Botti, L. Cantarini and A. Palucci, 'Surface-Enhanced Raman Spectroscopy for Trace-Level Detection of Explosives,' *J. Raman Spectrosc.*, vol. 41, no. 8, pp. 866–869, 2010, ISSN: 03770486. DOI: 10.1002/jrs.2649.

[221] S. Botti, M. Carpanese, L. Cantarini, G. Giubileo, V. Lazic, S. Jovicevic, A. Palucci and A. Puiu, 'Trace Detection of Explosive Compounds by Different Laser-Based Techniques at the ENEA Laboratories,' no. May 2010, 76650O, 2010, ISSN: 0277786X. DOI: 10.1117/12.850722.

[222] M. E. Farrell, E. L. Holthoff and P. M. Pellegrino, 'Surface-Enhanced Raman Scattering Detection of Ammonium Nitrate Samples Fabricated Using Drop-on-Demand Inkjet Technology,' *Appl. Spectrosc.*, vol. 68, no. 3, pp. 287–296, 2014, ISSN: 00037028. DOI: 10.1366/13-07035.

[223] G. Barbillon, T. Noblet and C. Humbert, 'Highly crystalline ZnO film decorated with gold nanospheres for PIERS chemical sensing,' *Phys. Chem. Chem. Phys.*, vol. 22, no. 37, pp. 21 000–21 004, 2020, ISSN: 14639076. DOI: 10.1039/d0cp03902k.

[224] R. M. Al-Shammari, M. A. Baghban, N. Al-Attar, A. Gowen, K. Gallo, J. H. Rice and B. J. Rodriguez, 'Photoinduced Enhanced Raman from Lithium Niobate on Insulator Template,' *ACS Appl. Mater. Interfaces*, vol. 10, no. 36, pp. 30 871–30 878, 2018, ISSN: 19448252. DOI: 10.1021/acsami.8b10076.

[225] Z. Y. Ke, C. J. Tsai, P. H. Liao and K. V. Kong, 'Photoinduced Enhanced Raman Probe for Use in Highly Specific and Sensitive Imaging for Tyrosine Dimerization in Inflammatory Cells,' *J. Phys. Chem. Lett.*, vol. 11, no. 17, pp. 7443–7448, 2020, ISSN: 19487185. DOI: 10.1021/acs.jpclett.0c01938.

[226] K. Abid, N. H. Belkhir, S. B. Jaber, R. Zribi, M. G. Donato, G. Di Marco, P. G. Gucciardi, G. Neri and R. Maâlej, 'Photoinduced Enhanced Raman Spectroscopy with Hybrid Au@WS2Nanosheets,' *J. Phys. Chem. C*, vol. 124, no. 37, pp. 20 350–20 358, 2020, ISSN: 19327455. DOI: 10.1021/acs.jpcc.0c04664.

[227] T. Man, W. Lai, M. Xiao, X. Wang, A. R. Chandrasekaran, H. Pei and L. Li, 'A versatile biomolecular detection platform based on photo-induced enhanced Raman spectroscopy,' *Biosens. Bioelectron.*, vol. 147, no. October 2019, 2020, ISSN: 18734235. DOI: 10.1016/j.bios.2019.111742.

[228] L. Zhou, J. Zhou, W. Lai, X. Yang, J. Meng, L. Su, C. Gu, T. Jiang, E. Y. B. Pun, L. Shao, L. Petti, X. W. Sun, Z. Jia, Q. Li, J. Han and

P. Mormile, 'Irreversible accumulated SERS behavior of the molecule-linked silver and silver-doped titanium dioxide hybrid system,' *Nat. Commun.*, vol. 11, no. 1, pp. 1–10, 2020, ISSN: 20411723. DOI: 10.1038/s41467-020-15484-6. [Online]. Available: http://dx.doi.org/10.1038/s41467-020-15484-6.

[229] B. Xiao, G. N. Rutherford, A. P. Sharma, S. K. Pradhan, C. E. Bonner and M. J. Bahoura, 'Surface Modification and Charge Injection in a Nanocomposite Of Metal Nanoparticles and Semiconductor Oxide Nanostructures,' *Sci. Rep.*, vol. 10, no. 1, pp. 1–7, 2020, ISSN: 20452322. DOI: 10.1038/s41598-020-66551-3.

[230] A. Fularz, S. Almohammed and J. H. Rice, 'Oxygen Incorporation-Induced SERS Enhancement in Silver Nanoparticle-Decorated ZnO Nanowires,' *ACS Appl. Nano Mater.*, vol. 3, no. 2, pp. 1666–1673, 2020, ISSN: 25740970. DOI: 10.1021/acsanm.9b02395.

[231] L. Panariello, K. Chuen To, Z. Khan, G. Wu, G. Gkogkos, S. Damilos, I. P. Parkin and A. Gavriilidis, 'Kinetics-based design of a flow platform for highly reproducible on demand synthesis of gold nanoparticles with controlled size between 50 and 150 nm and their application in SERS and PIERS sensing,' *Chem. Eng. J.*, vol. 423, no. November 2020, p. 129 069, 2021, ISSN: 13858947. DOI: 10.1016/j.cej.2021.129069. [Online]. Available: https://doi.org/10.1016/j.cej.2021.129069.

[232] S. Almohammed, F. Zhang, B. J. Rodriguez and J. H. Rice, 'Photo-induced surface-enhanced Raman spectroscopy from a diphenylalanine peptide nanotube-metal nanoparticle template,' *Sci. Rep.*, vol. 8, no. 1,

pp. 41–44, 2018, ISSN: 20452322. DOI: 10.1038/s41598-018-22269-x.

[233] M. Zhang, T. Chen, Y. Liu, J. Zhu, J. Liu and Y. Wu, 'Three-Dimensional TiO 2-Ag Nanopore Arrays for Powerful Photoinduced Enhanced Raman Spectroscopy (PIERS) and Versatile Detection of Toxic Organics,' *ChemNanoMat*, vol. 5, no. 1, pp. 55–60, 2019, ISSN: 2199692X. DOI: 10.1002/cnma.201800389. [Online]. Available: http://doi.wiley.com/10.1002/cnma.201800389.

[234] M. Zhang, H. Sun, X. Chen, J. Yang, L. Shi, T. Chen, Z. Bao, J. Liu and Y. Wu, 'Highly Efficient Photoinduced Enhanced Raman Spectroscopy (PIERS) from Plasmonic Nanoparticles Decorated 3D Semiconductor Arrays for Ultrasensitive, Portable, and Recyclable Detection of Organic Pollutants,' *ACS Sensors*, vol. 4, no. 6, pp. 1670–1681, 2019, ISSN: 23793694. DOI: 10.1021/acssensors.9b00562.

[235] M. E. Hankus, D. N. Stratis-Cullum and P. M. Pellegrino, 'Characterization of Next-Generation Commercial Surface-Enhanced Raman Scattering (SERS) Substrates,' *Chem. Biol. Radiol. Nucl. Explos. Sens. XII*, vol. 8018, no. June 2011, 80180P, 2011. DOI: 10.1117/12.886779.

[236] J. Gao, N. Zhang, D. Ji, H. Song, Y. Liu, L. Zhou, Z. Sun, J. M. Jornet, A. C. Thompson, R. L. Collins, Y. Song, S. Jiang and Q. Gan, 'Superabsorbing Metasurfaces with Hybrid Ag-Au Nanostructures for Surface-Enhanced Raman Spectroscopy Sensing of Drugs and Chemicals,' *Small Methods*, vol. 1800045, p. 1 800 045, 2018, ISSN: 23669608. DOI: 10.1002/smtd.201800045.

[237] M. Liszewska, B. Bartosewicz, B. Budner, B. Nasiłowska, M. Szala, J. L. Weyher, I. Dzięcielewski, Z. Mierczyk and B. J. Jankiewicz,

'Evaluation of Selected SERS Substrates for Trace Detection of Explosive Materials Using Portable Raman Systems,' *Vib. Spectrosc.*, vol. 100, no. November 2018, pp. 79–85, 2019, ISSN: 09242031. DOI: 10.1016/j.vibspec.2018.11.002. [Online]. Available: https://doi.org/10.1016/j.vibspec.2018.11.002.

[238] A. Hakonen, K. Wu, M. Stenbæk Schmidt, P. O. Andersson, A. Boisen and T. Rindzevicius, 'Detecting Forensic Substances Using Commercially Available SERS Substrates and Handheld Raman Spectrometers,' *Talanta*, vol. 189, no. June, pp. 649–652, 2018, ISSN: 00399140. DOI: 10.1016/j.talanta.2018.07.009. [Online]. Available: https://doi.org/10.1016/j.talanta.2018.07.009https://linkinghub.elsevier.com/retrieve/pii/S003991401830701X.

[239] A. Musumeci, D. Gosztola, T. Schiller, N. M. Dimitrijevic, V. Mujica, D. Martin and T. Rajh, 'SERS of semiconducting nanoparticles (TiO 2 hybrid composites),' *J. Am. Chem. Soc.*, vol. 131, no. 17, pp. 6040–6041, 2009, ISSN: 00027863. DOI: 10.1021/ja808277u.

[240] P. Ji, Z. Wang, X. Shang, Y. Zhang, Y. Liu, Z. Mao and X. Shi, 'Direct observation of enhanced Raman scattering on nano-sized ZrO 2 substrate: Charge-transfer contribution,' *Front. Chem.*, vol. 7, no. MAR, pp. 1–8, 2019, ISSN: 22962646. DOI: 10.3389/fchem.2019.00245.

[241] Y. Wang, W. Ruan, J. Zhang, B. Yang, W. Xu, B. Zhao and J. R. Lombardi, 'Direct observation of surface-enhanced Raman scattering in ZnO nanocrystals,' *J. Raman Spectrosc.*, vol. 40, no. 8, pp. 1072–1077, 2009, ISSN: 03770486. DOI: 10.1002/jrs.2241.

[242] L. Yang, Y. Yang, Y. Ma, S. Li, Y. Wei, Z. Huang and N. V. Long, 'Fabrication of semiconductor ZnO nanostructures for versatile SERS application,' *Nanomaterials*, vol. 7, no. 11, 2017, ISSN: 20794991. DOI: 10.3390/nano7110398.

[243] A Kudelski, W Grochala, J Bukowska, A Szummer and M Dolata, 'Surface-enhanced Raman scattering (SERS) at Copper (I) oxide Surface-Enhanced Raman Scattering (SERS) at Copper (I) Oxide,' *J. Raman Spectrosc.*, vol. 4555, no. May 1998, pp. 430–435, 2016, ISSN: 0377-0486.

[244] K. C. To, 'Flow chemistry synthesis of triacetone triperoxide (TATP) and its characterisation,' Tech. Rep., 2022.

[245] J. Oxley, J. Smith, J. Brady, F. Dubnikova, R. Kosloff, L. Zeiri and Y. Zeiri, 'Raman and infrared fingerprint spectroscopy of peroxide-based explosives,' *Appl. Spectrosc.*, vol. 62, no. 8, pp. 906–915, 2008, ISSN: 00037028. DOI: 10.1366/000370208785284420.

[246] J. Pachman, R. Matyáš and M. Künzel, 'Study of TATP: Blast characteristics and TNT equivalency of small charges,' *Shock Waves*, vol. 24, no. 4, pp. 439–445, 2014, ISSN: 09381287. DOI: 10.1007/s00193-014-0497-4.

[247] J. Tomlinson-Phillips, A. Wooten, J. Kozole, J. Deline, P. Beresford and J. Stairs, 'Characterization of TATP gas phase product ion chemistry *via* isotope labeling experiments using ion mobility spectrometry interfaced with a triple quadrupole mass spectrometer,' *Talanta*, vol. 127, pp. 152–162, 2014, ISSN: 00399140. DOI: 10.1016/j.talanta.2014.03.044.

[248] S. H. D.W. Sheel, R.J. McCurdy, *Method of depositing tin oxide and titanium oxide coatings on flat glass and the resulting coated glass, Patent Application*, 1998.

[249] A. Mills, A. Lepre, N. Elliott, S. Bhopal, I. P. Parkin and S. A. O'Neill, 'Characterisation of the photocatalyst Pilkington Activ™: A reference film photocatalyst?' *J. Photochem. Photobiol. A Chem.*, vol. 160, no. 3, pp. 213–224, 2003, ISSN: 10106030. DOI: 10.1016/S1010-6030(03)00205-3.

[250] A. Dey, S. Middya, R. Jana, M. Das, J. Datta, A. Layek and P. P. Ray, 'Light induced charge transport property analysis of nanostructured ZnS based Schottky diode,' *J. Mater. Sci. Mater. Electron.*, vol. 27, no. 6, pp. 6325–6335, 2016, ISSN: 1573482X. DOI: 10.1007/s10854-016-4567-5.

[251] G. Matin, A. R. Amani-Ghadim, A. A. Matin, N. Kargar and H. B. Buyukışık, 'Assessment of environmental applicability of TiO2 coated self-cleaning glass for photocatalytic degradation of estrone, 17β-estradiol and their byproducts,' *Ege J. Fish. Aquat. Sci.*, vol. 36, no. 4, pp. 347–359, 2019, ISSN: 13001590. DOI: 10.12714/egejfas.36.4.05.

[252] T. Ohsaka, F. Izumi and Y. Fujiki, 'Raman spectrum of anatase, TiO2,' *J. Raman Spectrosc.*, vol. 7, no. 6, pp. 321–324, 1978, ISSN: 10974555. DOI: 10.1002/jrs.1250070606.

[253] M. C. Biesinger, L. W. Lau, A. R. Gerson and R. S. C. Smart, 'Resolving surface chemical states in XPS analysis of first row transition metals, oxides and hydroxides: Sc, Ti, V, Cu and Zn,' *Appl. Surf. Sci.*, vol. 257, no. 3, pp. 887–898, 2010, ISSN: 01694332. DOI: 10.1016/j.

apsusc.2010.07.086. [Online]. Available: http://dx.doi.org/10.1016/j.apsusc.2010.07.086.

[254] Q. Zhu, Y. Peng, L. Lin, C. M. Fan, G. Q. Gao, R. X. Wang and A. W. Xu, 'Stable blue TiO2-x nanoparticles for efficient visible light photocatalysts,' *J. Mater. Chem. A*, vol. 2, no. 12, pp. 4429–4437, 2014, ISSN: 20507488. DOI: 10.1039/c3ta14484d.

[255] E. McCafferty and J. P. Wightman, 'Determination of the concentration of surface hydroxyl groups on metal oxide films by a quantitative XPS method,' *Surf. Interface Anal.*, vol. 26, no. 8, pp. 549–564, 1998, ISSN: 01422421. DOI: 10.1002/(sici)1096-9918(199807)26:8<549::aid-sia396>3.3.co;2-h.

[256] J. Spiridonova, A. Katerski, M. Danilson, M. Krichevskaya, M. Krunks and I. Oja Acik, 'Effect of the Titanium Isopropoxide:Acetylacetone Molar Ratio on the Photocatalytic Activity of TiO2 Thin Films,' *Molecules*, vol. 24, no. 23, p. 4326, 2019, ISSN: 1420-3049. DOI: 10.3390/molecules24234326.

[257] H. Idriss, 'On the wrong assignment of the XPS O1s signal at 531–532 eV attributed to oxygen vacancies in photo- and electro-catalysts for water splitting and other materials applications,' *Surf. Sci.*, vol. 712, no. April, pp. 2–7, 2021, ISSN: 00396028. DOI: 10.1016/j.susc.2021.121894.

[258] S. Yamamoto, H. Bluhm, K. Andersson, G. Ketteler, H. Ogasawara, M. Salmeron and A. Nilsson, 'In situ x-ray photoelectron spectroscopy studies of water on metals and oxides at ambient conditions,' *J. Phys. Condens. Matter*, vol. 20, no. 18, 2008, ISSN: 09538984. DOI: 10.1088/0953-8984/20/18/184025.

[259] R. D. Deegan, O. Bakajin, T. F. Dupont, G. Huber, S. R. Nagel and T. A. Witten, 'Capillary flow as the cause of ring stains from dried liquid drops,' *Nature*, vol. 389, no. 6653, pp. 827–829, 1997, ISSN: 00280836. DOI: 10.1038/39827.

[260] S. J. Kang, V. Vandadi, J. D. Felske and H. Masoud, 'Alternative mechanism for coffee-ring deposition based on active role of free surface,' *Phys. Rev. E*, vol. 94, no. 6, pp. 1–8, 2016, ISSN: 24700053. DOI: 10.1103/PhysRevE.94.063104. arXiv: 0906.3878.

[261] H. Hu and R. G. Larson, 'Analysis of the Microfluid Flow in an Evaporating Sessile Droplet,' *Langmuir*, vol. 21, no. 9, pp. 3963–3971, 2005, ISSN: 0743-7463. DOI: 10.1021/la047528s. [Online]. Available: https://pubs.acs.org/doi/10.1021/la047528s.

[262] W. Q. Ma, Y. Fang, G. L. Hao and W. G. Wang, 'Adsorption behaviors of 4-mercaptobenzoic acid on silver and gold films,' *Chinese J. Chem. Phys.*, vol. 23, no. 6, pp. 659–663, 2010, ISSN: 16740068. DOI: 10.1088/1674-0068/23/06/659-663.

[263] A. Michota and J. Bukowska, 'Surface-enhanced Raman scattering (SERS) of 4-mercaptobenzoic acid on silver and gold substrates,' *J. Raman Spectrosc.*, vol. 34, no. 1, pp. 21–25, 2003, ISSN: 03770486. DOI: 10.1002/jrs.928.

[264] H. Ma, S. Liu, N. Zheng, Y. Liu, X. X. Han, C. He, H. Lu and B. Zhao, 'Frequency Shifts in Surface-Enhanced Raman Spectroscopy-Based Immunoassays: Mechanistic Insights and Application in Protein Carbonylation Detection,' *Anal. Chem.*, vol. 91, no. 15, pp. 9376–9381, 2019, ISSN: 15206882. DOI: 10.1021/acs.analchem.9b02640.

[265] K. W. Kho, U. S. Dinish, A. Kumar and M. Olivo, 'Frequency shifts in SERS for biosensing,' *ACS Nano*, vol. 6, no. 6, pp. 4892–4902, 2012, ISSN: 19360851. DOI: 10.1021/nn300352b.

[266] X. Wang, S. Chang, J. Yang, J. Tan, H. Jia, H. Yin, X. Li and G. Peng, 'Detection of TNT in acetone using Raman spectroscopic signature,' *Int. Symp. Photoelectron. Detect. Imaging 2007 Laser, Ultraviolet, Terahertz Technol.*, vol. 6622, no. February 2008, p. 662 219, 2007, ISSN: 0277786X. DOI: 10.1117/12.790827.

[267] S. Y. Ding, E. M. You, Z. Q. Tian and M. Moskovits, 'Electromagnetic theories of surface-enhanced Raman spectroscopy,' *Chem. Soc. Rev.*, vol. 46, no. 13, pp. 4042–4076, 2017, ISSN: 14604744. DOI: 10.1039/c7cs00238f.

[268] X. Pan, M. Q. Yang, X. Fu, N. Zhang and Y. J. Xu, 'Defective TiO2 with oxygen vacancies: Synthesis, properties and photocatalytic applications,' *Nanoscale*, vol. 5, no. 9, pp. 3601–3614, 2013, ISSN: 20403364. DOI: 10.1039/c3nr00476g.

[269] X. Zhang, Y. Liu, M. Soltani, P. Li, B. Zhao and B. Cui, 'Probing the Interfacial Charge-Transfer Process of Uniform ALD Semiconductor-Molecule-Metal Models: A SERS Study,' *J. Phys. Chem. C*, vol. 121, no. 48, pp. 26 939–26 948, 2017, ISSN: 19327455. DOI: 10.1021/acs.jpcc.7b10086.

[270] W. H. Park and Z. H. Kim, 'Charge transfer enhancement in the SERS of a single molecule,' *Nano Lett.*, vol. 10, no. 10, pp. 4040–4048, 2010, ISSN: 15306984. DOI: 10.1021/nl102026p.

[271] M. Jakob, H. Levanon and P. V. Kamat, 'Charge distribution between UV-irradiated TiO2 and gold nanoparticles: Determination of shift in

the Fermi level,' *Nano Lett.*, vol. 3, no. 3, pp. 353–358, 2003, ISSN: 15306984. DOI: 10.1021/nl0340071.

[272] M. Parente, S. Sheikholeslami, G. V. Naik, J. A. Dionne and A. Baldi, 'Equilibration of Photogenerated Charge Carriers in Plasmonic Core@Shell Nanoparticles,' *J. Phys. Chem. C*, vol. 122, no. 41, pp. 23 631–23 638, 2018, ISSN: 19327455. DOI: 10.1021/acs.jpcc.8b05003. [Online]. Available: https://pubs.acs.org/doi/10.1021/acs.jpcc.8b05003.

[273] P. Mulvaney, J. Pérez-Juste, M. Giersig, L. M. Liz-Marzán and C. Pecharromán, 'Drastic surface plasmon mode shifts in gold nanorods due to electron charging,' *Plasmonics*, vol. 1, no. 1, pp. 61–66, 2006, ISSN: 15571955. DOI: 10.1007/s11468-005-9005-0.

[274] H. Sun, M. Yao, Y. Song, L. Zhu, J. Dong, R. Liu, P. Li, B. Zhao and B. Liu, 'Pressure-induced SERS enhancement in a MoS2/Au/R6G system by a two-step charge transfer process,' *Nanoscale*, vol. 11, no. 44, pp. 21 493–21 501, 2019, ISSN: 20403372. DOI: 10.1039/c9nr07098b.

[275] T. Sen and A. Patra, 'Resonance energy transfer from rhodamine 6G to gold nanoparticles by steady-state and time-resolved spectroscopy,' *J. Phys. Chem. C*, vol. 112, no. 9, pp. 3216–3222, 2008, ISSN: 19327447. DOI: 10.1021/jp0768367.

[276] S. Bai, D. Serien, A. Hu and K. Sugioka, '3D Microfluidic Surface-Enhanced Raman Spectroscopy (SERS) Chips Fabricated by All-Femtosecond-Laser-Processing for Real-Time Sensing of Toxic Substances,' *Adv. Funct. Mater.*, vol. 28, no. 23, pp. 1–10, 2018, ISSN: 16163028. DOI: 10.1002/adfm.201706262.

[277] S. Terdale and A. Tantray, 'Spectroscopic study of the dimerization of rhodamine 6G in water and different organic solvents,' *J. Mol. Liq.*, vol. 225, pp. 662–671, 2017, ISSN: 01677322. DOI: 10.1016/j.molliq.2016.10.090. [Online]. Available: http://dx.doi.org/10.1016/j.molliq.2016.10.090.

[278] Q. Su, C. Jiang, D. Gou and Y. Long, 'Surface Plasmon-Assisted Fluorescence Enhancing and Quenching: From Theory to Application,' *ACS Appl. Bio Mater.*, vol. 4, no. 6, pp. 4684–4705, 2021, ISSN: 25766422. DOI: 10.1021/acsabm.1c00320.

[279] M. Barzan and F. Hajiesmaeilbaigi, 'Effect of gold nanoparticles on the optical properties of Rhodamine 6G,' *Eur. Phys. J. D*, vol. 70, no. 5, pp. 1–6, 2016, ISSN: 14346079. DOI: 10.1140/epjd/e2016-70088-6.

[280] V. Levchenko, M. Grouchko, S. Magdassi, T. Saraidarov and R. Reisfeld, 'Enhancement of luminescence of Rhodamine B by gold nanoparticles in thin films on glass for active optical materials applications,' *Opt. Mater. (Amst).*, vol. 34, no. 2, pp. 360–364, 2011, ISSN: 09253467. DOI: 10.1016/j.optmat.2011.04.022. [Online]. Available: http://dx.doi.org/10.1016/j.optmat.2011.04.022.

[281] R. Reisfeld, V. Levchenko and T. Saraidarov, 'Interaction of luminescent dyes with noble metal nanoparticles in organic-inorganic glasses for future luminescent materials,' *Polym. Adv. Technol.*, vol. 22, no. 1, pp. 60–64, 2011, ISSN: 10427147. DOI: 10.1002/pat.1842.

[282] E. Dulkeith, A. C. Morteani, T. Niedereichholz, T. A. Klar, J. Feldmann, S. A. Levi, F. C. van Veggel, D. N. Reinhoudt, M. Möller and D. I. Gittins, 'Fluorescence Quenching of Dye Molecules near Gold

Nanoparticles: Radiative and Nonradiative Effects,' *Phys. Rev. Lett.*, vol. 89, no. 20, pp. 12–15, 2002, ISSN: 10797114. DOI: 10.1103/PhysRevLett.89.203002.

[283] M. Bauch, K. Toma, M. Toma, Q. Zhang and J. Dostalek, 'Plasmon-Enhanced Fluorescence Biosensors: A Review,' *Plasmonics*, vol. 9, no. 4, pp. 781–799, 2014, ISSN: 15571963. DOI: 10.1007/s11468-013-9660-5.

[284] B. R. Kumar, N. S. Basheer, A. Kurian and S. D. George, 'Study of concentration-dependent quantum yield of Rhodamine 6G by gold nanoparticles using thermal-lens technique,' *Appl. Phys. B Lasers Opt.*, vol. 115, no. 3, pp. 335–342, 2014, ISSN: 09462171. DOI: 10.1007/s00340-013-5608-x.

[285] Y. Bian, S. Liu, Y. Zhang, Y. Liu, X. Yang, S. Lou, E. Wu, B. Wu, X. Zhang and Q. Jin, 'Distance-Dependent Plasmon-Enhanced Fluorescence of Submonolayer Rhodamine 6G by Gold Nanoparticles,' *Nanoscale Res. Lett.*, vol. 16, no. 1, 2021, ISSN: 1556276X. DOI: 10.1186/s11671-021-03546-7.

[286] F. M. Zehentbauer, C. Moretto, R. Stephen, T. Thevar, J. R. Gilchrist, D. Pokrajac, K. L. Richard and J. Kiefer, 'Fluorescence spectroscopy of Rhodamine 6G: Concentration and solvent effects,' *Spectrochim. Acta - Part A Mol. Biomol. Spectrosc.*, vol. 121, pp. 147–151, 2014, ISSN: 13861425. DOI: 10.1016/j.saa.2013.10.062. [Online]. Available: http://dx.doi.org/10.1016/j.saa.2013.10.062.

[287] K. Cyprych, D. Chateau, A. Désert, S. Parola and J. Mysliwiec, 'Plasmonic Nanoparticles Driven Enhanced Light Amplification in a Local 2D and 3D Self-Assembly,' *Nanomaterials*, vol. 8, no. 12, p. 1051,

2018, ISSN: 2079-4991. DOI: 10.3390/nano8121051. [Online]. Available: http://www.mdpi.com/2079-4991/8/12/1051.

[288] K.-X. Xie, L.-T. Xu, Y.-Y. Zhai, Z.-C. Wang, M. Chen, X.-H. Pan, S.-H. Cao and Y.-Q. Li, 'The synergistic enhancement of silver nanocubes and graphene oxide on surface plasmon-coupled emission,' *Talanta*, vol. 195, no. September 2018, pp. 752–756, 2019, ISSN: 00399140. DOI: 10.1016/j.talanta.2018.11.112. [Online]. Available: https://doi.org/10.1016/j.talanta.2018.11.112https://linkinghub.elsevier.com/retrieve/pii/S003991401831258X.

[289] A. K. Gupta, C. H. Hsu, C. H. Chen, A. Purwidyantri, B. A. Prabowo, J. L. Wang, Y. C. Tian and C. S. Lai, 'Au-spotted zinc oxide nanohexagonrods structure for plasmon-photoluminescence sensor,' *Sensors Actuators, B Chem.*, vol. 290, no. March, pp. 100–109, 2019, ISSN: 09254005. DOI: 10.1016/j.snb.2019.03.020. [Online]. Available: https://doi.org/10.1016/j.snb.2019.03.020.

[290] C. K. Kim, R. R. Kalluru, J. P. Singh, A. Fortner, J. Griffin, G. K. Darbha and P. C. Ray, 'Gold-nanoparticle-based miniaturized laser-induced fluorescence probe for specific DNA hybridization detection: Studies on size-dependent optical properties,' *Nanotechnology*, vol. 17, no. 13, pp. 3085–3093, 2006, ISSN: 09574484. DOI: 10.1088/0957-4484/17/13/001.

[291] S. W. Cao, Z. Yin, J. Barber, F. Y. Boey, S. C. J. Loo and C. Xue, 'Preparation of Au-BiVO 4 heterogeneous nanostructures as highly efficient visible-light photocatalysts,' *ACS Appl. Mater. Interfaces*, vol. 4, no. 1, pp. 418–423, 2012, ISSN: 19448244. DOI: 10.1021/am201481b.

[292] V. Subramanian, E. E. Wolf and P. V. Kamat, 'Catalysis with TiO2/Gold Nanocomposites. Effect of Metal Particle Size on the Fermi Level Equilibration,' *J. Am. Chem. Soc.*, vol. 126, no. 15, pp. 4943–4950, 2004, ISSN: 00027863. DOI: 10.1021/ja0315199.

[293] S. Kohtani, K. Yoshida, T. Maekawa, A. Iwase, A. Kudo, H. Miyabe and R. Nakagaki, 'Loading effects of silver oxides upon generation of reactive oxygen species in semiconductor photocatalysis,' *Phys. Chem. Chem. Phys.*, vol. 10, no. 20, pp. 2986–2992, 2008, ISSN: 14639076. DOI: 10.1039/b719913a.

[294] H. Xu and K. S. Suslick, 'Water-soluble fluorescent silver nanoclusters,' *Adv. Mater.*, vol. 22, no. 10, pp. 1078–1082, 2010, ISSN: 09359648. DOI: 10.1002/adma.200904199.

[295] I. Díez and R. H. Ras, 'Fluorescent silver nanoclusters,' *Nanoscale*, vol. 3, no. 5, pp. 1963–1970, 2011, ISSN: 20403364. DOI: 10.1039/c1nr00006c.

[296] H. Tang, H. Berger, P. E. Schmid, F. Lévy and G. Burri, 'Photoluminescence in TiO2 anatase single crystals,' *Solid State Commun.*, vol. 87, no. 9, pp. 847–850, 1993, ISSN: 00381098. DOI: 10.1016/0038-1098(93)90427-0.

[297] X. Wang, Z. Feng, J. Shi, G. Jia, S. Shen, J. Zhou and C. Li, 'Trap states and carrier dynamics of TiO2 studied by photoluminescence spectroscopy under weak excitation condition,' *Phys. Chem. Chem. Phys.*, vol. 12, no. 26, pp. 7083–7090, 2010, ISSN: 14639076. DOI: 10.1039/b925277k.

[298] D. K. Pallotti, L. Passoni, P. Maddalena, F. Di Fonzo and S. Lettieri, 'Photoluminescence Mechanisms in Anatase and Rutile TiO 2,' *J. Phys.*

Chem. C, vol. 121, no. 16, pp. 9011–9021, 2017, ISSN: 1932-7447. DOI: 10.1021/acs.jpcc.7b00321. [Online]. Available: https://pubs.acs.org/doi/10.1021/acs.jpcc.7b00321.

[299] S. Mathew, A. Kumar Prasad, T. Benoy, P. P. Rakesh, M. Hari, T. M. Libish, P. Radhakrishnan, V. P. Nampoori and C. P. Vallabhan, 'UV-visible photoluminescence of TiO2 nanoparticles prepared by hydrothermal method,' *J. Fluoresc.*, vol. 22, no. 6, pp. 1563–1569, 2012, ISSN: 10530509. DOI: 10.1007/s10895-012-1096-3.

[300] F. J. Knorr, C. C. Mercado and J. L. McHale, 'Trap-state distributions and carrier transport in pure and mixed-phase TiO2: Influence of contacting solvent and interphasial electron transfer,' *J. Phys. Chem. C*, vol. 112, no. 33, pp. 12 786–12 794, 2008, ISSN: 19327447. DOI: 10.1021/jp8039934.

[301] A. Stevanovic, S. Ma and J. T. Yates, 'Effect of gold nanoparticles on photoexcited charge carriers in powdered TiO2-long range quenching of photoluminescence,' *J. Phys. Chem. C*, vol. 118, no. 36, pp. 21 275–21 280, 2014, ISSN: 19327455. DOI: 10.1021/jp507156p.

[302] N. Gogoi, G. Borah, P. K. Gogoi and T. R. Chetia, 'TiO2 supported gold nanoparticles: An efficient photocatalyst for oxidation of alcohol to aldehyde and ketone in presence of visible light irradiation,' *Chem. Phys. Lett.*, vol. 692, pp. 224–231, 2018, ISSN: 00092614. DOI: 10.1016/j.cplett.2017.12.015. [Online]. Available: https://doi.org/10.1016/j.cplett.2017.12.015.

[303] R. Li, H. Lv, X. Zhang, P. Liu, L. Chen, J. Cheng and B. Zhao, 'Vibrational spectroscopy and density functional theory study of 4-mercaptobenzoic acid,' *Spectrochim. Acta - Part A Mol. Biomol. Spec-*

trosc., vol. 148, pp. 369–374, 2015, ISSN: 13861425. DOI: 10.1016/j.saa.2015.03.132. [Online]. Available: http://dx.doi.org/10.1016/j.saa.2015.03.132.

[304] D. Glass, R. Quesada-Cabrera, S. Bardey, P. Promdet, R. Sapienza, V. Keller, S. A. Maier, V. Caps, I. P. Parkin and E. Cortés, 'Probing the Role of Atomic Defects in Photocatalytic Systems through Photoinduced Enhanced Raman Scattering,' *ACS Energy Lett.*, pp. 4273–4281, 2021, ISSN: 2380-8195. DOI: 10.1021/acsenergylett.1c01772. [Online]. Available: https://pubs.acs.org/doi/10.1021/acsenergylett.1c01772.

[305] C. Muehlethaler, M. Leona and J. R. Lombardi, 'Towards a Validation of Surface-Enhanced Raman Scattering (SERS) for Use in Forensic Science: Repeatability and Reproducibility Experiments,' *Forensic Sci. Int.*, vol. 268, pp. 1–13, 2016, ISSN: 18726283. DOI: 10.1016/j.forsciint.2016.09.005.

[306] M. Fan and A. G. Brolo, 'Silver nanoparticles self assembly as SERS substrates with near single molecule detection limit,' *Phys. Chem. Chem. Phys.*, vol. 11, no. 34, p. 7381, 2009, ISSN: 1463-9076. DOI: 10.1039/b904744a. [Online]. Available: http://xlink.rsc.org/?DOI=b913171jhttp://xlink.rsc.org/?DOI=b904744a.

[307] R. Que, M. Shao, S. Zhuo, C. Wen, S. Wang and S. T. Lee, 'Highly reproducible surface-enhanced raman scattering on a capillarity-assisted gold nanoparticle assembly,' *Adv. Funct. Mater.*, vol. 21, no. 17, pp. 3337–3343, 2011, ISSN: 1616301X. DOI: 10.1002/adfm.201100641.

[308] G. F. Andrade, M. K. Fan and A. G. Brolo, 'Multilayer silver nanoparticles-modified optical fiber tip for high performance SERS remote sensing,'

Biosens. Bioelectron., vol. 25, no. 10, pp. 2270–2275, 2010, ISSN: 09565663. DOI: 10.1016/j.bios.2010.03.007. [Online]. Available: http://dx.doi.org/10.1016/j.bios.2010.03.007.

[309] E. Food and S. Authority, 'Peer review of the pesticide risk assessment of the active substance thiram,' *EFSA J.*, vol. 15, no. 7, 2017, ISSN: 18314732. DOI: 10.2903/j.efsa.2017.4700.

[310] N. Kaur, A. Khunger, S. L. Wallen, A. Kaushik, G. R. Chaudhary and R. S. Varma, 'Advanced green analytical chemistry for environmental pesticide detection,' *Curr. Opin. Green Sustain. Chem.*, vol. 30, no. March, p. 100 488, 2021, ISSN: 24522236. DOI: 10.1016/j.cogsc.2021.100488. [Online]. Available: https://doi.org/10.1016/j.cogsc.2021.100488.

[311] S. Pang, T. Yang and L. He, 'Review of surface enhanced Raman spectroscopic (SERS) detection of synthetic chemical pesticides,' *TrAC - Trends Anal. Chem.*, vol. 85, pp. 73–82, 2016, ISSN: 18793142. DOI: 10.1016/j.trac.2016.06.017. [Online]. Available: http://dx.doi.org/10.1016/j.trac.2016.06.017.

[312] G. Barbillon, 'Oxygen vacancy dynamics in highly crystalline zinc oxide film investigated by piers effect,' *Materials (Basel).*, vol. 14, no. 16, 2021, ISSN: 19961944. DOI: 10.3390/ma14164423.

[313] H. Pu, Z. Huang, F. Xu and D. W. Sun, 'Two-dimensional self-assembled Au-Ag core-shell nanorods nanoarray for sensitive detection of thiram in apple using surface-enhanced Raman spectroscopy,' *Food Chem.*, vol. 343, no. October 2020, p. 128 548, 2021, ISSN: 18737072. DOI: 10.1016/j.foodchem.2020.128548. [Online]. Available: https://doi.org/10.1016/j.foodchem.2020.128548.

[314] B. Wang, L. Zhang and X. Zhou, 'Synthesis of silver nanocubes as a SERS substrate for the determination of pesticide paraoxon and thiram,' *Spectrochim. Acta - Part A Mol. Biomol. Spectrosc.*, vol. 121, pp. 63–69, 2014, ISSN: 13861425. DOI: 10.1016/j.saa.2013.10.013. [Online]. Available: http://dx.doi.org/10.1016/j.saa.2013.10.013.

[315] S Sanchez-Cortes, M Vasina, O Francioso and J. Garcia-Ramos, 'Raman and surface-enhanced Raman spectroscopy of dithiocarbamate fungicides,' *Vib. Spectrosc.*, vol. 17, no. 2, pp. 133–144, 1998, ISSN: 09242031. DOI: 10.1016/s0924-2031(98)00025-3.

[316] C. Chenal, R. L. Birke and J. R. Lombardi, 'Determination of the degree of charge-transfer contributions to surface-enhanced Raman spectroscopy,' *ChemPhysChem*, vol. 9, no. 11, pp. 1617–1623, 2008, ISSN: 14397641. DOI: 10.1002/cphc.200800221.

[317] N. A. Milas and A. Golubovic, 'Studies in Organic Peroxides . XXV . Preparation , Separation and Identification of Peroixdes Derived from Methyl Ethyl Ketone and Hydrogen Peroxide,' *J. Am. Chem. Soc.*, vol. 81, no. 21, pp. 5824–5826, 1959, ISSN: 0002-7863. DOI: 10.1021/ja01530a068.

[318] O. Reany, M. Kapon, M. Botoshansky and E. Keinan, 'Rich polymorphism in triacetone-triperoxide,' *Cryst. Growth Des.*, vol. 9, no. 8, pp. 3661–3670, 2009, ISSN: 15287483. DOI: 10.1021/cg900390y.

[319] B. S. Leigh, K. L. Monson and J. E. Kim, 'Visible and UV resonance Raman spectroscopy of the peroxide-based explosive HMTD and its photoproducts,' *Forensic Chem.*, vol. 2, pp. 22–28, 2016, ISSN:

24681709. DOI: 10.1016/j.forc.2016.08.002. [Online]. Available: http://dx.doi.org/10.1016/j.forc.2016.08.002.

[320] S. Chang, H. Ko, S. Singamaneni, R. Gunawidjaja and V. V. Tsukruk, 'Nanoporous membranes with mixed nanoclusters for Raman-based label-free monitoring of peroxide compounds,' *Anal. Chem.*, vol. 81, no. 14, pp. 5740–5748, 2009, ISSN: 00032700. DOI: 10.1021/ac900537d.

[321] H. Ko, S. Chang and V. V. Tsukruk, 'Porous substrates for label-free molecular level detection of nonresonant organic molecules,' *ACS Nano*, vol. 3, no. 1, pp. 181–188, 2009, ISSN: 19360851. DOI: 10.1021/nn800569f.

[322] D. Sülzle, P. Klaeboe, D. S. B. Grace, H. Hopf, P. Klaeboe, F. Lehrich, C. J. Nielsen, D. L. Powell and M. Trætteberg, 'The Infrared, Raman and NMR Spectra of Hexamethylene Triperoxide Diamine.,' *Acta Chem. Scand.*, vol. 42a, no. January 1988, pp. 165–170, 1988, ISSN: 0904-213X. DOI: 10.3891/acta.chem.scand.42a-0165.

[323] S. Liang, W. Chen, S. Yin, S. J. Schaper, R. Guo, J. Drewes, N. Carstens, T. Strunskus, M. Gensch, M. Schwartzkopf, F. Faupel, S. V. Roth, Y. J. Cheng and P. Müller-Buschbaum, 'Tailoring the Optical Properties of Sputter-Deposited Gold Nanostructures on Nanostructured Titanium Dioxide Templates Based on in Situ Grazing-Incidence Small-Angle X-ray Scattering Determined Growth Laws,' *ACS Appl. Mater. Interfaces*, vol. 13, no. 12, pp. 14 728–14 740, 2021, ISSN: 19448252. DOI: 10.1021/acsami.1c00972.

[324] G. Davison, Y. Yin, T. Jones, I. P. Parkin, W. J. Peveler and T.-c. Lee, 'Multi-mode enhanced Raman scattering spectroscopy using

aggregation-free hybrid metal/metal-oxide nanoparticles with intrinsic oxygen vacancies,' *J. Mater. Chem. C*, 2023, ISSN: 2050-7526. DOI: 10.1039/D2TC05069B. [Online]. Available: http://xlink.rsc.org/?DOI=D2TC05069B.

[325] H. Taz, R. Ruther, A. Malasi, S. Yadavali, C. Carr, J. Nanda and R. Kalyanaraman, 'In situ localized surface plasmon resonance (LSPR) spectroscopy to investigate kinetics of chemical bath deposition of CdS thin films,' *J. Phys. Chem. C*, vol. 119, no. 9, pp. 5033–5039, 2015, ISSN: 19327455. DOI: 10.1021/jp512738b.

[326] R. Prabhu, K. Bramhaiah, K. K. Singh and N. S. John, 'Single sea urchin-MoO3 nanostructure for surface enhanced Raman spectroscopy of dyes,' *Nanoscale Adv.*, vol. 1, no. 6, pp. 2426–2434, 2019, ISSN: 25160230. DOI: 10.1039/c9na00115h.

[327] M. Gao, G. Xing, J. Yang, L. Yang, Y. Zhang, H. Liu, H. Fan, Y. Sui, B. Feng, Y. Sun, Z. Zhang, S. Liu, S. Li and H. Song, 'Zinc oxide nanotubes decorated with silver nanoparticles as an ultrasensitive substrate for surface-enhanced Raman scattering,' *Microchim. Acta*, vol. 179, no. 3-4, pp. 315–321, 2012, ISSN: 00263672. DOI: 10.1007/s00604-012-0898-y.

[328] X. He, Y. Liu, Y. Liu, S. Cui, W. Liu and Z. Li, 'Controllable fabrication of Ag-NP-decorated porous ZnO nanosheet arrays with superhydrophobic properties for high performance SERS detection of explosives,' *CrystEngComm*, vol. 22, no. 4, pp. 776–785, 2020, ISSN: 14668033. DOI: 10.1039/c9ce01430f.

[329] N. D. Jayram, S. Sonia, S. Poongodi, P. S. Kumar, Y. Masuda, D. Mangalaraj, N. Ponpandian and C. Viswanathan, 'Superhydrophobic

Ag decorated ZnO nanostructured thin film as effective surface enhanced Raman scattering substrates,' *Appl. Surf. Sci.*, vol. 355, pp. 969–977, 2015, ISSN: 01694332. DOI: 10.1016/j.apsusc.2015.06.191. [Online]. Available: http://dx.doi.org/10.1016/j.apsusc.2015.06.191.

[330] I. Alessandri and J. R. Lombardi, 'Enhanced Raman Scattering with Dielectrics,' *Chem. Rev.*, vol. 116, no. 24, pp. 14 921–14 981, 2016, ISSN: 15206890. DOI: 10.1021/acs.chemrev.6b00365.

[331] G. Song, S. Cong and Z. Zhao, 'Defect engineering in semiconductor-based SERS,' *Chem. Sci.*, vol. 13, no. 5, pp. 1210–1224, 2022, ISSN: 20416539. DOI: 10.1039/d1sc05940h.

[332] J. Yao, Y. Quan, R. Gao, J. Li, L. Chen, Y. Liu, J. Lang, H. Shen, Y. Wang, J. Yang and M. Gao, 'Improved Charge Transfer and Hot Spots by Doping and Modulating the Semiconductor Structure: A High Sensitivity and Renewability Surface-Enhanced Raman Spectroscopy Substrate,' *Langmuir*, vol. 35, no. 27, pp. 8921–8926, 2019, ISSN: 15205827. DOI: 10.1021/acs.langmuir.9b00754.

[333] X. Xue, W. Ji, Z. Mao, Z. Li, W. Ruan, B. Zhao and J. R. Lombardi, 'Effects of Mn doping on surface enhanced Raman scattering properties of TiO 2 nanoparticles,' *Spectrochim. Acta - Part A Mol. Biomol. Spectrosc.*, vol. 95, pp. 213–217, 2012, ISSN: 13861425. DOI: 10.1016/j.saa.2012.04.101. [Online]. Available: http://dx.doi.org/10.1016/j.saa.2012.04.101.

[334] J. Yao, Y. Quan, M. Gao, R. Gao, L. Chen, Y. Liu, J. Lang, H. Shen, Y. Zhang, L. Yang and J. Yang, 'AgNPs decorated Mg-doped ZnO heterostructure with dramatic SERS activity for trace detection of food

contaminants,' *J. Mater. Chem. C*, vol. 7, no. 27, pp. 8199–8208, 2019, ISSN: 20507526. DOI: 10.1039/c8tc06588h.

[335] S. Kalasung, I. Chatnuntawech, V. Patthanasettakul, S. Limwichean, K. Lertborworn, M. Horprathum, N. Nuntawong, P. Eiamchai and K. Aiempanakit, 'Au-decorated ZnO nanorod arrays for SERS-active substrates towards trace detection and classification of pentaerythritol tetranitrate,' *Mater. Today Proc.*, vol. 47, pp. 3517–3524, 2021, ISSN: 22147853. DOI: 10.1016/j.matpr.2021.03.511. [Online]. Available: https://doi.org/10.1016/j.matpr.2021.03.511.

[336] V. Srikant and D. R. Clarke, 'On the optical band gap of zinc oxide,' *J. Appl. Phys.*, vol. 83, no. 10, pp. 5447–5451, 1998, ISSN: 00218979. DOI: 10.1063/1.367375.

[337] D. Glass, E. Cortés, S. Ben-Jaber, T. Brick, R. Quesada-Cabrera, W. J. Peveler, Y. Zhu, C. S. Blackman, C. R. Howle, I. P. Parkin and S. A. Maier, 'Photo-induced enhanced Raman spectroscopy (PIERS): sensing atomic-defects, explosives and biomolecules,' in *Chem. Biol. Radiol. Nucl. Explos. Sens. XX*, J. A. Guicheteau and C. R. Howle, Eds., SPIE, 2019, p. 13, ISBN: 9781510626850. DOI: 10.1117/12.2518948. [Online]. Available: https://www.spiedigitallibrary.org/conference-proceedings-of-spie/11010/2518948/Photo-induced-enhanced-Raman-spectroscopy-PIERS--sensing-atomic-defects/10.1117/12.2518948.full.

[338] R. S. Mane and C. D. Lokhande, 'Chemical deposition method for metal chalcogenide thin films,' *Mater. Chem. Phys.*, vol. 65, no. 1, pp. 1–31, 2000, ISSN: 02540584. DOI: 10.1016/S0254-0584(00)00217-0.

[339] A. Galdámez-Martinez, G. Santana, F. Güell, P. R. Martínez-Alanis and A. Dutt, 'Photoluminescence of zno nanowires: A review,' *Nanomaterials*, vol. 10, no. 5, 2020, ISSN: 20794991. DOI: 10.3390/nano10050857.

[340] M. Shahul Hameed, J. Joseph Princice, N. Ramesh Babu and A. Arunachalam, 'Effect of silver doping on optical properties of nanoflower ZnO thin films prepared by spray pyrolysis technique,' *J. Mater. Sci. Mater. Electron.*, vol. 28, no. 12, pp. 8675–8683, 2017, ISSN: 1573482X. DOI: 10.1007/s10854-017-6592-4.

[341] J. Fan and R. Freer, 'The roles played by Ag and Al dopants in controlling the electricalproperties of ZnO varistors,' *J. Appl. Phys.*, vol. 77, no. 9, pp. 4795–4800, 1995, ISSN: 00218979. DOI: 10.1063/1.359398.

[342] O. Volnianska, P. Boguslawski, J. Kaczkowski, P. Jakubas, A. Jezierski and E. Kaminska, 'Theory of doping properties of Ag acceptors in ZnO,' *Phys. Rev. B - Condens. Matter Mater. Phys.*, vol. 80, no. 24, pp. 1–8, 2009, ISSN: 10980121. DOI: 10.1103/PhysRevB.80.245212.

[343] L. Bai, Y. Chang and S. Zong, 'Effort of ionic radius on doped style of silver and copper/zinc oxide nanorods for photodegradation of methylene blue,' *Environ. Technol.*, vol. 43, no. 25, pp. 4010–4018, 2022, ISSN: 0959-3330. DOI: 10.1080/09593330.2021.1939793. [Online]. Available: https://doi.org/10.1080/09593330.2021.1939793https://www.tandfonline.com/doi/full/10.1080/09593330.2021.1939793.

[344] V. A. Solodukha, A. S. Turtsevich, Y. A. Solovyev, O. E. Sarychev, S. V. Gaponenko and O. V. Milchanin, 'Identification of nickel silicide phases on a silicon surface from Raman spectra,' *J. Appl. Spectrosc.*, vol. 79, no. 6, pp. 1002–1005, 2013, ISSN: 00219037. DOI: 10.1007/s10812-013-9704-9.

[345] C. A. Arguello, D. L. Rousseau and S. P. Porto, 'First-order raman effect in wurtzite-type crystals,' *Phys. Rev.*, vol. 181, no. 3, pp. 1351–1363, 1969, ISSN: 0031899X. DOI: 10.1103/PhysRev.181.1351.

[346] O. Lupan, V. Cretu, V. Postica, M. Ahmadi, B. R. Cuenya, L. Chow, I. Tiginyanu, B. Viana, T. Pauporté and R. Adelung, 'Silver-doped zinc oxide single nanowire multifunctional nanosensor with a significant enhancement in response,' *Sensors Actuators, B Chem.*, vol. 223, pp. 893–903, 2016, ISSN: 09254005. DOI: 10.1016/j.snb.2015.10.002. [Online]. Available: http://dx.doi.org/10.1016/j.snb.2015.10.002.

[347] X. B. Wang, C. Song, K. W. Geng, F. Zeng and F. Pan, 'Luminescence and Raman scattering properties of Ag-doped ZnO films,' *J. Phys. D. Appl. Phys.*, vol. 39, no. 23, pp. 4992–4996, 2006, ISSN: 00223727. DOI: 10.1088/0022-3727/39/23/014.

[348] A. Kaphle and P. Hari, 'Variation of index of refraction in cobalt doped ZnO nanostructures,' *J. Appl. Phys.*, vol. 122, no. 16, 2017, ISSN: 10897550. DOI: 10.1063/1.5001713. [Online]. Available: http://dx.doi.org/10.1063/1.5001713.

[349] A. H. Rakhsha, H. Abdizadeh, E. Pourshaban, M. R. Golobostanfard, V. R. Mastelaro and M. Montazerian, 'Ag and Cu doped ZnO nanowires: A pH-Controlled synthesis via chemical bath deposition,'

Materialia, vol. 5, no. November 2018, p. 100 212, 2019, ISSN: 25891529. DOI: 10.1016/j.mtla.2019.100212. [Online]. Available: https://doi.org/10.1016/j.mtla.2019.100212.

[350] A. Rajan, H. K. Yadav, V. Gupta and M. Tomar, 'Sol-gel derived Ag-doped ZnO thin film for UV photodetector with enhanced response,' *J. Mater. Sci.*, vol. 48, no. 22, pp. 7994–8002, 2013, ISSN: 00222461. DOI: 10.1007/s10853-013-7611-3.

[351] J. Wang, Z. Wang, B. Huang, Y. Ma, Y. Liu, X. Qin, X. Zhang and Y. Dai, 'Oxygen vacancy induced band-gap narrowing and enhanced visible light photocatalytic activity of ZnO,' *ACS Appl. Mater. Interfaces*, vol. 4, no. 8, pp. 4024–4030, 2012, ISSN: 19448244. DOI: 10.1021/am300835p.

[352] X. G. Han, H. Z. He, Q. Kuang, X. Zhou, X. H. Zhang, T. Xu, Z. X. Xie and L. S. Zheng, 'Controlling morphologies and tuning the related properties of nano/microstructured ZnO crystallites,' *J. Phys. Chem. C*, vol. 113, no. 2, pp. 584–589, 2009, ISSN: 19327447. DOI: 10.1021/jp808233e.

[353] S. Guan, L. Yamawaki, P. Zhang and X. Zhao, 'Charge-Transfer Effect of GZO Film on Photochemical Water Splitting of Transparent ZnO@GZO Films by RF Magnetron Sputtering,' *Top. Catal.*, vol. 61, no. 15-17, pp. 1585–1590, 2018, ISSN: 10225528. DOI: 10.1007/s11244-018-0916-3. [Online]. Available: http://dx.doi.org/10.1007/s11244-018-0916-3.

[354] A. Vasil'kov, T. Batsalova, B. Dzhambazov and A. Naumkin, 'XPS study of silver and copper nanoparticles demonstrated selective anticancer, proapoptotic, and antibacterial properties,' *Surf. Interface Anal.*,

vol. 54, no. 3, pp. 189–202, 2022, ISSN: 10969918. DOI: 10.1002/sia.7038.

[355] J. Jadhav and S. Biswas, 'Structural and electrical properties of ZnO:Ag core-shell nanoparticles synthesized by a polymer precursor method,' *Ceram. Int.*, vol. 42, no. 15, pp. 16 598–16 610, 2016, ISSN: 02728842. DOI: 10.1016/j.ceramint.2016.07.081. [Online]. Available: http://dx.doi.org/10.1016/j.ceramint.2016.07.081.

[356] A. B. Djurišić, Y. H. Leung, K. H. Tam, L. Ding, W. K. Ge, H. Y. Chen and S. Gwo, 'Green, yellow, and orange defect emission from ZnO nanostructures: Influence of excitation wavelength,' *Appl. Phys. Lett.*, vol. 88, no. 10, pp. 1–4, 2006, ISSN: 00036951. DOI: 10.1063/1.2182096.

[357] R. Khokhra, B. Bharti, H. N. Lee and R. Kumar, 'Visible and UV photodetection in ZnO nanostructured thin films via simple tuning of solution method /639/301/1005 /639/301/357/551 /140/146 article,' *Sci. Rep.*, vol. 7, no. 1, pp. 1–14, 2017, ISSN: 20452322. DOI: 10.1038/s41598-017-15125-x. [Online]. Available: http://dx.doi.org/10.1038/s41598-017-15125-x.

[358] C. L. Hsu, Y. D. Gao, Y. S. Chen and T. J. Hsueh, 'Vertical p-type Cu-doped ZnO/n-type ZnO homojunction nanowire-based ultraviolet photodetector by the furnace system with hotwire assistance,' *ACS Appl. Mater. Interfaces*, vol. 6, no. 6, pp. 4277–4285, 2014, ISSN: 19448252. DOI: 10.1021/am406030d.

[359] R. Crapanzano, I. Villa, S. Mostoni, M. D'arienzo, B. Di Credico, M. Fasoli, R. Scotti and A. Vedda, 'Morphology related defectiveness in zno luminescence: From bulk to nano-size,' *Nanomaterials*,

vol. 10, no. 10, pp. 1–19, 2020, ISSN: 20794991. DOI: 10.3390/nano10101983.

[360] A. X. Wang and X. Kong, 'Review of recent progress of plasmonic materials and nano-structures for surface-enhanced raman scattering,' *Materials (Basel).*, vol. 8, no. 6, pp. 3024–3052, 2015, ISSN: 19961944. DOI: 10.3390/ma8063024.

[361] J. P. Richters, T. Voss, D. S. Kim, R. Scholz and M. Zacharias, 'Enhanced surface-excitonic emission in ZnO/Al2O3 core-shell nanowires,' *Nanotechnology*, vol. 19, no. 30, 2008, ISSN: 09574484. DOI: 10.1088/0957-4484/19/30/305202.

[362] X. Zhang, J. Qin, Y. Xue, P. Yu, B. Zhang, L. Wang and R. Liu, 'Effect of aspect ratio and surface defects on the photocatalytic activity of ZnO nanorods,' *Sci. Rep.*, vol. 4, pp. 4–11, 2014, ISSN: 20452322. DOI: 10.1038/srep04596.

[363] J. R. Lombardi and R. L. Birke, 'A unified approach to surface-enhanced raman spectroscopy,' *J. Phys. Chem. C*, vol. 112, no. 14, pp. 5605–5617, 2008, ISSN: 19327447. DOI: 10.1021/jp800167v.

[364] Y. Pan, W. Wang, S. Guo, S. Jin, E. Park, Y. Sun, L. Chen and Y. M. Jung, 'Charge transfer on the surface-enhanced raman scattering of Ag/4-MBA/PEDOT:PSS system: Intermolecular hydrogen bonding,' *Chemosensors*, vol. 9, no. 5, 2021, ISSN: 22279040. DOI: 10.3390/chemosensors9050111.

[365] R. Han, W. Song, X. Wang, Z. Mao, X. X. Han and B. Zhao, 'Investigation of charge transfer at the TiO2-MBA-Au interface based on surface-enhanced Raman scattering: SPR contribution,' *Phys. Chem.*

Chem. Phys., vol. 20, no. 8, pp. 5666–5673, 2018, ISSN: 14639076. DOI: 10.1039/c8cp00014j.

[366] X. Jiang, L. Xu, W. Ji, W. Wang, J. Du, L. Yang, W. Song, X. Han and B. Zhao, 'One plus one greater than Two: Ultrasensitive Surface-Enhanced Raman scattering by TiO2/ZnO heterojunctions based on Electron-Hole separation,' *Appl. Surf. Sci.*, vol. 584, no. January, p. 152 609, 2022, ISSN: 01694332. DOI: 10.1016/j.apsusc.2022.152609. [Online]. Available: https://doi.org/10.1016/j.apsusc.2022.152609.

[367] G. R. Li, T. Hu, G. L. Pan, T. Y. Yan, X. P. Gao and H. Y. Zhu, 'Morphology-function relationship of ZnO: Polar planes, oxygen vacancies, and activity,' *J. Phys. Chem. C*, vol. 112, no. 31, pp. 11 859–11 864, 2008, ISSN: 19327447. DOI: 10.1021/jp8038626.

[368] A. A. Selim, A. Al-Sunaidi and N. Tabet, 'Effect of the surface texture and crystallinity of ZnO nanoparticles on their toxicity,' *Mater. Sci. Eng. C*, vol. 32, no. 8, pp. 2356–2360, 2012, ISSN: 09284931. DOI: 10.1016/j.msec.2012.07.007.

[369] B Darwent, *Bond Dissociation Energies*. 1970, pp. 539–544. DOI: 10.1201/9781420015195-11.

[370] H. K. Lee, Y. H. Lee, C. S. L. Koh, G. C. Phan-Quang, X. Han, C. L. Lay, H. Y. F. Sim, Y. C. Kao, Q. An and X. Y. Ling, 'Designing surface-enhanced Raman scattering (SERS) platforms beyond hotspot engineering: Emerging opportunities in analyte manipulations and hybrid materials,' *Chem. Soc. Rev.*, vol. 48, no. 3, pp. 731–756, 2019, ISSN: 14604744. DOI: 10.1039/c7cs00786h.

[371] J. V. Janovsky, 'Ueber eine Reaction der Dinitrokörper,' *Berichte der Dtsch. Chem. Gesellschaft*, vol. 24, no. 1, pp. 971–972, 1891, ISSN: 0365-9496. DOI: 10.1002/cber.189102401177. [Online]. Available: https://onlinelibrary.wiley.com/doi/10.1002/cber.189102401177.

[372] J. Meisenheimer, 'Ueber Reactionen arornatischer Nitrokorper,' *J. Ann. Chem*, vol. 323, p. 205, 1902.

[373] G. Artamkina, M. Egorov and I. Beletskaya, 'Some Aspects of Anionic σ Complexes,' *Chem. Rev.*, vol. 82, no. 4, pp. 427–459, 1982.

[374] D. Wu, Y. Li, R. Ganguly and R. Kinjo, 'A snapshot of inorganic Janovsky complex analogues featuring a nucleophilic boron center,' *Chem. Commun.*, vol. 53, no. 95, pp. 12 734–12 737, 2017, ISSN: 1364548X. DOI: 10.1039/c7cc07616a.

[375] A. Üzer, E. Erçağ and R. Apak, 'Selective spectrophotometric determination of trinitrotoluene, trinitrophenol, dinitrophenol and mononitrophenol,' *Anal. Chim. Acta*, vol. 505, no. 1, pp. 83–93, 2004, ISSN: 00032670. DOI: 10.1016/S0003-2670(03)00674-3.

[376] R. J. Pollitt and E. C. Saunders, 'The Janovsky Reaction 4616,' *J. Am. Chem. Soc.*, pp. 4615–4628, 1965.

[377] T. F. Jenkins, P. W. Schumacher, J. G. Mason and P. G. Thorne, 'On-site analysis for high concentrations of explosives in soil : extraction kinetics an dilution procedures,' *This Digit. Resour. was Creat. Microsoft Word Adobe Acrobat*, no. May, 1996. [Online]. Available: https://erdc-library.erdc.dren.mil/jspui/handle/11681/12170.

[378] K. C. To, S. Ben-Jaber and I. P. Parkin, 'Recent Developments in the Field of Explosive Trace Detection,' *ACS Nano*, 2020, ISSN: 1936-0851. DOI: 10.1021/acsnano.0c01579.

[379] J. Qian, M. Hua, C. Wang, K. Wang, Q. Liu, N. Hao and K. Wang, 'Fabrication of L-Cysteine-Capped CdTe Quantum Dots Based Ratiometric Fluorescence Nanosensor for Onsite Visual Determination of Trace TNT Explosive,' *Anal. Chim. Acta*, vol. 946, pp. 80–87, 2016, ISSN: 18734324. DOI: 10.1016/j.aca.2016.10.007. [Online]. Available: http://dx.doi.org/10.1016/j.aca.2016.10.007.

[380] S. S. Dasary, A. K. Singh, D. Senapati, H. Yu and P. C. Ray, 'Gold nanoparticle based label-free SERS probe for ultrasensitive and selective detection of trinitrotoluene,' *J. Am. Chem. Soc.*, vol. 131, no. 38, pp. 13 806–13 812, 2009, ISSN: 00027863. DOI: 10.1021/ja905134d.

[381] F Pedregosa, G Varoquaux, A Gramfort, V Michel and B Thirion, 'Scikit-learn: Machine Learning in Python,' *J. ofMachine Learn. Res.*, vol. 12, pp. 2825–2830, 2011, ISSN: 15529924. DOI: 10.1289/EHP4713.

[382] S. Guo, J. Popp and T. Bocklitz, 'Chemometric analysis in Raman spectroscopy from experimental design to machine learning–based modeling,' *Nat. Protoc.*, vol. 16, no. 12, pp. 5426–5459, 2021, ISSN: 17502799. DOI: 10.1038/s41596-021-00620-3.

[383] P. H. Eilers, 'A perfect smoother,' *Anal. Chem.*, vol. 75, no. 14, pp. 3631–3636, 2003, ISSN: 00032700. DOI: 10.1021/ac034173t.

[384] S. Kasera, L. O. Herrmann, J. D. Barrio, J. J. Baumberg and O. A. Scherman, 'Quantitative multiplexing with nano-self-assemblies in

SERS,' *Sci. Rep.*, vol. 4, pp. 1–6, 2014, ISSN: 20452322. DOI: 10.1038/srep06785.

[385] I. T. Jollife and J. Cadima, 'Principal component analysis: A review and recent developments,' *Philos. Trans. R. Soc. A Math. Phys. Eng. Sci.*, vol. 374, no. 2065, 2016, ISSN: 1364503X. DOI: 10.1098/rsta.2015.0202.

[386] J. Turkevich, P. C. Stevenson and J. Hillier, 'A study of the nucleation and growth processes in the synthesis of colloidal gold,' *Discuss. Faraday Soc.*, vol. 11, no. c, p. 55, 1951, ISSN: 0366-9033. DOI: 10.1039/df9511100055. [Online]. Available: http://xlink.rsc.org/?DOI=df9511100055.

[387] L. Panariello, S. Damilos, H. du Toit, G. Wu, A. N. P. Radhakrishnan, I. P. Parkin and A. Gavriilidis, 'Highly reproducible, high-yield flow synthesis of gold nanoparticles based on a rational reactor design exploiting the reduction of passivated Au(iii),' *React. Chem. Eng.*, vol. 5, no. 4, pp. 663–676, 2020, ISSN: 20589883. DOI: 10.1039/c9re00469f. [Online]. Available: http://dx.doi.org/10.1039/C9RE00469F.

[388] Y. Li, P. Zhang, J. Duan, S. Ai and H. Li, 'One-step seeded growth of monodisperse, quasi-spherical, Tris-stabilized gold nanocrystals with sizes from 17 to 325 nm,' *CrystEngComm*, vol. 19, no. 2, pp. 318–324, 2017, ISSN: 14668033. DOI: 10.1039/C6CE01971D.

[389] S. Kundu, K. Wang and H. Liang, 'Size-selective synthesis and catalytic application of polyelectrolyte encapsulated gold nanoparticles using microwave irradiation,' *J. Phys. Chem. C*, vol. 113, no. 13, pp. 5157–5163, 2009, ISSN: 19327447. DOI: 10.1021/jp9003104.

[390] M. K. Chow and C. F. Zukoski, 'Gold sol formation mechanisms: Role of colloidal stability,' *J. Colloid Interface Sci.*, vol. 165, no. 1, pp. 97–109, 1994, ISSN: 00219797. DOI: 10.1006/jcis.1994.1210.

[391] W. Leng, P. Pati and P. J. Vikesland, 'Room temperature seed mediated growth of gold nanoparticles: mechanistic investigations and life cycle assesment,' *Environ. Sci. Nano*, vol. 2, no. 5, pp. 440–453, 2015, ISSN: 20518161. DOI: 10.1039/c5en00026b.

[392] M. Wuithschick, A. Birnbaum, S. Witte, M. Sztucki, U. Vainio, N. Pinna, K. Rademann, F. Emmerling, R. Kraehnert and J. Polte, 'Turkevich in New Robes: Key Questions Answered for the Most Common Gold Nanoparticle Synthesis,' *ACS Nano*, vol. 9, no. 7, pp. 7052–7071, 2015, ISSN: 1936086X. DOI: 10.1021/acsnano.5b01579.

[393] N. G. Bastus, J. Comenge and V. Puntes, 'Kinetically Controlled Seeded Growth Synthesis of Citrate-Stabilized Gold Nanoparticles of up to 200 nm : Size Focusing versus Ostwald Ripening,' *Langmuir*, vol. 27, pp. 11 098–11 105, 2011. DOI: 10.1021/la201938u.

[394] E. Agunloye, L. Panariello, A. Gavriilidis and L. Mazzei, 'A model for the formation of gold nanoparticles in the citrate synthesis method,' *Chem. Eng. Sci.*, vol. 191, pp. 318–331, 2018, ISSN: 00092509. DOI: 10.1016/j.ces.2018.06.046. [Online]. Available: https://doi.org/10.1016/j.ces.2018.06.046.

[395] C. Xie, B. Liu, Z. Wang, D. Gao, G. Guan and Z. Zhang, 'Molecular imprinting at walls of silica nanotubes for TNT recognition,' *Anal. Chem.*, vol. 80, no. 2, pp. 437–443, 2008, ISSN: 00032700. DOI: 10.1021/ac701767h.

[396] W. Gao, T. Wang, C. Zhu, P. Sha, P. Dong and X. Wu, 'A 'sandwich' structure for highly sensitive detection of TNT based on surface-enhanced Raman scattering,' *Talanta*, vol. 236, no. August 2021, p. 122 824, 2022, ISSN: 00399140. DOI: 10.1016/j.talanta.2021.122824. [Online]. Available: https://doi.org/10.1016/j.talanta.2021.122824.

[397] M. Liu and W. Chen, 'Graphene nanosheets-supported Ag nanoparticles for ultrasensitive detection of TNT by surface-enhanced Raman spectroscopy,' *Biosens. Bioelectron.*, vol. 46, pp. 68–73, 2013, ISSN: 09565663. DOI: 10.1016/j.bios.2013.01.073. [Online]. Available: http://dx.doi.org/10.1016/j.bios.2013.01.073.

[398] X. He, H. Wang, Z. Li, D. Chen and Q. Zhang, 'ZnO-Ag hybrids for ultrasensitive detection of trinitrotoluene by surface-enhanced Raman spectroscopy,' *Phys. Chem. Chem. Phys.*, vol. 16, no. 28, pp. 14 706–14 712, 2014, ISSN: 14639076. DOI: 10.1039/c4cp01723d.

[399] U. B. Patel, V. N. Mehta, M. A. Kumar and S. K. Kailasa, '4-Aminothiophenol functionalized gold nanoparticles as colorimetric sensors for the detection of cobalt using UV-Visible spectrometry,' *Res. Chem. Intermed.*, vol. 39, no. 2, pp. 771–779, 2013, ISSN: 15685675. DOI: 10.1007/s11164-012-0773-9.

[400] D. Y. Wu, X. M. Liu, Y. F. Huang, B. Ren, X. Xu and Z. Q. Tian, 'Surface catalytic coupling reaction of p-mercaptoaniline linking to silver nanostructures responsible for abnormal SERS enhancement: A DFT study,' *J. Phys. Chem. C*, vol. 113, no. 42, pp. 18 212–18 222, 2009, ISSN: 19327447. DOI: 10.1021/jp9050929.

[401] G. Ara, M. S. Miran, M. M. Islam, M. Y. A. Mollah, M. M. Rahman and M. A. B. H. Susan, '1,8-Diazabicyclo[5.4.0]-undec-7-ene based protic ionic liquids and their binary systems with molecular solvents catalyzed Michael addition reaction,' *New J. Chem.*, vol. 44, no. 32, pp. 13 701–13 706, 2020, ISSN: 13699261. DOI: 10.1039/d0nj03012k.

[402] T. Kinetics, X. C. Reactions, A. Nitro-compounds, L. Temperatures, S. Reuction and E. Ion, 'The Kinetics and Mechanisms of Xome Colour Reactions of Aromatic Nitro-compounds at Low Temperatures. Part IV.* 2:4:6-Trinitrotoluene: a second Reaction with Ethoxide Ion,' *J. Chem. Soc.*, no. 0, pp. 2546–2549, 1956.

[403] C. F. Bernasconi, 'Kinetic and Spectral Study of Some Reactions of 2,4,6-Trinitrotoluene in Basic Solution. I. Deprotonation and Janovsky Complex Formation,' *J. Org. Chem.*, vol. 36, no. 12, pp. 1671–1679, 1971, ISSN: 15206904. DOI: 10.1021/jo00811a022.

[404] C. Hubert, H. Dossmann, X. Machuron-Mandard and J. C. Tabet, 'ESI formation of a Meisenheimer complex from tetryl and its unusual dissociation,' *J. Mass Spectrom.*, vol. 48, no. 3, pp. 306–311, 2013, ISSN: 10765174. DOI: 10.1002/jms.3156.

[405] Y Okamoto, E. J. Chou, M Croce, D Freeman, M Roth and O Colitti, 'Removal of TNT and RDX from aqueous solutions with surfactants,' *Propell. Explos. Pyrotech*, vol. 7, pp. 18–21, 1982.

[406] T. F. Jenkins and M. E. Walsh, 'Development of field screening methods for TNT, 2,4-DNT and RDX in soil,' *Talanta*, vol. 39, no. 4, pp. 419–428, 1992, ISSN: 00399140. DOI: 10.1016/0039-9140(92)80158-A.

[407] T. Abe, 'Absorption Spectra of Unstable Colored Intermediates from Picryl Chloride by the Action of Sodium Hydroxide,' *Bull. Chem. Soc. Jpn.*, vol. 34, no. 1, pp. 21–25, 1961, ISSN: 0009-2673. DOI: 10.1246/bcsj.34.21.

[408] M. H. Kroll, N. A. Roach, B. Poe and R. J. Elin, 'Mechanism of interference with the Jaffe reaction for creatinine,' *Clin. Chem.*, vol. 33, no. 7, pp. 1129–1132, 1987, ISSN: 00099147. DOI: 10.1093/clinchem/33.7.1129.

[409] G. Cook, J, 'Factors Influencing the Assay of Creatinine,' *Ann. din. Biochem*, vol. 12, no. 36, pp. 219–232, 1975.

[410] R. W. Beal and T. B. Brill, 'Vibrational behavior of the -NO 2 group in energetic compounds,' *Appl. Spectrosc.*, vol. 59, no. 10, pp. 1194–1202, 2005, ISSN: 00037028. DOI: 10.1366/000370205774430873.

[411] X. Wang, S. Chang, J. Yang, J. Tan, H. Jia, H. Yin, X. Li and G. Peng, 'Detection of TNT in acetone using Raman spectroscopic signature,' *Int. Symp. Photoelectron. Detect. Imaging 2007 Laser, Ultraviolet, Terahertz Technol.*, vol. 6622, no. February 2008, p. 662 219, 2007, ISSN: 0277786X. DOI: 10.1117/12.790827.

[412] M. L. Lewis, I. R. Lewis and P. R. Griffiths, 'Evaluation of a dispersive Raman spectrometer with a Ge array detector and a 1064 nm laser for the study of explosives,' *Vib. Spectrosc.*, vol. 38, no. 1-2, pp. 11–16, 2005, ISSN: 09242031. DOI: 10.1016/j.vibspec.2005.04.002.

[413] A. Puiu, G. Giubileo, S. N. Cesaro and L. Bencivenni, 'Comprehensive Infrared Study of Tetryl, Dinitrotoluene, and Trinitrotoluene Compounds,' *Appl. Spectrosc.*, vol. 69, no. 12, pp. 1472–1486, 2015, ISSN:

0003-7028. DOI: 10.1366/14-07763. [Online]. Available: http://journals.sagepub.com/doi/10.1366/14-07763.

[414] X. Zhou, H. Liu, L. Yang and J. Liu, 'SERS and OWGS Detection of Dynamic Trapping Molecular TNT Based on a Functional Self-Assembly Au Monolayer Film,' *Analyst*, vol. 138, no. 6, pp. 1858–1864, 2013, ISSN: 13645528. DOI: 10.1039/c3an36683a.

[415] K. Qian, H. Liu, L. Yang and J. Liu, 'Functionalized shell-isolated nanoparticle-enhanced Raman spectroscopy for selective detection of trinitrotoluene,' *Analyst*, vol. 137, no. 20, pp. 4644–4646, 2012, ISSN: 13645528. DOI: 10.1039/c2an35947b.

[416] K. Milligan, N. C. Shand, D. Graham and K. Faulds, 'Detection of Multiple Nitroaromatic Explosives via Formation of a Janowsky Complex and SERS,' *Anal. Chem.*, vol. 92, no. 4, pp. 3253–3261, 2020, ISSN: 0003-2700. DOI: 10.1021/acs.analchem.9b05062. [Online]. Available: https://pubs.acs.org/doi/10.1021/acs.analchem.9b05062.

[417] K. Kneipp, 'Chemical Contribution to SERS Enhancement: An Experimental Study on a Series of Polymethine Dyes on Silver Nanoaggregates,' *J. Phys. Chem. C*, vol. 120, no. 37, pp. 21 076–21 081, 2016, ISSN: 19327455. DOI: 10.1021/acs.jpcc.6b03785.

[418] N. M. Ralbovsky and I. K. Lednev, 'Towards development of a novel universal medical diagnostic method: Raman spectroscopy and machine learning,' *Chem. Soc. Rev.*, vol. 49, no. 20, pp. 7428–7453, 2020, ISSN: 14604744. DOI: 10.1039/d0cs01019g.

[419] L. Pan, P. Zhang, C. Daengngam, S. Peng and M. Chongcheawchamnan, 'A review of artificial intelligence methods combined with Raman

spectroscopy to identify the composition of substances,' *J. Raman Spectrosc.*, jrs.6225, 2021, ISSN: 0377-0486. DOI: 10.1002/jrs.6225. arXiv: 2104.04599. [Online]. Available: https://onlinelibrary.wiley.com/doi/10.1002/jrs.6225.

[420] D. Fisher, S. R. Lukow, G. Berezutskiy, I. Gil, T. Levy and Y. Zeiri, 'Machine Learning Improves Trace Explosive Selectivity: Application to Nitrate-Based Explosives,' *J. Phys. Chem. A*, vol. 124, no. 46, pp. 9656–9664, 2020, ISSN: 1089-5639. DOI: 10.1021/acs.jpca.0c05909. [Online]. Available: https://pubs.acs.org/doi/10.1021/acs.jpca.0c05909.

[421] C.-W. Tsai, S. J. Milam and C. A. Tipple, 'Exploring the analysis and differentiation of plastic explosives by comprehensive multidimensional gas chromatography-mass spectrometry (GC × GC–MS) with a statistical approach,' *Forensic Chem.*, vol. 6, pp. 10–18, 2017, ISSN: 24681709. DOI: 10.1016/j.forc.2017.08.003. [Online]. Available: https://doi.org/10.1016/j.forc.2017.08.003https://linkinghub.elsevier.com/retrieve/pii/S2468170917300498.

[422] F. Büttner, J. Hagemann, M. Wellhausen, S. Funke, C. Lenth, F. Rotter, L. Gundrum, U. Plachetka, C. Moormann, M. Strube, A. Walte and H. Wackerbarth, 'Surface enhanced vibrational spectroscopy for the detection of explosives,' *Electro-Optical Infrared Syst. Technol. Appl. X*, vol. 8896, no. October 2013, p. 889 609, 2013, ISSN: 0277786X. DOI: 10.1117/12.2028736.

[423] S. Wold, M. Sjöström and L. Eriksson, 'PLS-regression: A basic tool of chemometrics,' *Chemom. Intell. Lab. Syst.*, vol. 58, no. 2, pp. 109–130, 2001, ISSN: 01697439. DOI: 10.1016/S0169-7439(01)00155-1.

[424] L Eriksson, T Byrne, E Johansson, J Trygg and C Vikström, *Multi- and Megavariate Data Analysis Basic Principles and Applications*. Umetrics Academy, 2013.

[425] C. A. Schneider, W. S. Rasband and K. W. Eliceiri, 'NIH Image to ImageJ: 25 years of image analysis,' *Nat. Methods*, vol. 9, no. 7, pp. 671–675, 2012, ISSN: 15487091. DOI: 10.1038/nmeth.2089.